Physical Modeling of Microtubule Force Generation And Self-Organization

Catalin Tanase

2004

Physical Modeling of Microtubule Force Generation and Self-Organization

Promotor:	Prof. Dr. Bela M. Mulder Hoogleraar Theoretische Celfysica Wageningen Universiteit
Promotor:	Prof. Dr. Marileen A. Dogterom Hoogleraar Biofysica Universiteit Leiden
Promotiecommisie:	Prof. dr. M. A. Cohen-Stuart Wageningen Universiteit, Wageningen
	Prof. dr. F. Jülicher Max Planck Institute-Physics of Complex Systems, Dresden, Germany
	Prof. dr. H. G. Muller Vrije Universiteit, Amsterdam
	Prof. dr. A. M. C. Emons Wageningen Universiteit, Wageningen

Cătălin C. Tănase

Physical Modeling of Microtubule Force Generation and Self-Organization

Proefschrift

ter verkrijging van de graad van doctor
op gezag van de rector magnificus
van Wageningen Universiteit,
Prof. dr. ir. L. Speelman,
in het openbaar te verdedigen
op woensdag 30 iuni 2004
des namiddags te 13:30 uur in de Aula

ISBN 90-8504-021-3

pentru Mirela

Contents

1 General Introduction and Motivation **11**
1.1 The Physical Approach in Life Sciences . . . 11
1.2 The Cytoskeleton . . . 11
1.3 Microtubule Dynamics . . . 12
1.4 Microtubule Structure . . . 12
1.5 Thesis Outline . . . 14
1.5.1 Microtubule Self-Assembly . . . 14
1.5.2 Microtubule Self-Organization . . . 15

I Microtubule Self-Assembly **19**

2 Brownian Ratchet Model for Stiff and Semi-Flexible Polymers **21**
2.1 Introduction . . . 21
2.2 Thermodynamics . . . 21
2.3 The Force Velocity Relation And The Stall Force . . . 23
2.4 A Brownian Ratchet . . . 24
2.5 A Brownian Ratchet Model For Semi-Flexible Polymers . . . 27
2.6 A Simplified Geometrical Picture . . . 30
Appendix A . . . 31
Appendix B . . . 34

3 Microtubule Force Production **35**
3.1 Introduction . . . 35
3.2 A Single Filament Model for Microtubules . . . 36
3.3 A Model for Collective Growth . . . 38
3.3.1 Definition of the Model . . . 40
3.3.2 The *Force-Velocity* Relation . . . 42
3.3.3 The Expression of the Stall Force and its Derivation . . . 43
3.3.4 Comments on the Stall Force . . . 46
3.4 Monte Carlo Simulations of the Model . . . 47
3.4.1 The *Force-Velocity* Relation . . . 47
3.4.2 The Lateral Offset of the Filaments and its Implications in Growth . . . 50
3.4.3 The Distribution of Filament Tips . . . 52
3.4.4 The Stall Force . . . 52
3.4.5 Load Effect on the off-Rate . . . 54
3.5 Discussions and Conclusions . . . 55

Appendix A: Exact Expressions for the Velocity of Growth in Two Particular Cases . . . 56
Appendix B: Periodicity and Mirror Symmetry in the *Velocity-Shift* Characteristics . . . 56
Appendix C: The Magic Numbers in *Velocity-Shift* Characteristics . . . 58

4 The Lateral Affinity Between Microtubule Proto-Filaments 59
4.1 Introduction . . . 59
4.2 The Strong Lateral Limit: A Helical Growth Model . . . 59
4.2.1 The Helical Growth . . . 59
4.2.2 The Helical Growth Criterion . . . 61
4.2.3 The Force-Velocity Relation in the Helical Growth Regime . . . 62
4.2.4 *Force-Velocity* Renormalization and Fit Analysis . . . 62
4.2.5 The Structure of Microtubule End in the Helical Growth Regime . . . 64
4.3 The Weak Limit: Developing Open Sheet Structures at Microtubule Ends . . . 65
4.4 Conclusions . . . 67
Appendix A: Derivation of the *Force-Velocity* Relation for Helical Growth Regime . . . 68
Appendix B: The Effective on- and off- Rates . . . 69

II Microtubule Self-Organization 73

5 Microtubule Self-Organization in Higher Plant Cells 75
5.1 Introduction . . . 75
5.2 Interphase Nematic Order Parameter . . . 77
5.3 A Helical Spring Model . . . 79
5.4 Elastic properties of flexible chains in confined geometry . . . 80
5.4.1 Example: A long string with one end free and the other clamped . . . 82
5.5 A Confined Elastic String . . . 83
5.5.1 Plane Capped Cylinder . . . 83
5.5.2 Spherocylinder . . . 84
5.5.3 Elastic string under the action of an external force . . . 84
5.6 Discussion and Conclusion . . . 86

6 Generic Aspects of Microtubule Self-Organization 89
6.1 Introduction . . . 89
6.2 Mean Field Theory . . . 90
6.2.1 Hypotheses . . . 90
6.2.2 General Equations . . . 91
6.2.3 Geometrical Constraints and Boundary Conditions . . . 93
6.2.4 Evolution Equations . . . 94
6.3 Linear Stability Analysis . . . 95
6.3.1 Periodic Boundary Conditions . . . 96
6.3.2 The Phase Diagram . . . 97
6.3.3 The Eigenstates . . . 99
6.4 Non-Linear Regime . . . 101
6.4.1 Adiabatic Approximation . . . 101
6.4.2 A Stationary Solution . . . 104
6.5 Conclusions and Open Questions . . . 105

7 Modeling Microtubule Self-Organization Driven by Active Components 107
7.1 Introduction . . . 107
7.2 A Microscopic Model . . . 108
7.2.1 The Dynamic Time Scale . . . 108
7.2.2 Modeling Motor-Filament Interaction . . . 109
7.2.3 An Active Force Model . . . 112
7.2.4 The Linear and Angular Velocities (Summary) . . . 115
7.3 Smoluchowski Equation and Moment Expansion . . . 115
7.3.1 Diffusion of Free Rods . . . 116
7.3.2 Excluded Volume Interaction . . . 117
7.3.3 Active Interaction . . . 121
7.3.4 The Evolution Equations of Moments (Summary) . . . 123
7.4 Linear Stability Analysis . . . 124
7.4.1 Linear Coupled Moment Equation . . . 124
7.4.2 Periodic Boundary Conditions . . . 125
7.4.3 Variable Separation and Eigenvalue Problem . . . 127
7.4.4 Isotropic-Nematic Instability . . . 127
7.4.5 Instabilities at Constant Density . . . 128
7.4.6 Instabilities towards Inhomogeneous States . . . 131
7.5 Discussion and Open Questions . . . 137
Appendix A: Technical Background . . . 138
A.1 Moments of the Distribution Function . . . 138
A.2 Irreducible Tensors . . . 139
A.3 Expansion into Irreducible Tensor Series . . . 141

Bibliography 143

Summary 151

Samenvatting 155

List of Publications 159

Acknowledgments 161

Chapter 1

General Introduction and Motivation

1.1 The Physical Approach in Life Sciences

Life means motion, and motion is the essential feature of life. What is the innate motive force of living matter? It looks like the nature of our world is such that questions like this one, in spite of being formidably simple to pose, are in fact insuperable to answer. The challenge of understanding living matter stems from its complexity, which is primarily due to the heterogeneity of biological systems and the huge regulatory network of interactions between their components. To meet this challenge implies dealing with information, in fact a huge quantity of information, and it is the hope that the processing of this gargantuan amount of data becomes more systematic by the use of the methods of the physical sciences.

The central dogma of biology, *evolution*, assumes that living organisms have evolved from simpler to more complex forms.. This perfectly fits the *reductionist* view of a physicist, who usually strips off all unnecessary details when he/she is interested in a particular phenomenology. Indeed, along the evolutionary path, we expect that a new and more complex characteristic can be acquired *only* by exploiting the already available and simpler possibilities. This point of view lends support for the physicist's *credo*, that *simple* governing principles may explain the complex behavior of living systems. In other words, the study of life becomes a form of reverse engineering, wherein we first try to identify the individual components of living systems, and subsequently we try to understand their emergent properties from the relationship between these components.

1.2 The Cytoskeleton

Let us illustrate the previous statements with the example of the *cytoskeleton*, which is a key component of a living eukaryotic cell.

The cytoskeleton is a network of protein filaments that is deeply involved in the functioning of the cell. For example, it is due to the cytoskeleton that cells can adopt a certain shape. Further, the locomotion of the cell is made possible by the continuous reorganization of the cytoskeletal network [1]. The cytoskeletal filaments also serve as tracks for motor proteins that transport cargos with cellular material across the cell.

There are three types of protein filaments in the cytoskeleton, *i.e. actin filaments, microtubules*, and *intermediate filaments*. What is particular to actin filaments and microtubules is that their corresponding protein subunits, *i.e.* actin and tubulin, are highly conserved along the evolutionary path of eukaryotes. This high degree of conservation suggests that these protein subunits already posses all the properties that fit the protein filaments to basic cellular activities that remain un-

changed along the evolutionary time line. This makes them particularly interesting objects for a bottom-up study, since this fact recommends them as being the simplest among other components of the cell.

Because filaments are one of the simplest components inside the living cell, it may come as a surprise to learn that microtubules are the building blocks of the mitotic spindle formed during the cell division. Indeed, the division machinery is expected to be extremely complex, since it is responsible for the segregation of the chromosomes, and very few mistakes are tolerated when the genetic material is distributed to the daughter cells. A repeated malfunction in the division mechanism implies the inheritance of potentially serious genetic defects. For life to persists, the offsprings must have the best starting position.

1.3 Microtubule Dynamics

How it is possible that microtubules can form a reliable scaffold for the mitotic spindle? It is not yet fully understood today, how the mitotic mechanism precisely works. However, significant progress in this direction was made in 1984 with the discovery of the *dynamic instability* of microtubules [2]. Dynamic instability is the alternation in time of microtubules between, the two dynamically different states of growing and shrinking. More precisely, after a period of *growth* due to polymerization, which typically lasts for minutes, microtubules suddenly switch to a phase of rapid *shrinking*, due to the loss of subunits, and it could be a matter of seconds for them to eventually disappear. This switch from the growing to the shrinking state is called a *catastrophe*. Sometimes, *rescue* events are possible, *i.e.* microtubules switch from disassembling to the growing state again. There is a number of factors that regulate the dynamics of microtubules. For instance, microtubule associated proteins (MAPs) bind to microtubules and regulate their dynamics. During metaphase, when all chromosomes are aligned at the median plane of the spindle, a chemical signal triggers catastrophes in all microtubules simultaneously. While shrinking, microtubules drive the attached chromosome halves towards each of the two spindle poles, where the nuclei of the two daughter cells will be formed.

Dynamic instability is a property of microtubules unique among all polymers. It is also a crucial property, since microtubules need to self-organize in different structures during the cell cycle. For example, asters and the mitotic spindle are built up with the reuse of the same material, *i.e.* tubulin.

Since its discovery in 1984, further biochemical studies have shown [3] that dynamic instability is a profound non-equilibrium process that is powered by the hydrolysis of GTP, which binds to the microtubules. Although dynamic instability is a dominant effect in many microtubule arrays, its precise mechanism and biological function are still open questions.

1.4 Microtubule Structure

Let us have a closer look at the structure of a microtubule for a better understanding of its properties.

The subunits of a microtubule come in the form of heterodimers composed of two different strains of tubulin, *i.e.* α and β tubulin, with slightly different biochemical properties. The subunits are of $\delta = 8\,nm$ in size, and they chain head-to-tail in the form of linear aggregates, which we call *protofilaments*. These protofilaments connect laterally to form a cylindrical sheet, resulting in a tubular hollow aggregate with a diameter of $25\,nm$, *i.e.* the microtubule (see Fig. 1.1).

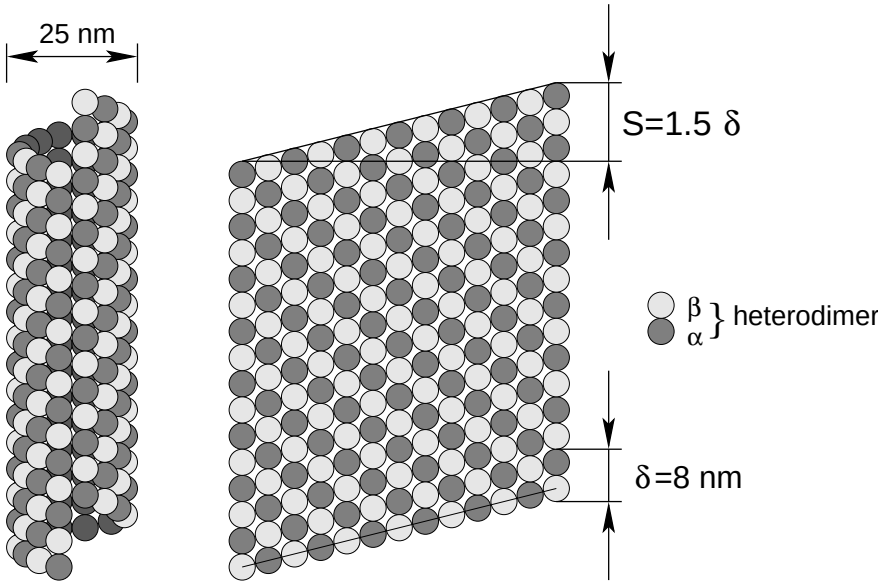

(a) A Lattice

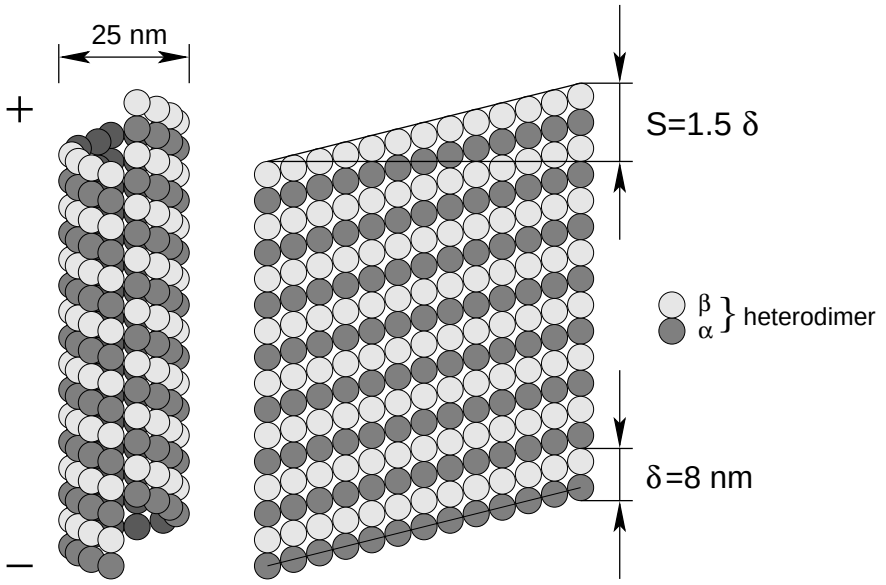

(b) B Lattice

Figure 1.1: Microtubule structure. Dimers, that consists of $\alpha - \beta$ tubulin are head-to-tail assembled in the form of protofilaments. These protofilaments are laterally bonded on a cylindrical sheet, giving the tubular shape of microtubules. There are two types of lattice: the A Lattice (a) and the B Lattice (b). Experimental evidence strongly favors the case of B Lattice, which presents also a seam. The value of the offset between adjacent filaments is such that the seam does not exist in the case of 10 or 16 profilaments.

Direct observation from cryo-electron micrographs suggests that under normal conditions the microtubule is made of $N = 13$ protofilaments. Between any adjacent protofilaments there is a longitudinal positional offset, such that the overall offset between the first and the last protofilament, counted around the circle, is $S = 1.5\,\delta$.

The protofilaments can be arranged into two different types of lattice, the A Lattice and the B Lattice, due to different possible orientations of the heterodimer inside the protofilaments (see Fig 1.1 (a) and (b)) [4]. A significant difference between the two cases is the existence of a seam in the case of the B Lattice, which is the consequence of a lateral misfit between the α and β tubulin, at the lateral contact between the first and the last filament. Cryo-electron micrographs bring compelling evidence for the existence of the seam, which then favors the model of the B Lattice. We mention that in the case of the B Lattice, the seam does not exist if the there are $N = 10$ or $N = 16$ filaments in the assembly.

Another important consequence of the B lattice is the existence of an inherent polarity in microtubule structure. In the case of the A Lattice, the orientation of dimers alternate from one protofilament to the next, and although the individual protofilaments are polar, the assembly as a whole is not. However, a polar assembly guarantees the possibility of the directional transport of cargos with the help of motor proteins. In other words, the microtubule polarity is the symmetry breaking factor that defines the direction of motion for motor proteins.

The asymmetry of the two microtubule ends also shows up in different biochemical properties. For instance, polymerization is possible at both ends, but one end is growing much faster than the other. In the literature, the *plus end* is referred to as the end that exposes the β tubulin monomers outward and the other end is called the *minus* end. The plus end is the faster growing of the two ends.

Due to the addition and removal of subunits, the microtubule ends are not expected to be regular. Cryo-electron microscope images show that depending on the microtubule dynamic state [5], the microtubule plus ends show three different topological forms. More exactly, during the state of growth, the plus end looks like an open sheet, with the microtubule seam opened up for over a length of $100\,nm$ or more [5] (see also Fig. 1.5.1 and Fig. 1.3). In the shrinking state, the images suggest that the lateral bonds between protofilaments are breaking from the microtubule end and the protofilaments are peeling off. There is possibly also an *intermediate* state between growing and shrinking, which corresponds to blunt ends of microtubules [5].

1.5 Thesis Outline

1.5.1 Microtubule Self-Assembly

In the first part of this thesis, we investigate some physical aspects of growing microtubules. An important aspect of microtubules is their ability to generate pushing forces during the process of polymerization. Force generation makes a microtubule act like a particular type of molecular motor. For example, this process helps in nuclear positioning in fission yeast [6, 7], or in the positioning of the spindle poles during mitosis. *In-vitro* experiments also demonstrate the aster positioning in micro-fabricated chambers [8].

The key concept that we use in order to understand the force generation mechanism is the *Brownian ratchet* [9]. This concept explains how it is possible to extract work from an isothermal reservoir provided that the system is out of equilibrium. We will discus this concept in detail in Chapter 2 and illustrate it on the case of rigid one-filament polymers. The second major aim of this chapter is to generalize and adapt this concept to semi-flexible and more composite polymers like

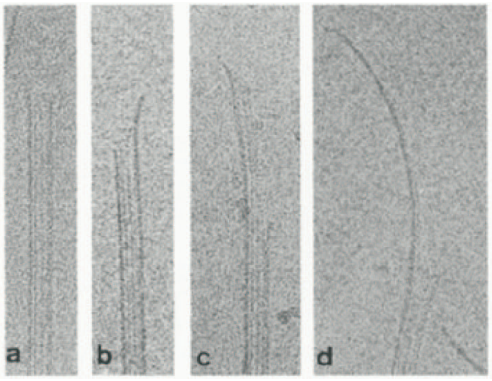

Figure 1.2: Cryo-electron microscope images show polymorphic microtubule ends, blunt ends (a), and open sheets (b), (c), and (d) (from Ref. [10]).

microtubules.

In Chapter 3 we will develop an explicit model for microtubule growth and compare this directly to experimental data. Direct quantitative comparisons with experiments shows the possibility to extract hints about both microtubule internal structure and the force generation mechanism itself. Unlike other models used in the literature, it is possible to address relevant physical issues of the growth mechanism on a minimal modeling basis. For example, we will see in Chapter 4 that without any reference to GTP hydrolysis, the model at hand can qualitatively reproduce the open sheet structure that exist at the plus ends of growing microtubules.

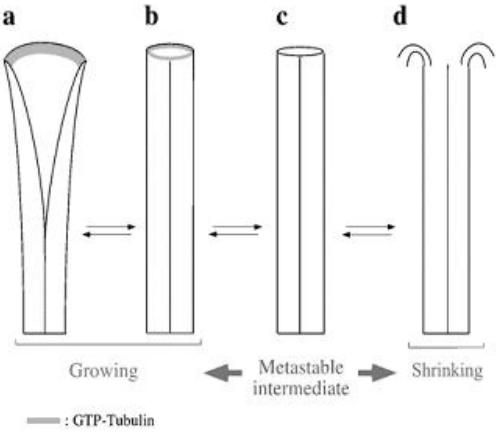

Figure 1.3: A cartoon after the cryo-electron microscope images. It is suggested that the microtubule plus end is structured like an open sheet during the growth (a), and the protofilaments are peeling off during disassembling (d). It is proposed the existence of an intermediate state that corresponds to blunt ends (c) (after Ref. [5]).

1.5.2 Microtubule Self-Organization

Self-organization of microtubules is another important feature of living cells that involves dynamics on a very different time and length scale than that of the growth process. It might be surprising that such a regime exists since, as we have previously seen, the microtubule internal structure is not particularly sophisticated. However, a variety of MAPs are responsible for creating such a multi scale dynamics.

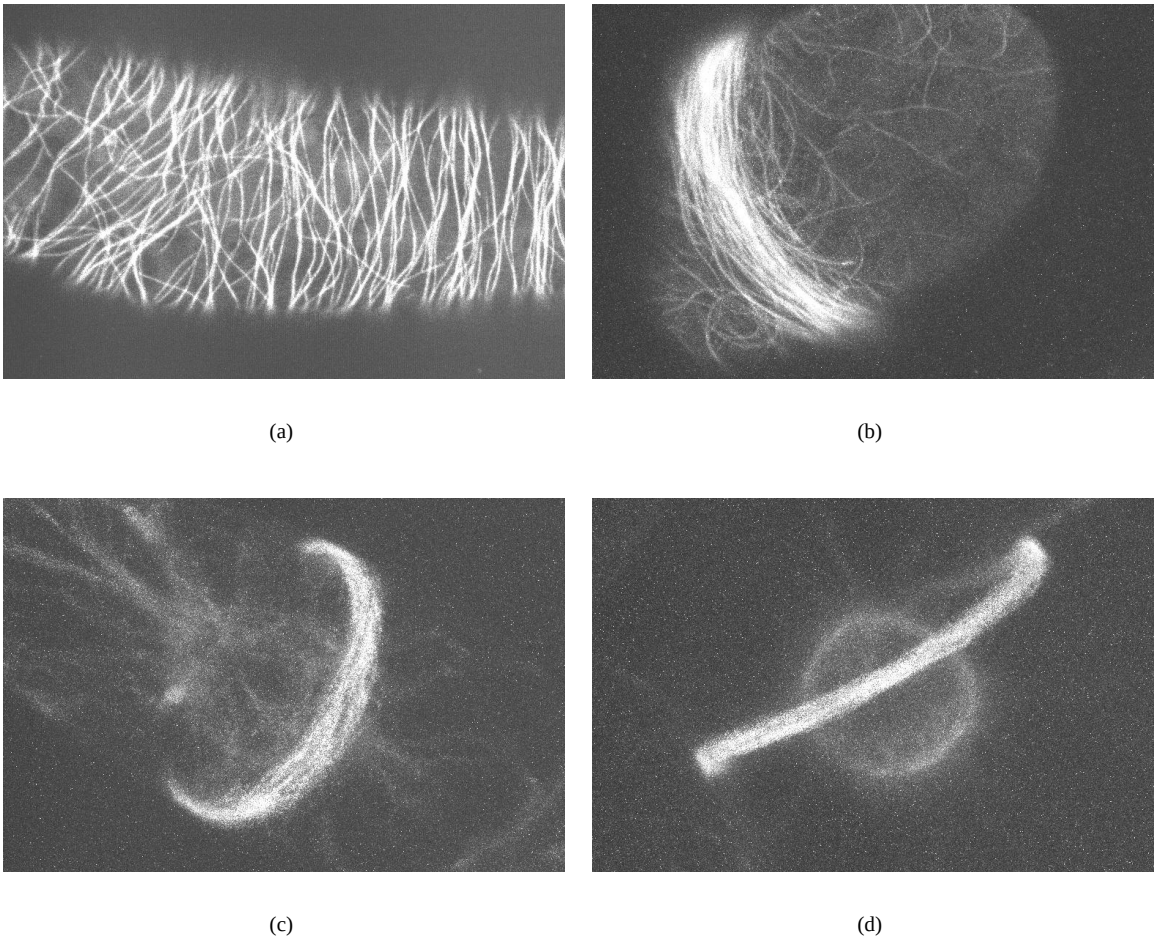

Figure 1.4: The cortical self-organization of microtubules in higher plant cells. A plant cell is shaped as a cylinder with a length of $60 - 100\,\mu m$ and a diameter of $30\,\mu m$. These images show GFP labeled microtubules in tobacco BY-2 cells. During interphase, the microtubules show a transversal regular array (a). As the cell progresses toward division, the array becomes narrower and keeps its transversal orientation (b), (c), and (d), forming the preprophase band (PPB). After the break down of PPB, the tubulin is reused to form the mitotic spindle. In the late stage of the PPB, part of the labeled tubulin already marks the nucleus (d). (Courtesy of Jan Vos, EMBL Heidelberg, Germany)

Cells of different types develop different cytoskeletal structure, depending on their specific functionality. Radically different microtubule structures are observed in higher plant cells, with no direct analog in animal cells. For example, it is particular for higher plant cells to develop a regular transverse array of microtubules during interphase. During preprophase, *i.e.* just at the onset of the division, the wide interphase array narrows down to a $3 - 4\,\mu m$ wide band around the nucleus. The position of this so-called the preprophase band (PPB) correlates with the position of the future separation wall between the daughter cells. However, the precise biological function of these two particular microtubule arrangements is still poorly understood.

The aim of the second part of these thesis is to investigate the possible mechanisms that drive these particular arrangements in higher plant cells. In Chapter 5 we present a detailed description of the system. We first try to ignore the presence of MAPs and derive the self-organization of microtubules as driven by passive ingredients only. More precisely we will explore the interplay between the elastic properties of extended polymers and their confinement in a closed system.

In Chapter 6, we explore the role of the active factors, *i.e.* motor proteins that actively cross

link microtubules and drives them into large scale pattern formation. The method of choice is *mean field theory* and we adopt a *top-down* approach in the sense that we do not make any specific assumptions concerning the motor-filament interaction at the microscopic level. The macroscopic equations are derived on the basis of invariance properties that have to be obeyed by the physical system that we study. In this way, based on symmetry analysis alone, our aim is to derive a minimal set of conditions that could explain patterns like the PPB.

In Chapter 7 we develop the complementary *bottom-up* approach, by defining a specific microscopic model from which we derive the macroscopic evolution equations of the system. The aim of this chapter is rather broad. First of all we can analyze how the results in this case correlate with the generic results that we derive in Chapter 6. Second, the methods that we develop allow the application of our theory to both 2D and 3D systems, which means that we can in principle apply it to many other systems as well. Third, due to the generality of the issues that we can address, we can easily fit this work into the much broader context of pattern formation in non-equilibrium systems.

Part I

Microtubule Self-Assembly

Chapter 2

Brownian Ratchet Model for Stiff and Semi-Flexible Polymers

2.1 Introduction

Along the evolutionary path, living cells developed different chemical energy transducers needed to supply the motility processes with the required mechanical force. Molecular motors like kinesins, dyneins and myosins use chemical energy stored in fuel molecules of ATP to produce mechanical force needed, for example, in vesicle transport across the cell or in muscle contractions.

A different type of motors are the polymerization ratchets. The chemical binding energy available from the polymerization of cytoskeletal polymers is transformed into mechanical work exerted on a given target. There is already strong evidence that actin polymerization is harnessed to produce force in cells [11]. An example is actin-dependent motility such as cell crawling and *Listeria* propulsion [12]. Other cellular processes like filopodial and lamellipodial protrusions are good examples as well. *In vitro* evidence of force generation from chemical energy comes from experiments on actin polymerization within liposomes [13]. It was observed that the polymerizing fibers extruded long spikes, just like filopodia, from the otherwise spherical liposomes. Similar observations were made using tubulin [14, 15]. These experiments prove that polymerization can produce a pushing force strong enough to deform a lipid bilayer.

2.2 Thermodynamics

General thermodynamic arguments can be used to support the idea of converting polymerization energy into work. It can be shown that the free energy release at a polymerization event can be adequate to generate mechanical force ([16], [17]).

We present a simple kinetic picture of a rigid polymer that is undergoing polymerization against a given load (see Fig. 2.1). The polymerization and de-polymerization rates, k_{on} and k_{off} can be related to the chemical energy ΔG, which is released for each inserted subunit. The probability rate that corresponds to polymerization is determined by the energy barrier ΔG^* and is given by Kramers formula ([18, 16]):

$$k_{on} = const \, \exp\left(-\frac{\Delta G^*}{k_B T}\right) \tag{2.1}$$

A similar relation holds true for the de-polymerization process. The *off*-rate is given now by a

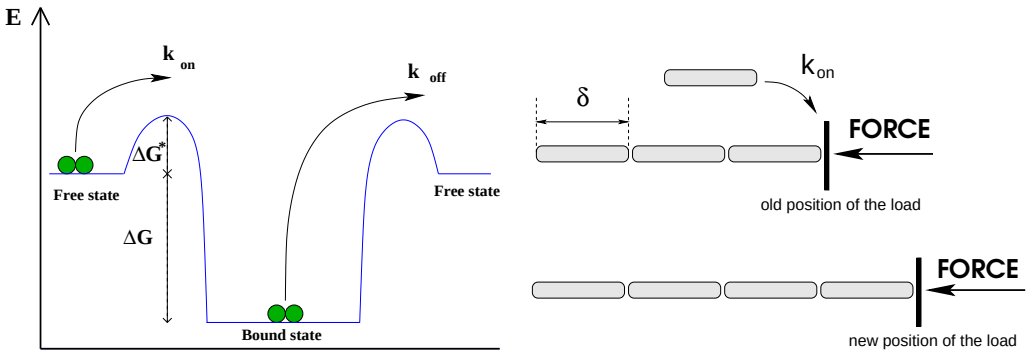

(a) (b)

Figure 2.1: A kinetic picture for the polymerizing ratchet

different energy barrier, *i.e.* $\Delta G + \Delta G^*$:

$$k_{off} = const \, \exp\left(-\frac{\Delta G + \Delta G^*}{k_B T}\right) \tag{2.2}$$

The proportionality constant $const$ is the same in the last two equations because if there is no chemical energy ΔG then the polymer is not growing on average and therefore the *on*- and *off*-rates must be equal.

Dividing the last two equations, the energy barrier ΔG^* is eliminated and we have the following *general* relations between the kinetic coefficients, k_{on} and k_{off}, and the released free energy ΔG:

$$\frac{k_{on}}{k_{off}} = \exp\left(\frac{\Delta G}{k_B T}\right) \tag{2.3}$$

For a *freely* growing polymer, *i.e.* in the absence of any load, the chemical energy has a specific value $\Delta G = \Delta G^0$, which is fully released to the bath. For this particular case, the *on*- and *off*-rates, k^0_{on} and k^0_{off}, are satisfying the same kinetic equation as Eq. (2.3):

$$\frac{k^0_{on}}{k^0_{off}} = \exp\left(\frac{\Delta G^0}{k_B T}\right) \tag{2.4}$$

Let us consider now the case of a load. The load is imagined as an object which is pushed against the polymer by a force F. If a subunit is inserted, then the load is displaced against the applied force by a distance that is equal to the subunit size δ. This means that the amount of work $W = F\,\delta$ is done. The energy needed for this work is supplied by the chemical energy ΔG^0, which is released after a polymerization event. In the presence of the load only a part of this energy, $\Delta G = \Delta G^0 - W$, is released to the bath of free subunits. The rest of it is *converted* into work by a specific mechanism. An example of such a mechanism is discussed in the next section, when we will discuss the concept of the *brownian ratchet*.

In the presence of the load, the kinetic rates are modified from their values in the free case. From Eq. (2.3) we see that the ratio of their values is given only by the chemical energy ΔG that is released to the bath. Since $\Delta G = \Delta G^0 - W$, and with the use of Eq. (2.4), from Eq. (2.3), we have:

$$\frac{k_{on}}{k_{off}} = \frac{k^0_{on}}{k^0_{off}} \exp\left(-\frac{W}{k_B T}\right) \tag{2.5}$$

This is the most general relation, derived on the thermodynamical grounds, which relates the kinetic rates in the presence and in the absence of the load. In plain words, the last relation shows that the ratio of the *on*- and *off*- rates decreases from the free case in the presence of the load by a Boltzmann factor that depends on the work done against the load.

2.3 The Force Velocity Relation And The Stall Force

Of course, if we know the *on*- and *off*- rates, k_{on} and k_{off}, we can evaluate how fast the polymer can grow on average. The velocity of growth is simply given by the product between the step size δ and the difference of the *on*- and *off*- rates:

$$v = \delta\,(k_{on} - k_{off}) \tag{2.6}$$

We expect a dependency of the velocity of growth on the load F, more precisely, a decrease of the velocity of growth when the applied force F increases. Our key relation for deriving this dependency is Eq. (2.5). However, this relation does not fix separately the rates k_{on}, k_{off} to the corresponding values in the absence of the load k^0_{on} and k^0_{off}. A convenient choice for such relations is:

$$\begin{cases} k_{on} &= k^0_{on}\,\exp\left(-q\frac{W}{k_BT}\right) \\ k_{off} &= k^0_{off}\,\exp\left(-(q-1)\frac{W}{k_BT}\right) \end{cases} \tag{2.7}$$

These relations satisfy the most general condition expressed in Eq. (2.5), and Eq. (2.7) represent one of the most simple choices that we can make. We have just introduced a new parameter, q, which takes a real value. If the value of this parameter lies within the interval $0 < q < 1$, we see from Eq. (2.7) that, in the presence of the load, the polymerization rate is depressed, while the de-polymerization is enhanced. However, the choice that we made in Eq. (2.7) provides no physical interpretation of the parameter q, and therefore we cannot provide a strong argument of why the values of this parameter should be confined to the interval $0 < q < 1$. It may sound surprising that the polymerization could be stimulated in the presence of load, which could happen in the case of negative values $q < 0$. One might speculate that at the physical contact between the polymer end and the load some sticking proteins may regulate the dynamics of the polymer growth. For this reason we leave open the question of the restriction of the values of q to a certain interval.

With the help of Eq. (2.5), the velocity of growth can be rewritten explicitly from Eq. (2.6) (if we write also $W = F\,\delta$):

$$v(F) = \delta\left(k^0_{on}\,\exp\left(-q\frac{F\,\delta}{k_BT}\right) - k^0_{off}\,\exp\left(-(q-1)\frac{F\,\delta}{k_BT}\right)\right) \tag{2.8}$$

In Fig. 2.2 we can see different profiles of the force-velocity relation for different values of the parameter q. Particularly, when the de-polymerization rate is not affected by the presence of the load, *i.e.* $q = 1$, the velocity becomes:

$$v(F) = \delta\left(k^0_{on}\,\exp\left(-\frac{F\,\delta}{k_BT}\right) - k^0_{off}\right) \tag{2.9}$$

The velocity of growth decreases with the applied force, and the growth stops for a finite value of the force. We call the corresponding value of that force the *stall* force, F_{stall}. Equating to zero

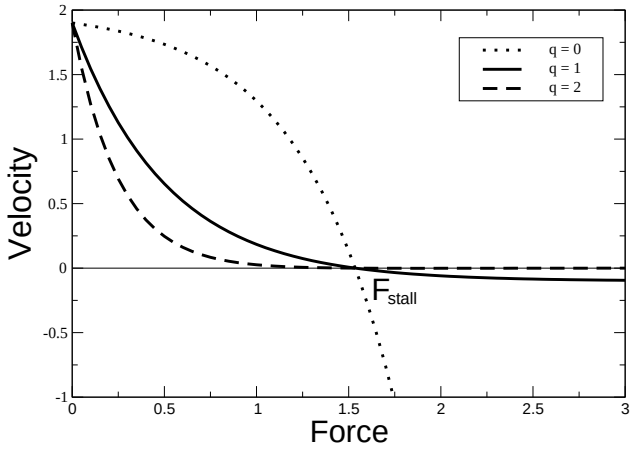

Figure 2.2: The *force-velocity* relation for a stiff polymer

the velocity from Eq. (2.8) we derive the following expression for the stall force:

$$F_{stall} = \frac{k_B T}{\delta} \ln\left(\frac{k_{on}^0}{k_{off}^0}\right) \tag{2.10}$$

The expression Eq. (2.10) for the stall force is independent on the parameter q. We stress that it is even independent on the choice Eq. (2.7). The reason is evident from Eq. (2.5): when the growth is stalled the effective rates k_{on} and k_{off} are equal, and if we set to unity the *lhs* of Eq. (2.5) we recover Eq. (2.10).

2.4 A Brownian Ratchet

However, thermodynamic arguments tell us little about the underlying mechanism of how work is produced from chemical energy. In this section we will present such a mechanism, which is called *Brownian ratchet*. In our brief introduction to this concept we will learn that thermal fluctuations play the key role in transducing the chemical energy into *directed motion*, and hence why the epithet *Brownian*.

In 1993 Peskin *et al* ([9]) proposed a model of how a polymerization process can generate force. They imagined a one dimensional object that was diffusing in the presence of an external force (see Fig. 2.3). The external force pushes the object against a stiff polymer, which is growing by polymerization. We can see from Fig. 2.3 that as the polymer is growing, the average position of the diffusive object was displaced and hence work was done on the diffusive object as it is being pushed to the right.

In this system a monomer can be inserted by polymerization if it is sterically allowed in the gap between the polymer tip and the brownian object. In the absence of the force the density distribution $c(x)$ of the object is wide and the object is not restricting the growth of the polymer. In this case subunits are inserted with a rate k_{on}^0. In the presence of the force F the probability $P_{x>\delta}$ of having the gap wider than the subunit size δ is limiting the polymerization rate to:

$$k_{on} = k_{on}^0 \, P_{x>\delta} \tag{2.11}$$

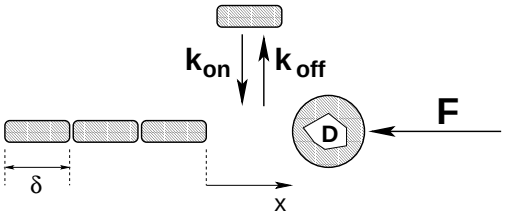

Figure 2.3: A Brownian ratchet: a diffusive object is moving in the presence of an external field against a growing stiff polymer

This model thus presents obvious corrections to be made for the *effective* polymerization rate in the presence of a load. However, it predicts no change for the de-polymerization rate, *i.e.* $k_{off} = k^0_{off}$. A load can have an effect on the de-polymerization as well. For example the induced stress in the polymer body by the mechanical contact between the polymer end and the moving object can induce slight deformations in the monomers. In the case of proteins, like tubulin, a 3D conformational change does have an effect on the biochemical properties, and hence on the de-polymerization rate of monomers. However, understanding how this change comes into action is beyond the aim of our presentation of the Brownian ratchet model and we will not delve into unnecessary details.

In the remainder of this section we will evaluate the average velocity of growth of the polymer and from this the stall force F_{stall}. Since the velocity $v = \delta\,(k_{on} - k_{off})$ is given by:

$$v = \delta\,(k^0_{on}\,P_{x>\delta} - k^0_{off}) \tag{2.12}$$

it follows that we need to evaluate the probability $P_{x>\delta}$. In a statistical ensemble, if we know the number of objects at a distance larger than a subunit size from the polymer tip, $I_1 = \int_{x=\delta}^{\infty} dx\, c(x)$, and the total number of the objects $N = \int_{x=0}^{\infty} dx\, c(x)$, then the probability of having the gap with the required size, $P_{x>\delta} = I_1/N$, is given by:

$$P_{x>\delta} = \frac{\int_{x=\delta}^{\infty} dx\, c(x)}{\int_{x=0}^{\infty} dx\, c(x)} \tag{2.13}$$

Then, the velocity of growth Eq. (2.12) can be written in a more explicit form:

$$v = \delta\left(k^0_{on}\frac{\int_{x=\delta}^{\infty} dx\, c(x)}{\int_{x=0}^{\infty} dx\, c(x)} - k^0_{off}\right) \tag{2.14}$$

Following Peskin *et al* [9] (see also Appendix), we can derive the equation for the density distribution of the diffusing object:

$$\frac{\partial\, c}{\partial t} = D\frac{\partial^2 c}{\partial\, x^2} + \frac{F\,D}{k_B\,T}\frac{\partial\, c}{\partial\, x} + k^0_{on}\left(c(x+\delta,t) - \Theta(x-\delta)\,c(x,t)\right) + k^0_{off}\left(\Theta(x-\delta)\,c(x-\delta,t) - c(x,t)\right) \tag{2.15}$$

where $\Theta(x-\delta)$ is the Heaviside step function:

$$\Theta(x) = \begin{cases} 1 & \text{if } x > 0 \\ 0 & \text{if } x < 0 \end{cases} \tag{2.16}$$

We have an interesting limiting case when we suppose that the diffusion time scale is much smaller than the corresponding scale associated with the polymerization and de-polymerization

processes, *i.e.*

$$\begin{cases} k_{on}^0 \ll D/\delta^2 \\ k_{off}^0 \ll D/\delta^2 \end{cases} \tag{2.17}$$

We introduce now the parameter

$$\varepsilon = \frac{k_{on}^0\,\delta^2}{D} \tag{2.18}$$

which is arbitrarily small in the regime of fast diffusion limit. In this regime the velocity of growth can be expressed as an expansion in ε, which in the case of small de-polymerization $k_{off}^0 \ll k_{on}^0$ takes the form (see Appendix):

$$v(F) = \delta\, k_{on}^0 \left(e^{-\frac{F\,\delta}{k_B\,T}} - 2\,\varepsilon\, \frac{e^{-2\frac{F\,\delta}{k_B\,T}} \left(e^{\frac{F\,\delta}{k_B\,T}} - \frac{F\,\delta}{k_B\,T} - 1 \right)}{\left(\frac{F\,\delta}{k_B\,T} \right)^2} \right) + \mathcal{O}(\varepsilon^2) \tag{2.19}$$

Particularly, in the case of fast diffusion limit, *i.e.* $\varepsilon \to 0$, we get from the last equation that $v(F) = \delta\, k_{on}^0 \exp(-F\,\delta/k_B\,T)$. We can understand this result directly from the ratchet equation Eq. (2.15). Indeed, in the fast diffusion limit we can neglect the *reaction* terms from the Eq. (2.15) (*i.e.* the terms proportional to k_{on}^0 and k_{off}^0). We are left with a diffusion equation of a particle in an external field, which yields the stationary solution $c(x) = c_0\, \exp(-F\,x/k_B\,T)$. This is nothing else than the Boltzmann distribution known from equilibrium statistical mechanics. The reason why we get Boltzmann distribution in the present limiting case is apparent: the polymerization and de-polymerization are slow processes and the relaxation time scale of the diffusive particle is small.

Knowing that the density distribution scales as $c(x) \propto \exp(-F\,x/k_B\,T)$ in the fast diffusion limit of Eq. (2.17), from Eq. (2.13) we have

$$P_{x>\delta} = \exp\left(-\frac{F\,\delta}{k_B\,T} \right) \tag{2.20}$$

and the velocity of growth Eq. (2.12) becomes [9]:

$$v(F) = \delta \left(k_{on}^0 \exp\left(-\frac{F\,\delta}{k_B\,T} \right) - k_{off}^0 \right) \tag{2.21}$$

Another observation is to note the identity of Eq. (2.21) to Eq. (2.9). This is not a simple coincidence. The later equation was derived in the previous section on general grounds by using arguments from thermodynamics and equilibrium statistics. This corresponds precisely to the conditions of fast diffusion limit from which Eq. (2.21) was derived, since the system has enough time to relax between two events of polymerization and/or de-polymerization. The *stall force* F_{stall} can be derived from Eq. (2.21) by solving the equation $v(F) = 0$, and of course, we get the same result as Eq. (2.10), $F_{stall} = k_B\,T/\delta\, \ln(k_{on}^0/k_{off}^0)$.

It is interesting to notice that this result for the stall force is not dependent on the equilibrium statistics assumptions that we made in deriving it in the previous section, *i.e.* the result is the same for an arbitrary value for the diffusion constant. We can understand this as follows. Eq. (2.15) is in fact a *reaction-diffusion* equation of an object which is diffusing in an external field. The *reaction terms* are due to the polymerization and de-polymerization processes. Indeed the origin of the coordinate system is set to the polymer end which is shifted to the right or to the left when a subunit is inserted or extracted. As a result the diffusive particle is seen as jumping from one

position to another with a step size equal to the subunit size and with a rate given by the *on*- and *off*- rates, k_{on}^0 and k_{off}^0 respectively (see Appendix for a detailed mathematical description of the model). In the case of stalled growth we expect that the *reaction* terms are identically zero, since the particle is not displaced on *average*:

$$\begin{cases} k_{on}^0\, c(x+\delta) - k_{off}^0\, c(x) = 0 \\ \Theta(x-\delta)\big(k_{on}^0\, c(x) - k_{off}^0\, c(x-\delta)\big) = 0 \end{cases} \tag{2.22}$$

If the jumping events cancel out, we are left from Eq. (2.15) with a pure diffusion equation, which gives the stationary solution:

$$c(x) = c_0\, \exp\!\left(-\frac{F_{stall}\, x}{k_B T}\right) \tag{2.23}$$

The value of the stall force is computed from this solution by imposing the conditions from Eq. (2.22), which gives exactly the same expression as the *thermodynamic* result Eq. (2.10). One can check that the velocity of growth, given by Eq. (2.14), is zero when we take the ansatz Eq. (2.23) from the density distribution $c(x)$ and the value of the stall force as it is given by the thermodynamic formula Eq. (2.10). In short, the stall force for a Brownian ratchet is *generally* given by

$$F_{stall}^{B.R.} = \frac{k_B\, T}{\delta} \ln\!\left(\frac{k_{on}^0}{k_{off}^0}\right) \tag{2.24}$$

and is *not* restricted by any thermodynamic assumption.

2.5 A Brownian Ratchet Model For Semi-Flexible Polymers

We have learned from the previous section that thermal fluctuations of the mechanical barrier play the key role in converting the chemical energy into work. However, one of the major features of the model is the stiffness of the polymer, which is obviously unrealistic. For example, the *in-vitro* experiments [19] show that *breathing* modes are induced in microtubules, due to thermal fluctuations, when microtubules were pushing against the chamber wall.

We present a cartoon of this situation under discussion in Fig. 2.4, where we draw a microtubule that was growing from its fixed seed toward a *fixed* wall, which is exactly the case of the experiments described in [19, 20]. Video microscopy images showed that the microtubule end was eventually caught by wall aspersions, which prevented the microtubule end to slip along the wall [19]. Elastic stress was built up in the microtubule body, since the microtubules were seen to buckle as they were pushing against the wall. As the microtubules touched the wall they continued to grow in length but at a slower rate. The thermal fluctuations were visible in the video images, which means that gaps can be opened between the end of the microtubule and the wall. This explains why polymerization can be still possible under the condition that mechanical stress was developing in microtubules.

The present situation suggests that the mechanism of force generation is similar in nature with the polymerization ratchet that we have described in the preceding section. The role of the old thermally fluctuating object is played now by the microtubule end itself, and the role of the applied force is played by the elastical stress in the microtubules.

Let us closely adapt the stiff polymerization ratchet to semi-flexible polymers. As a *very* first step, for the sake of simplicity, we imagine a *single filament* semi-flexible polymer. In a similar manner like Mogilner and Oster [21, 22], we can map the *buckled* semi-flexible filament from Fig. 2.4 (a) to a *one dimensional* elastic spring, Fig. 2.4 (b), which is oscillating against a *fixed* wall

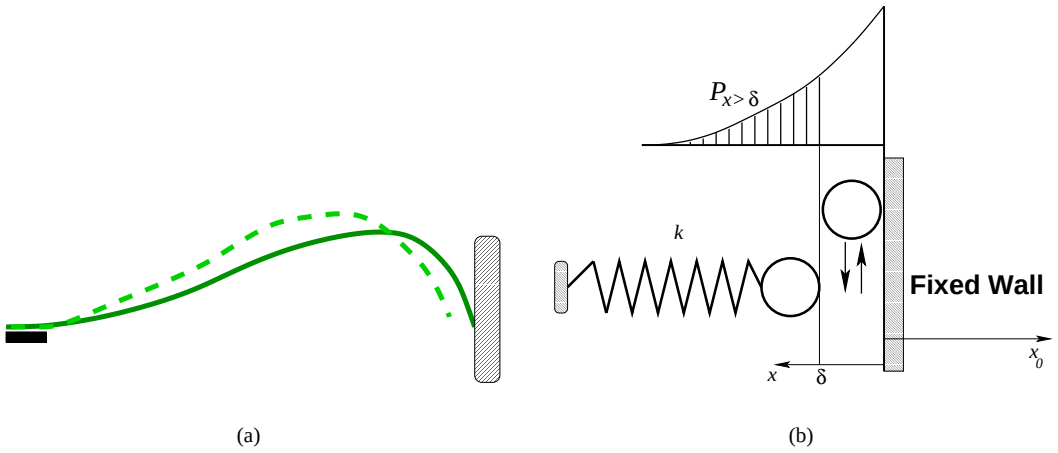

Figure 2.4: A semi-flexible filament as a polymerizing brownian ratchet. (a): Elastic stress builds up in the filament body as a result of polymerization, and the filament buckles. Thermal fluctuations of the filament allow gap openings between filament tip and the wall, which makes polymerization possible. (b): Thermal fluctuations are much faster than the subunit addition-removal events. On the time scale of thermal fluctuations, the semi-flexible filament is viewed as a 1D spring, which fluctuates against the fixed wall. The elastic stress in the spring narrows the probability $P_{x>\delta}$ for gap opening, which limits the polymerization rate $k_{on} = k_{on}^0 P_{x>\delta}$. Between two polymerization events, the thermal average of the elastic force is actually the equivalent of the load from the Brownian ratchet model with a diffusive barrier (Peskin et, al. [9], see also Fig. 2.3).

due to thermal fluctuations. The bending elastic properties of the filament can be mapped to the elastic constant of the spring k only between two events of subunit addition or removal. We make the observation that, during growth, the spring constant is changing as the length of the polymer increases.

Another major assumption that is relevant for the rest of the present thesis is to suppose that the time scale of the thermal fluctuations is much smaller than the corresponding time scale related to the polymerization and de-polymerization processes [23, 21]. This implies that the density distribution of the spring end from Fig. 2.4 (b) is given from equilibrium statistical mechanics as

$$P(x) = c_0 \, \exp\left(-\frac{k\,(|x_0| + x)^2}{2\,k_B\,T}\right) \tag{2.25}$$

Indeed, the above is the Boltzmann distribution of a particle under the action of a an elastic spring. The origin of the coordinate axis is at the wall position and the x axis is oriented to the left, towards the spring (see Fig. 2.4 (b)). The relaxation position of the spring x_0 is negative in value since it is on the right side of the wall, because we suppose that the wall is compressing the spring. Therefore, the elastic energy of the situation presented in Fig. 2.4 (b) is $E = k\,(|x_0| + x)^2/2$ and hence the distribution Eq. (2.25).

In order for a polymerization event to happen, a gap wider that a subunit length δ needs to be opened in order to sterically fit a monomer between the filament end and the wall. The job of gap opening is done by the thermal fluctuations and the probability of having the gap wide enough is calculated from Eq. (2.25) as $P_{x>\delta} = \int_\delta^\infty dx\, c(x) / \int_0^\infty dx\, c(x)$. We write this in the explicit form:

$$P_{x>\delta} = \frac{\int_\delta^\infty dx\, \exp\left(-\frac{k\,(|x_0|+x)^2}{2\,k_B\,T}\right)}{\int_0^\infty dx\, \exp\left(-\frac{k\,(|x_0|+x)^2}{2\,k_B\,T}\right)} \tag{2.26}$$

For convenience we choose y as a dimensionless integration variable, and we get:

$$P_{x>\delta} = \frac{\int_{\sqrt{k/2k_BT}(\delta+|x_0|)}^{\infty} dy\ \exp\left(-y^2\right)}{\int_{\sqrt{k/2k_BT}|x_0|}^{\infty} dx\ \exp\left(-y^2\right)} \tag{2.27}$$

In the case of persistent polymers, like microtubules, we can show (see Appendix B)

$$\sqrt{k/2k_BT}\,|x_0| \gg 1 \tag{2.28}$$

Then, with the help of the expansion [24]

$$\frac{2}{\sqrt{\pi}}\int_{\alpha}^{\infty} du\, e^{-u^2} = \frac{e^{-\alpha^2}}{\sqrt{\pi}}\left(\frac{1}{\alpha} - \frac{1}{2\alpha^3} + \cdots + (-1)^n \frac{(2n-1)!!}{2^n\alpha^{2n}}\right) \tag{2.29}$$

we approximate Eq. (2.27), if we keep only the first dominant term:

$$P_{x>\delta} = \frac{|x_0|}{(\delta+|x_0|)}\exp\left(-\frac{k}{2k_BT}(\delta^2+2\delta|x_0|)\right) \tag{2.30}$$

In video microscopy images [19] the velocity of microtubules was observed to be about $1\mu m\, min^{-1}$, *i.e.* the relevant changes in microtubule lengths were in the order of micrometers, given also the resolution of the processed images. Because the size of a subunit $\delta = 8nm$ is in the order of magnitude of nanometers, we have $\delta \ll |x_0|$ for most of the practical situations, and with this we can further approximate Eq. (2.30) to:

$$P_{x>\delta} = \exp\left(\frac{-k|x_0|\,\delta}{k_B\,T}\right) \tag{2.31}$$

The elastic force in the spring is precisely $F_{el} = k\,|x_0|$, which is interpreted as the load of our ratchet. Therefore, if we put the last formula in the form:

$$P_{x>\delta} = \exp\left(\frac{-F_{el}\,\delta}{k_BT}\right) \tag{2.32}$$

we see that we arrived at the same startlingly simple formula for the gap probability $P_{x>\delta}$, which we have discussed about in the preceding section in the case of the ***stiff*** polymerizing ratchet in the fast diffusion limit.

Finally, the polymerization rate of a ***semi-flexible*** filament is given by

$$k_{on} = k_{on}^0\ \exp\left(-\frac{F_{el}\,\delta}{k_B\,T}\right) \tag{2.33}$$

Since we did not make any assumption regarding the modification of the ***off***-rate, we derive a perfectly identical formula for the velocity of growth, Eq. (2.21).

Aside

We have to notice some geometrical artifacts due to the mapping between the real filament and the spring in Fig. 2.4. If we zoom in the details of the filament end at the wall contact (see Fig. 2.5), we have to realize that, because of the filament tilt at the wall, the ***effective*** subunit size δ^* should be given by the projection of the subunit size δ on the perpendicular direction on the wall, *i.e.* $\delta^* = \delta\cos\theta$. Because we map onto the one dimensional spring as in Fig. 2.4, then δ^* is the correct geometrical quantity that should enter the formula for the effective ***on-rate*** Eq. (2.33), $k_{on} \propto \exp(-F_{el}\,\delta^*/k_B\,T)$. However, the force ***reaction*** from the

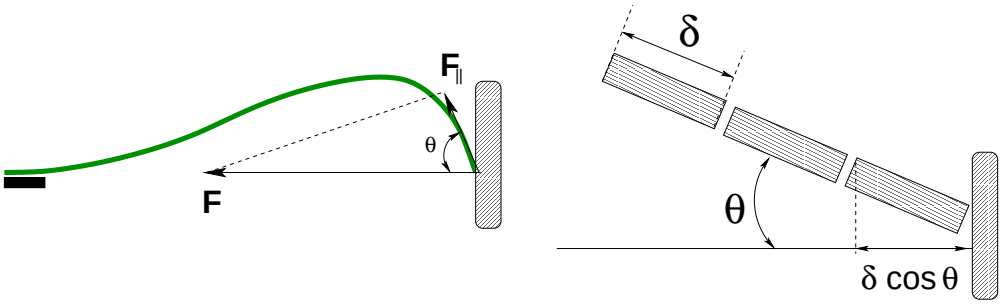

Figure 2.5: The detail at the wall contact of the filament tip suggests that the effective size of the inserted subunit should be its longitudinal projection $\delta^* = \delta \cos\theta$. An alternative interpretation is to regard the applied force not as the full force F but *only* its tangential component F_p, since the right physical quantity that should enter the model is the work $F\,\delta^* = F\,\delta\,\cos\theta = F_p\,\delta$.

wall F is supposed to be perpendicular to the wall, and the component which is tangent to the filament is $F_{||} = F\,\cos\theta$. Then $F\delta^* = F\delta\cos\theta = F_{||}\delta$. In other words, we can keep the effective size of the monomer as being equal to its full size, $\delta = \delta^*$, but we have to interpret the force F_{el} from Eq. (2.33) as not being the *reactio* force from the wall, which acts on the filament, but its projection to the tangent on the filament at its contact point on the wall, $k_{on} \propto \exp(-F_{||}\,\delta/k_B\,T)$. It is worth to mention that, in the case of force measurements in Ref. [19], it was precisely the parallel component of the force $F_{||}$ which was measured and interpreted as the load, which the *force-velocity* relation was determined from. Therefore, for the sake of simplicity, we make the convention that the Eq. (2.33) corresponds to the real physical situation.

2.6 A Simplified Geometrical Picture

In the view of the coming chapter, it is worthwhile to conclude our discussion with a simplified but relevant picture of a force producing mechanism from a semi-flexible polymerizing filament. Throughout this chapter we have seen as an emerging characteristic that, in the presence of a load, the on-rate of a polymerizing polymer scales with a Boltzmann factor, which is given by the work done against the load for each inserted monomer, *i.e.* $k_{on} \propto \exp(-F\delta/k_BT)$. This scaling was found when we discussed the generic thermodynamic aspects of a polymerizing motor, but it was also derived from specific models, like the Brownian Ratchet with a diffusive barrier, or from the semi-flexible filament model. The reason behind this scaling is expected to hold true for microtubules, because of the fast thermal fluctuations in semi-flexible polymers like microtubules.

Actually, the two specific Brownian Ratchet models, *i.e.* the diffusive barrier and the semi-flexible filament model, are mathematically equivalent in the limit of fast thermal fluctuations for the simple reason that the polymerization rate is identical

$$k_{on} = k_{on}^0 \exp\left(-\frac{F\,\delta}{k_B\,T}\right) \tag{2.34}$$

Therefore, both models can be further mapped to an even more simplified *geometrical* polymerization ratchet that we are going to present in the following. Instead of a semi-flexible polymer, whose end is moving from a fixed wall due to thermal fluctuations (see Fig. 2.4), we consider an *infinitely stiff* filament which is polymerizing against a *non-fixed wall* that is propped up by a force F (see Fig. 2.6). The polymerization rate is given by Eq. (2.34). In our geometrical model there are no explanations of how gaps are opened between the filament tip and the wall and therefore how monomers can be inserted with rate from Eq. (2.34). However, it is precisely this rate that

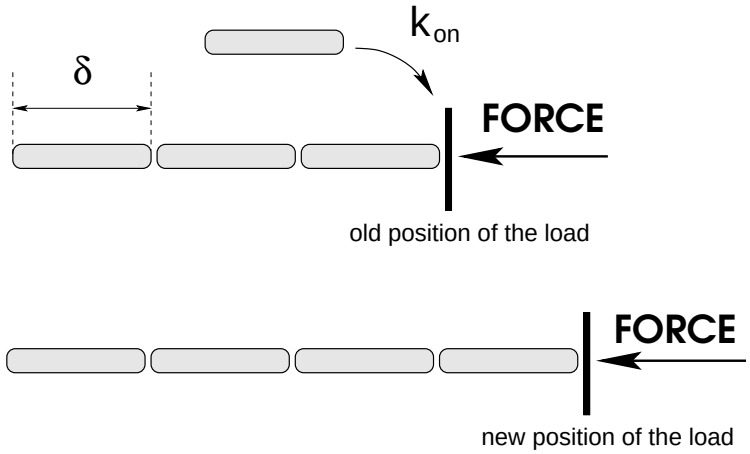

Figure 2.6: A geometrical picture of the polymerizing ratchet. A stiff polymer is growing against a *non-fixed* wall, which is pushed by a force F against the filament. The polymerization rate is normalized by a Boltzmann factor (see Eq. (2.34)). The *off-rate* k^*_{off} is not affected by the load in this model.

includes the physical details. In the previous sections, we showed that thermal fluctuations can help gaps to open, and how these fluctuations are integrated out in the form of the polymerization rate as it is expressed in Eq. (2.34).

The motivation for this *geometrical* picture should become clear in the next section. We will see that our *one-filament geometrical ratchet* can be generalized to a multi-filamentous complex in a straightforward manner. The reason of this generalization is obvious since microtubules are multi-filamentous assemblies and we will see the importance of the collective contribution from protofilaments to the microtubule force production mechanism.

Appendix A

In this Appendix we will derive the ratchet equation Eq. (2.15) and the growth velocity Eq. (2.19).

The Brownian ratchet equation

As it was described by *Peskin et. al.* [9], the Brownian ratchet was represented by a growing polymer and a one dimensional diffusive object which moves under the action of an external force $-F$. The Brownian motion of the particle is described by its diffusion constant D. The external force imprints to the particle a drift velocity $v = -D\,F/k_B\,T$.

The origin of the coordinate system is set at the polymer end (see Fig. 2.7). If a polymerization event takes place then the origin of the coordinate system jumps from left to right by a distance equal to the size of a monomer δ. Effectively the particle is seen as jumping from right to left by the same distance with a rate equal to the polymerization rate k^0_{on}. As we can see from the diagram shown in Fig. 2.7, for a polymerization event, when the position of the particle is $x < \delta$, the only contribution from jumps are coming from particles positioned at $x + \delta$. In the case of $x > \delta$, there are jumps of particles coming to x from $x + \delta$, however, particles that were already at x prior to polymerization are lost, since these particles are jumping to $x - \delta$. Similar reasonings are made also in the case of de-polymerization. To summarize we can write the following *diffusion-reaction*

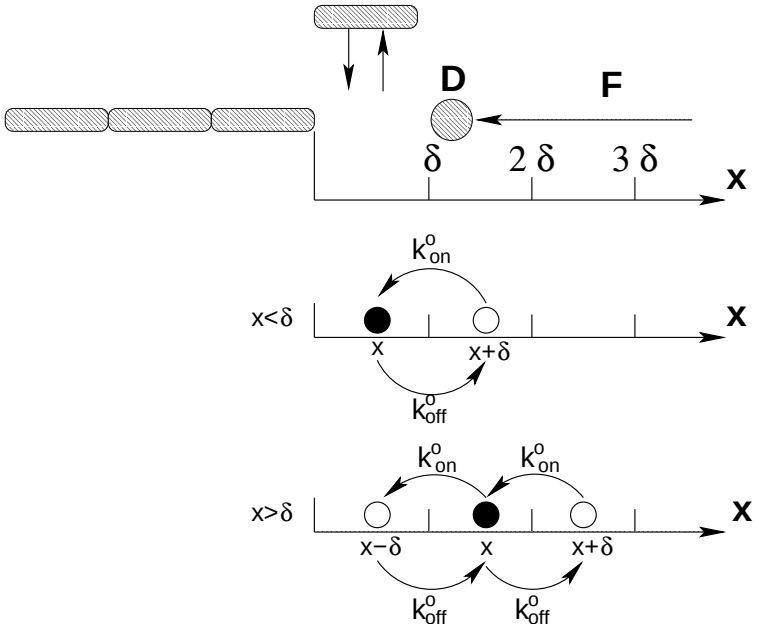

Figure 2.7: The diagram of the Brownian ratchet (after Peskin *el. al* [9])

equations:

$$\frac{\partial\, c}{\partial t} = D\frac{\partial^2 c}{\partial\, x^2} + \frac{F\, D}{k_B\, T}\frac{\partial\, c}{\partial\, x} + k^0_{on}\left(c(x+\delta,t) - k^0_{off}\, c(x,t)\right) \text{ if } x < \delta \tag{2.35}$$

and

$$\frac{\partial\, c}{\partial t} = D\frac{\partial^2 c}{\partial\, x^2} + \frac{F\, D}{k_B\, T}\frac{\partial\, c}{\partial\, x} + k^0_{on}\left(c(x+\delta,t) - c(x,t)\right) + k^0_{off}\left(c(x-\delta,t) - c(x,t)\right) \text{ if } x > \delta \tag{2.36}$$

These equations can be rewritten in a more compact form line Eq. (2.15).

Given the geometry, particles cannot cross the boundary at the left at $x = 0$, so we have to impose the condition that the current on this boundary is zero:

$$-D\frac{\partial c(0,t)}{\partial x} - \frac{DF}{k_B T}c(0,t) = 0 \tag{2.37}$$

Derivation of the growth velocity Eq. (2.19)

We are going to solve the Eq. (2.15) in the stationary case $\partial c/\partial t = 0$, *i.e.* $c(x,t) = c(x)$ in the case of high diffusion, and considering no polymerization $k^0_{off} = 0$. Then Eq. (2.15) becomes:

$$\frac{\partial^2 c}{\partial x^2} + \frac{F}{k_B T}\frac{\partial c}{\partial x} + \frac{k^0_{on}}{D}\big(c(x+\delta) - \Theta(x-\delta)\, c(x)\big) = 0 \tag{2.38}$$

We introduce the Laplace transform

$$\tilde{c}(s) = \int_0^\infty dx\, \exp(-s\, x)\, c(x) \tag{2.39}$$

After making some partial integration, we have:

$$\int_0^\infty dx\, \exp(-s\,x)\frac{\partial c}{\partial x} = -c_0 + s\,\tilde{c}(s) \tag{2.40}$$

$$\int_0^\infty dx\, \exp(-s\,x)\frac{\partial^2 c}{\partial x^2} = -\left.\frac{\partial c}{\partial x}\right|_{x=0} - s\,c_0 + s^2\tilde{c}(s) \tag{2.41}$$

We multiply both sides of Eq. (2.38) by $\exp(-s\,x)$, and we integrate after x in order to derive the corresponding equation for the Laplace transform $\tilde{c}(s)$. Using the last two equations and the boundary condition from Eq. (2.37) we can express the Laplace transform as

$$\tilde{c}(s) = \frac{s\,c_0 + \frac{k_{on}^0}{D}\Big(1-\exp(s\,\delta)\Big)\int_\delta^\infty dx\, \exp(-s\,x)\,c(x)}{s^2 + \frac{F}{k_BT}s} \tag{2.42}$$

With the help of the general formula for the inverse Laplace transform of the following two functions [25]:

$$\mathcal{L}^{-1}\left[\frac{1}{s+a}\right] = \exp(-a\,x) \tag{2.43}$$

$$\mathcal{L}^{-1}\left[\frac{\exp(-b\,s)}{s^2+as}\right] = \frac{1-\exp(a(b-x))}{a}\Theta(x-b) \quad \text{if } b>0 \tag{2.44}$$

we calculate the inverse Laplace tranform in Eq. (2.42) and the result is the integral equation:

$$c(x) = c_0\,e^{-\frac{F\,x}{k_B\,T}} + \frac{k_{on}^0}{D}\frac{k_BT}{F}\int_0^\infty dy\, c(y)\,\Theta(y-\delta)\left(\Theta(x-y)\left(1-e^{\frac{F(y-x)}{k_B\,T}}\right) - \Theta(x-y+\delta)\left(1-e^{\frac{F(y-x-\delta)}{k_B\,T}}\right)\right) \tag{2.45}$$

We use this self-consistent equation in order to find a *perturbative* solution $c(x)$ in the high diffusion limit, *i.e.* for small parameter $\varepsilon = \frac{k_{on}^0\delta^2}{D} \ll 1$. In the absolute limit of infinite diffusion the solution is obviously in the zero-approximation $c_0(x) = c_0\,e^{-\frac{F\,x}{k_B\,T}}$. If we insert this solution into Eq. (2.45) we obtain as a first order approximation:

$$c_1(x) = c_0\,e^{-\frac{F\,x}{k_B\,T}} + \varepsilon\,c_0\frac{\left(1+\frac{F\,x}{k_B\,T}\right)e^{-\frac{F(x+\delta)}{k_B\,T}} - e^{-\frac{F\,\delta}{k_B\,T}}}{\left(\frac{F\,\delta}{k_B\,T}\right)^2}, \quad \text{if } x<\delta \tag{2.46}$$

$$c_1(x) = c_0\,e^{-\frac{F\,x}{k_B\,T}} + \varepsilon\,c_0\frac{\left(1+\frac{F\,x}{k_B\,T}\right)e^{-\frac{F(x+\delta)}{k_B\,T}} - \left(1+\frac{F\,(x-\delta)}{k_B\,T}\right)e^{-\frac{F\,x}{k_B\,T}}}{\left(\frac{F\,\delta}{k_B\,T}\right)^2}, \quad \text{if } x>\delta \tag{2.47}$$

It is important to notice the continuity of the above solution at $x=\delta$, a property that is true for the general solution Eq. (2.45) also. Given the above approximate solution, we can evaluate

$P_{x>\delta} = \frac{\int_\delta^\infty dx\, c_1(x)}{\int_0^\infty dx\, c_1(x)}$, and the growth velocity $v = \delta\, k_{on}^0\, P_{x>\delta}$ is given finally by:

$$v(F) = \delta\, k_{on}^0 \left(e^{-\frac{F\,\delta}{k_B\,T}} - 2\,\varepsilon\, \frac{e^{-2\frac{F\,\delta}{k_B\,T}} \left(e^{\frac{F\,\delta}{k_B\,T}} - \frac{F\,\delta}{k_B\,T} - 1 \right)}{\left(\frac{F\,\delta}{k_B\,T} \right)^2} \right) + \mathcal{O}(\varepsilon^2) \tag{2.48}$$

We can check that in the high diffusion limit, $\varepsilon \to 0$, the velocity becomes the thermodynamic expression (see main text):

$$v(F) = \delta\, k_{on}^0\, e^{-\frac{F\,\delta}{k_B\,T}} \tag{2.49}$$

Appendix B

In this appendix we show that for buckled semi-flexible polymers

$$\sqrt{k/2k_BT}\,|x_0| \gg 1 \tag{2.50}$$

The shape equation for a buckled rod is given by ([26])

$$EI\,\mathbf{t} \times \frac{d^2\,\mathbf{t}}{d\,s^2} = \mathbf{F} \times \mathbf{t} \tag{2.51}$$

where EI is the bending rigidity, $\mathbf{t}$ is the tangent, s is the arc-length, and $\mathbf{F}$ is the applied force. Based on dimensional analysis, from this equation we expect the force to be of the form

$$F \approx \frac{EI}{\xi^2} \tag{2.52}$$

where ξ is a characteristic length, which is given by the deformation of the rod. In the case of large deflections, this length must be smaller than the contour length L

$$\xi \lesssim L \tag{2.53}$$

In the limit of small fluctuations, the deflected rod is mapped to a Hook spring which is compressed by an amount $|x_0|$. Therefore

$$F = k\,|x_0| \tag{2.54}$$

From Eq. (2.52) and Eq. (2.54), it follows that the spring constant must be

$$k \approx \frac{EI}{\xi^2 |x_0|} \tag{2.55}$$

We use the last formula together with the relation between the bending rigidity and the persistence length l_p,

$$EI = l_p\, k_B T \tag{2.56}$$

and evaluate

$$\sqrt{k/2k_BT}\,|x_0| \approx \sqrt{\frac{l_p|x_0|}{\xi^2}} \gg 1 \tag{2.57}$$

Indeed, $\xi \lesssim L$, for semi-flexible polymers we have $l_p \gtrsim L$, and therefore $l_p \gg \xi$. On the other hand $|x_0| \approx L \gtrsim \xi$.

Chapter 3

Microtubule Force Production

3.1 Introduction

Polymerization ratchets form a subclass of molecular motors, that includes microtubules as a very important component in many cellular processes. This is so because microtubules are able to develop pushing and pulling forces due to polymerization and depolymerization. For example, *in vivo* studies demonstrate the role played by microtubules in orgalelle positioning, like anchoring the nucleus, or chromosome position control during the cell division [27, 28].

In vitro experiments make it possible to evaluate the values of the forces that microtubules can develop during their polymerization. Experimental data of this kind first became available in 1997 [19]. In the experiment in question, microtubules are let to grow against a glass barrier. The microtubule ends then sit caught underneath the barrier overhang and eventually buckle, which proves that internal elastic stress is developed during growth. Video microscopy techniques are used in order to monitor the evolution of microtubule length in time, so that their velocity of growth can be evaluated. The elastic force can be evaluated also by analyzing the shape of the polymers on the basis on elastic theory for bent rods [26]. Subsequent experiments generated new data showing that microtubules can develop forces in the range of a couple of piconewtons [19, 29, 20].

Modeling the measured *force-velocity* relation could lead to insight in both the polymerization mechanism and microtubule structure. Indeed, the obvious first thing to do is to employ the Brownian ratchet concept, that we presented Chapter 2, and to apply it in the form of a single pushing filament. We will see that this *one-filament* representation of the microtubule cannot satisfactorily interpret the data, and therefore modeling is needed for a multi-filamentous complex. This is obviously expected to be more realistic since *in-vivo* microtubules are composed of $N = 13$ filaments [4]. It is the aim of this chapter to theoretically investigate in detail different aspects of the collective growth of a filamentous bundle. Simply having N filaments in our system does not only have the consequence of generating higher forces during pushing. For example, the collective features of the model also introduces additional details of a geometric origin, like the lateral offset between filaments, for which we anticipate a non-trivial influence on the velocity of growth. Modeling microtubules as a *N-filament* complex, it is the right place to introduce the lateral affinity between filaments, based on model and data interpretation. The affinity between filaments is what keeps them together in a tubular complex like microtubules. The value of the corresponding parameter is expected to be also important to other aspects of microtubule dynamics, not only growth, like the loss of GTP-cap, or microtubule disassembly after the event of catastrophes.

Based on the polymerization ratchet mechanism that we presented in the previous chapter, we show in the following a force generation mechanism for growing microtubule, which converts into

work the chemical polymerization energy of GTP tubulin. In our model, the hydrolysis of GTP tubulin, which takes place shortly after its addition, does not play any role in force production. For this to be true it is sufficient to assume that the conformational change of tubulin during hydrolysis is not significant, and therefore it cannot result in a new step size during pushing against the load.

3.2 A Single Filament Model for Microtubules

For our analysis we use three sets of data for the *force-velocity* relation [19, 29, 20], which we define as S0, S1, and S2 (see Fig. 3.1). In the following we will first review a naive interpretation of this data based on the general formula, Eq. (2.8). If all the thermodynamic requirements that validate this equation are fulfilled, we still have to remember that Eq. (2.8) describes only a single filament polymer, and *not* multi-filamentous complexes like real microtubules. In this case, the key difference will be the value of the step size δ^*, which is expected to be different than the size of a subunit, ***i.e.*** $\delta = 8\,nm$:

$$v(F) = \delta^* \left(k_{on}^0 e^{-\frac{q\,F\,\delta^*}{k_B\,T}} - k_{off}^0 e^{-\frac{(q-1)\,F\,\delta^*}{k_B\,T}} \right) \tag{3.1}$$

The value of the parameter q was predicted by the Brownian ratchet model to be $q = 1$ (see Eq. (2.8)). However, we have already suggested that different values for this parameter may actually correspond to different dynamic processes than just polymerization. Nevertheless we argue that it is reasonable to stick to the value $q = 1$ in order to make an analysis that is based on a minimal set of assumptions.

Indeed, Dogterom *et. al.* [19] kept in their discussion *only* two different values, $q = 1$ and $q = 0$, in order to keep the number of fitting parameters to a minimum. They found that the choice $q = 1$ is the most appropriate of the two, as long as the other fitting parameters were k_{on}^0, k_{off}^0, and the step size δ^*. However, their result for the step size δ^* was higher than the expected value, which is simply the average step per inserted subunit[1]:

$$\delta^* = \frac{\delta}{N} \tag{3.2}$$

where N is the number of protofilaments in the assembly.

Since this is the only reasonable assumption in the absence of any more detailed model of the microtubule structure, a higher value of δ^* only proves the need for such a model, which hopefully might cast more insight into the force production mechanism in microtubules [19]. These conclusions apply as well to the newer sets of data, S1 and S2, as we can see from the summary of our analysis that we present in Table 3.1 and in Fig 3.1.

A different point of view to the same problem was adopted by Kolomeisky *et.al.* [30]. Unlike [19], these authors considered the parameter q as a fully independent fitting parameter, together with the polymerization rates k_{on}^0 and k_{off}^0, and the step size δ^*. The full expression used for data fitting was Eq. (3.1). However, little discussion was devised to the physics that q describes, which may correspond to different dynamics and have the unfortunate feature that it has the same time scale as the polymerization process itself. In other words, in the case of good fit quality, it cannot be obvious from Eq. (3.1) what are the exact factors responsible for force generation in growing microtubules.

[1] If the filaments grow equally, and if M is the number of monomers within a single filament, then the total number of the inserted monomers is $M_{total} = N\,M$. The length of the polymer is $L = \delta\,M$, so the average step per inserted subunit must be $\delta^* = L/M_{total} = \delta\,M/N\,M = \delta/N$.

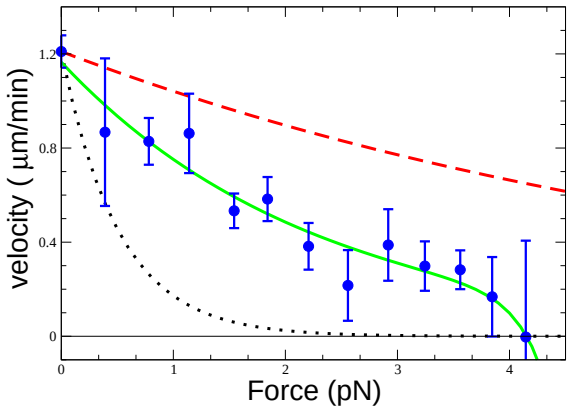

(a)

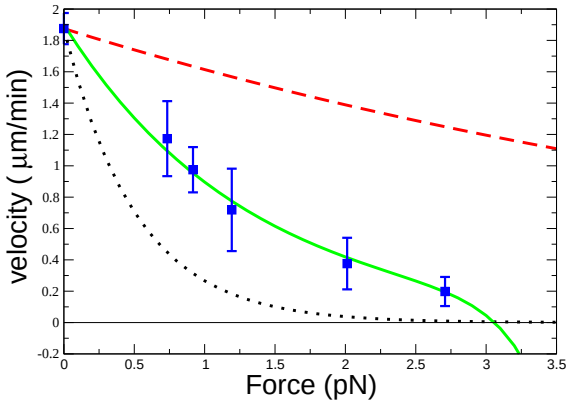

(b)

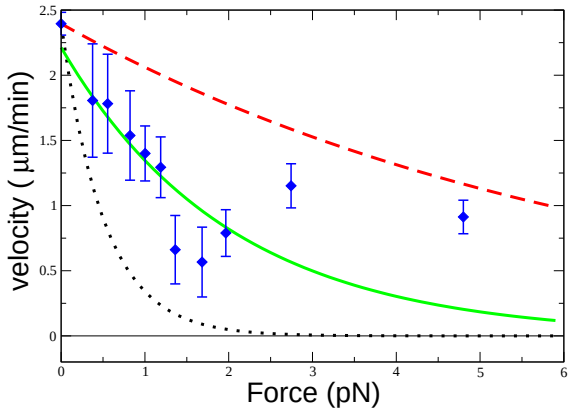

(c)

Figure 3.1: In the simplest approach one can approximate mirotubules as single filament complexes. A generic analytical formula Eq. (3.1) gives a good fit quality, but the growth step size could be overestimated in this naive description. The size of a tubulin dimer is $\delta = 8\,nm$. Fitting these data suggests that the average step size δ^* could be well beyond the value of $8\,nm$. A similar fit quality was reproduced by Kolomeisky *et. al.* [30] on the data set S0, but the average step size was constrained of having an upper bound at $8\,nm$. However, the general premises, on which the fit formula Eq. (3.1) was derived, cannot justify this limit for the step size δ^*. In conclusion, these results call into question the internal structure of microtubules and models are needed. Dashes line: $v(F) = v(0)\exp(-F\,\delta/k_B\,T\,N)$. Dotted line: $v(F) = v(0)\exp(-F\,\delta/k_B\,T)$. (a) Set S0, $\delta^* = 18\,nm$, $F_{stall} \approx 4.1\,pN$; (b) Set S1, $\delta^* = 18\,nm$, $F_{stall} \approx 3\,pN$; (c) Set S2, $\delta^* = 12\,nm$, F_{stall} was not defined (see also Table 3.1).

Following Kolomeisky *et.al.* [30], we employ Eq. (3.1) in fitting all three sets of data. The results, shown in Table 3.1, are consistent with Ref. [30], where the analysis was done on the only available data set at the time, S0. In making the fit on S0, we obtain slightly different values for the *on-* and *off-* rates, similar values for the stall force (data not shown), but exactly the same values for q.

A rather major difference with Ref. [30] in our analysis is the interpretation and the value of the step parameter δ^*. Unlike Ref. [30], we do not set any upper limit to δ^*. The premises of Eq. (3.1) do not impose such a restriction. As we show in Table 3.1, we have obtained an *even better* fit quality for $\delta^* > 8\,nm$. This is true for all data sets, and we show some examples in Fig. 3.1 for $\delta^* = 12\,nm$ and $\delta^* = 18\,nm$.

A close look at the results in Table 3.1, shows that for a wide interval of values $4\,nm < \delta^* < 18\,nm$ the fit quality is not significantly different for all sets of data. We thus face an indeterminacy in the value for δ^*, quite apart from the fact that this interval is well beyond the expected value suggested in Eq. (3.2).

Could it be that the too high degree of generality, and hence ambiguity of Eq. (3.1), is responsible for the unexpected high values for the average step size? Could it be that open sheet like structures [31, 5, 10], which normally span more than a couple of dimer lengths in growing microtubules, be in reality responsible for the apparent large step sizes? These questions underscore that the next natural step is modeling the internal structure of microtubules in order to see its implications on the force production mechanism.

3.3 A Model for Collective Growth

Given the high value for the step size δ^*, obtained from fitting the *force-velocity* relation, Dogterom *et.al.* speculated that the internal structure of the microtubule end might be responsible [19]. Indeed, if a single microtubule protofilament is pushing against the barrier, subunits can be added at the tip of this protofilament in a Brownian ratchet fashion, and the step size δ^* could be close to the full length of a tubulin dimer. However, under the action of the force, it is expected that the growth velocity of this protofilament should decrease, and nothing then prevents the other protofilaments from caching up in length with the most advanced protofilaments. If so, we guess that the microtubule end is rather blunt, and this may justify Eq. (3.2) for the step size.

A more detailed description of how the microtubule end structure might be involved in the mechanism of growth was given by A. Mogilner & G. Oster [23] in 1999. Cording to this model a *subsidy* effect could explain the observed *force-velocity* data. More precisely, it is assumed that there is a most forward filament, which is propping up the microtubule against the wall. This means that gaps between the wall and the tips of the other filaments are wide enough for subunits to be inserted with high probability rate in the fashion of a thermal ratchet, allowing the other filaments to catch up. Does this really mean that in the presence of a *high* force, the microtubule end is *blunt*?

In the following, we present a modified version of the original model that Mogilner & Oster proposed for the microtubule growth. The spirit of the model is the same, *i.e.* the subsidy effect is still at the heart of the model. As a first difference, while the original model defines a continuous distribution of filament tips, the discrete character or our model version is shown to be the right feature, since, besides being more realistic it also gives the right thermodynamic expression for the stall force (see below). Another important difference is that we take into account the lateral bonding between filaments. The prime reason is, of course, this is a realistic feature. Moreover we will show that there is a relation between the spatial distribution of the filament tips, which corresponds to microtubule geometrical structure, and the velocity of growth. And we will see that

Set	$\delta^*\,(nm)$	$k^0_{on}\,(min^{-1})$	$k^0_{off}\,(min^{-1})$	q	χ^2
S0	8/13	3822	1976	1	0.119
	1	1601	457	1	0.115
	2	628	55	0.69	0.104
	4	290	3.09	0.40	0.101
	6	192	2.9×10^{-1}	0.28	0.098
	8	144	3.2×10^{-2}	0.21	0.095
	12	96.7	4.4×10^{-4}	0.14	0.089
	16	72.72	6.4×10^{-6}	0.11	0.086
	18	64.7	7.8×10^{-7}	0.09	0.085
S1	8/13	9369	6304	1	0.0147
	1	3752	1863	1	0.10
	2	1215	270.5	1	0.019
	4	486.8	14.06	0.7	0.0088
	6	317.5	2	0.48	0.009
	8	237.2	3.5×10^{-1}	0.37	0.01
	12	158.2	1.4×10^{-2}	0.254	0.011
	16	118.7	6.7×10^{-4}	0.19	0.011
	18	105.5	1.5×10^{-4}	0.17	0.011
S2	8/13	5780	1914	3.86	1.6
	1	2253	0	2.70	1.6
	2	1175	0.19	1.20	1.4
	4	574	0	0.50	1.33
	6	383	0	0.38	1.32
	8	288	0	0.28	1.31
	12	184	0	0.16	1.27
	16	126	0	0.10	1.27
	18	116	0	0.10	1.27

Table 3.1: The *force-velocity* data is available as three independent sets: S0, S1, and S2. In evaluating χ^2 we set the average standard deviation in velocity as being the same for all data. Different values of the step size δ^* are chosen, and for each such value the fit parameters are the kinetic rates k^0_{on}, k^0_{off}, and the parameter q. A striking feature of these results show 1) an improved fit quality for higher and higher step size δ^*, and 2) small values for q at large step size values, suggesting stronger effects of the load on the *off*-rate rather *on*-rate. The values of δ^* could be even higher as the corresponding χ^2 is found to be even slightly lower (data not shown).

lateral bonding does make a difference in the distribution of the filament tips.

3.3.1 Definition of the Model

We have presented in Section 2.6 a simple geometrical picture of a semi-flexible filament which is growing against a fixed barrier. This geometrical representation is the most convenient one in order to generalize the Brownian ratchet model from a single filament to a more complex assembly, which consists of many filaments.

Following [23] the tubular polymer is represented as a cylinder unfolded in a plane. We consider the microtubule as a complex of N protofilaments, which grows against a non-fixed wall. A *constant* force F is pushing the wall, opposing the microtubule growth (see Fig. 3.2). The longest filament supports the load and defines the wall position. Each filament polymerizes and depolymerizes with rates that depend on the gap between the wall and the filament tip. We denote by $k_{on}(i)$ the addition rate of a new subunit at the tip of the $i-$th filament, and by $k_{off}(i)$ its removal rate. Let $x(i)$ be the distance between the wall and the tip of the $i-$th filament. Consider the situation in Fig. 3.2. The newly added subunit has with adjacent filaments lateral contacts of lengths

$$\begin{aligned} y_1(i) &= x(i-1) - x(i) \\ y_2(i) &= x(i+1) - x(i) \end{aligned} \tag{3.3}$$

We assume that the energy that comes from the direct lateral contact is proportional to the length of the direct lateral contact between adjacent filaments. Then the corresponding free energy that comes from the lateral interaction is $\Delta G_{||}(i) = \varepsilon_{||}\left(y_1(i) + y_2(i)\right)$, for the case shown in the figure, where the constant $\varepsilon_{||}$ represents the energy per unit of length of lateral contact. In the most general case, one can write this energy as

$$\Delta G_{||}(i) = \varepsilon_{||}\left(\mathcal{H}(y_1(i)) + \mathcal{H}(y_2(i))\right) \tag{3.4}$$

where

$$\mathcal{H}(y) = \begin{cases} 0, & \text{if } y < 0 \\ y, & \text{if } 0 \le y < \delta \\ \delta, & \text{if } y \ge \delta. \end{cases} \tag{3.5}$$

In defining the function $\mathcal{H}(y)$, we take into account that the lateral contact between a *subunit* and an adjacent filament cannot be larger than the subunit size δ, and also a negative argument of $\mathcal{H}(y)$ means no lateral contact.

We consider ΔG^0 as the free energy that comes from the *end-to-end* contact between any two subunits. If due to the polymerization of the considered $i-$th filament the wall advances by a distance $\delta - x(i)$, then the work done against the wall is

$$W(i) = F\left(\delta - x(i)\right) \tag{3.6}$$

The net free energy that is released after the polymerization of the considered filament is:

$$\Delta G(i) = \Delta G^0 + \Delta G_{||}(i) - W(i) \tag{3.7}$$

Following the arguments presented in Section 2.2, the net free energy can be related to the ratio between the polymerization and depolymerization rates:

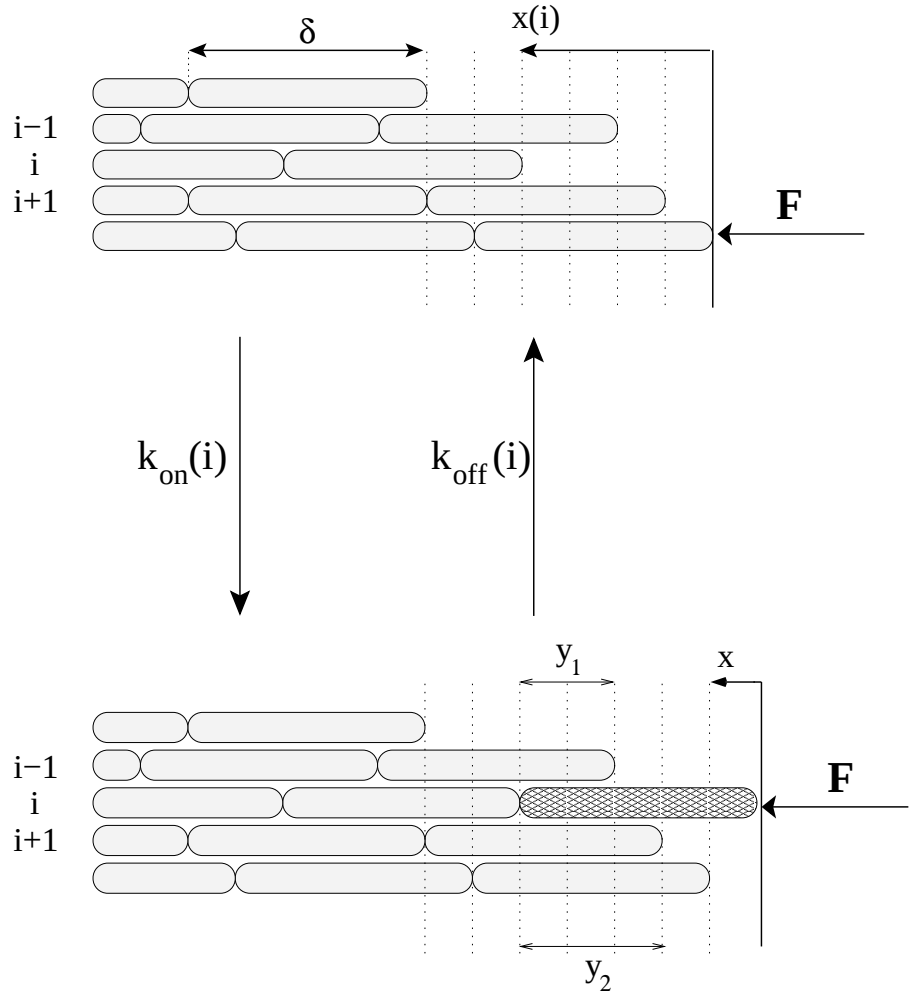

Figure 3.2: The polymerizing microtubule: the simple geometrical picture of a pushing semiflexible filament, presented in Fig. 2.6, allows a straightforward generalization from a single filament model to a bundle made of an arbitrary number of filaments. If we consider the $i-$th filament, for a newly inserted subunit (shown shaded) the individual *on*- and *off*- rates, $k_{on}(i)$ and $k_{off}(i)$, are given by a) the corresponding amount of work, used to push against the load F, *i.e.* $W(i) = F\,(\delta - x(i))$, and b) energy gain due to the lateral affinity between the inserted subunit and adjacent filaments, which is modeled as being proportional to the new lateral contact length $y_1 + y_2$, *i.e.* $\Delta\, G_{||}(i) = \varepsilon_{||}\,(y_1 + y_2)$.

$$\frac{k_{on}(i)}{k_{off}(i)} = \exp\left(\frac{\Delta G^0 + \Delta G_{||}(i) - W(i)}{k_B T}\right) \tag{3.8}$$

The last relation is simply a generalization of Eq. (2.3) to a multi-filamentous assembly. If we define the *bare* probability rates k^0_{on} and k^0_{off} by relating them to the free energy ΔG^0, as was done in Eq. (2.4), then Eq. (3.8) becomes

$$\frac{k_{on}(i)}{k_{off}(i)} = \frac{k^0_{on}}{k^0_{off}} \exp\left(\frac{\Delta G_{||}(i) - W(i)}{k_B T}\right) \tag{3.9}$$

We write the individual of *on*- and *off*- rates separately in perfect analogy with Eq. (2.7):

$$\begin{cases} k_{on}(i) = k^0_{on} \exp\left(\frac{q_1 \Delta G_{||}(i) - q_2 W(i)}{k_B T}\right) \\ k_{off}(i) = k^0_{off} \exp\left(\frac{(q_1 - 1)\Delta G_{||}(i) - (q_2 - 1) W(i)}{k_B T}\right) \end{cases} \tag{3.10}$$

We stress that the only condition that these relations should fulfill is compatibility Eq. (3.9). The parameter q_2 describes the change of the *off*- rates in the presence of the load, just as we have described in Section 2.2. Similar arguments allow us to introduce the parameter q_1.

We mention that, if we take $\varepsilon_{||} = 0$ ($\Delta G_{||} = 0$) and $q_2 = 1$, we exactly return to the models proposed in Ref. [23] and Ref. [32], *i.e.* no lateral interaction and no change in *off*- rate k^0_{off} in the presence of the load.

3.3.2 The *Force-Velocity* Relation

In the frame of the current model, we define the velocity of a growing polymer as given by the average displacement of the wall per unit of time. Naturally, the velocity can be defined as a time average of the length increase of the polymer assembly that grows following Eq. (3.10). However, in a steady state this time average can be replaced by an average over an ensemble, which is defined by the set of all possible states of the polymer. For our problem, the *state* of a growing polymer is defined by the set of all filament tips positions from the wall, *i.e.* $\alpha = \{x(i)\}_{i=\overline{1,N}}$ (see Fig. 3.2). We define in this way the *polymer state* α because the microtubule is supposed to be very long (eventually infinite), so the length of a microtubule does not matter in defining the configuration. Indeed, for the Markovian process described by Eq. (3.10), the initial conditions are not relevant, and so neither is the length of the polymer. If a long enough time for a microtubule to grow and reach the steady state is given, any configuration α appears with a certain frequency that defines the probability $p(\alpha)$ for the occurrence of that configuration.

Since the average displacement is given by the difference between the displacement due to subunit assembly and the displacement due to subunit removal, we can write the velocity of growth as

$$v(F) = v_{on} - v_{off} = \langle k_{on}(F)\Delta x_{on}\rangle_\alpha - \langle k_{off}(F)\Delta x_{off}\rangle_\alpha \tag{3.11}$$

The above averages are computed over all possible microtubule states (configurations) $\alpha \in \mathcal{C}$. Let us consider a particular configuration α. If the i-th filament polymerizes or depolymerizes, the distance that wall advances or regresses depends, of course, on the considered configuration α. We denote those distances by $\Delta x_{on}(i, \alpha)$ and $\Delta x_{off}(i, \alpha)$, respectively. Also, the rates given by Eq. (3.10) depend on the configuration, and the dependence comes from the displacement

of the wall and the added or removed lateral contact lengths, which we denote as $y_{on}(i,\alpha)$ and $y_{off}(i,\alpha)$, respectively. Indeed, these rates are dependent on the other filament tips positions. For the considered configuration, the velocity of growth is:

$$v(F,\alpha) = \sum_{i=1}^{N} \Big(k_{on}(i,\alpha)\,\Delta x_{on}(i,\alpha) - k_{off}(i,\alpha)\,\Delta x_{off}(i,\alpha) \Big) \tag{3.12}$$

To compute the *force-velocity* relation Eq. (3.11), we average the last equation over the whole set $\mathcal{C} = \{\alpha\}$ of configurations:

$$\begin{aligned} v(F) &= \sum_{\alpha\in\mathcal{C}} p(\alpha)\, v(F,\alpha) \\ &= \sum_{\alpha\in\mathcal{C}} \sum_{i=1}^{N} p(\alpha) \Big(k_{on}(i,\alpha)\,\Delta x_{on}(i,\alpha) - k_{off}(i,\alpha)\,\Delta x_{off}(i,\alpha) \Big) \end{aligned} \tag{3.13}$$

The force dependence of the velocity of growth comes from the force dependence of the probability distribution $p(\alpha)$, and from the kinetic rates $k_{on}(i,\alpha)$ and $k_{off}(i,\alpha)$ according to the rules Eq. (3.10).

3.3.3 The Expression of the Stall Force and its Derivation

An important quantity is the maximal force that can be produced by microtubules due to the polymerization process. We call as the maximal force the *stall force*, and it is defined as the force for which the average velocity of growth becomes zero. Given the model considered, we can give an exact analytical expression for the stall force. What follows is the most general derivation, while in Ref. [32] we already presented a restricted analysis based on a particular case of the present model.

Let us consider an arbitrary configuration α_{old}, and the configuration α_{new} which is obtained from α_{old} if a subunit is added at the $i-$th filament. The probability rate of the transition from the old to the new state is

$$\mathcal{R}(\alpha_{old} \to \alpha_{new}|i+) = p(\alpha_{old}) k_{on}(i,\alpha_{old}) \tag{3.14}$$

and the corresponding reversal rate from the new to the old state

$$\mathcal{R}(\alpha_{new} \to \alpha_{old}|i-) = p(\alpha_{new}) k_{off}(i,\alpha_{new}) \tag{3.15}$$

for the same $i-$th filament depolymerizes back to its original state. If the above transition rates are equal for *every* filament and for *every* configuration (*detailed balance* condition)

$$\mathcal{R}(\alpha_{old} \to \alpha_{new}|i+) = \mathcal{R}(\alpha_{new} \to \alpha_{old}|i-), \quad \text{for all } i = \overline{1,N},\ \forall \alpha_{old} \in \mathcal{C} \tag{3.16}$$

then this condition is sufficient for the microtubule to be stalled. Here we show how such a detailed balance condition can be used to derive the stall force.

We consider first the Eq. (3.16) in more detail:

$$\begin{aligned} p(\alpha_{old}) k^0_{on} \exp\left(\frac{q_1 \varepsilon_{||} y_{on}(i,\alpha_{old}) - q_2 F \Delta x_{on}(i,\alpha_{old})}{k_B T} \right) = \\ p(\alpha_{new}) k^0_{off} \exp\left(\frac{(q_1-1) \varepsilon_{||} y_{off}(i,\alpha_{new}) - (q_2-1) F \Delta x_{off}(i,\alpha_{new})}{k_B T} \right) \end{aligned} \tag{3.17}$$

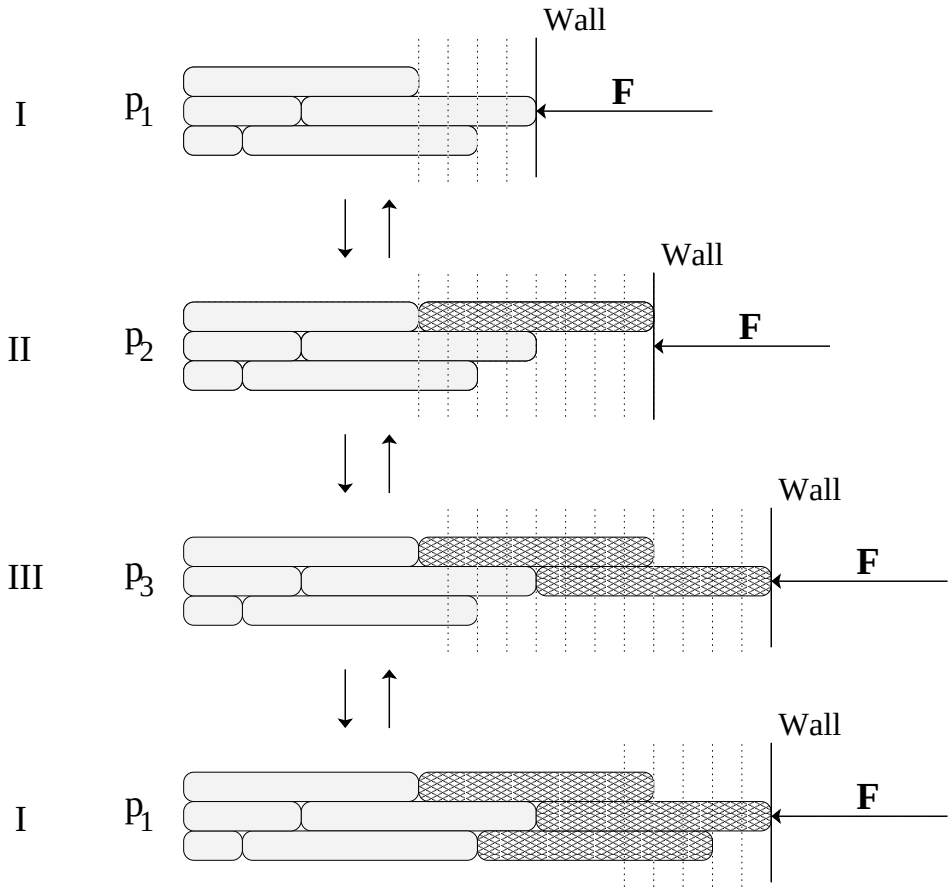

Figure 3.3: How the detailed balance principle can be used in order to derive the stall force. We exemplify the proof by taking an example of a polymer made of N=3 filaments. In three different steps, a subunit is added at each filament, which means that we end up in the same configuration. The overall displacement of the wall is δ and the total added lateral length is $N\,\delta = 3\,\delta$.

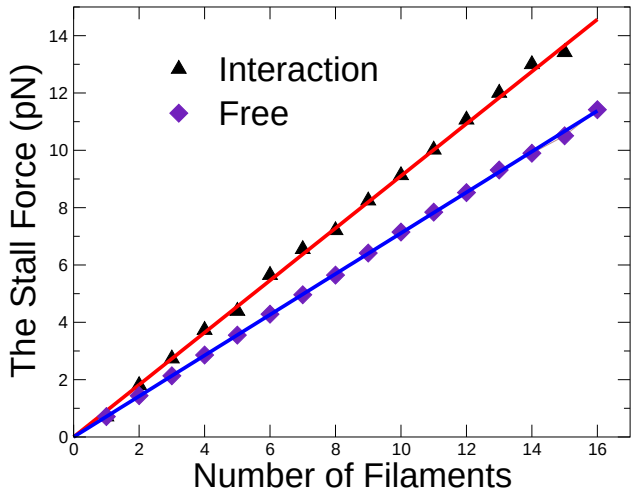

Figure 3.4: The stall force in both interacting and non-interacting filaments case. In both cases the ratio $k_{on}/k_{off} = 4$. The interaction constant was $\epsilon_{||} = 0.2\,pN$. The simulation data clearly shows that the value for the stall force given by Eq. (3.24), solid lines, was successfully verified.

where $y_{on}(i, \alpha_{old})$ and $\Delta x_{on}(i, \alpha_{old})$ are the added lateral contact length and wall displacement, respectively, if the $i-$th filament polymerizes and the mirotubule is initially in the state α_{old}. Analogous, $y_{off}(i, \alpha_{new})$ and $\Delta x_{off}(i, \alpha_{new})$ are the removed lateral contact length and wall displacement if the microtubule is in the state α_{new} and from the same $i-$th filament a subunit is removed. Given that $y_{on}(i, \alpha_{old}) = y_{off}(i, \alpha_{new})$ and $\Delta x_{on}(i, \alpha_{old}) = \Delta x_{off}(i, \alpha_{new})$, the above equation becomes:

$$p(\alpha_{old})k^0_{on} = p(\alpha_{new})k^0_{off} \exp\left(-\frac{\varepsilon_{||} y_{on}(i, \alpha_{old}) - F\Delta x_{on}(i, \alpha_{old})}{k_B T}\right) \tag{3.18}$$

Starting from a given configuration, it is possible to end up in the same configuration after a *finite* number of steps removing and/or adding subunits, although the wall position is changed. For example, this may happen if a subunit is added to each filament (see as an example Fig. 3.3). Let us consider the microtubule in an arbitrary configuration α_{i_1}. Suppose that at the i_1-th filament a subunit is added through the polymerization process, and as a consequence the microtubule is in a new state α_{i_2}. Now, we consider the new state and suppose that the i_2-th filament (different from the previous one) polymerizes, and the new configuration of the microtubule becomes now α_{i_3}, etc. We continue this reasoning until a subunit is added at each filament. The overall displacement of the wall is precisely δ, as we show in Fig 3.3. Of course, the last state $\alpha_{i_{N+1}}$ is identical to the original one α_{i_1}. We rewrite Eq. (3.18) explicitly for each step described above.

$$\begin{aligned}
p(\alpha_{i_1})k^0_{on} &= p(\alpha_{i_2})k^0_{off} \exp\left(-\frac{\varepsilon_{||} y_{on}(i_1, \alpha_{i_1}) - F\Delta x_{on}(i_1, \alpha_{i_1})}{k_B T}\right) \\
p(\alpha_{i_2})k^0_{on} &= p(\alpha_{i_3})k^0_{off} \exp\left(-\frac{\varepsilon_{||} y_{on}(i_2, \alpha_{i_2}) - F\Delta x_{on}(i_2, \alpha_{i_2})}{k_B T}\right) \\
&\cdots \\
p(\alpha_{i_N})k^0_{on} &= p(\alpha_{i_1})k^0_{off} \exp\left(-\frac{\varepsilon_{||} y_{on}(i_N, \alpha_{i_N}) - F\Delta x_{on}(i_N, \alpha_{i_N})}{k_B T}\right)
\end{aligned} \tag{3.19}$$

Multiplying all of the above equations, all the probabilities $\{p(\alpha_{i_k})\}_{k=1,2,\ldots,N}$ cancel and we obtain:

$$\left(\frac{k_{on}^0}{k_{off}^0}\right)^N = \exp\left(-\frac{\varepsilon_{||}\sum_{k=1}^N y_{on}(i_k,\alpha_{i_k}) - F\sum_{k=1}^N \Delta x_{on}(i_k,\alpha_{i_k})}{k_BT}\right) \tag{3.20}$$

If a subunit is added at each filament tip then the total wall displacement is precisely the subunit size δ (see also Fig. 3.3)

$$\sum_{k=1}^N \Delta x_{on}(i_k,\alpha_{i_k}) = \delta \tag{3.21}$$

In the same condition, we can show that the total added lateral contact length is $N\delta$

$$\sum_{k=1}^N y_{on}(i_k,\alpha_{i_k}) = N\delta \tag{3.22}$$

Indeed, consider the N filament microtubule in a certain configuration α_{i_1}. If we add a subunit at each filament, and we end up in the same configuration, then the newly added total lateral contact length $\sum_{k=1}^N y_{i_k}$ can be written as a sum of all newly added lateral contact length between any two adjacent filaments. Between any two adjacent filaments there is a δ newly added lateral contact length. Because there are N lateral contacts for a tubular N filament polymer, it follows $\sum_{k=1}^N y_{i_k} = N\delta$. Then, using Eq. (3.21) and Eq. (3.22), the condition Eq. (3.20) becomes

$$\left(\frac{k_{on}^0}{k_{off}^0}\right)^N = \exp\left(-\frac{\varepsilon_{||}\,N\,\delta - F\,\delta}{k_BT}\right) \tag{3.23}$$

The last equation is a necessary condition for detailed balance, which is equivalent to the condition for the microtubule to be stalled. From this the value of the stall force follows

$$F_{stall} = N\left(\frac{k_BT}{\delta}\log\frac{k_{on}^0}{k_{off}^0} + \varepsilon_{||}\right) \tag{3.24}$$

3.3.4 Comments on the Stall Force

The derivation of the stall force is the first output that we have presented from our model. Before proceeding further we have to make some remarks about the result Eq. (3.24)

1. First of all we note the linearity in the number of filaments of the stall force expression in Eq. (3.24). The expression presented by Mogilner & Oster [23] does not reproduce this feature. The origin of this difference is the continuous interpretation of their filament tip distribution [32]. We consider that our discrete rendering of this distribution is a more realistic feature.

2. The proportionality relation $F_{stall} \propto N$ is an interesting feature. For instance, if we neglect $\varepsilon_{||}$, we notice that the stall force is exactly N times larger than the stall force a single filament Brownian ratchet, Eq. 2.10. In spite of its simplicity, this additive property of the stall force is far from trivial. Indeed, not all the filaments are pushing the wall at once, as we can see in the example shown in Fig. 3.2.

3. A couple of important parameters of the model do not show up in the expression Eq. (3.24). Two of them are q_1 and q_2, *i.e.* the parameters that describes the distribution for the *weight* of the lateral affinity and the load on the *on-* and *off-* rates (see Eq. (3.10)). There is still another parameter that has no influence on the stall force. This parameter is the lateral offset between

filaments. We anticipate that computer simulations show a strong dependence of the velocity of growth on this parameter, as is shown in Fig. 3.7. The absence of all these details in the stall force expression, makes Eq. (3.24) a strong candidate for independent experiments and stall force measurements, which hopefully will help in evaluating numerically the small *off*- rate k^0_{off} in growing microtubules, and even the lateral affinity $\varepsilon_{||}$ [32].

4. Considering the phenomenological nature of the one-filament representation for the *force-velocity* relation Eq. (3.1), together with the step size δ^* given by Eq. (3.2), it quite remarkably predicts the same expression for the stall force, Eq. (3.24). We will see, however, from computer simulations, that the calculated *force-velocity* relation cannot be approximated by the same equation Eq. (3.1). In other words, the stall force is the *only* point on the *force-velocity* curve, which the phenomenological approach Eq. (3.1) and our model have in common.

5. Given the lateral affinity between filaments, we can model the microtubule seam by choosing a different value for the constant $\varepsilon_{||}$. Even in this case the stall force is linear in the number of filaments. If the linear density energy constant is $\varepsilon'_{||}$ at the seam, and $\varepsilon_{||}$ for the rest, then we get after repeating the same steps of as before

$$F_{stall} = \frac{k_B\,T}{\delta}\left(N\,\log\frac{k^0_{on}}{k^0_{off}} + (N-1)\,\varepsilon_{||} + \varepsilon'_{||}\right) \tag{3.25}$$

3.4 Monte Carlo Simulations of the Model

We simulated the growth of a polymer consisting of $N = 13$ parallel filaments, each consisting of a linear array of subunits of size δ. As the initial condition, the microtubule tips were set equidistantly, so that the longitudinal offset between adjacent filaments had a given value σ. The overall shift between the most and the last advanced tip is $S = (N-1)\,\sigma$. We have illustrated the definition of this geometric parameter in Fig 3.7 (a) in the case of $N = 4$ filaments. Although in the case of a real microtubule we have $S = 1.5\,\delta$ [4], we can input different values for the overall shift in our simulations in order to investigate its influence on the growth velocity.

For each time step $d\tau$ we choose N times a filament at random. For each chosen filament, a subunit was added or removed with a probability $k_{on}(i)d\tau$ and $k_{off}(i)d\tau$, where the index i is the index of the $i-$th filament, and the kinetic rates $k_{on}(i)$ and $k_{off}(i)$ were given by Eq. (3.10).

3.4.1 The *Force-Velocity* Relation

In the following, we will present the fitting procedure that we used in order to compare the model with the three experimental data sets $S0$, $S1$, and $S2$ [19, 29, 20]. From our Monte Carlo simulations the growth velocity was computed by dividing the displacement of the wall over m time steps by $md\tau$. This was repeated for many values of the force F in order to obtain the *force-velocity* relation.

In looking for the optimal fit parameter values, we can first make the important observation that instead of two free parameters k^0_{on} and k^0_{off}, we can use only their ratio k^0_{off}/k^0_{on}. The reason is very simple, if we look back at our definition for the velocity of growth Eq. (3.13). Indeed, the configurational probability $p(\alpha)$ is in fact a function only of the rate ratio k^0_{off}/k^0_{on}. Then, with the help of Eq. (3.13), we have for an arbitrary λ

$$v(F, \lambda\,k^0_{on}, \lambda\,k^0_{off}) = \lambda\,v(F, k^0_{on}, k^0_{off}) \tag{3.26}$$

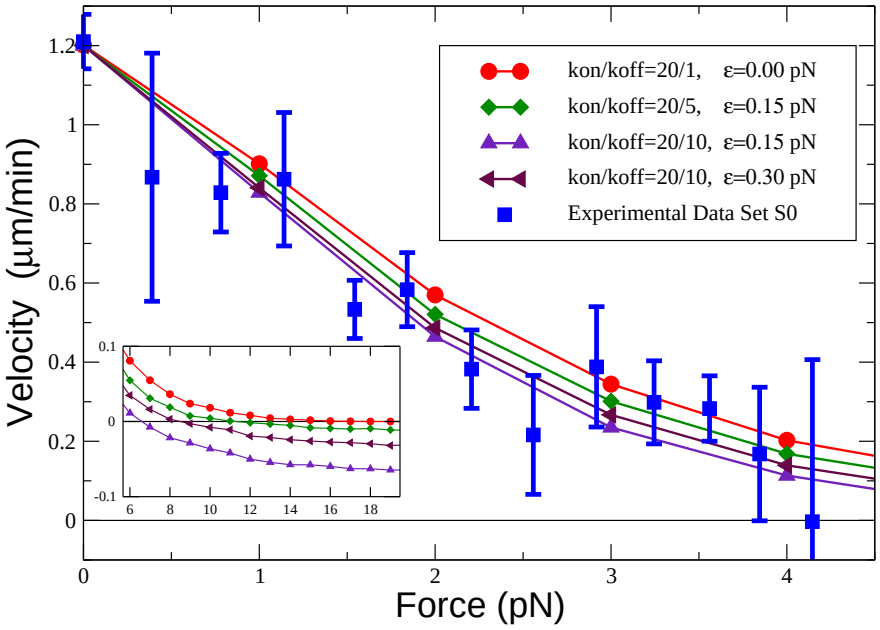

Figure 3.5: Comparison between the simulated model and experimental data set S0. The computed *force-velocity* curve shows little sensitivity in changing the rate ratio k^0_{on}/k^0_{off}. The inset shows the large interval of the calculated stall force values $6\,pN < F_{stall} < 20\,pN$. Other parameters: $k_B\,T = 4.1\,pN\,nm$, $S = 1.5\,\delta$, $\delta = 8\,nm$.

If we chose $\lambda = 1/k^0_{on}$, the last equation becomes

$$v(F, k^0_{on}, k^0_{off}) = k^0_{on}\, v(F, 1, k^0_{off}/k^0_{on}) \tag{3.27}$$

For an arbitrary ratio k^0_{off}/k^0_{on}, we can tune the value for k^0_{on} in such a way that the calculated velocity at zero force equals the corresponding experimental value. We stress that the values of the velocity at no force are measured in independent experiments, since these are the velocities of freely growing microtubules [19]. Moreover, we can notice the small error bars of these velocities in Fig. 3.1.

The only free parameter values, which we adjusted in our simulations, were the ratio k^0_{off}/k^0_{on} and the lateral affinity parameter $\varepsilon_{||}$. We kept fixed the value $q_1 = 0.5$ in the rates Eq. (3.10) for all simulations that we present in this chapter. The choice of this value for the parameter q_1 is largely an aesthetic one. First, different values for this parameter do not lead to qualitatively different results, and second, we do not need to complicate our analysis into by performing unnecessary parameter tuning. We also set $q_2 = 1.0$ in all simulations that computed the *force-velocity* relations presented in this chapter, based on arguments already presented both in the previous and present chapter. We will still present, however, a brief discussion on this choice at the end of this section.

The results of our simulations are presented in Fig. 3.5 and Fig. 3.6. Having only two free parameters, k^0_{off}/k^0_{on} and $\varepsilon_{||}$, we see from these figures that a good fit quality can be obtained for significantly different values of the free parameters. For example, in the case of data set $S0$, the *force-velocity* is not very sensitive to the model parameters in the regime of small force values (Fig. 3.5). The difference between these curves is significant only for large forces, and hence the ambiguity in the stall force value for this set of data. The inset of Fig. 3.5 shows that, in the frame of our model, the stall force values are within the interval $6\,pN < F_{stall} < 20\,pN$.

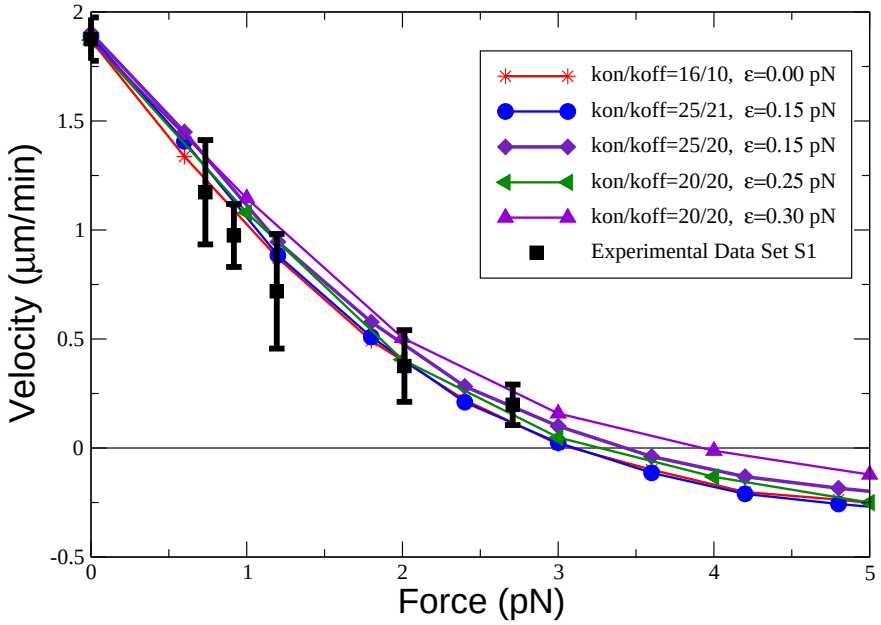

(a)

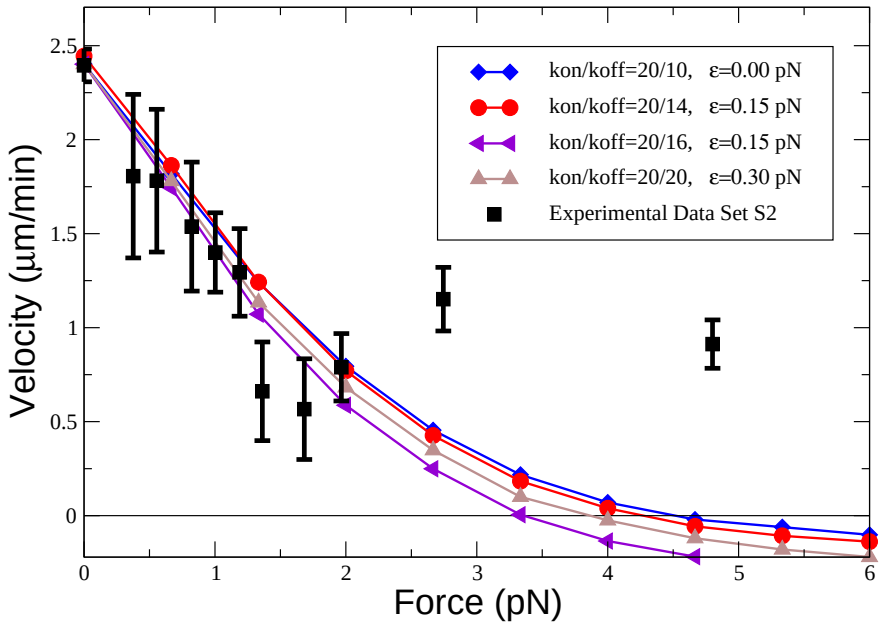

(b)

Figure 3.6: Comparison between the simulated model and experimental data sets S1 & S2. Other parameters: $k_B\,T = 4.1\,pN\,nm$, $S = 1.5\,\delta$, $\delta = 8\,nm$.

Data Set	n (# pts)	v(F=0) ($\mu m/min$)	k^0_{on}/k^0_{off}	$\varepsilon_{\|\|}$ (pN)	F_{stall} (pN)	q_1	q_2	χ^2	$\tilde{\chi}^2 = \chi^2/(n-1)$
S0	13	1.21	20/1	0	19.9	0.5	1	0.21	0.017
			20/5	0.15	11.1	0.5	1	0.15	0.012
			20/10	0.15	6.5	0.5	1	0.13	0.011
			20/10	0.30	8.51	0.5	1	0.13	0.011
S1	6	1.88	16/1	0	3.13	0.5	1	0.04	0.008
			25/21	0.15	3.11	0.5	1	0.07	0.014
			25/20	0.15	3.31	0.5	1	0.12	0.024
			20/20	0.25	3.25	0.5	1	0.09	0.018
			20/20	0.30	3.90	0.5	1	0.18	0.036
S2	11	2.4	20/10	0	4.61	0.5	1	2.5	0.25
			20/14	0.15	4.32	0.5	1	2.1	0.21
			20/16	0.15	3.43	0.5	1	2.47	0.24
			20/20	0.30	3.9	0.5	1	2.18	0.218

Table 3.2: Summary of the simulation based analysis of the *force velocity* experimental data sets $S0$, $S1$ and $S2$. We computed χ^2 considering that the standard errors σ_0 are the same for all data. The *non-weighted* χ^2 is computed as the sum of the squares of the differences between experimental and calculated values. The *weighted* parameter is calculated as $\tilde{\chi}^2 = \chi^2/(n-1)$, where n is the number of points in the corresponding data set. The first point of each data set, *i.e.* the velocity at zero force, was used in order to derive a constraint between the rates k^0_{on} and k^0_{off}. With this constraint, the resulting free parameter is the rate ratio. However the number of independent data points becomes $n-1$. We note that $\tilde{\chi}^2$ falls in the same range of values for data sets $S0$ and $S1$, suggesting a difference in the composition of these sets and the set $S2$. In making the fit, the only free parameters were the rate ratio k^0_{off}/k^0_{on} and affinity ε. Other parameters: $k_B\,T = 4.1\,pN\,nm$, $S = 1.5\,\delta$, $\delta = 8\,nm$.

In the case of data sets $S1$ and $S2$, simulations with different sets of values for the free parameters also gave a good fit quality. Unlike data set $S0$, these new data sets suggested a rather more narrow window for the stall force, $3.5\,pN < F_{stall} < 4.5\,pN$. The reason might be that while these data sets are in the same range regarding the force values, $F_{stall} < 5\,pN$, the velocities of freely growing microtubules are in a different range in the cases of $S1$ and $S2$ data sets than in the case of $S0$. Then, a faster decay of the velocity with the increase of force in the cases of $S1$ and $S2$ data sets could result in a smaller ambiguity in making the extrapolations when the stall force is evaluated.

Although the stall force can be better evaluated in the case of data sets $S1$ and $S2$, we can see that the present model can only poorly extract the lateral affinity between microtubule filaments. The original calculations and simulations were done in the case of no lateral bonding, $\varepsilon_{||} = 0$ [23, 32]. The same holds true also for the new data sets $S1$ and $S2$, as we can see also from Table 3.2. Interesting enough, we will see in the next chapter, that the same values for the goodness-of-fit parameter χ^2 can be obtained in the hypothesis of strong lateral bonding, even if *only one* free parameter is used in making the fit.

3.4.2 The Lateral Offset of the Filaments and its Implications in Growth

The decay rate of the velocity with increasing force is strongly dependent on the the longitudinal offset between protofilaments S. Of course, the longitudinal offset (see Fig. 3.7 (a)) is a fixed parameter during the growth of the real microtubule and has the value $S = 1.5\,\delta$ [4]. However, we can realize that during the growth against a rigid barrier, like in the experiments described in Ref. [19], the microtubule is pushing against the wall at a certain angle, when it buckles. This tilt translates the intrinsic shift S into an effective shift S^*. We can understand the existence of such

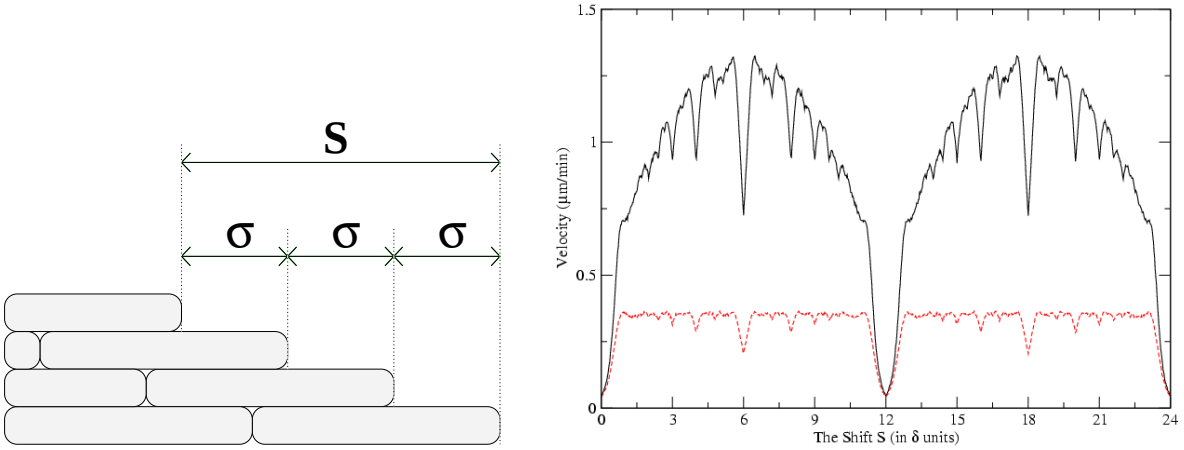

(a) (b)

Figure 3.7: (a) The definition of the shift S, exemplified for the case of four filaments. (b) The velocity of growth at a fixed force $v(F,S)$ *vs.* the longitudinal offset parameter S. Thin line: $\varepsilon_{||} = 0.0\,pN$. Thick line: $\varepsilon_{||} = 1.5\,pN$. Other parameters: $k_{on} = 160\,min^{-1}$, $k_{off} = 10\,min^{-1}$, $F = 3\,pN$, $k_B\,T = 4.1\,pN\,nm$, $\delta = 8\,nm$.

an effective parameter S^* if we take the case of $S = 0$. Indeed according to our model the step size is precisely the size of a dimer $\delta^* = \delta$, when the microtubule is pushing against the wall at a right angle. But in the case of an arbitrary tilt, there are different step sizes. In the following, we are not going to develop a mapping between different cases of tilt angles onto a space of the effective parameter S^*. We just suggest a possible source of systematic errors when the velocity of growth is experimentally evaluated.

In Fig. 3.7 (b) we show the simulation data for the velocity of growth for different shift values at the same force $F = 3\,pN$. Two different cases are presented: one with no lateral interaction between filaments and the other case with a non zero value for the lateral affinity constant $\varepsilon_{||}$. These data clearly show a dependence of velocity on the geometrical structure of the microtubule. One immediately notices some special values for the shift S for which the velocity drops in magnitude significantly. In Appendix B we identify these *magic* numbers as those shift values S for which at least two filament tips may be at the same distance from the wall. As an example, the most unfavorable case for the velocity, *i.e.* the lowest value at a given force, corresponds to the situation when all filaments are perfectly aligned (no offset, $\sigma = 0$ and $S = 0$, so $\delta = \delta^*$, see Fig. 3.7 (b)). This simulation proves that we get higher velocities of growth in the case of smaller steps δ^*, since the rates of growth Eq. (3.10) are normalized by the Boltzmann factor, and become exponentially smaller with the work done against the barrier $W = F\,\delta^*$.

Even when the lateral affinity parameter $\varepsilon_{||}$ is switched on, there is no gain in the growth velocity, under the condition of pushing against a load Fig. 3.7 (b), if $S = 0$. Here we give a simple argument why this should be so. As the next subsection will show, computer simulations prove that, at a given force, the protofilament tips tend be distributed closely to the wall. Eventually at very high force all the protofilaments are pushing against the wall, when $S = 0$. In this case the distribution of filament tips is nearly maximal and the velocity of growth is $v(F) \approx N\,\delta\,k_{on}^0 \exp(-F\,\delta/k_B\,T)$. We obtain the same velocity when we switch on the lateral attraction, since the distribution of tips is already maximal.

For both cases presented in Fig. 3.7 (b), the velocity is periodic with the shift S, and the periodicity given by $S_{period} = (N-1)\delta$. Looking at the first period interval only, *i.e.* for S ranging from 0 to $(N-1)\delta$, one can notice a symmetry axis at the midpoint of the interval. The reason of these symmetries is given by the Markovian property of the microtubule growth (according to the model), which is discussed in detail in Appendix B.

3.4.3 The Distribution of Filament Tips

Another set of computer simulations is concerned with the distribution of filament tips. Given the discrete nature of our model, it follows that the tips of the protofilaments can be found only at certain distances from the wall (see Fig. 3.2). We considered the discrete set of the positions where the tips can be found. The microtubule was let to grow according to the rules described above. After each time step $d\tau$, the number of filament tips were counted for each geometrically allowed distance from the wall. Then, the number of filament tips found at each allowed position was averaged after a large number of growth steps. The time of growth was large enough in order to obtain as a result the steady state distribution of tips.

The results presented in Fig. 3.8 are given for a 13 filament microtubule and the shift was chosen to be the realistic one $S = 1.5\,\delta$ [4]. We can notice that, keeping $\varepsilon_{||} = 0$ as constant, the number of *working filaments*, *i.e.* the average number of filament tips within a distance δ from the wall, grows with the applied force F (see Fig. 3.8 (a), (b), (c)). A similar increase in the number of working filaments holds true if the force is kept constant and only the affinity constant $\varepsilon_{||}$ is increased. We demonstrate this simple feature only for the case of zero force in Fig. 3.8 (c) and (d).

In the case of no force and no lateral interaction, Fig. 3.8 (c), the distribution of tips is trivial, *i.e.* the average number of filament tips at any distance from the wall is zero, except at the wall where it is one. In this case the average distance between the tips of any two filaments grows as square root in time, like a random walk problem, and hence we find a flat distribution. This means that at least for small forces the growth is not collective and the velocity of growth is simply that of a single filament polymer. Also, it appears that the microtubule does not assemble into a multi-filamentous complex. However, if the lateral interaction between filaments is switched on, then the filament tips grow together. This is exemplified in Fig. 3.8 (d) where it is shown that the tip distribution becomes non-trivial even at zero force.

3.4.4 The Stall Force

In Section 3.3.3 we defined and computed analytically the stall force, *i.e.* the maximal force that can be generated by pushing against the barrier. From the computer simulation data of the model, the stall force can also be estimated from the force velocity curves by locating the force where these curves cross the zero-velocity axis. The simulations were repeated for different number of filaments N.

We present these results in Fig. 3.4, where we show a perfect agreement between the computer simulation data and the analytical results Eq. (3.24). We stress that, as it follows from Eq. (3.24), the stall force F_{stall} does not depend on the parameters q_1, q_2, and neither on the geometrical parameter S, although the velocity was shown to be highly sensitive on the shift S (see Fig. 3.7 (b)). In performing the simulations, we explicitly checked the independence of the stall force on these parameters.

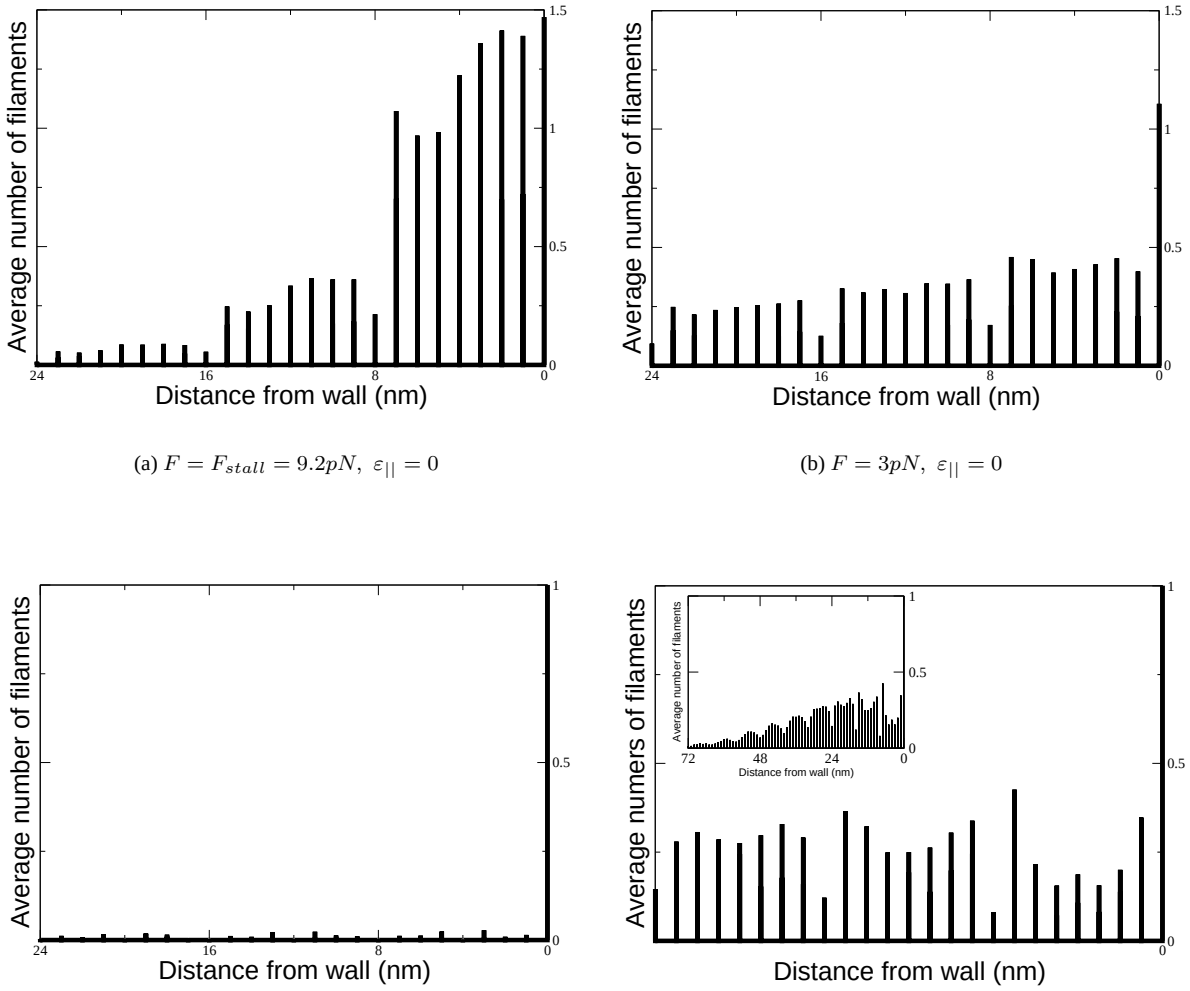

(a) $F = F_{stall} = 9.2pN,\ \varepsilon_{||} = 0$

(b) $F = 3pN,\ \varepsilon_{||} = 0$

(c) $F = 0pN,\ \varepsilon_{||} = 0$

(d) $F = 0pN,\ \varepsilon_{||} = 0.8pN$

Figure 3.8: Distribution of tips. For any value of the lateral energy constant, $\varepsilon_{||}$, the average number of filaments in a given position from the wall is less and less as the load force is smaller and smaller (see (a), (b), (c)). The distribution is trivially null for no load force and no lateral attraction ((c)). However, this is healed by the lateral attraction model: for non-zero lateral energy constant $\varepsilon_{||}$, the tips tends to stay together (non-trivial distribution) even at zero force, as (d) shows. Other parameters: $k_{on} = 160\,min^{-1}$, $k_{off} = 40\,min^{-1}$, $k_B\,T = 4.1\,pN\,nm$, $S = 1.5\,\delta$, $\delta = 8\,nm$.

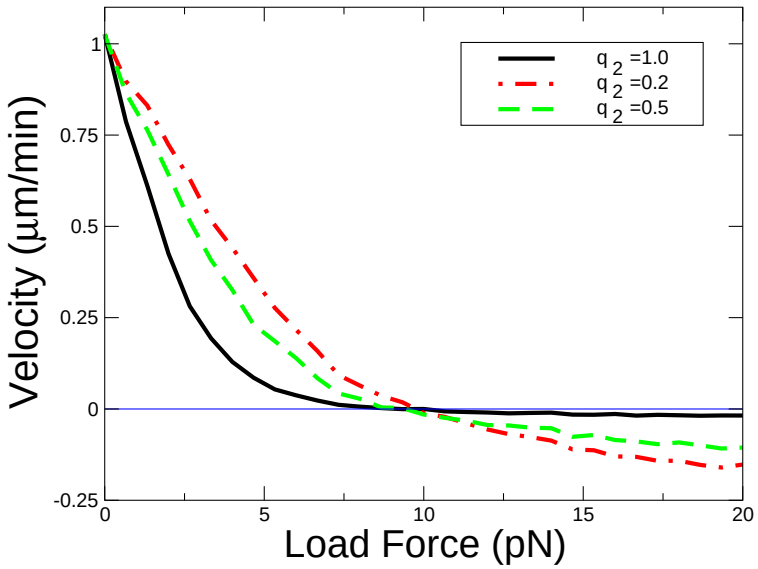

Figure 3.9: The velocity of growth in the presence of load force for different values of q_2: $q_2 = 1.0$ (continuous line), $q_2 = 0.5$ (dashed line), and $q_2 = 0.2$ (dot-dashed line). Other parameters: $\varepsilon_{||} = 0\,pN$, $k_{on} = 160\,min^{-1}$, $k_{off} = 40\,min^{-1}$, $f_{stall} = 9.2\,pN$, $k_B\,T = 4.1\,pN\,nm$, $S = 1.5\,\delta$, $\delta = 8\,nm$.

3.4.5 Load Effect on the off-Rate

In the final series of our simulation, we are concerned with the phenomenological parameter q_2, which describes the influence of the load on both the on- and off- rates. We exemplify in Fig. 3.9 the influence of this parameter on the velocity of growth. The particular values given to the other fixed parameters in these simulations are not qualitatively relevant. The general feature of these simulations is that the velocity decay rate decreases as q_2 is lowered from the value $q_2 = 1$, *i.e.* no influence of the load on k_{off} rate, to the value $q_2 = 0$, *i.e.* no influence of the load on the k_{on} rate.

It is interesting to note in Fig. 3.9 the qualitative influence of the parameter q_2 on the velocity of growth at large forces. Indeed, although the stall force remains invariant at the change of q_2, some distinctive features show up at forces larger than the stall value. For example, if $q_2 = 1$, the velocity is lagging close to its zero value even when the force is well larger than the stall force. In the case of low values $q_2 = 0.5$ or $q_2 = 0.2$, the simulations suggest that the negative velocity could become significantly large in absolute values, even in the regime of forces close to the stall value. This can be understood directly from the equation for the rates Eq. 3.10. Indeed, if $0 < q_2 < 1$, the off rates increase exponentially with force, and hence the low values of the velocity when $F > F_{stall}$. However, in the case of smaller off rate k^0_{off}, we calculated smaller absolute values for the velocity in the regime of *negative* growth.

With the help of these results, we speculate that, if the load has an effect on *both* kinetic rates, k_{on} and k_{off}, then it should in principle be possible to observe microtubules "growing" at negative velocities, *i.e.* shrinking without undergoing catastrophes. However, this effect could seriously interfere with the dynamics of GTP microtubule cap. Indeed, if the GTP-cap is narrow, as evidence suggests, it is expected to be lost immediately, and therefore a catastrophe event is triggered. Here we suggest that catastrophe events are more likely at forces close to the stall force and more evident in the case when the load affects the subunit removal rate k^0_{off}. In this context, there is evidence that the frequency of catastrophes is not modified in the presence of the load even at low velocities

[33]. Therefore, this simulation study brings additional evidence to those presented in Ref. [33] that there might be only little influence of the load on the k_{off} rate.

If it is possible that $q_2 = 1$ in the case of real microtubules, like those observed during the *in vitro* grow-and-push experiments, then it could be a serious challenge to experimentally determine when microtubules are stalled. This might be especially because there is a wide interval of force values for which the microtubules appear *stalled* within the experimental errors.

The final observation concerns the overall shape of the *force-velocity* curve. If we look back at the data fit Fig. 3.1, which was based on the *one-filament* theory, Eq. (3.1), we can notice an interesting $\mathcal{S}$ shape of the fit, which suggests small values for the stall force when $q_2 < 1$, and high values if $q_2 = 1$. The convexity part of this shape could be regarded as a signature of the force effect on the removal kinetic rate. Here we report that, based on our computer simulations, this qualitative feature does exist only in the *one-filament* case. The *subsidy* effect smears out this feature even in the case of two filaments. In the more realistic case of $N = 13$ filaments, there was no convexity emerging in the *force-velocity* curve even when we modified the longitudinal offset parameter S.

3.5 Discussions and Conclusions

We have presented a collective model for the microtubule growth, developed on the basis of the Brownian ratchet concept. The model provided a good fit quality when compared to three available experimental data sets. The statistical analysis and data interpretation, which we have presented in this chapter, is based on two free model parameter left for tuning, *i.e.* the rate ratio k^0_{off}/k^0_{on} and lateral affinity constant $\varepsilon_{||}$. We reported a wide range for the values for these parameters that gives the same fit quality.

An important result of the model is the prediction for the value of the stall force, *i.e.* the force for which the microtubule growth stops. The stall force is interpreted as the maximal force that can be generated by growing microtubule. Based on the model, we have derived an exact analytical expression, Eq. (3.24), which shows that the stall force depends only on the two fitting parameter that we mentioned above. For two of the data sets, S1 and S2, the fit analysis suggests that, in spite of the ambiguity of the fitted parameter values, the value of the stall force could lie within a narrow interval of values, *i.e.* $3.5\,pN < F_{stall} < 4.5\,pN$ (see also Fig. 3.6). However, for a third set of data, S0 [19], it is possible to have good fit quality even for stall forces up to $20\,pN$ [32] (see also the inset in Fig. 3.5). In the case of this data set, microtubules were growing in the same range of forces, but at lower velocities, presumably due to a lower tubulin concentration. In this case, with the force increase, the decay rate for the velocity was lower, which made it difficult to have a clear extrapolation at higher forces, out of data range, where the stall value is supposed to be (see Fig. 3.5).

Although, the stall force is shown not to depend on many details of the model, the velocity of growth is sensitive to the other parameters. For example, the computer simulations show a strong dependence of the velocity on the longitudinal offset between filaments. On the basis on the computed data, shown in Fig. 3.7, we suggested that high velocities are possible if the microtubules grow in small steps, since in this case we have a higher probability rate of growth. In real microtubules, $S = 1.5\,\delta$ [4], and the corresponding velocity lies in a local minimum of the velocity *vs* shift curve shown in Fig. 3.7 (see also Appendix B).

There is another parameters, q_2, which describes the influence of the load on the *off*-rate. This parameter was introduced in our model on phenomenological grounds, strengthened by similar kinetic arguments like those used in the previous chapter. The Brownian ratchet model predicts

the value $q_2 = 1$, which is precisely the case when the load has an influence only on the addition rate k_{on}. Although the stall force is invariant with this parameter, the shape of the *force-velocity* relation could be slightly influenced. However, we used $q_2 = 1$ in fitting the experimental data on the grounds of making minimal assumptions. Different values from $q_2 = 1$ are not excluded by the available data sets. The fit procedure then gives different values for the other parameters, but still the same range of values for the stall force (data not shown).

In conclusion, the *collective Brownian ratchet* is obviously more successful than the former single filament variant Eq. (3.1), when compared to *force-velocity* data S0, S1, and S2 [19, 29, 20]. With the collective model we also lose the issues of the mysterious large step size values $\delta^* > \delta = 8nm$. The same data fit quality can also be obtained by making no specific assumption on the way that the *off*-rate is modified in the presence of the load. The numerical comparison between the model and the all three available data sets gave consistent values for the stall force and also the model parameters, *i.e.* the rate ratio k^0_{off}/k^0_{on} and lateral affinity $\varepsilon_{||}$. We are still left with the open questions of what are the precise values for the affinity $\varepsilon_{||}$, and to which extent the *off*-rate is truly modified by the load. The values obtained for these parameters can be tested in different types of experiments, since the values of these parameters could have implications in microtubule dynamic instability, and in shaping the mictrotubule end.

Appendix A: Exact Expressions for the Velocity of Growth in Two Particular Cases

Case: $S = 0,\ k^0_{off} = 0,\ \varepsilon_{||} = 0$

The velocity of growth for an assembly with an arbitrary number of filaments has the expression:

$$v(F,\ k^0_{on}) = \delta\, k^0_{on}\, \frac{N\, e^{-\frac{F\,\delta}{k_B\,T}}}{1 + (N-1)\, e^{-\frac{F\,\delta}{k_B\,T}}} \tag{3.28}$$

Case: $N = 2,\ \varepsilon_{||} = 0$

For an arbitrary shift value S, the velocity of growth is

$$v(F,\ k^0_{on},\ k^0_{off}) = \delta \frac{{k^0_{on}}^2 e^{-\frac{F\,\delta}{k_B\,T}} - {k^0_{off}}^2}{k^0_{on} + k^0_{off}} \left(1 + \frac{k^0_{on}\left(1 - e^{-\frac{F\,\delta}{k_B\,T}}\right)}{k^0_{on} e^{-\frac{(1-S)\,F\,\delta}{k_B\,T}} + k^0_{on} e^{-\frac{S\,F\,\delta}{k_B\,T}} + 2k^0_{off}} \right) \tag{3.29}$$

We note that the stall force in this case verifies Eq. (3.24) in the case of $N = 2$ and $\varepsilon_{||} = 0$, and it is independent on the shift parameter S.

Appendix B: Periodicity and Mirror Symmetry in the *Velocity-Shift* Characteristics

We analyze the reasons of periodicity and reflection symmetry shown in Fig. 3.7. For the considered model, the microtubule growth is defined as a Markovian chain and the memory of the initial condition is lost. We can define, in a more explicit manner, the initial condition by using Fig. 3.7. As the microtubule seed is fixed and only the wall is moving, we can choose the origin as the position of the least advanced tip in Fig. 3.7 (positive axis arrow is pointing to right). We

associate to each filament an index i running from 0, for the least advanced tip, to $N-1$, for the most advanced tip. The tip of the filament i has the position

$$l(i) = \sigma i \quad i = 0,\ 1,\ 2, \ldots,\ N-1 \tag{3.30}$$

The *shift* S was defined as the distance between the least and the most advanced tips, given that the microtubule is at initial configuration like the one in Fig. 3.7:

$$S = (N-1)\sigma \tag{3.31}$$

Due to polymerization and depolymerization processes, at each filament i there is added or removed an integer number of subunits, $m(i)$, and the positions of filament tips are now (*in δ units*):

$$l(i) = \sigma i + m(i) \qquad \text{for } i = 0,\ 1,\ 2, \ldots,\ N-1, \text{ and } m(i) \text{ is an integer} \tag{3.32}$$

If in the Eq. 3.32 we take $m(i) = i$, i.e. given the initial condition 3.31 at each filament there is added a number of subunits equal to the filament index, then the new tip positions are given by:

$$l(i) = (\sigma + 1)i \quad i = 0,\ 1,\ 2, \ldots,\ N-1 \tag{3.33}$$

This equation has the same form like Eq. 3.30 and it can be taken as an initial condition as well, the only difference being that it defines a new shift $\tilde{S}$:

$$\tilde{S} = (N-1)(\sigma + 1) \tag{3.34}$$

Given the definition 3.31 for the initial shift S, one has:

$$\tilde{S} = S + (N-1) \tag{3.35}$$

and from Markov property there is no difference in the velocity of growth if the original configuration is taken as the one with S or $\tilde{S}$:

$$v(F, \tilde{S}) = v(F, S) \tag{3.36}$$

or

$$v(F, S + (N-1)) = v(F, S) \tag{3.37}$$

The last equation shows the periodicity of the velocity in shift, and the period (in δ units) is given by $S_{period} = N - 1$.

The reflection symmetry is explained if we consider the same initial condition like 3.30 and we make few transformations:

- We count the filaments in a reverse order $i \to (N-1) - i$, so the tip positions are expressed as
$$l(i) = \sigma((N-1) - i) \tag{3.38}$$
- Translate the coordinate system to right by a distance $\sigma(N-1)$ so that the new tip positions become
$$l(i) = -\sigma i \tag{3.39}$$
- At each filament i is added a number of $m(i) = i$ subunits:
$$l(i) = (-\sigma + 1)i \tag{3.40}$$

m=0												
$\|i-j\|$	1	2	3	4	5	6	7	8	9	10	11	12
S	0	0	0	0	0	0	0	0	0	0	0	0
m=1												
$\|i-j\|$	1	2	3	4	5	6	7	8	9	10	11	12
S	12	6	4	3	12/5	2	12/7	3/2	4/3	6/5	12/5	1
m=2												
$\|i-j\|$	1	2	3	4	5	6	7	8	9	10	11	12
S	24	12	8	6	24/5	4	24/7	3	8/5	12/5	24/5	2

Table 3.3: The magic numbers. These values, see Eq. (3.43), for the lateral offset S correspond to the local minima in the velocity of growth, and are independent from the values of the force F (see Fig. 3.7).

The last equation is similar to Eq. 3.30, and, as an initial condition, it defines a shift $\tilde{\tilde{S}} = (N-1)+S$. Like before, the velocities are identical:

$$v(F,(N-1)-S) = v(F,S) \tag{3.41}$$

Looking at the first interval of the shift, i.e. $S \in (0, N-1)$, the last equation shows the symmetry axis at the midpoint of the interval.

Appendix C: The Magic Numbers in *Velocity-Shift* Characteristics

The *magic numbers* are defined as being those values for the shift, expressed in δ units, for which the velocity has local minima (see Fig. 3.7). From the *velocity-shift* characteristics it can be guessed that, in the situation when at least two filaments from the same microtubule can be perfectly aligned (i.e. the distance between their tips is a multiple of the subunit size δ), the growth is slower and the velocity can drop significantly.

We can derive the special values of the shift by imposing the condition of filaments alignment. In order to do that, we use the same system of coordinates as in Appendix B and use for the tips positions the Eq. 3.32. In general, the filaments i and j are aligned if their tip positions differ by an integer number times the dimer size δ, which is taken as unity for convenience:

$$l(i) - l(j) = m \Leftrightarrow |i-j|\sigma = m \tag{3.42}$$

Then the shift $S = (N-1)\sigma$ is

$$S = (N-1)\frac{m}{|i-j|}, \quad 1 \le |i-j| \le (N-1), \;\; m = \text{integer} \tag{3.43}$$

The numerical values for the shift from the last formula are shown in Table 3.3 for the first three orders $m = 0$, $m = 1$, $m = 2$. A direct comparison of these values with the magic numbers from Fig. 3.7 shows that they are identical to a a very good approximation, at least for the most evident depths. It can be noticed that the more aligned filaments, the deeper the depth of the velocity from the *velocity-shift* characteristics. As an example, the case of $S = 0$ corresponds to all filaments aligned, and the velocity in this case has the lowest values.

Chapter 4

The Lateral Affinity Between Microtubule Proto-Filaments

4.1 Introduction

We have presented in the last chapter the *collective Brownian ratchet* model for growing microtubules, which successfully explained the experimental *force velocity* data. We found that on the one hand the model can successfully fit the data, but on the other hand leaves considerable ambiguity in values of the fitted model parameters. As a consequence, different types of experiments are needed, like those that involve microtubule dynamic instability, for an independent evaluation for the values of the same parameters.

Building on our model for the microtubule growth, we present in this chapter a closer analysis of the influence of the lateral affinity constant $\varepsilon_{||}$ on the microtubule end structure. Indeed, if we look at the computer simulation data for the tip distribution Fig. 3.8 (d) we notice that, in the absence of the force, there are many filament tips within a range that spans many dimers in length. The snapshots from the corresponding simulations (see Fig. 4.3) revealed open-sheet like structures at the microtubule end, which recalls those observed in microtubule cryo-electron micrographs [31, 5, 10].

In the following sections we exploit the model at hand in order to investigate the behavior of the microtubule growth in two extremal regimes, defined by weak and strong lateral affinity between microtubule proto-filaments.

4.2 The Strong Lateral Limit: A Helical Growth Model

4.2.1 The Helical Growth

The introduction of the lateral interaction between filaments is justified by the tip distribution at zero force. Indeed, in the absence of any force and lateral affinity, Fig. 3.8 (c) shows that the distribution of tips is totally flat. This suggests that a free microtubule does not exist as an assembly and something else is needed to keep the tips close together.

When the lateral affinity between filaments is switched on, the filament tips indeed grow close together. We can see that, for a given force, the interval over which the tips are distributed becomes smaller and smaller as the lateral affinity constant $\varepsilon_{||}$ is set to higher values (compare Fig. 3.8 (c) & (d)). When the lateral attraction is large enough the filament tips are at the minimal distance from each other and the microtubule polymerizes in an ordered sequential pattern.

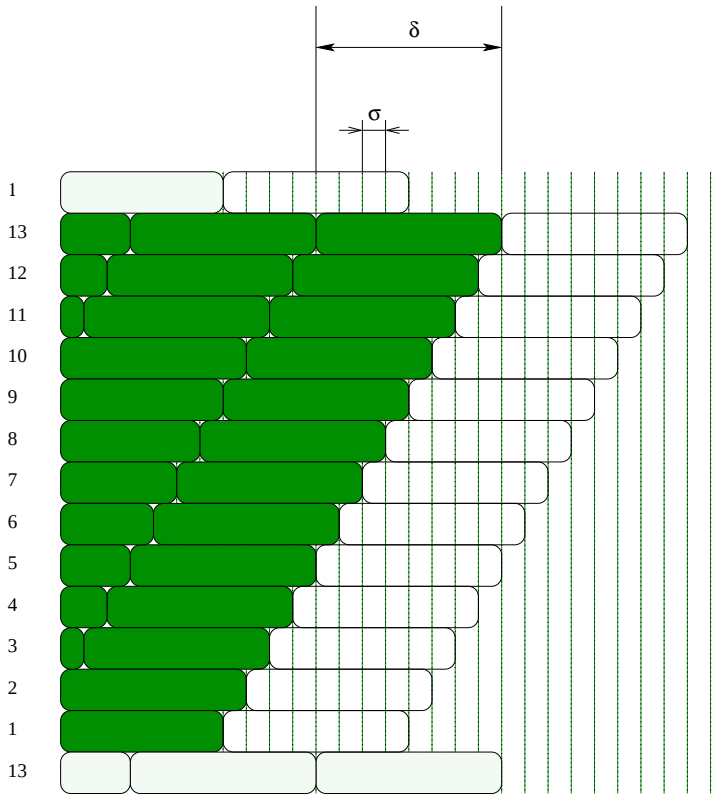

Figure 4.1: The growth of a microtubule in the regime of strong affinity $\varepsilon_{||}$between filaments (helical growth model). The overall offset between filaments is $S = 1.5\,\delta$ [4]. A microtubule is a tubular bundle of $N = 13$ filaments disposed around a cylindrical sheet. For a $2 - D$ representation, we unfolded the cylindrical sheet onto the figure plane. We assign a number for each filament, for identification. The $13-$th filament is displayed twice in order to show its area of lateral contact with the first filament. The lateral contact between the $1-$st and the $13-$th filaments correspond to the microtubule seam. For the helical growth regime, we assign for $\varepsilon_{||}$ the same value like for any other pair of filaments with direct lateral contact. We consider the initial configuration of the microtubule as it is displayed by the shaded subunits. For large $\varepsilon_{||}$, the highest probability rate for polymerization corresponds to the first filament, since the gain in lateral contact for the incoming subunit is $9\,\sigma$, the highest among all other possibilities. The next filament to grow is the second, then the third, etc. It is due to this staircase pattern of growing why we call this as the regime of helical growth. In this regime, the step size is $\delta^* = \sigma$. Given the geometry, we have $8\,\sigma = \delta$.

We consider only the case that the overall offset between filaments is $S = 1.5\,\delta$. We show in Fig. 4.1 a microtubule that is composed of $N = 13$ filaments. In the case of strong lateral affinity between filaments the order of growth is the one suggested in the figure. More precisely, after the polymerization event of a given filament, the most probable filament to polymerize next is its direct neighbor, being the one with the highest amount of lateral direct contact to be gained, and hence free energy from lateral bonding to be released. Therefore, subunits are added sequentially to one filament, then to its neighbor and so on. Given the offset between filaments, the microtubule end looks like it is growing following a helical pattern. For this reason we call the regime of strong lateral affinity.

4.2.2 The Helical Growth Criterion

Following Fig. 4.1, and given the offset $S = 1.5\,\delta$, it follows that the step size of growth $\delta^* = \sigma$ is given by

$$\sigma = \frac{S/\delta}{N-1} = \frac{1}{8} \tag{4.1}$$

Given this value, it is useful to divide a subunit into eight equal pieces because there is always an integer number of such pieces with direct lateral contact to neighboring protofilaments.

At high enough value of contact energy parameter $\varepsilon_{||}$ the microtubule is expected to grow in an ordered fashion. More precisely, for the situation shown in Fig. 4.1 the order the filaments to polymerize is 1-2-3-...-13-1-2-... etc. In order to evaluate the minimal value of $\varepsilon_{||}$, for which this ordered growth occurs, we take the filament number nine as an example. If this filament polymerizes independently (that is, the neighbors 8 and 10 did not polymerize yet) then the rate of growth at this filament is

$$k_{on}(independent) = k_{on}^0 \exp\left(\frac{\varepsilon_{||}\sigma\delta}{k_B\,T}\right) \tag{4.2}$$

This is because there is only a contact of length σ with the $10-$th filament. In the case of helical growth one has to take the contact length with the just polymerized filament 8, *i.e.*

$$k_{on}(helical) = k_{on}^0 \exp\left(\frac{8\,\varepsilon_{||}\sigma\delta}{k_B\,T}\right) \tag{4.3}$$

The criteria of having a helical growth is derived from the condition of having the last rate the most dominant one, i.e. $k_{on}(helical) \gg k_{on}(independent)$ or

$$\exp\left(\frac{7\varepsilon_{||}\sigma\delta}{k_B\,T}\right) \gg 1 \tag{4.4}$$

A value of 10 on *lhs* in Eq. (4.4) is enough for defining the helical growth regime. At room temperature, *i.e.* about $T = 4.1pNnm$, it means that

$$\varepsilon_{||} \geq 1.34\,pN \quad \text{or} \quad \varepsilon_{||}\delta \geq 2.63\,k_B\,T \tag{4.5}$$

4.2.3 The Force-Velocity Relation in the Helical Growth Regime

In the following it is useful to use the notations:

$$\begin{cases} r &= \exp\left(-\frac{F\sigma\delta}{k_B T}\right) \\ u &= \exp\left(\frac{\varepsilon_{||}\sigma\delta}{k_B T}\right) \\ A &= \frac{k^0_{off}/k^0_{on}}{u^8} \end{cases} \tag{4.6}$$

Given these new notations, then the helical growth criteria Eq. (4.4) suggests that the minimal value for u must be:

$$u \geq u_{min} = 1.4 \tag{4.7}$$

In the Appendix we derive that, in the case of the helical growth regime, the *force-velocity* relation has the form:

$$v(F, \varepsilon_{||}) = 8\,\sigma\delta k^0_{on}\,\frac{r^8 - A^{13}}{\mathcal{F}(A, u, r)} \tag{4.8}$$

The exact expression for the factor $\mathcal{F}(A, u, r)$ is given in the Appendix. Given the notations Eq. (4.6), we can easily verify that the stall force, as derived from Eq. (4.8), is exactly the same as given by Eq. (3.24), which was derived as the most general expression for an arbitrary value of $\varepsilon_{||}$.

We use the full expression for the factor $\mathcal{F}(A, u, r)$, and derive the *force-velocity* relation for the following subregimes.

Case A: No off-rate: $k^0_{off} = 0$ gives $A = 0$

$$v(F, \varepsilon_{||}) = 8\,\sigma\delta\frac{k^0_{on}u^9}{1 + 4u + \exp(F\delta/8/k_B T)(7u + u^2)} \tag{4.9}$$

Case B: The minimal decay rate: $k^0_{off} = 0, u \to \infty, k^0_{on} \to 0, k^0_{on}u^7 \to \text{const} = B$

$$v(F, \varepsilon_{||}) = 8\sigma\delta B\exp(-F\delta/8/k_B T) \tag{4.10}$$

Case C: The limit of small off-rate or large lateral affinity: $A \ll 1$. Keeping the terms for small A in the equation Eq. (4.20)

$$v(F, \varepsilon_{||}) = \frac{8\sigma\delta k^0_{on}u^8\,(r^8 - A^{13})}{r^8(1 + 4u) + r^7(7u + u^2) + A(r^8(1 + 3u) + 2r^7u + r^6(6u + u^2)) + O(A^2)} \tag{4.11}$$

Case D: Strong lateral affinity, strong linear dimer repulsion: $u \to \infty$, $A = finite$. For Eq. (4.20) we make an expansion in $1/u$ for $\mathcal{F}(A, u, r)$ and keep the smallest order term.

$$v(F, \varepsilon_{||}) = 8\sigma\delta\frac{k^0_{off}}{A^{12}u}\frac{(r^8 - A^{13})}{\left(\frac{1-1/A^5}{1-1/A} + \frac{r}{A^5}\frac{1-(r/A)^7}{1-r/A}\right)} \tag{4.12}$$

4.2.4 *Force-Velocity* Renormalization and Fit Analysis

We consider Eq. (4.8) in order to fit the *force-velocity* data sets $S0, S1$ and $S2$ introduced in the previous chapter. We tried to use the Eq. (4.9-4.12) to see which of the subregimes identified above

applies. The results suggest that the best fit quality can be obtained in the case of extremely large parameter u, but finite A, *i.e.* the subregime D.

In the case of subregime D, and looking at the definitions Eq. (4.6) for the parameters u and A, we see that the lateral affinity $\varepsilon_{||}$ is extremely large, while a finite A implies that the stall force must be *finite*. Another important observation is that, since $u \to \infty$ and $A = k^0_{off}/k^0_{on}/u^8 < \infty$, we must have $k^0_{off}/k^0_{on} \to \infty$. In spite of this perhaps unrealistic feature, we report a good fit quality given by Eq. (4.12), and it is remarkable that A is the *only* fitting parameter. The reason is that, the prefactor $8\sigma\delta\frac{k^0_{off}}{A^{12}u}$ in Eq. (4.12) can be evaluated independently from the value of the velocity at zero force $v(F=0,\varepsilon_{||})$. This is possible because the data of *freely* growing microtubules can be regarded as statistically independent from the rest.

The positive and negative terms in the *force-velocity* expression from Eq. (4.12) corresponds to the addition and removal events respectively, and we can write the velocity as

$$v(F,\varepsilon_{||}) = v_{on}(F,\varepsilon_{||}) - v_{off}(F,\varepsilon_{||}) \tag{4.13}$$

For the last equation we have defined

$$\begin{cases} v^{eff}_{on}(F,\varepsilon_{||}) &=& 8\sigma\delta\frac{k^0_{off}}{A^{12}u}\ \frac{r^8}{\left(\frac{1-1/A^5}{1-1/A}+\frac{r}{A^5}\frac{1-(r/A)^7}{1-r/A}\right)} \\ \\ v^{eff}_{off}(F,\varepsilon_{||}) &=& 8\sigma\delta\frac{k^0_{off}}{A^{12}u}\ \frac{A^{13}}{\left(\frac{1-1/A^5}{1-1/A}+\frac{r}{A^5}\frac{1-(r/A)^7}{1-r/A}\right)} \end{cases} \tag{4.14}$$

From these velocities, we can further define the *effective addition* and *removal rates*, k^{eff}_{on} and k^{eff}_{off} as

$$\begin{cases} k^{eff}_{on}(F,\varepsilon_{||}) &=& v_{on}(F,\varepsilon_{||})/\delta \\ \\ k^{eff}_{off}(F,\varepsilon_{||}) &=& v_{off}(F,\varepsilon_{||})/\delta \end{cases} \tag{4.15}$$

In Appendix B, we argue that these effective quantities are the experimental observables which are measured in experiments like [34], for freely growing microtubule, *i.e.* $F = 0\,pN$, at different tubulin concentrations. The expressions given by Eq. (4.14) and Eq. (4.15) are introduced as theoretical definitions on the basis of the model under discussion. Indeed, we generalize the arguments discussed in Appendix B to arbitrary values of the force. However, the *physical sense* for the effective dissociation velocity at an arbitrary force, $v^{eff}_{off}(F)$, is given by the experiments which provide the *force-velocity* data from growing microtubules under different buffer conditions, *i.e.* different tubulin concentration. It is exactly what we can check on the data sets S_0, S_1, and S_2, since the values for the fitted parameters are consistent among themselves (Table 4.1).

In Table 4.1 we present the summary of our fit analysis, when Eq. (4.12) was used. We note that the values that we obtained from the fit for the effective offrates are consistent with other values from the literature [35, 4], which are obtained from independent measurements. We can compare these results with the former results based on computer simulations from Table 3.2, and we can note that we get similar values for the stall force and the fit quality parameter χ^2. Finally, the very low value for k^0_{on} rate as compared to k^0_{off} cannot escape our observation. This result implies a huge barrier for the end-to-end contact between microtubule subunits. To offset this feature, our fit suggests instead a huge value for the lateral energy constant, making it possible that the microtubule assembly nevertheless has a very small effective offrate k^{eff}_{off}.

In order to test the large barrier at the end-to-end contacts between subunits, one interesting observation is that, after a catastrophe, the proto-filaments peels off during dissasembly, which

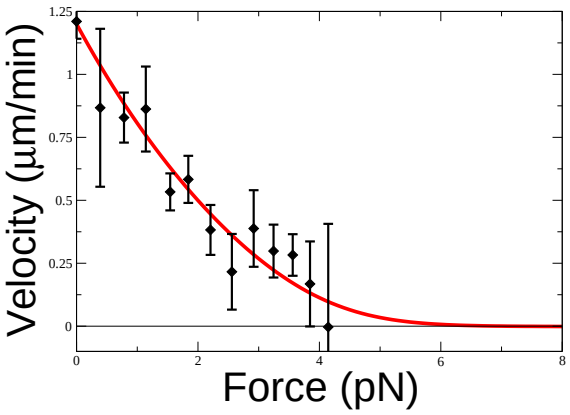

(a) S_0

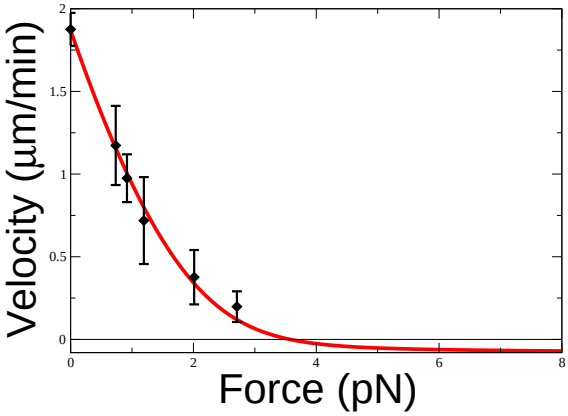

(b) S_1

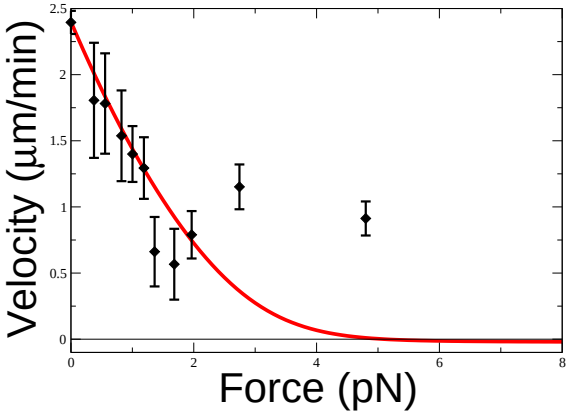

(c) S_2

Figure 4.2: The fit of the experimental data S_0, S_1, and S_2 using Eq. (4.12). We use the constraint that the velocity at zero force has fixed value. Therefore, in making this fit we use A as the only fit parameter. The results are summarized in Table 4.1.

rather suggests linear attraction instead of repulsion. However, it is the GDP-tubulin which is disassembling, which is expected to have different biochemical properties from the polymerizing GTP-tubulin.

4.2.5 The Structure of Microtubule End in the Helical Growth Regime

In the following we continue to explore the consequences of the unexpected features, which arise from the fit analysis performed in the previous section. In the identified regime, we have $\varepsilon_{||} \to \infty$ and $k^0_{off}/k^0_{on} \to \infty$ with the consequence of subunit addition at the microtubule end in a helical pattern as described in Fig. 4.1.

We can also consider the influence of a seam that potentially exists between the first and the $13-$th filament. The way that we can model this seam is simply to assign the value of $\varepsilon_{||} = 0$ at this contact. In this case the polymerization rate of the first filament drops dramatically, and eventually

Set	$v_{on}^{eff}(F=0)$ $(\mu m/min)$	k_{on}^{eff} $(1/min)$	k_{on}^{0} $(1/min)$	$v_{off}^{eff}(F=0)$ $(\mu m/min)$	k_{off}^{eff} $(1/min)$	k_{off}^{0} $(1/min)$
S0	1.21	150	1×10^{-5}	1×10^{-6}	1.2×10^{-4}	770
S1	1.88	176	4×10^{-5}	9×10^{-4}	0.11	2310
S2	2.36	296	5×10^{-5}	1×10^{-4}	1.3×10^{-2}	2560
Set	n # pts	F_{stall} (pN)	χ^2	$\tilde{\chi}^2$		
S0	13	7.10	0.12	0.01		
S1	6	3.70	0.015	0.003		
S2	11	5.10	1.855	0.185		

Table 4.1: The results of the fit analysis obtained from the helical growth model described by Eq. (4.12).

the growth of the whole assembly halts. Indeed, in the case of a seam, the polymerization rate for *any* of the filaments is given by Eq. (4.2), which becomes in the notation of Eq. (4.6)

$$k_{on}(independent) = k_{on}^{0}\, u = \frac{k_{off}^{0}}{Au^{7}} \rightarrow 0 \tag{4.16}$$

We obtained the zero limit in the last equation because we consider the case of $A = finite$ and $k_{off}^{0} = finite$ as was suggested by the fit analysis (see also Table 4.1). In summary, this result means that a microtubule with strong lateral affinity between protofilaments and with an open seam cannot grow.

This result is of course also contrary to what the experimental evidence suggests. Indeed, the model that we have just described for a microtubule with an open seam is expected to correspond to an open sheet as conformational cap. In the case that we have just described, the microtubule can grow *only* when the seam is closed. But in this regime the microtubule end is blunt, as we can also see in Fig. 4.1. This is exactly the reverse of what the evidence suggests, since the microtubule growing state can be correlated to the open sheet conformational cap, and the non-growing "intermediate state", to blunt ends [5].

4.3 The Weak Limit: Developing Open Sheet Structures at Microtubule Ends

We have seen in the previous chapter, that the Brownian ratchet model can explain the *force-velocity* data in a very satisfactory way for a very broad range values for the protofilament affinity constant $\varepsilon_{||}$. In the previous section we have seen a similar good quality of fit for the same model in the extremal case of strong lateral affinity between microtubule protofilaments. However, in spite of the successful use of a *single* fit parameter, there is the unexpected predicted feature of having extremely strong repulsive patches on the tubulin dimer. We argued that the consequence of this is that the growing microtubule cannot develop a open sheet cap structure in the *growing* state.

In the following, using simple computer simulations, we investigate the relationship between the microtubule cap structure and affinity parameter $\varepsilon_{||}$ in the opposite limit of low interaction. If we look at Fig. 3.8 (c) & (d), we see from the inset that at low force there is a non-trivial distribution of filament tips at the microtubule end that spans several tens of nm's, depending on how strong is the lateral affinity $\varepsilon_{||}$.

We define the *sheet cap* structure at the microtubule end as being that of the microtubule lying between the protofilament tips of the two filaments with the *highest* and the *lowest* polymerization

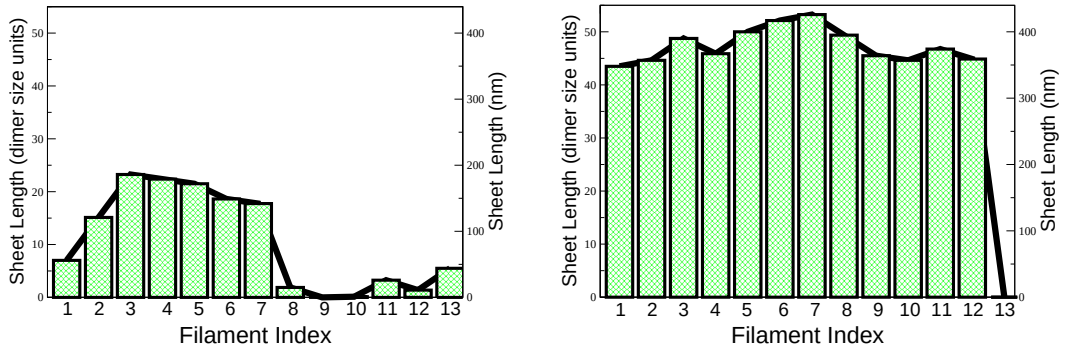

(a) (b)

Figure 4.3: (a) Seamless microtubule; (b) Seamed microtubule. The *sheet length* is defined as the distance between the tips of the shortest and the longest filaments. These are snapshots from the computer data for the microtubule sheet structures, which develop at the end of the assembly. For a fairly weak lateral affinity between protofilaments, the sheet develops as a long connected structure for seamed microtubules (see (b)). For seamless microtubules the size of the sheet is significalty lower. Parameters: $k_{on}^0 = 160\,min^{-1}$, $k_{off}^0 = 0\,min^{-1}$, $\varepsilon_{||} = 0.10\,pN \approx 0.2\,k_B\,T/\delta$, $S = 1.5\,\delta$, $\delta = 8\,nm$.

degree. Then we can define the *length* of this sheet cap as being simply given by the distance between the most advanced filament tip and the tip of the least polymerized filament.

We considered in our study the possibility of having a *seam* [4]. In the cartoon Fig. 4.1, the seam is located at the contact between the filaments $\#\,1$ and $\#\,13$. In order to study the influence of the seam, we set $\varepsilon_{||} = 0$ at this protofilament lateral contact.

The snapshots, taken from simulations, show the *sheet cap* as a long connected structure in the case of a seam and non zero lateral affinity constant $\varepsilon_{||}$ (Fig. 4.3 (b)). The sheet cap became clearly shorter in the case of non-existing seam at the same value $\varepsilon_{||}$. There is also a qualitative influence of constant $\varepsilon_{||}$ value on the physical aspect of the *sheet cap*. Indeed at very low values, presumably $\varepsilon_{||} \to 0\,pN$, the *sheet cap* became a *non-connected* geometrical structure. Indeed, for a *free* microtubule, the filament tips follow a simple random walk which leaves a "broken" structure for the microtubule cap.

Fig. 4.3 shows the case of $\varepsilon_{||} = 0.10\,pN$, *i.e.* $\varepsilon_{||}\,\delta \approx 0.2\,k_B\,T$. This corresponds to a fairly small value of the lateral affinity energy along the side of a *single* dimer compared to the thermal energy. However, this energy is strong enough to give *integrity* to the sheet cap in the case of a seam Fig 4.3 (b). In this case we predict a relatively large length for the sheet cap, which spans several tens of a dimer size. Direct observations confirms the existence of such long structures at the microtubule end [31, 5, 10]. Note that the least polymerized filament is located at the seam. Indeed, the probability rates are the lowest for the seam filaments. In the case of no existing seam, there is no broken symmetry factor and the shortest filament can occupy an arbitrary position inside the microtubule (see Fig. 4.3 (a)). In that case, the size of the sheet is dramatically reduced, as we can see in the constant between Fig. 4.3 (a) $\&$ (b).

We plot in Fig. 4.4 (a) the sheet size as a function of the lateral affinity constant $\varepsilon_{||}$, for a freely growing microtubule in both cases of the *open* and *closed* seam. In both cases, the length of the sheet is decreasing with the strength of protofilament lateral affinity $\varepsilon_{||}$. However, this length is increasing for more dynamic microtubules, *i.e.* for higher values of k_{on}^0 or k_{off}^0 rates. In Fig. 4.4 (b) we show how the calculated sheet length depends on the off rate k_{off}^0. The computer simulation

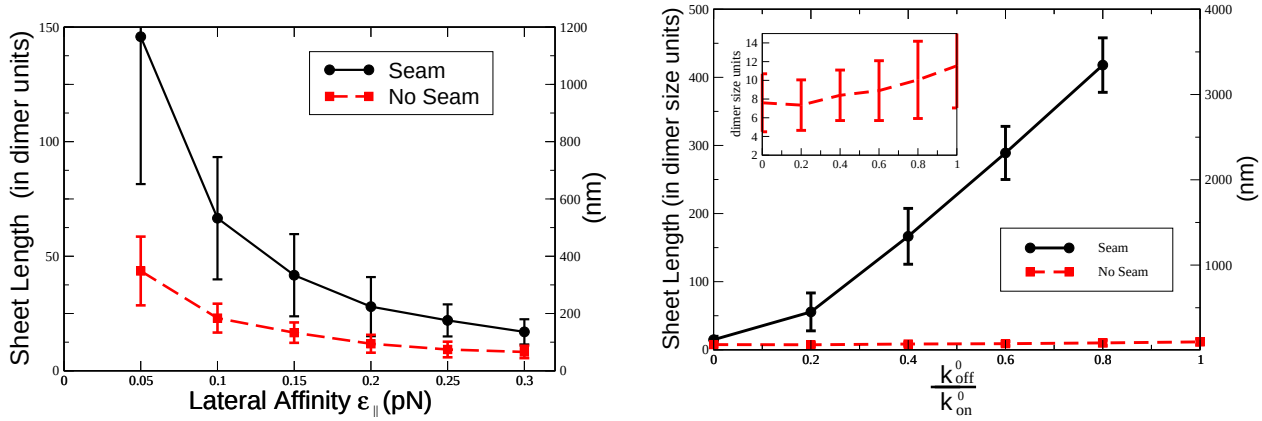

(a) (b)

Figure 4.4: Computer data suggest a large end structure (the *sheet cap*) in the case of seamed microtubule. It is argued that blunt microtubule ends exist for seamless or less dynamic microtubules. (a) Keeping the probability rates, k^0_{on} and k^0_{off} as constant, the size of the end structure decreases at larger lateral affinity constant $\varepsilon_{||}$. $k^0_{on} = 160\,min^{-1}$, $k^0_{off} = 0\,min^{-1}$; (b) We obtain larger sheet lengths for more dynamic microtubules, with higher k^0_{off} at constant k^0_{on}. $k^0_{on} = 50\,min^{-1}$, $\varepsilon_{||} = 0.30\,pN$; Other parameters $S = 1.5\,\delta$, $\delta = 8\,nm$, $k_B\,T = 4.1\,pN\,nm$

data simply show a strong dependence in the case of seamed microtubule and a weak or almost no dependence in the case of seamless assembly.

4.4 Conclusions

The compelling features of the strong lateral affinity limit of our theory are the appearance of just a single fit parameter, and the consistency of the fit results for the three independent sets of data, especially regarding the result for the stall force, lateral affinity and the values for the effective rates from Eq. (4.15).

Besides the good fit quality, obtained from this theory, the helical growth regime offers consistent physical reasons in defining *effective* on- and off-rates, *i.e.* k^{eff}_{on} and k^{eff}_{off}. The fitted values for these quantities are in excellent agreement with other experiments. Even more, the effective rates can be measured in different experiments, like growing free microtubules at different tubulin concentrations, which gives also an independent evaluation of the fit parameters.

However there is no prediction of an open sheet-like feature at microtubule ends in the strong lateral affinity regime. This feature, which is clearly observed from cryo-electron microscope images, is easily reproduced by our growth model in the limit of weak and intermediate lateral affinity. The microtubule dynamic parameters, *i.e.* the association and dissociation rates, are the tuning variables that control the length of the sheet. The evidence [5, 10] suggests sheets of $100\,nm$ or more in length. Such a size can be easily reproduced by our model in both cases of seamed and seamless microtubules (see Fig. 4.4).

Appendix A: Derivation of the *Force-Velocity* Relation for Helical Growth Regime

In this section we consider the helical growth model and derive the *force-velocity* relation Eq. (4.8).

The *state* of a microtubule is defined by its tip distribution. We attempt to analyze and solve the probability equations in order to derive the velocity of growth at arbitrary force.

In a helical growth there are 13 distinct configurations. We denote each configuration by k, and the associated probability by p_k. In the k configuration all filaments from 1 to k ($1 \leq k \leq 13$) have the same degree of polymerization and for the rest of them the polymerization degree is one less. It is convenient to make the following notations Eq. (4.6):

The steady equations for the configuration probabilities are (see Fig. 4.1)

$$\begin{aligned}
p_1(k_{on}^0 u^8 + k_{off}^0) &= p_{13} k_{on}^0 u^9 + p_2 k_{off}^0 \\
p_2(k_{on}^0 u^8 + k_{off}^0) &= p_1 k_{on}^0 u^8 + p_3 k_{off}^0 \\
p_3(k_{on}^0 u^8 + k_{off}^0) &= p_2 k_{on}^0 u^8 + p_4 k_{off}^0 \\
p_4(k_{on}^0 u^8 + k_{off}^0) &= p_3 k_{on}^0 u^8 + p_5 k_{off}^0 \\
p_5(k_{on}^0 u^8 r + k_{off}^0) &= p_4 k_{on}^0 u^8 + p_6 k_{off}^0 \\
p_6(k_{on}^0 u^8 r + k_{off}^0) &= p_5 k_{on}^0 u^8 r + p_7 k_{off}^0 \\
p_7(k_{on}^0 u^8 r + k_{off}^0) &= p_6 k_{on}^0 u^8 r + p_8 k_{off}^0 \\
p_8(k_{on}^0 u^8 r + k_{off}^0) &= p_7 k_{on}^0 u^8 r + p_9 k_{off}^0 \\
p_9(k_{on}^0 u^8 r + k_{off}^0) &= p_8 k_{on}^0 u^8 r + p_{10} k_{off}^0 \\
p_{10}(k_{on}^0 u^8 r + k_{off}^0) &= p_9 k_{on}^0 u^8 r + p_{11} k_{off}^0 \\
p_{11}(k_{on}^0 u^8 r + k_{off}^0) &= p_{10} k_{on}^0 u^8 r + p_{12} k_{off}^0 \\
p_{12}(k_{on}^0 u^7 r + k_{off}^0) &= p_{11} k_{on}^0 u^8 r + p_{13} k_{off}^0
\end{aligned} \tag{4.17}$$

This are to be solved together with normalization condition:

$$\sum_{k=1}^{13} p_k = 1 \tag{4.18}$$

The velocity is computed as (see Fig. 4.1)

$$v(F, \epsilon_{||}) = \sigma\delta(\sum_{k=5}^{11}(p_k k_{on}^0 u^8 r - p_{k+1} k_{off}^0) + p_{12} k_{on}^0 u^7 r - p_{13} k_{off}^0) \tag{4.19}$$

Solving the Eq. (4.17) a direct computation of Eq. (2.6) gives:

$$v(F, \epsilon_{||}) = 8\,\sigma\,\delta\,k_{on}^0\left(r^8 - A^{13}\right)/\mathcal{F}(A, u, r) \tag{4.20}$$

A simple check shows that equating to zero $r^8 - A^{13} = 0$ one has the exact expression for the stall force Eq. (3.24).

$$
\begin{aligned}
\mathcal{F}(A,u,r) = \quad & \left(\tfrac{r^8}{u^9} + \tfrac{r^8}{u^8}Q_1(1/r) + \tfrac{r^7}{u^7}\right) \\
+ \quad & A\left(\tfrac{r^8}{u^9} + \tfrac{r^8}{u^8}Q_2(1/r) + \tfrac{r^6}{u^7}\right) \\
+ \quad & A^2\left(\tfrac{r^8}{u^9} + \tfrac{r^8}{u^8}Q_3(1/r) + \tfrac{r^5}{u^7}\right) \\
+ \quad & A^3\left(\tfrac{r^8}{u^9} + \tfrac{r^8}{u^8}Q_4(1/r) + \tfrac{r^4}{u^7}\right) \\
+ \quad & A^4\left(\tfrac{r^8}{u^9} + \tfrac{r^8}{u^8}Q_5(1/r) + \tfrac{r^3}{u^7}\right) \\
+ \quad & A^5\left(\tfrac{r^7}{u^9} + \tfrac{r^8}{u^8}Q_6(1/r) + \tfrac{r^2}{u^7}\right) \\
+ \quad & A^6\left(\tfrac{r^6}{u^9} + \tfrac{1}{u^8}Q_6(r) + \tfrac{r}{u^7}\right) \\
+ \quad & A^7\left(\tfrac{r^5}{u^9} + \tfrac{1}{u^8}Q_5(r) + \tfrac{1}{u^7}\right) \\
+ \quad & A^8\left(\tfrac{r^4}{u^9} + \tfrac{1}{u^8}Q_4(r) + \tfrac{1}{u^7}\right) \\
+ \quad & A^9\left(\tfrac{r^3}{u^9} + \tfrac{1}{u^8}Q_3(r) + \tfrac{1}{u^7}\right) \\
+ \quad & A^{10}\left(\tfrac{r^2}{u^9} + \tfrac{1}{u^8}Q_2(r) + \tfrac{1}{u^7}\right) \\
+ \quad & A^{11}\left(\tfrac{r}{u^9} + \tfrac{1}{u^8}Q_1(r) + \tfrac{1}{u^7}\right) \\
+ \quad & 13\tfrac{A^{12}}{u^8}
\end{aligned}
$$

where $Q_k(x)$ are the following polynomials

$$
\begin{aligned}
Q_1(x) &= 7x + 4 \\
Q_2(x) &= 6x^2 + 2x + 3 \\
Q_3(x) &= 5x^3 + 2x^2 + 2x + 2 \\
Q_4(x) &= 4x^4 + 2x^3 + 2x^2 + 2x + 1 \\
Q_5(x) &= 3x^4 + 2x^3 + 2x^2 + 2x + 2 \\
Q_6(x) &= 2x^5 + 2x^4 + 2x^3 + 2x^2 + 2x + 1
\end{aligned} \tag{4.22}
$$

Appendix B: The Effective on- and off- Rates

In this Appendix we try to justify the definitions Eq. (4.15) for the *effective association* and *dissociation* rates, as *physical* quantities for the helical growth model. For the definitions Eq. (4.14)

and Eq. (4.15) to be correct, these relations have to comply with the corresponding experimental observable quantities. The association and dissociation rates were evaluated in the experiments like Ref. [34] for growing microtubules in buffer conditions at different tubulin concentrations. Without insisting into much details, we mention that the main argument ruled in these experiments is that the tubulin association rate scales linearly with the tubulin concentration of the existing pool

$$k_{on}^0 = c\,\alpha_{on} \tag{4.23}$$

In the last equation we denoted the tubulin concentration by c, and α_{on} is a proportionality constant, which is concentration independent. If the microtubule is modeled as a single filaments, then its growth velocity is in the absence of any force given by

$$v(F=0) = \delta^*(\,c\,\alpha_{on} - k_{off}^0) \tag{4.24}$$

As usual, we call δ^* as the *average* step size. Since the removal rate is not expected to depend on tubulin concentration, the *off*-rate is evaluated from the $y-$ intercept from a plot of the velocity at different tubulin concentration values c.

The microtubules stop growing at a critical value of the concentration c_{crt}, which if given from Eq. (4.24) as

$$c_{crt} = \frac{k_{off}^0}{\alpha_{on}} \tag{4.25}$$

In the following, we consider the helical model in order to derive the dependency for the velocity of growth with tubulin concentration at *zero force*.

In the case of $F=0$, then $r=1$ in the notations of Eq. (4.6), and Eq. (4.8) becomes:

$$v(F=0,\varepsilon_{||}) = 8\,\sigma\,\delta\,k_{on}^0 u^8 \frac{1-A}{(1-u)^2\frac{1-A^{12}}{1-A^{13}} + 13\,u} \tag{4.26}$$

In the case of helical growth, the criterion Eq. (4.7) predicts a minimal value for u as $u_{min} = 1.4$. For this value of u, the denominator in the last expression has simply a *weak* dependency on A. Therefore, for minimal values for the lateral affinity, we can approximate the above relation as

$$v(F=0,\varepsilon_{||}) = 8\,\sigma\,\delta\,k_{on}^0 u^8 \frac{(1-A)}{13\,u} \tag{4.27}$$

Now, in analogy with Eq. (4.23) we can introduce an *effective* quantity α_{on}^{eff} as

$$k_{on}^0\,u^8 = c\,\alpha_{on}^{eff} \tag{4.28}$$

Indeed, the effective polymerization rate is given by both longitudinal and lateral affinity, and this is supposed to scale linearly with the concentration of tubulin.

Then, Eq. (4.27) becomes

$$v(F=0,\varepsilon_{||}) = \frac{8\,\sigma\,\delta}{13\,u}\left(c\;\alpha_{on}^{eff} - k_{off}^0\right) \tag{4.29}$$

According to this equation, the microtubule growth stops at a critical tubulin concentration

$$c_{crt} = \frac{k_{off}^0}{\alpha_{on}^{eff}} \tag{4.30}$$

We can note the similarity between this critical value and the value suggested by Eq. (4.25). The only difference is that the effective parameter α_{on}^{eff} incorporates the lateral bonding energy between the protofilaments.

Above the critical value given by Eq. (4.30), the expression Eq. (4.29) suggests a perfect linear dependency for the velocity of growth with the tubulin concentration. This qualitative aspect is more than sufficient to make possible the definition for the *effective* association-dissociation velocities for the *freely* growing microtubules. Although the equation Eq. (4.27) was derived at the minimal value for the lateral affinity for which the helical growth is still possible, we confirm that this equation remains linear above the critical concentration for any other possible subregimes of the helical growth. Below the critical concentration, it is possible for the velocity to become slightly non-linear.

Part II

Microtubule Self-Organization

Chapter 5

Microtubule Self-Organization in Higher Plant Cells

5.1 Introduction

The proper functioning of a living cell depends on the organization of its cytoskeleton. Specific functions are associated to different cytoskeletal structures, and the complexity of the performed tasks depends on the various forms in which the cytoskeleton can be organized. In the introduction of this thesis we mentioned the mitotic spindle as a clear example of an organized microtubule system that plays a very important role in positioning and segregating the chromosomes during division. Asters represent a completely different form in which microtubules organize after the exit of mitosis, in the case of animal cells, and play an important role in generating shape and rigidity to the cell.

Among the other cytoskeletal components, like actin and the intermediate filaments, the organization of microtubules involves a phenomenology with its own agenda. The dynamic instability makes possible that tubulin can be recycled and quickly assembled into microtubules that assume a completely different organized form [2]. In the case of higher plant cells, microtubules organize in 5 different cytoskeletal forms that show little resemblance to those from animal cells [39, 40, 41].

The various microtubule arrays that organize in higher plant cells are summarized in Fig. 5.1. In the case of elongating interphase cells, the microtubules appear in the cell cortex as a transversal array, *i.e.* perpendicular to the main axis of the cell. Before the onset of mitosis, the widely dispersed interphase array of microtubules narrows to a tight $3 - 4\,\mu m$ wide band, which wraps on the cortex around the nucleus (see *e.g.* [42, 43]). This band is called the *preprophase band* (PPB), since it starts forming in the early prophase cells. When the cell enters mitosis, the nuclear membrane breaks down at the same time as the PPB. The PPB tubulin is recycled and assembled into the microtubules that form the mitotic spindle. When the cell exits mitosis, a new and very important cytoskeletal complex is formed: *the phragmoplast*. This is a complex array of short and longitudinal microtubules, which contains also actin, membranous filaments, and vesicles. The phragmoplast helps in building the separation wall between the daughter cells during a process which is called *cytokinesis*. Finally, cortical microtubules re-appear in the form of a disordered array of short microtubules in early interphase cells, roughly radiating outward from the nucleus. During interphase, this random array is replaced by ordered tranversal microtubules.

The biological role of these geometrical arrays is only partially understood. For example, immunofluorescence or GFP imaging techniques (*e.g.* [44, 45, 46]), clearly show that the location of PPB precisely coincides with that of the new separation wall, which is built during cytokine-

sis. Different studies show a relation between PPB, the orientation of the mitotic spindle, nuclear positioning and the cytokinetic apparatus [47, 42, 48, 49]. Studies with selective drug treatment suggest that the microtubule arrays could in fact play a complementary role together with actin components to ensure a precise orientation of the division plane [47, 50].

Also, the role played by the interphase microtubule array is not fully elucidated. The *transverse* array is observed mainly in elongating cells, and hence the belief that this microtubule system must be correlated with the process of growth. Indeed, the orientation of interphase microtubules correlates with that of cellulose microfibrils [51, 52]. As the cellulose wall hardens, the turgor pressure makes possible only a longitudinal growth of the cell. However, there is no convincing evidence that could support the direct relationship between these two components, and secondly, the cellulose microfibrils can, in principle, be deposited into the wall by a mechanism that is independent of microtubules [53, 54, 55, 56].

While the biological role of these microtubule components is under discussion, the underlying mechanisms that are responsible for the organization of these arrays are even more mysterious. In order to elucidate what are the possible factors that might be involved, different methods were used to study the behavior of cells under different conditions. For example, mechanical stress, auxin, red or blue light make the reorientation of transverse interphase microtubules possible [57, 58, 59, 60, 61]. Drug treatment, like ethylene or abscisic acid, lead to reorientation of interphase microtubules from transversal to longitudinal [62]. When the cells were treated with microtubule stabilizing drugs like taxol, the PPB failed to organize properly, and the interphase microtubules persisted until late prophase [63]. This experiment suggests that dynamic instability of microtubule is required for PPB formation. This result is consistent with more recent studies that show that microtubules are becoming more dynamic at the onset of PPB formation [64, 43].

Other studies, carried on mutants like MOR1, suggest the existence of a key biomolecular component that is responsible for microtubule organization [65]. Particularly, these studies show that MOR1 cells display short microtubules in a disorganized interphase array, which is similar to the wilde type cells during their early interphase. We will use later this observation for our arguments in this chapter.

Besides MOR1, many other microtubule associated proteins (MAPs) were also identified. These proteins are known to regulate the microtubule dynamics, and therefore, are involved in the organization of the microtubule cytoskeleton [66]. Among them, the protein class MAP 65 is responsible for cross linking, and appears to be characteristic to plants [67, 68]. Another example is MAP 60, which promotes the growth and stabilization of neuronal microtubules *in vitro* [69]. The presence of katanin, a microtubule severing protein, suggests that microtubules might be independent from their nucleation sites, which make for the cytoskeletal network more flexible to organize [40]. There is, however, evidence for mobile nucleation sites [70].

Finally, it order to elucidate which are the most important factors that drive the microtubule organization, it is necessary to investigate more closely the relationship between microtubules and actin. For example, in trying to understand the role that actin is playing during the formation of PPB, root-tip cells of allium were treated with actin depolymerization drug cytochalasin D. In this case the PPB failed to organize or remained much wider than in control cells [71]. Although the result of this experiment points to a possible involvement in PPB maturation, the microtubules kept their transversal alignment even in the absence of actin. However, in a similar experiment, cytochalasin B was used as acting depolymerizing drug instead of cytochalasin D. In this case, the treatment showed no influence on the PPB organization, while all the actin was shown to be fully depolymerized [45]. Although, it can be argued the possible side effects of cytochalasin treatment, the second experiment strongly suggests that PPB organization is independent of actin.

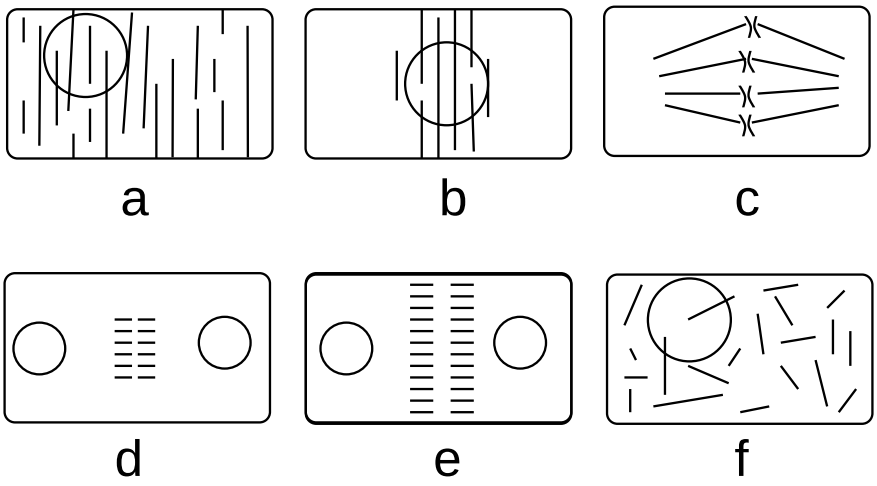

Figure 5.1: The microtubule cytoskeleton in higher plant cells. a) In interphase cells, the microtubules are organized transversely on the cortex of the cell. b) The preprophase microtubules organize within a narrow transverse band on the cortex, around the nucleus (the circle), which is positioned at the mid of the cell. c) The mitotic spindle is not bipolar, the centrosomes are dispersed, unlike animal cells. d) and e) Cytokinesis. The phragmoplast helps in building the separation wall between daughter cells, from inside the cell toward the wall. f) Early interphase cell. The microtubules appear on the cortex as being short and randomly oriented.

In spite of the plethora of information that experiments provide, it remains still a mystery what might be the precise mechanism that drives the organization of microtubules in higher plant cells. The complexity of the system is as yet responsible for frustrating us in the understanding of these processes. The most relevant factor might be hidden by other factors whose role are only complementary, and their presence is justified only to give accuracy to the processes that are involved.

The aim of the present chapter is to initiate a study based on the most simple physical processes that might drive a complex phenomenon such as the *self-organization* of the cytoskeleton. Our focus will be on interphase microtubule arrays in higher plant cells. In the following we will present two different passive factors that might be responsible for the transversal alignment of microtubules. Modeling the self-organization in such a complex system, like plant cells, has two main reasons. One of them is programmatic, *i.e.* we aim to derive a minimal set of conditions that are relevant to a particular organized system. The second one, as we have seen from the brief presentation of experiments during this introduction, there is no direct evidence that involves other components, like actin, in driving the organization of microtubules.

5.2 Interphase Nematic Order Parameter

The most direct and striking observation that we can make about microtubule interphase array is their parallel alignment. This brings us close to the hypothesis that microtubules can display in plant cells something similar to a nematic crystalline phase. *In vitro* experiments could indeed prove the possibility that microtubules can undergo isotropic-nematic transition, displaying a liquid crystalline structure [72].

Nematic phase is known as an intermediate liquid-solid phase that appears in systems of rod-like particles. Today it is widely established that entropy alone can drive a system of hard rods into an ordered nematic state [73]. Without going into much details, we mention that such a phenomenon is possible, since an aligned system of hard rods can have higher entropy, and therefore less free

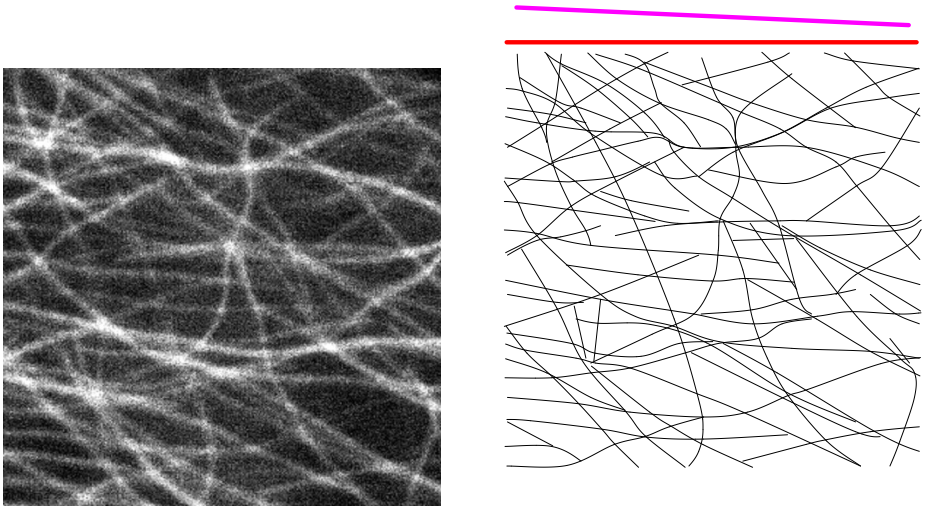

(a) (b)

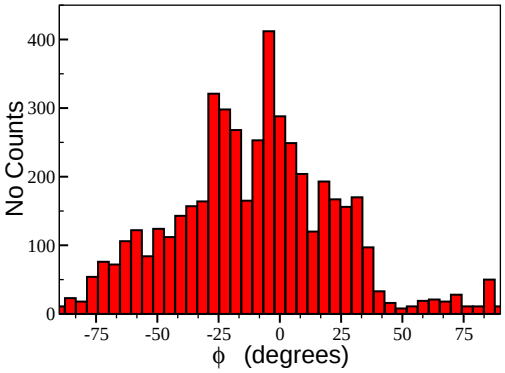

(c)

Figure 5.2: a) Cortical GFP labeled microtubules from BY2 cells (courtesy of Jan Vos, University of Wageningen). b) Manual tracking of microtubules from the image shown in a). The scale bar (the horizontal thick line) is $18.3\,\mu m$. The measured order parameter is $m = 0.53$. The tilted line is the nematic director. c) Angular distributions of filaments.

energy, if the density of rods is above a critical value $\rho > \rho_{cr}^{nem}$. In fact, the rods avoid jamming if they become more aligned, which means that they gain more translational degrees of freedom. As a consequence, the *effective* phase space is larger, and above the critical density, the gain in translational entropy dominates the loss of orientational entropy. This makes possible of having higher entropy in the ordered than isotropic state in a system of rigid rods.

The nematic order parameter [75] (or see for example Eq. (6.11)) increases as the density of rods increases. The corresponding dependency can be calculated with the help of Monte Carlo simulations [74, 77]. These calculations, which were done for a quasi 2 dimensional system of hard rods, can be compared directly to the experimental results from both *in vitro* and *in vivo* systems of microtubules [77].

The microtubule array of interphase cells can be visualized at the single filament level with confocal imaging techniques [76, 43]. However, most of the time the density of microtubules is too high to measure their length, since the ends cannot be easily distinguished. The density

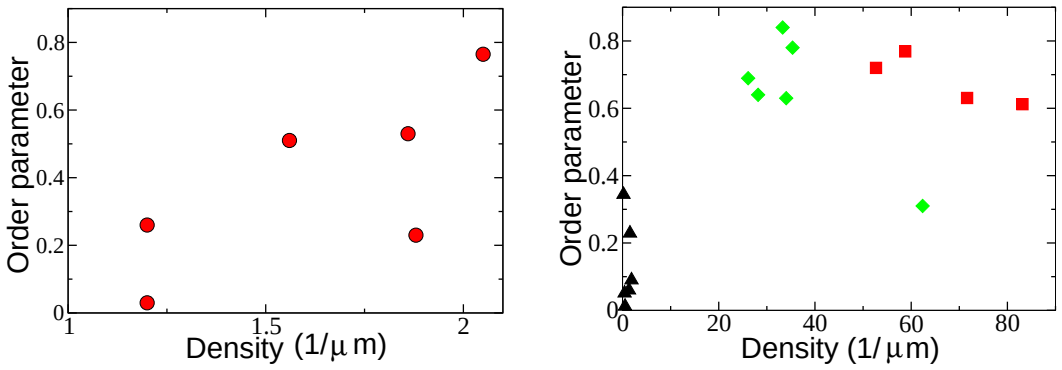

Figure 5.3: Comparison between *in-vitro* (a) and *in-vivo* (b) data. The density was defined in both cases as the total microtubule length divided by the field area.

and main angle of microtubules can be measured by direct observation of the cells. With this we can compare the nematic order parameter of cortical microtubules from different samples that display different microtubule density. Also, density and order parameter measurements can be done for microtubules that were let to grow *in vitro* in microfabricated chambers. These chambers were quasi 2 dimensional confinements in order to reproduce the *in vivo* conditions of cortical microtubules. This experiment is described and analyzed in details in the PhD thesis of Marco Cosentino Lagomarsino [77].

In Fig. 5.3 we plot the nematic order parameter versus the microtubule density for both *in vivo* (Fig. 5.3 (a)) and *in vitro* (Fig. 5.3 (b)) experiments. The *in vitro* data clearly show a correlation between the density and the order degree, which is a close resemblance from ordinary liquid crystals [74]. On the other hand, the corresponding *in vivo* data is not convincing enough to derive a conclusion, and it clearly indicates the need for more data points.

Finally, looking at the microtubule arrays in interphase cells, we cannot avoid the question of the existence of a symmetry breaking factor that might exist in the case of a hypothetical nematic transition. Normal cells never display longitudinal microtubules. The interphase microtubules are transversal in most cases, and sometimes tilted. Even more, a transversal array seems to be an unfavorable configuration, since microtubules are stiff polymers and we expect them to be bent as they follow the curvature of the cortex. This brings us to the analysis of the elastic properties of cortical microtubules in the next sections.

5.3 A Helical Spring Model

Besides entropically driven nematic transitions, elasticity is another interesting candidate for a mechanism of passive self-organizing semi-flexible polymers. Here we explore what the possible configurations are of a long confined polymer bundle, if the only ingredient is its elastic bending energy.

The motivation of this idea is given by images like Fig. 5.4 of a interphase plant cell. It looks as if long coils of microtubule wrap around the cell in a helical pattern. Very little is known about

how long microtubules could be in such cells, or what the possible ways are that short microtubules could form long bundles with the help of cross-linkers. The idea of helical microtubule springs wrapping around the cell is not new. Different images suggest the same idea independent of cell type or imaging techniques, like immunolabeling of root tips of Arabidopsis [52] and cortical parenchyma cells from pea [78], or YFP-CLIP170 and GFP-MAP4 labeling of BY-2 cells [64], or even electron microscope images. Even more, rotation of a confocal optical series projections reveals that oblique microtubule orientation is consistent around the circumference of the cell [52].

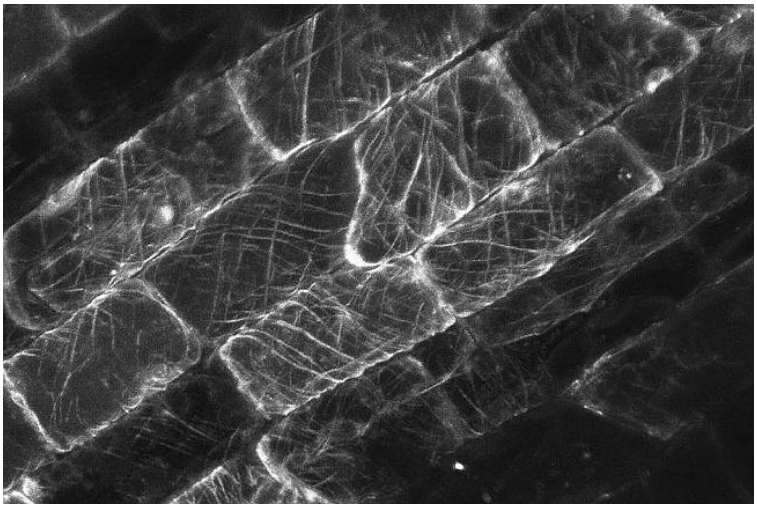

Figure 5.4: GFP images of BY2 labeled cells. These images show for each interphase cell an apparent helical microtubule coil that wraps around the cell several times.

Following Lloyd *et. al* [80, 78, 79, 81], a list of arguments can be presented in order to favor the idea that interphase microtubules may not be simply hoops, but rather long microtubule bundles that circle around the cell more than once. For example, in order to test the integrity of the microtubule helical coil, Lloyd and Seagull [78] show how ethylene inhibits the elongation of epidermal cells by reorientating microtubules. Thus, the frequency of oblique microtubule orientation increases, but this transition from transversal alignment appears like the unwinding of compressed helices rather than depolymerization followed by repolymerization of microtubules in a different configuration. However, this study does not mention explicitly that the rate of the pitch change of the helix is the same along the whole range of the length of the cell. The presented images clearly show a constant helical pitch, no matter if the array was tilted or transversal.

5.4 Elastic properties of flexible chains in confined geometry

In the previous section we showed some evidence of existing long microtubules or microtubule bundles in interphase plant cells. The evidence is not very strong, however, as it remains an experimental challenge to measure the length distribution of microtubules in living plant cells. In this section we are going to test the logical implications of long semi-flexible polymer bundle in a confined cylindrical geometry.

We consider a long inextensible string, which is confined on the 2D surface of a cylinder of radius r. We aim to derive the shape equation of this string. The way we derive the equation is to

minimize the elastic energy stored in this string:

$$W = \frac{E\,I}{2}\int ds \frac{1}{R^2} \tag{5.1}$$

where $E\,I$ is the bending rigidity and R is the radius of curvature, which is given by:

$$\frac{1}{R^2} = \left(\frac{d\mathbf{t}}{ds}\right)^2$$

Using cylindrical coordinates, we denote the unit vectors by $\hat{\mathbf{e}}_r$, $\hat{\mathbf{e}}_\phi$, $\hat{\mathbf{e}}_z$. Since the string is wrapping up around a cylinder ($r = const$), the vector element becomes:

$$d\mathbf{r} = \hat{\mathbf{e}}_\phi\, r\, d\phi + \hat{\mathbf{e}}_z\, dz \tag{5.2}$$

The tangent $\mathbf{t} = d\mathbf{r}/ds$ is then

$$\mathbf{t} = \hat{\mathbf{e}}_\phi\, r\,\dot{\phi} + \hat{\mathbf{e}}_z\,\dot{z}$$

Because

$$\frac{d}{d\,s}\hat{\mathbf{e}}_\phi = -\hat{\mathbf{e}}_r\dot{\phi}$$

it follows then:

$$\dot{\mathbf{t}} = -\hat{\mathbf{e}}_r\, r\dot{\phi}^2 + \hat{\mathbf{e}}_\phi\, r\ddot{\phi} + \hat{\mathbf{e}}_z\,\ddot{z}$$

We use in addition the hypothesis that the string is inextensible, i.e.,

$$r^2\dot{\phi}^2 + \dot{z}^2 = 1$$

From this expression, $\dot{z}$ is substituted in the expression for $\dot{\mathbf{t}}$, and finally, the radius of curvature is given by

$$\frac{1}{R^2} = r^2\dot{\phi}^4 + \frac{r^2\ddot{\phi}^2}{1 - r^2\dot{\phi}^2} \tag{5.3}$$

We use this last equation for the expression of the elastic energy that is stored in the string. If we introduce the angle $\gamma(s)$ as $\cos\gamma(s) = r\,\dot{\phi}$, the the radius of curvature becomes:

$$\frac{1}{R(s)^2} = \frac{\cos^4\gamma(s)}{r^2} + \dot{\gamma}^2 \tag{5.4}$$

From the definition of the introduced angle, one can identify $\gamma(s)$ as being the angle between the unit vectors $\mathbf{t}$ and $\hat{\mathbf{e}}_\phi$. The string equation that we have to derive is in fact for the function $\gamma(s)$. Indeed, the cylindrical coordinates are given from solving the equations:

$$\begin{aligned} r\dot{\phi} &= \cos\gamma(s) \\ \dot{z} &= \sin\gamma(s) \end{aligned} \tag{5.5}$$

Suppose that the ends of the string are fixed (by some forces that acts on the string), we derive the string equation by minimizing the elastic energy W:

$$\delta W = 0 \tag{5.6}$$

From this "minimal action" principle we derive the *Lagrange* equation:

$$\ddot{\gamma}(s) + 2\cos^3\gamma(s)\sin\gamma(s) = 0 \tag{5.7}$$

From this equation we may derive a *first integral* if we multiply the equation by $\dot{\gamma}(s)$:

$$\dot{\gamma}^2 - \frac{\cos^4\gamma(s)}{r^2} = A \tag{5.8}$$

where A is a constant which is fixed by the end conditions of the string.

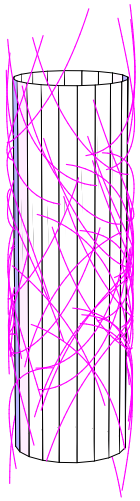

Figure 5.5: Cortical microtubules in cylindrical cells

5.4.1 Example: A long string with one end free and the other clamped

In the next step we identify the case $A = 0$ as corresponding to the case when one end of the string is free. Indeed, for a string long enough, $\gamma(s) \to \pi/2$ and $\dot{\gamma}(s) \to 0$, as $s \to \infty$, and from this it follows $A = 0$. If we set $\gamma(0) = 0$, *i.e.* at its seed the string is transversal to the cylinder axis, then, from Eq. [5.8] we derive as initial condition $\dot{\gamma}\,(0) = 1$. Therefore, for long strings the equation Eq. [5.8] becomes:

$$\dot{\gamma} \approx \frac{\cos^2 \gamma}{r} \tag{5.9}$$

We rewrite that last equation as:

$$\frac{d\,\gamma}{\cos^2 \gamma} \approx \frac{d\,s}{r} \tag{5.10}$$

After integration we get:

$$\tan\,\gamma\,(s) \approx \frac{s}{s} \tag{5.11}$$

Finally:

$$\gamma\,(s) \approx \arctan\frac{s}{r} \tag{5.12}$$

We introduce this solution in the equation for the cylindrical coordinates Eq. [5.5]:

$$\begin{cases} \dot{\phi} \approx \frac{1}{r}\frac{1}{\sqrt{1+(s/r)^2}} \\ \\ \dot{z} \approx \frac{s}{r}\frac{1}{\sqrt{1+(s/r)^2}} \end{cases} \tag{5.13}$$

After the integration we obtain the solution:

$$\begin{cases} \phi\,(s) \approx \operatorname{arcsinh}\frac{s}{r} \\ \\ z\,(s) \approx r\,\left(\sqrt{1+(s/r)^2}-1\right) \end{cases} \tag{5.14}$$

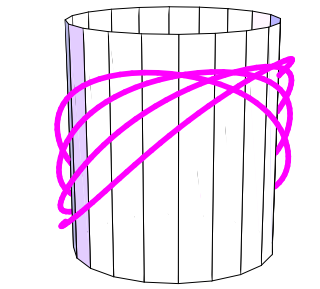

(a) $A < 0$

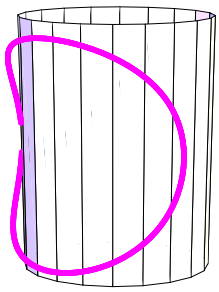

(b) $A > 0$

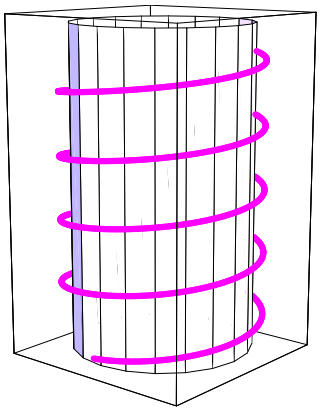

(c)

Figure 5.6: (a) and (b) Two examples of numerical solutions of the equation Eq. [5.8]. (c) A long helical microtubule bundle in cylindrical cells.

According to this solution, we show in Fig. 5.5 the organization of microtubules on the cortex of a cylindrical cell. It is assumed that the conformations are only due to bending elasticity and the confining forces [1]. The seeds of microtubules are fixed and the initial direction of growth at the seed is transversal for all microtubules.

5.5 A Confined Elastic String

In the following we investigate two different cylindrical geometries: a cylinder capped by two planes and a spherocylinder.

5.5.1 Plane Capped Cylinder

We consider a cylinder limited by two planes at its ends. We can make a comparison between two possible descriptions: one is the solution of the Lagrange equation (see Eq. [5.7]) for a bundle with *both* ends being clamped, and the other is a helical bundle, which is described by the equation $\gamma = const$. The two possible configurations are shown in Fig. 5.7 (a) & (b). Given the distance Z_m between the two limiting planes we plotted the ratio of the elastic energies as a function of Z_m. We can see in the figure Fig. 5.7 (c) that the helical configuration is not favored. since the

[1] The confining forces which are normal to the cell wall, *i.e.*, their direction is radial

elastic energy which is stored in it is larger for the same confinement height, which is the distance between the two limiting planes.

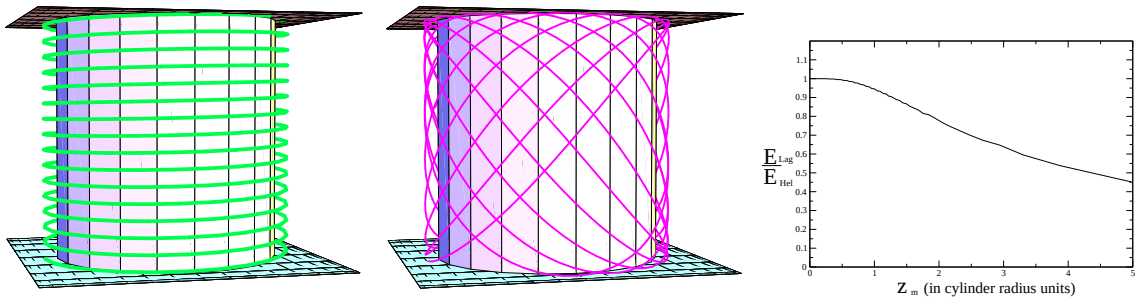

(a) (b) (c)

Figure 5.7: a) Helical bundle: a case of torque free ends. b) The solution of Lagrange equation in the case of applied torques at both ends. The solution depicted here corresponds to zero confinement force, *i.e* there is no confining force acting from the planes. c) Energy ratio between cases b) and a) *vs* the confinement height Z_m. It appears that the energy of the helical coil is always larger than in the case of the coil with clamped ends, for the same confinement height. This comparison suggests that the helical solution is not stable.

5.5.2 Spherocylinder

We consider the spherocylinder as being another interesting confined geometry. Indeed, the plane capped cylinder may be regarded as a rough approximation, since the ends of a real cell are round. The analysis of Lagrange equation is summarized in Fig. 5.8. The bundle is clamped transversally at one end, while the other is free. The round ends of the chamber allow the bundle to slip longitudinally around the cell. We regard this geometry as being more realistic, and since the bundle quickly wraps around the cell in a longitudinal way and not transversally, we have to suppose that some more additional forces might be present. At the origin of these external forces could be the cross linkers that exists between microtubules themselves, or between microtubules and plasma membrane. Therefore, we derive in the next section the equation of a bundle under the action of a external force. This case resembles closely the *in vitro* observations of microtubules in a elongated box [77].

5.5.3 Elastic string under the action of an external force

Suppose that one end of the string is fixed at its seed and a point force $\mathbf{F}$ is acting upon the other end. We consider, for simplicity, that this force is parallel to the cylinder axis, $\mathbf{F} \,||\, \hat{\mathbf{e}}_z$. If the $z-$coordinate of this string end is displaced by an amount $\delta\, z$, then the work done by the force, $F\, \delta\, z$, corresponds to a variation $\delta\, W$ of the elastic energy which is stored in the string:

$$\delta\, W = F\, \delta\, z \tag{5.15}$$

From this equation we obtain:

$$\delta\, (W - F\, z) = 0 \tag{5.16}$$

This means that the *action* that needs to be minimal is now:

$$\mathcal{F}[\gamma] = W[\gamma] - F\, z[\gamma] \tag{5.17}$$

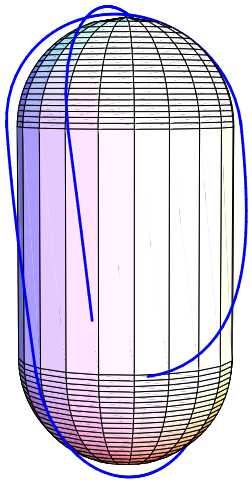

Figure 5.8: We consider the spherocylinder as the confinement chamber. If the polymer bundle has one end transversally clamped, and the other free, then in its optimal configuration the bundle assumes a rather longitudinal arrangement.

From the equation Eq. [5.5], we have for the $z-$coordinate:

$$z[\gamma] = \int_0^L ds\, \sin\,\gamma\,(s) \tag{5.18}$$

It follows:

$$\mathcal{F}[\gamma] = \int_0^L ds \left(\frac{k}{2}\Big(\dot{\gamma}^2 + \frac{\cos^4\gamma\,(s)}{r^2}\Big) - F\, \sin\gamma\,(s) \right) \tag{5.19}$$

We denoted the bending rigidity by k in the last equation.

From the *minimal action principle*, $\delta\mathcal{F} = 0$, we have the *Lagrange equation*:

$$\ddot{\gamma} + \frac{2\,\cos^3\,\gamma\,\sin\gamma}{r^2} + \frac{F}{k}\cos\gamma = 0 \tag{5.20}$$

If there is no torque applied at the end of the bundle, *i.e.* $\dot{\gamma}(0) = \dot{\gamma}(L) = 0$, the solution of the last equation is in fact a helix

$$\gamma(s) = \gamma_0 = const \tag{5.21}$$

and the confinement force is:

$$F = -\frac{2\,k}{r^2}\,\cos^2\,\gamma_0\,\sin\,\gamma_0 \tag{5.22}$$

We can estimate the value of this confinement force if we know that the radius of the cell is $r = 5\mu m$, and $k = l_p\, k_B\, T$, where the persistence length is $l_p = 6\, mm$, and the temperature is $k_B\, T = 4.1\, pN\, nm$

$$F \approx 1pN \tag{5.23}$$

This force is very low, and it is closed in value to the forces that are generated by molecular motors [102]. However, when microtubules are bundled, the bending rigidity $E\, I$ is expected to be higher, and it depends on how many microtubules are in the bundles. From the available experiments, this is hard to evaluate, and therefore we cannot know the real value of the confining force.

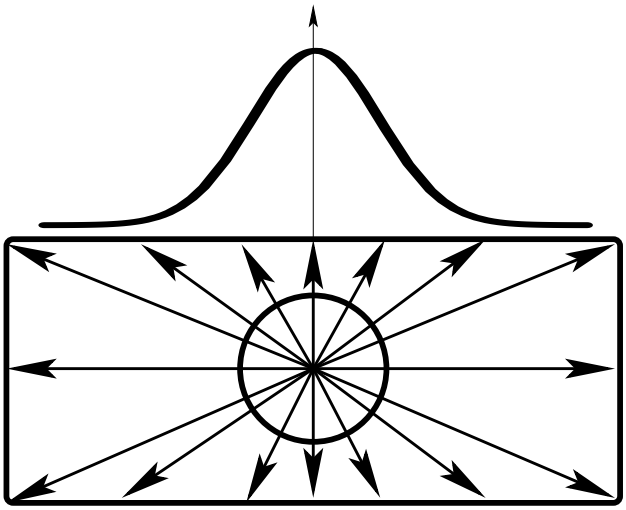

Figure 5.9: PPB formation. A hypothetical protein is isotropically released by the nucleus. However, due to the geometry, the density of this protein is not constant along the cell cortex, and it can be fairly approximated by a Gaussian. In the model that we propose, we assume that this protein is a microtubule growth promoting factor. Since its density is higher near the nucleus and less near the edges of the cell, we expect that microtubules tend to polymerize on the cortex only close to the nucleus.

5.6 Discussion and Conclusion

In the present chapter we have explored the possibility of having passive ingredients as driving factors in organizing microtubules in interphase higher plant cells. Physical modeling can help as a complementary tools, besides biomolecular methods, in understanding the complexity of such systems.

We have presented two main possible passive factors. One is a isotropic-nematic like transition in a system of long and stiff polymers, like microtubules. The other, is the bending elasticity of long polymers, since the internal elastic stress, which develops in confined polymer, can drive the system in a particular arrangement.

The second possibility is more promising than the first one from at least two reasons. The first reason is the need a symmetry breaking factor that explains the transversal alignment of microtubules in the nematic phase. The second reason comes from the fact that the transversal alignment corresponds to an elastic unfavorable configuration.

Simple arguments from the elasticity theory show that a transversal alignment of microtubules in cylindrical geometries is possible if a) there is a longitudinal confinement force, b) the ends of the polymer are torque free, and finally c) the polymer must be very long. For cells with a diameter of $D = 10\,\mu m$, without bundling we need microtubules with length of more than $100\,\mu m$ in order to wrap around the cell a couple of times. There is little evidence of such long microtubules for *in vivo* conditions, and neither *in vitro*. We consider this as the most unappealing feature of the helical coil model for interphase microtubules. However, MAP65 proteins, which were isolated from carrot cells, proved their ability to bundle neuronal microtubules [82]. This leaves open the possibility of long coiling bundles composed of short microtubules that form the elastic coil in interphase cells.

Finally, we mention that in order to realize what are other possible organizing factors for interphase microtubules, a close investigation of the relationship between interphase and preprophase microtubules could be helpful. Indeed, we could ask if the transversal aligning factor could be the

same in these two cytoskeletal arrays. The quest for PPB formation is twofold: what drives the dynamics of PPB narrowing, and what keeps the microtubules as transversely aligned during PPB formation? One way to address these questions is to observe that recent studies provided solid evidence that just before the formation of PPB, microtubules become more dynamic [64, 43]. Here it is worth to mention the *search-and-capture* model that is proposed by Vos *et. al.* [43]. This model assumes a combination between the increased dynamic instability of microtubules outside PPB and their bundling inside PPB. To fortify the arguments of these authors, we can speculate the existence of a yet undetermined biochemical agent, like a MAP, which is released isotropically by the nucleus. This protein is deposited on the cell cortex and acts as a microtubule growth promoting factor. However the density of this protein along the cortex is not constant from geometrical reasons (see Fig. 5.9), and is maximal nearby the nucleus. The microtubule density becomes higher where this protein is more abundant. There are analogies between this model and other more studied systems, like fission yeast [28, 6]. However we leave open the questions about the time dynamics of PPB, or which are the alignment factors for microtubules inside PPB.

So far, we have investigated what are the possible passive ingredients that help in organizing microtubules in plant cells. In the next incoming chapters, we change this perspective in the sense that these could be dissipative far from equilibrium structures, and their organization is driven by active ingredients like molecular motors.

Chapter 6

Generic Aspects of Microtubule Self-Organization

6.1 Introduction

In the previous chapter we tried to develop a model of microtubule self-organization in higher plant cells, which was solely based on passive ingredients. We speculated that the elastic properties of long microtubule bundles could explain the patterns on a large length scale, comparable to the size of a single cell. For the remainder of this thesis we will change this perspective by trying to understand how *active* ingredients could play a role in generating similar patterns like those that are observed in plant cells.

Motor proteins are ubiquitous in the living cell. *In-vitro* experiments [83, 84, 85, 86, 87, 88] prove that motor proteins are able to actively cross link filaments and thus make the self-organization of the cytoskeleton possible. The understanding of the involved dynamics can be explored with the help of computer modeling and simulations [89], in which the formation of various complexes like asters, vortices, or even spindles was demonstrated. There are also examples of one-dimensional analytic models that are able to predict the property of filamentous bundles to contract [90, 91, 92, 93]. These type of models are relevant in the mechanics of muscle contraction, or cleavage furrow formation, which separates the two daughter cells after division. Two dimensional models are developed as based on macroscopic equations that couples the diffusion of motors with the motion of the filaments [94, 95, 96]. Based on computer simulations, these models predict complex patterns such as asters or vortices. A recent generic approach for active viscoelastic materials shows the appearance of rotating spirals, as some particular topological defects in active gels [97]. These are particular dissipative dynamic structures that could play an important role for fragments of fish keratocytes, which move spontaneously when their symmetry is broken by a mechanical action.

However, the self-organization process is quite complex, given the large number of factors that may be involved, like types of motors, the specific affinity between motors and filaments, motor activity regulatory factors, flexibility of filaments, their mobility and viscous drag in the cytoplasm, steric exclusion at high density, hydrodynamic effects etc. Hence it is not always possible to fully understand the interplay between various factors and the patterns that emerge when modeling is solely based on experiments or computer simulations. In the case of computer simulations, the interesting regions in the phase space must be guessed, and it might even happen that some of them are overlooked. Of course, one cannot expect an analytical theory to include all the possible factors to a full extent. However, a theoretical method can help to derive relationships between

some of the factors that are considered relevant. Moreover, analytical relationships can help in guiding toward interesting regions of a big phase space in a more systematic and efficient manner. This argument justifies the use of analytical methods as complementary tools for understanding complex phenomena.

In this chapter we will use symmetry arguments in order to derive generic evolution equations of filamentous systems. Based on tensorial analysis, we include in the evolution equations all the possible contributions that are allowed by symmetry. Although the microscopic origins of the symmetric terms are undetermined in this *top-down* approach, the method can potentially reproduce all the possible topologies for pattern formation and also the associated tension map, which shows how motion is generated in these states. The results can be compared qualitatively to examples from biological systems, and a pattern of interest, like the preprophase band, can help in tracking down a particular region in the phase space where its formation is possible. In this way it is possible to derive a minimal set of conditions for a particular phenomenology.

We try to elucidate and demonstrate this method in the case of microtubule self-organization in higher plant cells. This particular system brings a number of new restrictions, which besides symmetry, help in reducing the mathematical complexity of our analysis.

6.2 Mean Field Theory

6.2.1 Hypotheses

In the case of self-organizing active filaments, the emerging patterns correspond to a scale which is, in general, larger than the size of a single filament. This means that there exists a *macroscopic* length scale which is characteristic for the dynamics of our system. In a macroscopic description like the one that we want to follow, we neglect the thermal fluctuations and consider only a reduced number of degrees of freedom, which are expressed as *local* averaged fields. The *continuity* of the mean fields is a feature that results after smoothing out the small scale fluctuations. This means that there is a lower limit on the length scale, *i.e.* a *cutoff* l_0, which is given by the size of a single filament. Indeed, this is the length scale on which individual filaments can be distinguished and fluctuations cannot be ignored.

When we come to characterize the state of a filamentous system, the density $\rho(\mathbf{r},\, t)$ is the first important quantity. Filaments are regarded as small and rigid elongated particles. When a motor protein walks on a filament, it has to make a difference between the two ends of it, and therefore a symmetry breaking factor must be involved to guide the motor in either direction. This symmetry breaking factor is intrinsically related to the internal structure of the filament, which defines its *polarization*. Indeed, microtubules and actin filamements are known to be polar assemblies. When we average the polarization of the individual filaments $\hat{\mathbf{u}}$, the result is the macroscopic polarization $\mathbf{t}(\mathbf{r},\, t)$:

$$\langle \hat{\mathbf{u}} \rangle = \mathbf{t}(\mathbf{r},\, t) \tag{6.1}$$

In the last relation, by $\langle \cdot \rangle$ we mean both a thermal and local average of all the filaments inside a box that is centered in $\mathbf{r}$ and having the sidelength equal to l_0. However, if we want to characterize the degree of ordering in the system, then polarization alone is not a sufficient choice. For example, filaments could be arranged in an anti-parallel fashion, which gives no macroscopic polarization $\mathbf{t} = 0$. This problem is avoided by introducing the *nematic order* parameter [75] (see

also Appendix A of Chapter 7):

$$\overline{\mathbf{Q}}^{(2)} = \left\langle \hat{\mathbf{u}}\,\hat{\mathbf{u}} - \frac{\mathbf{I}^{(d)}}{d} \right\rangle \tag{6.2}$$

This is a symmetric and traceless tensor. The parameter d is the number of dimensions, it refers to either $2D$ or $3D$ case, and $\mathbf{I}^{(d)}$ is the identity matrix of rank d.

It is precisely the case of zero macroscopic polarization $\mathbf{t} = 0$ that we want to study. One reason for this choice comes directly from the system on which we want to apply the method that we develop here. Indeed, there is evidence that microtubules have anti-parallel orientations in higher plant cells [70]. Another reason is that we want to describe the evolution of the macroscopic state by studying how pattern formation may result from a direct coupling between density and the nematic order parameter, without the emergence of polarization. This is a special issue, which it can be also addressed by making reference to an explicit microscopic model. For example, we can argue that there is no symmetry breaking factor that may be responsible for a non-zero macroscopic polarization in the case of equal numbers of two kinds of motors, which walk on microtubules toward their plus and minus ends respectively.

6.2.2 General Equations

We consider that the density $\rho(\mathbf{r},\, t)$ and the nematic order parameter $\overline{\mathbf{Q}}^{(2)}(\mathbf{r},\, t)$ give a satisfactory description for the macroscopic state of active filaments. Since we do not study the effect of the microtubule dynamics, we disregard both the nucleation of microtubules and their disappearance due to dynamic instability. In this case we write down the conservation law for the total number of filaments in the system, which is in fact the continuity equation for the density:

$$\partial_t\, \rho + \boldsymbol{\nabla} \cdot \mathbf{J} = 0 \tag{6.3}$$

In writing this conservation law, we neglect the nucleation of filaments and the dynamic instability that could happen in the case of microtubules. In the case of preprophase band formation, there is evidence that the amount of polymerized tubulin is constant until late preprophase [43].

The second equation is for the nematic order parameter. In our generic description we do not have a continuity law, like in the case of filament density. Indeed, the order in the system is *generated* during the process of self-organization, and the equation for $\overline{\mathbf{Q}}^{(2)}$ can be written in the most general form as:

$$\partial_t\, \overline{\mathbf{Q}}^{(2)} = \mathbf{W}^{(2)} \left(\rho,\, \overline{\mathbf{Q}}^{(2)}\right) \tag{6.4}$$

The last equation implies that the tensor $\mathbf{W}^{(2)} \left(\rho,\, \overline{\mathbf{Q}}^{(2)}\right)$ must fulfill the same properties like $\overline{\mathbf{Q}}^{(2)}$, *i.e.* it is symmetric and traceless:

$$\begin{cases} W^{(2)}_{\alpha\,\beta} = W^{(2)}_{\beta\,\alpha} \\ \\ \mathrm{Tr}\, \mathbf{W}^{(2)} = W^{(2)}_{\alpha\,\alpha} = 0 \end{cases} \tag{6.5}$$

In the next step we develop in a more explicit form the density and the order parameter equations, Eq. (6.3) and Eq. (6.4). Let us firstly have a look at the density equation. The gradients in the stress tensor $\boldsymbol{\sigma}^{(2)}$ are the driving force for generating currents in our active gel system:

$$\mathbf{J} = \eta^{-1}\, \boldsymbol{\nabla} \cdot \boldsymbol{\sigma}^{(2)} \tag{6.6}$$

Now, we can write the stress tensor $\boldsymbol{\sigma}^{(2)}$ as a Taylor expansion in the fields and their gradients around some reference state. For the purpose of this thesis, the reference state is considered to be the homogeneous isotropic state. Based on tensorial analysis, only the following combinations between the fields and their derivatives are possible:

$$\begin{aligned} -\eta^{-1}\,\boldsymbol{\sigma}^{(2)} &= \mathbf{I}^{(2)}\,(a_1\,\rho + a_2\,\Delta\,\rho) + a_3\,\boldsymbol{\nabla}\boldsymbol{\nabla}\,\rho \\ &+ a_4\,\mathbf{I}^{(2)}\,\rho^2 + a_5\,\boldsymbol{\nabla}\,\rho\,\boldsymbol{\nabla}\,\rho + a_6\,\mathbf{I}^{(2)}\,\rho\,\Delta\,\rho + \cdots \\ &+ b_1\,\overline{\mathbf{Q}}^{(2)} + b_2\,\mathbf{I}^{(2)}\,\boldsymbol{\nabla}\boldsymbol{\nabla} : \overline{\mathbf{Q}}^{(2)} + b_3\,\mathbf{I}^{(2)}\overline{\mathbf{Q}}^{(2)} : \overline{\mathbf{Q}}^{(2)} + \cdots + c_1\,\rho\,\overline{\mathbf{Q}}^{(2)} + \cdots \end{aligned} \tag{6.7}$$

Above, the dots mean higher order derivatives and higher order non-linear terms. The reason that we do not consider higher order derivatives is consistent with the coarse graining procedure of our approach, in the sense that only the large length scales are relevant to the dynamics of our system.

We also write a similar expression for the tensor $\mathbf{W}^{(2)}$. In this case we have to remember that this tensor is symmetric and traceless, as we can see from Eq. (6.5).

$$\begin{aligned} \mathbf{W}^{(2)} &= d_1\,\overline{\mathbf{Q}}^{(2)} + d_2\,\Delta\,\overline{\mathbf{Q}}^{(2)} + d_3\,\Delta\Delta\,\overline{\mathbf{Q}}^{(2)} + d_4\,\overline{\mathbf{Q}}^{(2)}\,\overline{\mathbf{Q}}^{(2)} : \overline{\mathbf{Q}}^{(2)} + \cdots \\ &+ f_1\left(\boldsymbol{\nabla}\boldsymbol{\nabla}\rho - \frac{\mathbf{I}^{(d)}}{d}\,\Delta\rho\right) + f_2\left(\boldsymbol{\nabla}\rho\,\boldsymbol{\nabla}\rho - \frac{\mathbf{I}^{(d)}}{d}\,(\boldsymbol{\nabla}\rho)^2\right) + \cdots \\ &+ g_1\,\rho\,\overline{\mathbf{Q}}^{(2)} + g_2\,\rho\,\Delta\,\overline{\mathbf{Q}}^{(2)} + \cdots \end{aligned} \tag{6.8}$$

Now, we can express the current $\mathbf{J}$ with the help of Eq. (6.6) and Eq. (6.7), and the result can be used for the density equation Eq. (6.3). Similarly, we introduce the general expression Eq. (6.8) in the order parameter equation Eq. (6.4). In summary we have the following results:

$$\begin{cases} \partial_t\rho &= \Delta\,(a_1\,\rho + a_2\,\Delta\,\rho) + a_3\,\Delta\Delta\,\rho \\ &+ a_4\,\Delta\,\rho^2 + a_5\,\boldsymbol{\nabla}\boldsymbol{\nabla} : (\boldsymbol{\nabla}\,\rho\,\boldsymbol{\nabla}\,\rho) + a_6\,\Delta\,(\,\rho\,\Delta\rho) + \cdots \\ &+ b_1\,\boldsymbol{\nabla}\boldsymbol{\nabla} : \overline{\mathbf{Q}}^{(2)} + b_2\,\Delta\,\boldsymbol{\nabla}\boldsymbol{\nabla} : \overline{\mathbf{Q}}^{(2)} + b_3\,\Delta\left(\overline{\mathbf{Q}}^{(2)} : \overline{\mathbf{Q}}^{(2)}\right) + \cdots \\ &+ c_1\,\boldsymbol{\nabla}\boldsymbol{\nabla} : \left(\rho\,\overline{\mathbf{Q}}^{(2)}\right) + \cdots \\ \\ \partial_t\overline{\mathbf{Q}}^{(2)} &= d_1\,\overline{\mathbf{Q}}^{(2)} + d_2\,\Delta\,\overline{\mathbf{Q}}^{(2)} + d_3\,\Delta\Delta\,\overline{\mathbf{Q}}^{(2)} + d_4\,\overline{\mathbf{Q}}^{(2)}\,\overline{\mathbf{Q}}^{(2)} : \overline{\mathbf{Q}}^{(2)} + \cdots \\ &+ f_1\left(\boldsymbol{\nabla}\boldsymbol{\nabla}\rho - \tfrac{\mathbf{I}^{(d)}}{d}\,\Delta\rho\right) + f_2\left(\boldsymbol{\nabla}\rho\,\boldsymbol{\nabla}\rho - \tfrac{\mathbf{I}^{(d)}}{d}\,(\boldsymbol{\nabla}\rho)^2\right) + \cdots \\ &+ g_1\,\rho\,\overline{\mathbf{Q}}^{(2)} + g_2\,\rho\,\Delta\,\overline{\mathbf{Q}}^{(2)} + \cdots \end{cases} \tag{6.9}$$

We can see that the form of the above equations is invariant under rotations, and we stress that this symmetry requirement was the main principle that we used in their derivation.

6.2.3 Geometrical Constraints and Boundary Conditions

A 2D System

We proceed now to explore possible predictions of the equations Eq. (6.9), by choosing a particular geometry which is close to the case of real plant cells. The cortical arrangement of microtubules in plant cells suggests that the choice at hand is the case of a 2-dimensional system that lies on a cylindrical sheet (see Fig. 6.1).

In the 2D case, the order parameter $\overline{\mathbf{Q}}^{(2)}$ is a square matrix of rank 2 of the following form:

$$\overline{\mathbf{Q}}^{(2)} = \begin{pmatrix} q_{11} & q_{12} \\ \\ q_{12} & -q_{11} \end{pmatrix} = \frac{1}{2} \begin{pmatrix} \langle \cos(2\phi) \rangle & \langle \sin(2\phi) \rangle \\ \\ \langle \sin(2\phi) \rangle & -\langle \cos(2\phi) \rangle \end{pmatrix} \tag{6.10}$$

where ϕ is the angle between the individual filament polarization $\hat{\mathbf{u}}$ and the main cylinder axis $\hat{\mathbf{e}}_x$, *i.e.* $\cos\,\phi = \hat{\mathbf{u}} \cdot \hat{\mathbf{e}}_x$ (Fig. 6.1).

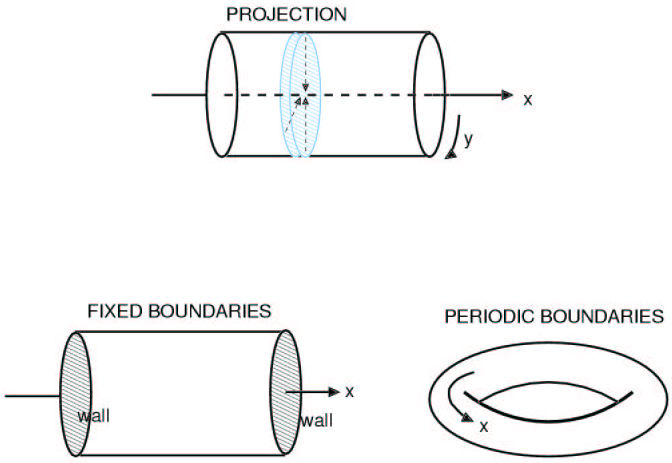

Figure 6.1: We consider the system of filaments on a 2D cylindrical sheet. This particular system closely resembles the case of cortical arrangement of microtubules in higher plant cells. In the natural case of a plant cell, the cylinder caps are closed and we impose *fixed boundary* conditions in the sense that we have no particle flux at the cylinder ends. However, we argue in this chapter that *periodic boundary* conditions are mathematically easier but still capture the relevant physical aspects of the system.

From this matrix we can derive two parameters:

$$\begin{cases} S &= 2\,\lambda = 2\,\sqrt{q_{11}^2 + q_{12}^2} \\ \\ \tan\tilde{\phi} &= \frac{\lambda - q_{11}}{q_{12}} \end{cases} \tag{6.11}$$

The parameter S is a scalar and is commonly referred to as the order parameter. This parameter is zero for fully disordered systems and unity for perfectly aligned systems, and therefore it measures the degree of alignment. The angle $\tilde{\phi}$ is the orientation angle of the nematic director. Its value is zero for alignment along the $x-$ axis, and $\pi/2$ if the alignment is along the $y-$ axis. For both horizontal and transverse alignment, we have $q_{12} = 0$, and one can show that the criterion for a specific alignment direction is the sign of q_{11}. Now, if we expand Eq. (6.11) up to the second order

in q_{12} we get for the orientation angle $\tilde{\phi}$:

$$\begin{aligned}
\tan\tilde{\phi} &= \frac{\sqrt{q_{11}^2+q_{12}^2}-q_{11}}{q_{12}} \\
&= \frac{|q_{11}|\left(1+\frac{1}{2}\frac{q_{12}^2}{q_{11}^2}\right)-q_{11}}{q_{12}} \\
&= \begin{cases} \frac{q_{12}}{2\,q_{11}} \to 0 & \text{if } q_{11}>0 \\ 2\frac{|q_{11}|}{q_{12}} \to \infty & \text{if } q_{11}<0 \end{cases}
\end{aligned} \tag{6.12}$$

For the 2D system, which we are going to consider from now on, we have to impose boundary conditions in order to solve the system of coupled equations Eq. (6.9).

6.2.4 Evolution Equations

Given the cylindrical geometry of our system, we proceed in making one more simplification for the equations Eq. (6.9). More precisely, we are going to neglect the azimuthal dependency in the fields, and consider only the dependency along the $x-$ axis. We can justify this simplification in two ways. First, if we look back at our model system, *i.e.* the plant cell, we notice the azimuthal symmetry for the cortical microtubules, both in the interphase arrangement and in the preprophase band. Thus, it is an obvious choice to use it as an ansatz and search for axially symmetric solutions. A second way to discard the azimuthal dependency in the fields is to introduce a *new kind* of average over the rotationally invariant equations Eq. (6.9), *i.e.* we average the fields over their angular variable, around the cylinder axis. Also we call this procedure projection onto the $x-$ axis (see Fig. 6.1). Then, the only dependency that is left in the system is the x-coordinate along the cylinder symmetry axis. In this case we rewrite all the equations from Eq. (6.9) by removing all the derivatives ∂_y:

$$\begin{cases}
\partial_t\,\rho &= \partial_x^2\,(a_1\,\rho + a_2\,\partial_x^2\,\rho) + a_3\,\partial_x^4\,\rho \\
&+ a_4\,\partial_x^2\,\rho^2 + a_5\,\partial_x^2\,(\partial_x\,\rho)^2 + a_6\,\partial_x^2\,(\,\rho\,\partial_x^2\rho) + \cdots \\
&+ b_1\,\partial_x^2\,q_{11} + b_2\,\partial_x^4\,q_{11} + 2\,b_3\,\partial_x^2\,(q_{11}^2+q_{22}^2) + \cdots + c_1\,\partial_x^2\,(\rho\,q_{11}) + \cdots \\
\partial_t\,q_{11} &= d_1\;q_{11} + d_2\,\partial_x^2\,q_{11} + d_3\,\partial_x^4\,q_{11} + 2\,d_4\,q_{11}\;(q_{11}^2+q_{22}^2) + \cdots \\
&+ \tfrac{1}{2}f_1\,\partial_x^2\rho + \tfrac{1}{2}f_2(\partial_x\rho)^2 + \cdots + g_1\,\rho\,q_{11} + g_2\,\rho\,\partial_x^2\,q_{11} + \cdots \\
\partial_t\,q_{12} &= d_1\,q_{12} + d_2\,\partial_x^2\,q_{12} + d_3\,\partial_x^4\,q_{12} + d_4\,q_{12}\;(q_{11}^2+q_{22}^2) + \cdots \\
&+ g_1\,\rho\,q_{12} + g_2\,\rho\,\partial_x^2\,q_{12} + \cdots
\end{cases} \tag{6.13}$$

Periodic Boundary Conditions

As a first step, we will develop our analysis in the case of *periodic boundary conditions*. This is equivalent to saying that the cylinder has its ends connected, as in the case of a torus (see Fig. 6.1). If we choose $\hat{\mathbf{e}}_x$ as the cylinder axis, and the length of the cylinder is L, then we can write the periodic boundary conditions as:

$$\begin{cases} \rho|_{x=0} = \rho|_{x=L} \\ \overline{\mathbf{Q}}^{(2)}\Big|_{x=0} = \overline{\mathbf{Q}}^{(2)}\Big|_{x=L} \\ J_x|_{x=0} = J_x|_{x=L} \end{cases} \tag{6.14}$$

6.3 Linear Stability Analysis

The homogeneous isotropic state is a stationary solution of the general equations Eq. (6.9), with the periodic boundary conditions Eq. (6.14).The same holds true for the axially symmetric equations Eq. (6.13). The first step in understanding the pattern formation out of a completely disordered state consists in performing the linear stability analysis [98]. With this procedure we investigate the stability of a certain state, which in our case is the disordered state, by considering an infinitesimal deviation from that state and analyzing if the dynamics drives the system further away or brings it back to its original state.

Let us consider an arbitrary deviation from the homogeneous isotropic state

$$\rho = \rho_0 + \delta\rho \tag{6.15}$$
$$q_{\alpha\,\beta} = \delta q_{\alpha\,\beta} \tag{6.16}$$

Then, we rewrite again the equations Eq.(6.13) by keeping only the linear contribution:

$$\partial_t \begin{pmatrix} \delta\rho \\ \delta q_{11} \\ \delta q_{12} \end{pmatrix} = \begin{pmatrix} D\,\partial_x^2 + P\,\partial_x^4 & F_1\,\partial_x^2 & 0 \\ F_2\,\partial_x^2 & E + G\,\partial_x^2 + Q\,\partial_x^4 & 0 \\ 0 & 0 & E + G\,\partial_x^2 + R\,\partial_x^4 \end{pmatrix} \begin{pmatrix} \delta\rho \\ \delta q_{11} \\ \delta q_{12} \end{pmatrix} \tag{6.17}$$

The expression of the linearized current is:

$$J_x = -\left(D\,\partial_x\,\delta\rho + F_1\,\partial_x\,\delta q_{11} + P\,\partial_x^3\,\delta\rho\right) \tag{6.18}$$

We have introduced a new set of coefficient in the linear equations Eq. (6.17), and we can express them in terms of the old coefficients as:

$$D = a_1 + 2\rho_0\,a_4, \quad F_1 = b_1 + c_1\,\rho_0, \quad F_2 = \frac{1}{2}f_1 \tag{6.19}$$
$$E = d_1 + g_1\,\rho_0, \quad G = d_2 + g_2\,\rho_0 \tag{6.20}$$

We call the coefficient D an *effective* difussion coefficient since its contribution in the linear equations can be formally written as

$$\partial_t\,\delta\rho \approx D\,\partial_x^2\,\delta\rho \tag{6.21}$$

if all the other coefficients are ignored. Naturally, in the case of pure diffusion, this coefficient is positive $D > 0$. However, when active elements are present in the system this coefficient can be negative, $D < 0$, and the homogeneous state is unstable.

In order to identify a possible interpretation for the coefficients E and G we can write for both components q_{11} and q_{12}

$$\partial_t \overline{\mathbf{Q}}^{(2)} \approx \left(E + G\boldsymbol{\nabla}^2\right) \overline{\mathbf{Q}}^{(2)} \tag{6.22}$$

We will see in Chapter 7 that E is in fact a *rotational diffusion* constant. Normally $E < 0$, and a change in its sign leads to the *isotropic-nematic* transition (see also Ref. [99, 100]). The coefficient G gives the length scale that corresponds to the change of the nematic order parameter, and is interpreted as an elastic constant or nematic rigidity [99, 100].

In the linear set of equations Eq. (6.17), there are also fourth order derivatives in the field perturbations present, which correspond to the coefficients P, Q and R. Since our purpose is to identify a *minimal* set of conditions that may correspond to a real system with a non-trivial phase diagram, the use of these terms may look like a complication. However, in the next section we will derive the phase diagram explicitly, and we will see that the case of negative values for these coefficients is sufficient to avoid small length scale instabilities. This is used as a consistency condition, because there is a natural cutoff l_0 on the small length scale, due to the coarse graining. Even more, below this scale the thermal fluctuations cannot be ignored and therefore the mean field theory breaks down. For convenience, we make the additional assumption that the absolute values for these coefficients are arbitrary small.

6.3.1 Periodic Boundary Conditions

In the case of periodic boundary conditions, we expand the fields as a Fourier $cosine$ series.

$$\begin{pmatrix} \delta\rho(x,\,t) \\ \delta q_{11}(x,\,t) \\ \delta q_{12}(x,\,t) \end{pmatrix} = \sum_k \cos(k\,x) \begin{pmatrix} \delta\tilde{\rho}(k,\,t) \\ \delta\tilde{q}_{11}(k,\,t) \\ \delta\tilde{q}_{12}(k,\,t) \end{pmatrix} \tag{6.23}$$

Then the re-write the equations Eq. (6.17) for the Fourier components:

$$\partial_t \begin{pmatrix} \delta\tilde{\rho} \\ \delta\tilde{q}_{11} \\ \delta\tilde{q}_{12} \end{pmatrix} = \begin{pmatrix} -D\,k^2 + P\,k^4 & -F_1\,k^2 & 0 \\ -F_2\,k^2 & E - G\,k^2 + Q\,k^4 & 0 \\ 0 & 0 & E - G\,k^2 + R\,k^4 \end{pmatrix} \begin{pmatrix} \delta\tilde{\rho} \\ \delta\tilde{q}_{11} \\ \delta\tilde{q}_{12} \end{pmatrix} \tag{6.24}$$

The periodic boundary conditions are satisfied for

$$k = \frac{\pi\,n}{L},\; n = 0,\,\pm 1,\,\pm 2,\,\cdots \tag{6.25}$$

If we apply the method of variable separation, then we can derive

$$\begin{pmatrix} \delta\tilde{\rho}(k,\,t) \\ \delta\tilde{q}_{11}(k,\,t) \\ \delta\tilde{q}_{12}(k,\,t) \end{pmatrix} = e^{\lambda t} \begin{pmatrix} \delta\tilde{\rho}^0(k) \\ \delta\tilde{q}^0_{11}(k) \\ \delta\tilde{q}^0_{12}(k) \end{pmatrix} \tag{6.26}$$

and the equations Eq. (6.24) become an eigenvalue problem:

$$\lambda \begin{pmatrix} \delta\tilde{\rho}^0(k) \\ \delta\tilde{q}^0_{11}(k) \\ \delta\tilde{q}^0_{12}(k) \end{pmatrix} = \begin{pmatrix} -D\,k^2 + P\,k^4 & -F_1\,k^2 & 0 \\ -F_2\,k^2 & E - G\,k^2 + Q\,k^4 & 0 \\ 0 & 0 & E - G\,k^2 + R\,k^4 \end{pmatrix} \begin{pmatrix} \delta\tilde{\rho}^0(k) \\ \delta\tilde{q}^0_{11}(k) \\ \delta\tilde{q}^0_{12}(k) \end{pmatrix} \tag{6.27}$$

Considering as initial condition at $t = 0$ the presence of some arbitrary field perturbations

$$\left(\delta\tilde{\rho}^0(k),\, \delta\tilde{q}^0_{11}(k),\, \delta\tilde{q}^0_{12}(k)\right)$$

we can see from Eq. (6.26) that these perturbations will grow beyond the linear regime when the real part of any eigenvalue λ is positive. In other words, the condition for having a linearly unstable isotropic and homogeneous state is

$$\mathcal{R}e\,\lambda > 0 \tag{6.28}$$

We now derive the expressions for the eigenvalues by solving the characteristic equation from Eq. (6.27):

$$\lambda_{1,2} = \frac{1}{2}\left(E - (D+G)k^2 \pm \sqrt{(E + (D-G)k^2)^2 + 4F_1F_2k^4}\right) + \mathcal{O}(P,\, Q) \tag{6.29}$$

$$\lambda_3 = E - G\,k^2 + R\,k^4 \tag{6.30}$$

We have expressed the first two eigenvalues in the limit of small parameters P and Q.

Before we proceed further in deriving the phase diagram, we have to observe from the equations Eq. (6.24) or Eq. (6.27) that the field variable $\delta\tilde{q}_{12}$ is decoupled from the other two fields. The solution for this field is

$$\delta\tilde{q}_{12} = e^{\lambda_3\,t}\,\delta\tilde{q}^0_{12} \tag{6.31}$$

where the coefficient $\delta\tilde{q}^0_{12}$ is left to be derived from the initial conditions.

6.3.2 The Phase Diagram

From Eq. (6.31), we have

$$\lambda_3 = E - G\,k^2 + R\,k^4 \tag{6.32}$$

The purpose of the parameter R was to make sure that the consistency condition, $\lambda_3 < 0$ for $k \to \infty$, is satisfied. However, a positive value of G is sufficient to fulfill this condition, and therefore we can discard higher order derivatives and simply consider that

$$R = 0 \tag{6.33}$$

Consistency Condition In Small Wavelength Limit ($k \to \infty$)

Since we do not allow instabilities to develop at small length scale, we now investigate when this condition is satisfied for the other two eigenvalues $\lambda_{1,2}$. A direct calculation from the characteristic equation gives

$$\begin{cases} \lambda_1 + \lambda_2 \approx (P+Q)\,k^4, & k \to \infty \\ \lambda_1\,\lambda_2 \approx P\,Q\,k^8, & k \to \infty \end{cases} \tag{6.34}$$

The condition is that both these eigenvalues must be negative in the limit of small wavelength, which implies directly that

$$P < 0, \;\; Q < 0 \tag{6.35}$$

If we choose P and Q as having small absolute values, then we do not expect that the phase diagram could depend on them at *finite* wavelengths. To simplify our exposition, we consider the case

$$P = Q = -\varepsilon < 0, \;\; \varepsilon \to 0 \tag{6.36}$$

Large Wavelength Limit ($k \to 0$)

With the choice Eq. (6.36), we can now derive that in the large wavelength limit:

$$\begin{cases} \lambda_1 &= \quad -D\,k^2 + \mathcal{O}(k^4) \\ \lambda_2 &= \; E - G\,k^2 + \mathcal{O}(k^4) \end{cases} \tag{6.37}$$

The second eigenvalue λ_2 can be positive in this regime, which means that the mode $k = 0$ is unstable, unless E is negative. The continuity equation for density Eq. (6.3) predicts that the perturbation in density for $k = 0$ must be always zero, *i.e* $\delta\,\tilde{\rho}^0(k = 0) = 0$. This make the instability case for $k = 0$ as not very interesting, and we consider only the case

$$E < 0 \tag{6.38}$$

However, the first eigenvalue λ_1 becomes *positive* in the case of negative diffusion coefficient $D < 0$. We mention that this large wavelength instability cannot be oscillatory (Hopf instability) since the eigenvalue λ_1 is a real number.

Finite Wavelength Regime

In the following we will derive the phase diagram by analyzing the sign of the sum and the product of the eigenvalues. With the choice Eq. (6.36) we derive

$$\lambda_1 + \lambda_2 = E - (D + G)\,k^2 - 2\varepsilon\,k^4 \tag{6.39}$$

$$\lambda_1\,\lambda_2 = k^2\,\mathcal{P}_3(k^2) \tag{6.40}$$

and their discriminant

$$\Delta = \left((D - G)^2 + 4\,F_1\,F_2\right)\,k^4 + 2\,E\,(D - G)\,k^2 + E^2 \tag{6.41}$$

where $\mathcal{P}_3(u)$ is the third order polynomial:

$$\mathcal{P}_3(u) = \varepsilon^2\,u^3 + \varepsilon(G + D)\,u^2 + (D\,G - F_1\,F_2 - \varepsilon\,E)\,u - D\,E \tag{6.42}$$

Case A. $D + G > 0$

In this case we can see that the sum $\lambda_1 + \lambda_2$ is always negative. We can identify instabilities from the condition $\lambda_1\lambda_2 = 0$. It turns out that we have to study the roots of the polynomial $\mathcal{P}_3(u)$. A close analysis shows that $\mathcal{P}_3(u)$ has either 2 or no *positive* roots if $D > 0$, and 1 or 3 *positive* roots if $D < 0$. Since we know the asymptotic behavior in the limit of small and large wave lengths (see Eq. (6.34) and Eq. (6.37)) we can determine exactly the number of roots at intermediate wavelengths. The behavior of the modes $\lambda_{1,2}$ is exemplified in Fig. 6.2, and the

summary of the detailed analysis is shown in in Fig. 6.3. We also mention that, although it is possible to have complex eigenvalues, it is not possible to have a Hopf bifurcation. Indeed, we can see from Eq. (6.39) that the real part is negative $\mathcal{R}e\lambda = (\lambda_1 + \lambda_2)/2 < 0$, and therefore no such instability is possible.

Case B. $D + G < 0$.

In this case $\lambda_1 + \lambda_2$ can have both signs. To derive what type of instabilities could be possible, we have to study both the roots of $\mathcal{P}_3(u)$ and the sign of the discriminant Δ. The behavior of $\mathcal{P}_3(u)$ is similar to the previous case. However, a Hopf bifurcation is possible when $\Delta < 0$ and $\lambda_1 + \lambda_2$ is changing the sign. A complete analysis show that this is possible when

$$D > 0,\ D + G < 0,\ F_1\, F_2 < 0,\ G > D - 2\sqrt{|F_1\, F_2|} \tag{6.43}$$

We sketched this particular instability in Fig. 6.2 (c).

In Fig. 6.3 we present the phase diagram as a result of the full algebraic analysis, which we have summarized before.

6.3.3 The Eigenstates

We now derive the eigenvectors from the eigenvalue problem Eq. (6.27) that corresponds to the eigenvalues $\lambda_{1,2}$ in the unstable conditions. Consider that λ_1 is the largest of the two eigenvalues,

$$\lambda_1 = \frac{1}{2}\left(E - (D+G)\,k^2 - 2\,\varepsilon\,k^4 + \sqrt{(E + (D-G)k^2)^2 + 4F_1F_2k^4}\right) \tag{6.44}$$

and therefore this eigenvalue corresponds to instabilities. Up to a normalization factor, the corresponding eigenvector is

$$\begin{pmatrix} \delta\tilde{\rho}^0(k,+) \\ \\ \delta\tilde{q}^0_{11}(k,+) \\ \\ \delta\tilde{q}^0_{12}(k,+) \end{pmatrix} = \begin{pmatrix} E + (D-G)\,k^2 - \varepsilon\,k^4 + \sqrt{(E + (D-G)k^2)^2 + 4F_1F_2k^4} \\ \\ 2F_2\,k^2 \\ \\ 0 \end{pmatrix} \tag{6.45}$$

Then, for the particular mode k, we have (see also the expansion Eq. (6.23))

$$\begin{pmatrix} \delta\rho^0(x) \\ \\ \delta q^0_{11}(x) \\ \\ \delta q^0_{12}(x) \end{pmatrix} = \cos(k\,x) \begin{pmatrix} \delta\tilde{\rho}^0(k,+) \\ \\ \delta\tilde{q}^0_{11}(k,+) \\ \\ 0 \end{pmatrix} \tag{6.46}$$

where the coefficients are $\delta\tilde{\rho}^0(k,+)$ and $\delta\tilde{q}^0_{11}(k,+)$ are given by Eq. (6.45). The off-diagonal term δq_{12} is zero, which means that the filaments are either longitudinal or transversal. The particular orientation depends on the sign of $\delta\tilde{q}_{11}(k,+)$ (see Eq. (6.12)) and therefore on the sign of F_2. In Fig. 6.4 we sketch the eigenstate that corresponds to the instability of the first mode $k = \pi/L$. This happens in the condition of negative diffusion constant $D < 0$, and for $G > 0$ and $F_1F_2 < 0$ (see also the diagram from Fig. 6.3). We stress that depending on the sign of F_2 we have the density and the order parameter modulated as in phase, Fig. 6.4 (a), *i.e.* preprophase rings with longitudinal alignment of filaments, or anti-phase Fig. 6.4 (b), *i.e.* preprophase rings with transversal alignment of filaments.

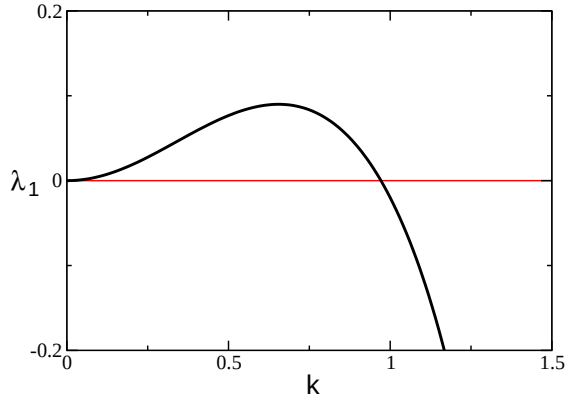

(a) Large wavelength instabilities

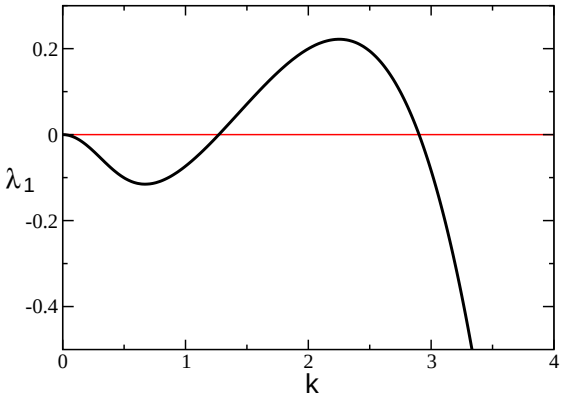

(b) Finite wavelength instabilities

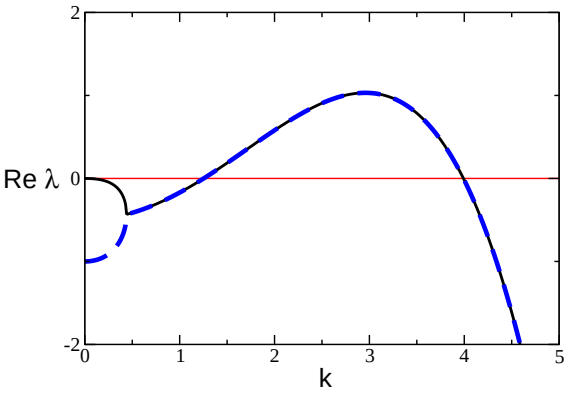

(c) Hopf Instability

Figure 6.2: Instabilities that occur in the case of periodic boundary conditions. We plot the largest real part of the two eigenvalues as a function of k in (a) and (b). Cases depend on the real roots of the polynomial $\mathcal{P}_3(k^2)$. (a) One real root of $\mathcal{P}_3(k^2)$ corresponds to large wavelength instabilities. (b) Three real roots of $\mathcal{P}_3(k^2)$, $\Delta > 0$, correspond to finite wavelength instabilities. (c) No real roots of $\mathcal{P}_3(k^2)$, $\Delta < 0$. The two eigenvalues are complex, however, their real part becomes positive at finite k, which corresponds to Hopf bifurcation.

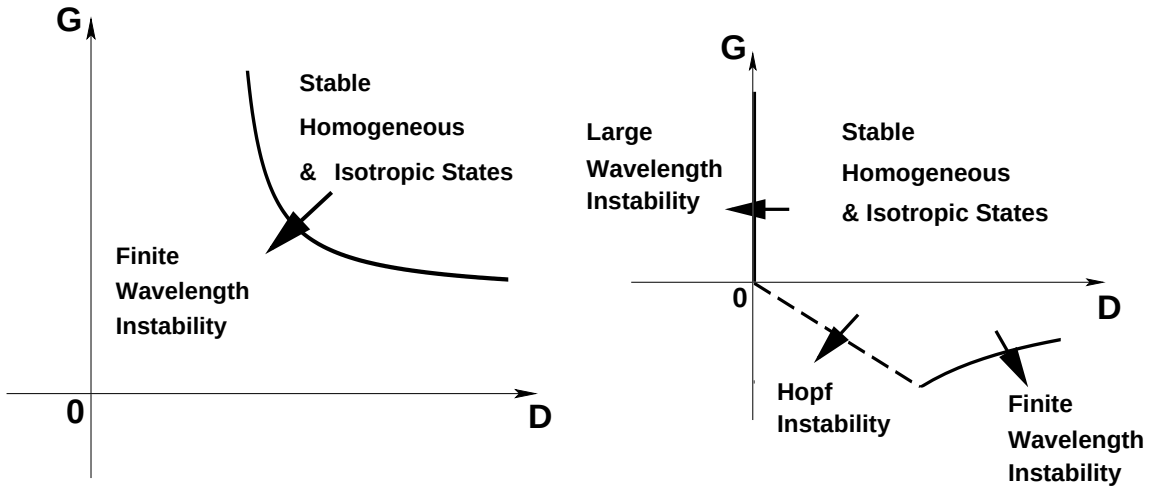

(a) $F_1\, F_2 > 0$ (b) $F_1\, F_2 < 0$

Figure 6.3: Instability phase diagram for the case of periodic boundary conditions. We plot instabilities as a function of the parameters D, G, F_1, F_2 in the limit of small ε. Three types of instabilities are possible when crossing the phase space region that corresponds to the stable homogeneous and isotropic states: large wavelength instabilities (see also Fig. 6.2 (a)), finite wavelength instabilities (see also Fig. 6.2 (b)), and Hopf instabilities (see also Fig. 6.2 (c)).

6.4 Non-Linear Regime

In the previous section we found some regions in the phase space where small deviations from the disordered state grow exponentially large in time and therefore violate the conditions of the linear approximation. In order to find the true stationary state in such cases, non-linear terms must be included. Technically speaking, the non-linear terms limit the exponentially explosive states to a non-trivial solution of the *non-linear* homogeneous evolution equations.

The problem of dealing with the non-linear evolution equations is still under development. However, in the following we can already present a demonstrative example of stripe formation, which resembles the preprophase band in plant cells.

6.4.1 Adiabatic Approximation

In the following we assume that the relaxation time of the order parameter $\overline{\mathbf{Q}}^{(2)}$ is much smaller than the corresponding relaxation time of the density. In addition to this hypothesis, we consider that the values of the order parameter components are small enough for the evolution equations to be still considered as linear in the order parameter. In this case, the equation for q_{12} can be ignored, since it is decoupled from the rest of the equations. We consider the "slaving" approximation from Eq. (6.13), *i.e.* $\partial_t\, q_{11} = 0$:

$$\begin{aligned} \partial_t \rho &= \partial_x^2 \left(a_1\, \rho + a_4\, \rho^2 + a_5\, (\partial_x \rho)^2 + a_6\, \rho\, \partial_x^2 \rho \right) \\ &+ \partial_x^2 \left(b_1\, q_{11} + 2 b_3\, (q_{11}^2 + q_{12}^2) + c_1\, \rho\, q_{11} \right) \qquad (6.47) \\ 0 &= d_1\, q_{11} + d_2\, \partial_x^2 q_{11} + \frac{f_1}{2}\, \partial_x^2 \rho + g_1\, \rho_0\, q_{11} + g_2\, \rho_0\, \partial_x^2 q_{11} \qquad (6.48) \end{aligned}$$

where we have considered only linear terms in the order parameter equation. In the next step we look for the stationary solutions of these equations. Again, since the order parameter is small, we

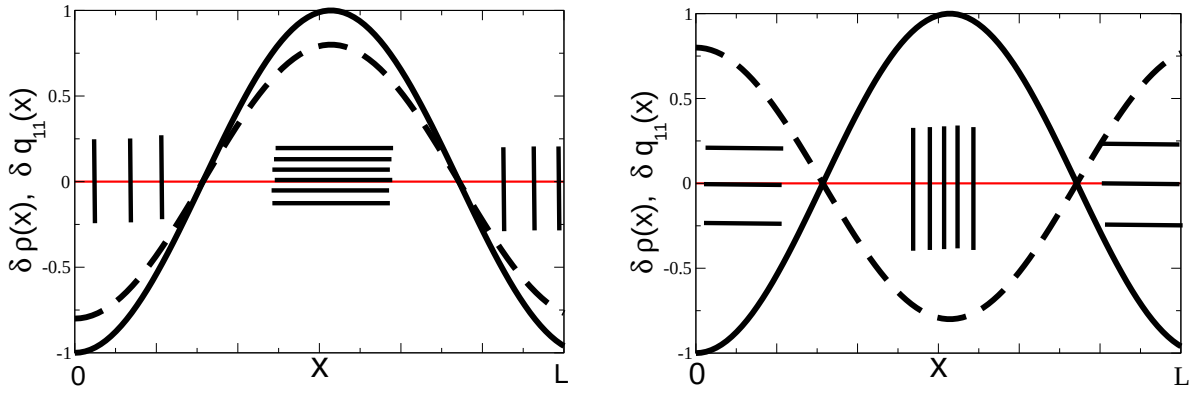

Figure 6.4: Periodic Boundary Conditions with instability of the first mode is possible for $D<0,\ G>0,\ F_1F_2<0$. (a): if $F_2>0$ the density and the order parameter are in phase, and the preprophase ring is longitudinal; (b): if $F_2<0$ the density and the order parameter are in anti-phase, and the preprophase ring is transversal.

consider only linear contributions from the order parameter in the density equation. For the case under discussion, we consider also that $c_1=0$. With the help of Eq. (6.19) and Eq. (6.20), we rewrite the last equations and use the new notations:

$$0 = \partial_x^2\left(a_1\,\rho + a_4\,\rho^2 + a_5\,(\partial_x\rho)^2 + a_6\,\rho\,\partial_x^2\rho + F_1\,q_{11}\right) \tag{6.49}$$

$$0 = E\,q_{11} + G\,\partial_x^2 q_{11} + F_2\,\partial_x^2\rho \tag{6.50}$$

Here we mention that the term $a_6\,\rho\,\partial_x^2\rho$ was not considered in the previous linear stability analysis, but its importance will be discussed below.

The solution for q_{11} from Eq. (6.50) can be written formally as

$$q_{11} = \frac{1}{2\pi}\int dk \int dx'\,\frac{F_2\,k^2}{E-k^2\,G}\,\rho(x')\,e^{i\,k\,(x'-x)} = -\int dx'\,\mathcal{G}(x-x')\,\rho(x') \tag{6.51}$$

where $\mathcal{G}(x)$ is the fundamental solution of the homogeneous equation, and it is given by:

$$\mathcal{G}(x) = -\frac{1}{2\pi}\int dk\,\frac{F_2\,k^2}{E-k^2\,G}\,e^{i\,k\,x} = \frac{F_2}{G}\,\delta(x) - \frac{F_2}{G}\,\sqrt{\left|\frac{E}{G}\right|}\,e^{-|x|\,\sqrt{\left|\frac{E}{G}\right|}} \tag{6.52}$$

Given the geometry of our system, we consider only the $x-$component of the current

$$J_x = \eta^{-1}\,\partial_x\,\sigma_{xx} \tag{6.53}$$

In the following we will focus on the stationary state for which the current is zero:

$$J_x = 0 \tag{6.54}$$

Then we can see from the last two expressions that the stress σ_{xx} is constant:

$$\eta^{-1}\,\sigma_{xx} = -\Gamma_0 \tag{6.55}$$

Under the condition Eq. (6.54), and taking into account the solution Eq. (6.51), we can integrate twice the equation Eq. (6.49) and the result is:

$$\Gamma_0 + a_1\,\rho + a_4\,\rho^2 + a_5\,(\partial_x\,\rho)^2 + a_6\,\rho\,\partial_x^2\rho - F_1\int dx'\,\mathcal{G}(x'-x)\,\rho(x') = 0 \tag{6.56}$$

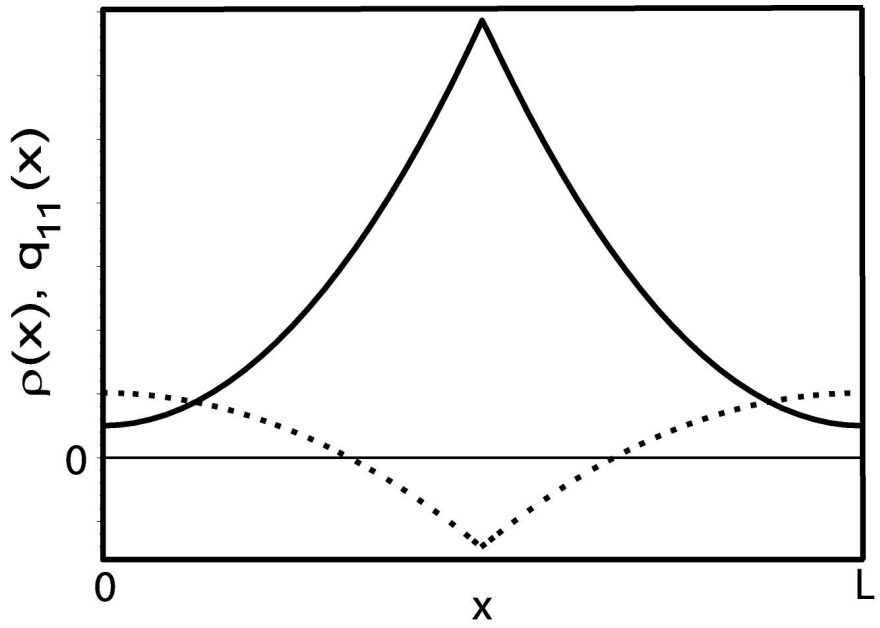

Figure 6.5: A demonstrative non-linear solution that corresponds to a stripe-like pattern. The density (solid) line and the order parameter component q_{11} (dotted line) are plotted as a function of the axial $x-$coordinate of the system. This solution corresponds to a transverse stripe (*i.e.* negative q_{11} in the region of high filament density).

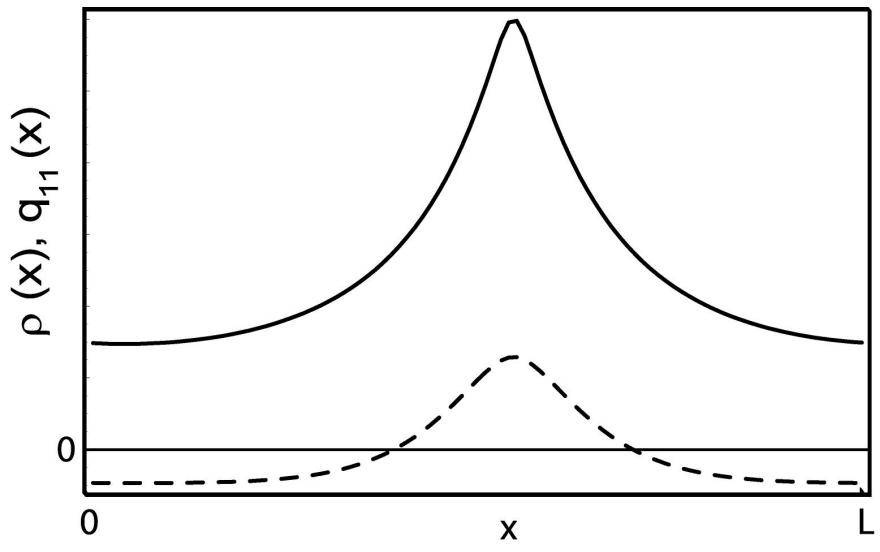

Figure 6.6: A numerical non-linear solution that resembles a strip-like pattern. The density $\rho(x)$ (solid line) and the order parameter component q_{11} (dashed line) are plotted as a function of the axial $x-$coordinate. Values of the parameters: $D = -1.5$, $G = 1.5$, $F_1\, F_2 = -1.0$, $E = -1.0$, $\varepsilon = 0.005$, $a_4 = -3.0$, $a_5 = 1.0$, $a_6 = -0.1$ (see Eq. (6.59)). The orientation of the stripe depends on the sign of q_{11}, which in turn depends on the sign of F_2 since $G > 0$, as we can see from Eq. (6.61). The plotted solution corresponds in this case to a longitudinal stripe.

6.4.2 A Stationary Solution

Let us consider the example of small rotational diffusion constant $E \approx 0$. Then from Eq. (6.52)

$$\mathcal{G}(x) = \frac{F_2}{G}\,\delta(x) \tag{6.57}$$

Now, Eq. (6.56) becomes

(6.58)

$$\Gamma_0 + \left(a_1 - \frac{F_1 F_2}{G}\right)\rho(x) + a_4\left(\rho^2 - \lambda^2(\partial_x\rho)^2\right) + a_6\,\rho\,\partial_x^2\,\rho = 0 \tag{6.59}$$

where

$$\lambda^2 = -\frac{a_5}{a_4} \tag{6.60}$$

Using Eq. (6.57) we can express the order parameter component from Eq. (6.51) as:

$$q_{11}(x) = -\frac{F_2}{G}\,\rho(x) \tag{6.61}$$

Case A: $a_6 = 0$**.** In this case we can write the density equation in the form [91]:

$$\Gamma_0 + \left(a_1 - \frac{F_1 F_2}{G}\right)\rho(x) + a_4\left(\rho^2 - \lambda^2(\partial_x\rho)^2\right) = 0 \tag{6.62}$$

where

$$\lambda^2 = -\frac{a_5}{a_4} \tag{6.63}$$

We can solve this equation analytically, and the solution is of the form:

$$\rho(x) = \alpha + \beta\,\cosh\left(\frac{x}{\lambda}\right) \tag{6.64}$$

$$q_{11}(x) = -\frac{F_2}{G}\left(\alpha + \beta\,\cosh\left(\frac{x}{\lambda}\right)\right) \tag{6.65}$$

where the coefficients α and β are

$$\alpha = -\frac{1}{2\,a_4}\left(a_1 - \frac{F_1 F_2}{G}\right),\ \beta^2 = \frac{1}{4\,a_4^2}\left(D - \frac{F_1 F_2}{G}\right)^2 \tag{6.66}$$

We plot the solutions Eq. (6.64) and Eq. (6.65) in Fig. 6.5, which show a transversal strip-like solution.

Case B: $a_6 \neq 0$**.** The discontinuity in the previous case is healed by the $a_6\ \rho\,\partial_x^2\,\rho$ term. In Fig. 6.6, we plot the numerical solution of the corresponding equation Eq. (6.59). We can see a fully continuous solution in its derivatives, which corresponds to a stripe that is similar to the preprophase band in higher plant cells.

6.5 Conclusions and Open Questions

In this chapter we have presented generic aspects of pattern formation in filamentous systems, which are driven by active components. Based on symmetry analysis, we wrote rotationally invariant evolution equations for the density and the nematic order parameter in the system. In spite of the generality of the problem, we demonstrated that, based on linear stability analysis, it is possible to systematically focus on the interesting regions of the phase space, where patterns could emerge. We derive non-linear solutions in some particular cases, showing how the unstable disordered state can evolve into a stable pattern.

We find as an encouraging result the stripe-like pattern solution of our generic equations, which closely resembles the preprophase ring that develops in plant cells at the onset of cell division. A characteristic of our analysis is the absence of the polarization in the stable ring state. The evidence of both orientations of microtubule being present does exists [70] for interphase and preprophase cells, but there is no quantitative measurement of the polarization. Moreover, a non-polar state is not forbidden by our generic symmetry assumptions, *i.e.* the $SO(2)$ invariance of the evolution equations.

The top-down approach that we have adopted in this chapter does not depend on any particular model specifying how the interaction between filaments could be mediated by motors. It is the aim of the next chapter to develop such a bottom-up approach in order to see how the corresponding evolution equations and phase diagram can be compared to the results that we have just presented.

Chapter 7

Modeling Microtubule Self-Organization Driven by Active Components

7.1 Introduction

In the previous chapter we have used a top-down approach to study the self-organization and pattern formation in active gels. Here we try to address the same problems by following the most direct route, *i.e.* starting from the microscopic level and modeling how the motor mediated interactions between filaments can lead to large scale organization of the system.

The bottom-up approach that we present in this chapter has at least two preliminary objectives. One is modeling the details of the dynamics of the motor-filament system, which makes possible the coupling between many individual filaments and, hopefully, leads to non-trivial patterns on a scale that is much larger than the size of a single filament. The second objective is to derive the macroscopic consequences of the microscopic model. The procedure that we use to reach this task is to integrate out all thermal fluctuations in the system, and to define the probability distribution function $\psi(\mathbf{r},\, \hat{\mathbf{u}},\, t)$, which describes the spatial distribution of the filaments with a given orientation $\hat{\mathbf{u}}$. This is accomplished by writing the Smoluchowski equation for the distribution $\psi(\mathbf{r},\, \hat{\mathbf{u}},\, t)$, including the active dynamics that emerges from the modeled interaction between motor proteins and filaments. After integrating out the angular degrees of freedom, we write the coupled evolution equation for the relevant macroscopic moments of interest, *i.e.* the density $\rho(\mathbf{r})$, the polarization $\mathbf{t}(\mathbf{r})$, and the nematic order parameter $\overline{\mathbf{Q}}^{(2)}(\mathbf{r})$.

The above procedure was introduced and applied for one dimensional systems in Ref. [92]. For 2 and 3 dimensional systems, Liverpool and Marchetti [101] derived the macroscopic moment equations only for the first two moments, *i.e.* density and polarization. However, the expressions for the active currents they present as being due to motor activity were not derived on the basis of a microscopic model. The general expressions for these currents are rather derived by imposing some specific symmetry constrains, which are fulfilled by the dynamics. Still, the treatment that was explored in Ref. [101] was far from being exhaustive, due to many symmetric possibilities in the active contributions.

Here we try to be more specific by writing the active terms in the Smoluchowski equation, using a specific microscopic model. It results that the analytical form of our active currents is different from those obtained Ref. [101], and as a consequence we must reevaluate the linear stability analysis and derive a new phase diagram of the system under discussion. We also aim to extend the discussion to include a second rank moment up to the third moment, *i.e.* the nematic order parameter. This gives us the opportunity for a better understanding of the coupling that might exist

between the polarization and the nematic order parameter.

7.2 A Microscopic Model

7.2.1 The Dynamic Time Scale

The fact that motor proteins can play a role in the self-organization of filamentous systems can be understood by showing that the corresponding *dynamic* time scale is much smaller than the *diffusive* time scale. This means that the effect of motor proteins on the filaments is not smeared out by diffusion. We can see this from the following simple argument. In order to derive the dynamic time scale τ_{dyn}, we must realize that the only input into the theory is the active force itself F, a drag coefficient ζ, and a length, which should be the linear size of a filament. Indeed, the following quantity

$$\tau_{Dyn} = \frac{\zeta\, l}{F} \tag{7.1}$$

has a time dimension, and it must be identified to the desired dynamic time scale. This must be obvious from the fact that, in order to see a significant displacement, the active force has to balance the viscous drag. Now, we can compare this time scale to the diffusive time scale $\tau_{Diff} = \frac{l^2}{D}$, where D is the diffusion coefficient. The ratio of the two time scales is

$$\frac{\tau_{Dyn}}{\tau_{Diff}} = \frac{\zeta\, D}{l\, F} \tag{7.2}$$

We can make use of Einstein relation $\zeta\, D = k_B\, T$, and the last relation becomes

$$\frac{\tau_{Dyn}}{\tau_{Diff}} = \frac{k_B\, T}{l\, F} \approx\ 10^{-3} \ll 1 \tag{7.3}$$

The above ratio was evaluated in the condition of room temperature $k_B\, T = 4.1\, pN\, nm$, for filaments of $1\, \mu m$ in length, and for an active force $F = 1\, pN$ [102]. We can interpret the relation Eq. (7.3) in the way that self-organization of filaments is possible in general even with motors that generate forces less than $1\, pN$ in strength.

In the next step, we have to realize that, although the filament dynamics is fast in comparison to the diffusion processes, the motion of the filaments is still slow enough for the dynamics to be inertialess. We can see that by looking at the corresponding *inertia* time scale

$$\tau_{In} = \frac{m}{\zeta} \tag{7.4}$$

where m is the mass of a filament. In order to compare this time scale with the dynamic time scale, we evaluate the ratio

$$\frac{\tau_{In}}{\tau_{Dyn}} = \frac{m\, F}{\zeta^2\, l} \tag{7.5}$$

We can relate the mass m of a particle to a new quantity, which is called the *diffusion length* $l_{Diff} = \sqrt{m\, k_B\, T/\zeta}$ (see Ref. [100]). The diffusion length is known to be much smaller than any relevant linear size of the object $l_{Diff}/l \approx 10^{-3}$ [100]. In other words, in the case of inertia dominated motion, a *free* object moves as a result of a thermal kick over a distance which is much smaller than the size of the object itself, and therefore a significant displacement can be recorded

only on the diffusion time scale. If we want to express the ratio from Eq. (7.5) in terms of the diffusion length, we can eliminate both the mass of the particle and the drag coefficient:

$$\frac{\tau_{In}}{\tau_{Dyn}} = \frac{F\,l}{k_B\,T}\left(\frac{l_{Diff}}{l}\right)^2 \approx 10^{-3} \ll 1 \tag{7.6}$$

In the last equation we have used the same values for the force, temperature, and linear size of the object as in Eq. (7.3). When talking about micron size objects, Eq. (7.6) simply shows that, for filaments under the action of motor proteins, we are in the case of inertialess dynamics.

7.2.2 Modeling Motor-Filament Interaction

Let us consider the case of a single filament under the action of an external *point* force $\mathbf{F}$. Then, according to Section 7.2.1, the dynamics of this object should be inertialess. In this case, the linear and angular velocities are, respectively, proportional to the force and torque exerted [100, 99]:

$$\begin{cases} \mathbf{v} &= \left(\frac{1}{\zeta_{||}}\hat{\mathbf{u}}\,\hat{\mathbf{u}} + \frac{1}{\zeta_{\perp}}(\mathbf{I}^{(2)} - \hat{\mathbf{u}}\,\hat{\mathbf{u}})\right)\cdot\mathbf{F} \\ \boldsymbol{\omega} &= \frac{1}{\gamma_R}\mathbf{N} \end{cases}$$

These are the equations of motion for a *rigid* rod under the action of a force $\mathbf{F}$ and torque $\mathbf{N}$, and $\mathbf{v}$ and $\boldsymbol{\omega}$ are, respectively, the center of mass translational and angular velocities. The unit vector $\hat{\mathbf{u}}$ gives the orientation of the filament. In the dilute limit, we have the following relations between the longitudinal $\zeta_{||}$, transversal $\zeta_{\perp}$, and rotational γ_R drag coefficients, (see [100, 99]):

$$\begin{cases} \zeta_{||} = \zeta_{\perp}/2 \\ \zeta_{||} = 6\,\gamma_R \end{cases} \tag{7.8}$$

We aim now to implement the equations Eq. (7.7) into a bit more complex system of *two* filaments that are cross linked by a double motor protein (see Fig. 7.1). In order to describe how the interaction between these two filaments is mediated by the motors, we consider that the two motor heads, which walk on the two filaments separately, are connected by a flexible and inextensible polypeptide *string*. The *tension* $\mathbf{T}$ that develops in this string plays the role of the active force, which puts both filaments into motion separately. In principle, the string tension $\mathbf{T}$ can be dependent on the relative angle between filaments, and even on the relative motion of the motor heads on the filaments. However, at zero level approximation we can make the hypothesis that these dependencies are weak and not relevant for driving homogeneous and isotropic instabilities in our system. In the next section, we will derive a dependency expression for $\mathbf{T}(\hat{\mathbf{u}},\,\hat{\mathbf{u}}',\,\boldsymbol{\xi})$, on the grounds of flexibility and inextensibility properties of the polypeptide string.

Translational Velocity

If we substitute the string tension $\mathbf{T}$ as the active force in Eq. (7.7), then the center of mass velocities for each filaments are given by:

$$\begin{cases} \mathbf{v} &= \left(\frac{1}{\zeta_{||}}\hat{\mathbf{u}}\,\hat{\mathbf{u}} + \frac{1}{\zeta_{\perp}}(\mathbf{I}^{(2)} - \hat{\mathbf{u}}\,\hat{\mathbf{u}})\right)\cdot\mathbf{T} \\ \mathbf{v}' &= -\left(\frac{1}{\zeta_{||}}\hat{\mathbf{u}}'\,\hat{\mathbf{u}}' + \frac{1}{\zeta_{\perp}}(\mathbf{I}^{(2)} - \hat{\mathbf{u}}'\,\hat{\mathbf{u}}')\right)\cdot\mathbf{T} \end{cases}$$

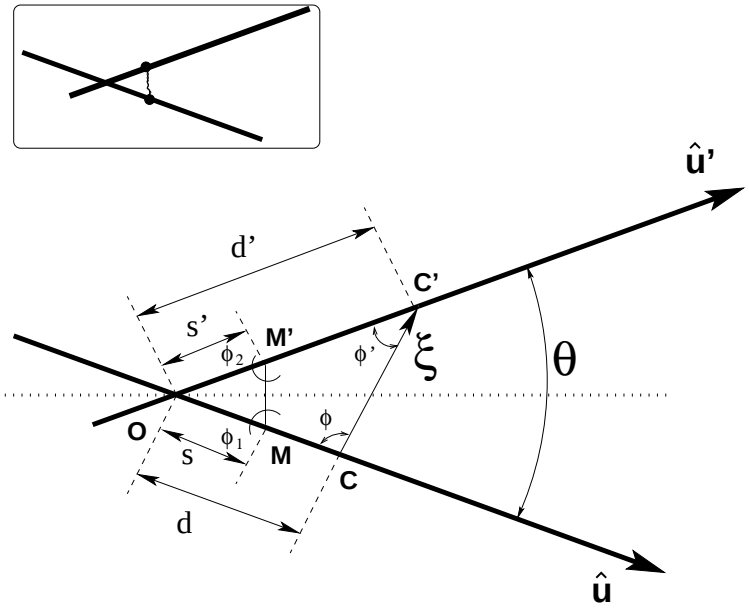

Figure 7.1: A double motor MM' walking on two filaments with orientations $\hat{\mathbf{u}}$ and $\hat{\mathbf{u}}'$ respectively.

The center of mass velocity for the two-filament system is non-zero for the two and three dimensional cases, unlike the unidimensional case studied in Ref. [91, 103, 93]:

$$\mathbf{v}_{CM} = \frac{\mathbf{v} + \mathbf{v}'}{2} = \frac{1}{2}\left(\frac{1}{\zeta_{||}} - \frac{1}{\zeta_{\perp}}\right)(\hat{\mathbf{u}}\,\hat{\mathbf{u}} - \hat{\mathbf{u}}'\,\hat{\mathbf{u}}') \cdot \mathbf{T} \tag{7.10}$$

The particle asymmetry, *i.e.* the difference in the longitudinal and transversal drag coefficients, makes possible for this system to "walk" in a viscous background.

We consider in more detail the situation depicted in Fig. 7.1. The connecting link between the motor heads $\mathbf{M}$ and $\mathbf{M}'$ can have many relative orientations with respect to the two filaments. In the following, we *average* over all possible microstates, which are defined by the relative positions $\mathbf{M}$ and $\mathbf{M}'$. We have to remember that the only constraint that we can impose on these microstates is a fixed distance $d_{\mathbf{MM}'}$ between the two motor heads, as we can see from the inextensibility hypothesis for the connecting polypeptide string. If we assume that all relative orientations for the cross link $\mathbf{MM}'$ are equally probable, then we can derive the following averages:

$$\langle \hat{\mathbf{u}} \cdot \mathbf{T} \rangle = -\langle \hat{\mathbf{u}}' \cdot \mathbf{T} \rangle = -\frac{T}{\pi/2}\,\sin\frac{\theta}{2} \tag{7.11}$$

$$\langle \mathbf{T} \rangle = \frac{T}{\pi/2}\,\frac{\hat{\mathbf{u}}' - \hat{\mathbf{u}}}{|\hat{\mathbf{u}}' - \hat{\mathbf{u}}|} \tag{7.12}$$

We insert these averages into Eq. (7.9), an we can derive the following expressions for the individual velocities:

$$\begin{cases} \mathbf{v} &= -\frac{\sqrt{2}T}{\pi}\left(\frac{1}{\zeta_{||}} - \frac{1}{\zeta_{\perp}}\right)\frac{1-\hat{\mathbf{u}}\cdot\hat{\mathbf{u}}'}{\sqrt{1-\hat{\mathbf{u}}\cdot\hat{\mathbf{u}}'}}\,\hat{\mathbf{u}} + \frac{\sqrt{2}T}{\pi}\frac{1}{\zeta_{\perp}}\frac{\hat{\mathbf{u}}'-\hat{\mathbf{u}}}{\sqrt{1-\hat{\mathbf{u}}\cdot\hat{\mathbf{u}}'}} \\ \mathbf{v}' &= -\frac{\sqrt{2}T}{\pi}\left(\frac{1}{\zeta_{||}} - \frac{1}{\zeta_{\perp}}\right)\frac{1-\hat{\mathbf{u}}\cdot\hat{\mathbf{u}}'}{\sqrt{1-\hat{\mathbf{u}}\cdot\hat{\mathbf{u}}'}}\,\hat{\mathbf{u}}' - \frac{\sqrt{2}T}{\pi}\frac{1}{\zeta_{\perp}}\frac{\hat{\mathbf{u}}'-\hat{\mathbf{u}}}{\sqrt{1-\hat{\mathbf{u}}\cdot\hat{\mathbf{u}}'}} \end{cases} \tag{7.13}$$

If we make similar averages, we obtain from Eq. (7.10) for the center of mass velocity

$$\mathbf{v}_{\mathbf{CM}} = -\frac{T}{\sqrt{2}\,\pi}\left(\frac{1}{\xi_{||}} - \frac{1}{\zeta_{\perp}}\right)\,(\hat{\mathbf{u}} + \hat{\mathbf{u}}')\sqrt{1 - \hat{\mathbf{u}}\cdot\hat{\mathbf{u}}'} \tag{7.14}$$

We have already mentioned that, in general, the tension $\mathbf{T}$ can depend on the filament relative orientations. However, even without these details, we see from the last formula that the system center of mass is not displaced in both parallel and anti-parallel configurations of the two filaments.

We will turn now our attention to the relative velocity $\mathbf{v}_{rel}\left(\boldsymbol{\xi},\,\hat{\mathbf{u}},\,\hat{\mathbf{u}}'\right) = \mathbf{v_1} - \mathbf{v_2}$:

$$\mathbf{v}_{rel}\left(\boldsymbol{\xi},\,\hat{\mathbf{u}},\,\hat{\mathbf{u}}'\right) = \left(\frac{1}{\zeta_{||}} - \frac{1}{\zeta_{\perp}}\right)\Big(\hat{\mathbf{u}}\left(\hat{\mathbf{u}}\cdot\mathbf{T}\right) + \hat{\mathbf{u}}'\left(\hat{\mathbf{u}}'\cdot\mathbf{T}\right)\Big) + \frac{2}{\zeta_{\perp}}\,\mathbf{T} \tag{7.15}$$

If $\mathbf{T}$ is substituted with its average values from Eq. (7.11) and Eq. (7.12), the relative velocity becomes

$$\mathbf{v}_{rel}\left(\boldsymbol{\xi},\,\hat{\mathbf{u}},\,\hat{\mathbf{u}}'\right) = \frac{T}{\pi/2}\left(\frac{1}{\zeta_{||}} - \frac{1}{\zeta_{\perp}}\right)\left(\hat{\mathbf{u}}' - \hat{\mathbf{u}}\right)\,\sin\frac{\theta}{2} + \frac{2}{\zeta_{\perp}}\,\frac{T}{\pi/2}\,\frac{\hat{\mathbf{u}}' - \hat{\mathbf{u}}}{|\hat{\mathbf{u}}' - \hat{\mathbf{u}}|} \tag{7.16}$$

or even:

$$\mathbf{v}_{rel}\left(\boldsymbol{\xi},\,\hat{\mathbf{u}},\,\hat{\mathbf{u}}'\right) = \frac{T}{\pi/2}\left(\frac{1}{\zeta_{||}} - \frac{1}{\zeta_{\perp}}\right)\frac{\left(\hat{\mathbf{u}}' - \hat{\mathbf{u}}\right)\left(1 - \hat{\mathbf{u}}\cdot\hat{\mathbf{u}}'\right)}{|\hat{\mathbf{u}}' - \hat{\mathbf{u}}|} + \frac{2}{\zeta_{\perp}}\,\frac{T}{\pi/2}\,\frac{\hat{\mathbf{u}}' - \hat{\mathbf{u}}}{|\hat{\mathbf{u}}' - \hat{\mathbf{u}}|} \tag{7.17}$$

We can bring this last expression into an even more convenient form:

$$\mathbf{v}_{rel}\left(\boldsymbol{\xi},\,\hat{\mathbf{u}},\,\hat{\mathbf{u}}'\right) = \frac{\sqrt{2}\,T}{\pi}\left(\frac{1}{\zeta_{||}} - \frac{1}{\zeta_{\perp}}\right)\frac{\left(\hat{\mathbf{u}}' - \hat{\mathbf{u}}\right)\left(1 - \hat{\mathbf{u}}\cdot\hat{\mathbf{u}}'\right)}{\sqrt{1 - \hat{\mathbf{u}}\cdot\hat{\mathbf{u}}'}} + \frac{\sqrt{2}\,T}{\pi}\,\frac{2}{\zeta_{\perp}}\,\frac{\hat{\mathbf{u}}' - \hat{\mathbf{u}}}{\sqrt{1 - \hat{\mathbf{u}}\cdot\hat{\mathbf{u}}'}} \tag{7.18}$$

Angular Velocity

The angular velocity for each filament:

$$\boldsymbol{\omega} = \dot{\mathbf{n}} = \frac{\mathbf{N}}{\gamma_R}, \quad \boldsymbol{\omega}' = \dot{\mathbf{n}}' = \frac{\mathbf{N}'}{\gamma_R} \tag{7.19}$$

With the help of Fig. 7.1, we can express the absolute value of the torque N_i for each filament

$$N = T_{\perp}\left(d - s\right) \approx T\,\sin\phi\,d, \quad N' = T'_{\perp}\left(d' - s'\right) \approx T\,\sin\phi'\,d' \tag{7.20}$$

In the last relations, we have approximated $d - s \approx d$, $d' - s' \approx d'$, for the very reason that the cross linked motor-pair is very small compared to the size of the filaments. In the next step, we perform the same kind of average over cross linked MM' microstates, *i.e.*

$$\langle T\,\sin\phi\rangle = T\,\langle\sin\phi\rangle = \langle T\,\sin\phi'\rangle = T\,\langle\sin\phi'\rangle = T\frac{\cos\theta/2}{\pi/2} \tag{7.21}$$

We apply now the sine theorem for the triangle formed by the crossing point and the mass centers of the two filaments (see Fig. 7.1):

$$\frac{\xi}{\sin\theta} = \frac{d'}{\sin\phi} = \frac{d}{\sin\phi'} \tag{7.22}$$

We substitute d and d' from the last equations into the torque equations Eq. (7.20), and making also the averages Eq. (7.21), we obtain finally the *absolute* values for the individual angular velocities from Eq. (7.19):

$$\omega = \frac{2\,T}{\pi\gamma_R}\,\frac{\cos\frac{\theta}{2}}{\sin\theta}\,\xi\sin\phi' \tag{7.23}$$

$$\omega' = \frac{2\,T}{\pi\gamma_R}\,\frac{\cos\frac{\theta}{2}}{\sin\theta}\,\xi\sin\phi \tag{7.24}$$

In the last step, we write these relations in the vectorial form:

$$\boldsymbol{\omega}(\boldsymbol{\xi},\, \hat{\mathbf{u}},\, \hat{\mathbf{u}}') = \frac{\sqrt{2}\,T}{\pi\gamma_R}\,\frac{\boldsymbol{\xi}\times\hat{\mathbf{u}}'}{\sqrt{1-\hat{\mathbf{u}}\cdot\hat{\mathbf{u}}'}} \tag{7.25}$$

$$\boldsymbol{\omega}'(\boldsymbol{\xi},\, \hat{\mathbf{u}},\, \hat{\mathbf{u}}') = -\frac{\sqrt{2}\,T}{\pi\gamma_R}\,\frac{\boldsymbol{\xi}\times\hat{\mathbf{u}}}{\sqrt{1-\hat{\mathbf{u}}\cdot\hat{\mathbf{u}}'}} \tag{7.26}$$

The *relative* angular velocity of the first filament with respect to the second is $\boldsymbol{\omega}_{rel}(\boldsymbol{\xi},\, \hat{\mathbf{u}},\, \hat{\mathbf{u}}') = \boldsymbol{\omega}(\boldsymbol{\xi},\, \hat{\mathbf{u}},\, \hat{\mathbf{u}}') - \boldsymbol{\omega}'(\boldsymbol{\xi},\, \hat{\mathbf{u}},\, \hat{\mathbf{u}}')$:

$$\boldsymbol{\omega}_{rel}(\boldsymbol{\xi},\, \hat{\mathbf{u}},\, \hat{\mathbf{u}}') = \frac{\sqrt{2}\,T}{\pi\,\gamma_{rot}}\,\frac{\boldsymbol{\xi}\times\hat{\mathbf{u}}+\boldsymbol{\xi}\times\hat{\mathbf{u}}'}{\sqrt{1-\hat{\mathbf{u}}\cdot\hat{\mathbf{u}}'}} \tag{7.27}$$

The expressions Eq. (7.18) Eq. (7.27) for the relative translational and angular velocities are different from the corresponding expressions used in Ref. [101], which were derived only on symmetry grounds. Still, the expressions developed in Ref. [101] were not exhaustive, and therefore not all symmetry allowed terms were analyzed. Since there is a significant difference in the analytical form between the two variants, we expect that the stability phase diagram cannot be the same.

7.2.3 An Active Force Model

In the previous section we have presented a microscopic model, in which a two headed motor cross linked two filaments. The polypeptide bond, which connects the motor heads, was modeled as a *flexible* and *inextensible* string. The string tension is actually the active force that generates the motion of the two filaments, and in principle can depend on many details like the orientation of the filaments, and their relative displacements.

The *string* feature of motor head linker makes our model different from the model used in the computer simulations that were described in Ref. [89].

In the present section, we use the physical properties of the string, *i.e.* flexibility and inextensibility, in order to derive a more exact expression for the string tension $\mathbf{T}$. The derived expression for the tension $\mathbf{T}$ will be used to obtain a detailed formula for the translational and angular velocities, which we have already discussed in Section 7.2.2.

We assume that the *force-velocity* relation for a motor protein that works against a tangential load is given by (see *Howard* [102]):

$$v\,(F) = v_M\,\left(1-\frac{F_{||}}{F_M}\right) \tag{7.28}$$

In writing Eq.[7.28], we assumed that the parameters v_M and F_M are independent on the transversal component which could be applied (see Fig. 7.3).

In the following we show how the string tension can be computed by using simple kinematical arguments. The velocity of a given motor head, let us say **M** (see Fig. 7.2), is given by the relative velocity $\mathbf{v}$ and the transport velocity, *i.e.* $\mathbf{V}_{||} + \mathbf{V}_{\perp} + \mathbf{V}_{\mathbf{rot}}$:

$$\mathbf{V_M} = \mathbf{v} + \mathbf{V}_{||} + \mathbf{V}_{\perp} + \mathbf{V_{rot}} \tag{7.29}$$

The inextensibility of the string implies that the velocities of the motor heads along the direction of the string must be equal:

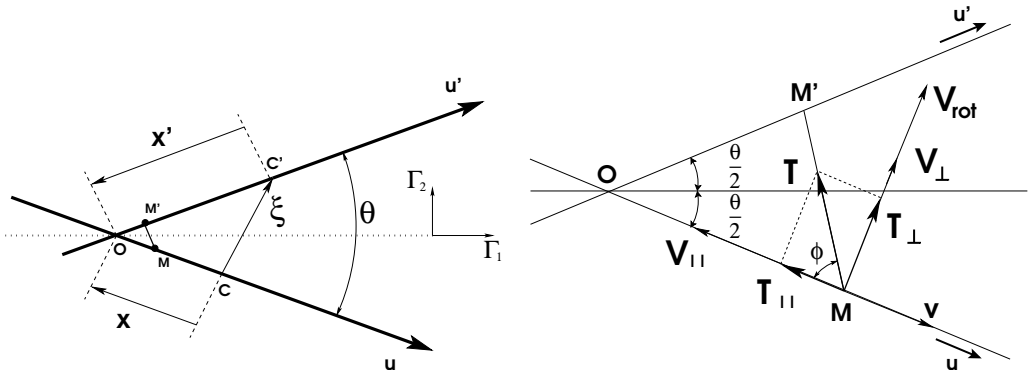

(a) (b)

Figure 7.2: Two filaments can be cross linked by a two head motor protein. Each motor head walks on each filament. The motion of the heads is constrained by the connecting string. As the motor heads walk, tension is developed in the string and plays the role of the active force which puts the filaments into motion.

$$V_M \cos\phi + V_{M'} \cos\phi' = 0 \tag{7.30}$$

We have explicit relations for the translational velocities of the center of mass of each rod:

$$V_{||} \cos\phi = \frac{T_{||} \cos\phi}{\zeta_{||}} = \frac{T \cos^2\phi}{\zeta_{||}} \tag{7.31}$$

$$V_{\perp} \sin\phi = \frac{T_{\perp} \sin\phi}{\zeta_{\perp}} = \frac{T \sin^2\phi}{\zeta\perp} \tag{7.32}$$

For the angular velocity around the center of mass we have:

$$\boldsymbol{\omega} = \frac{\mathbf{N}}{\gamma_{rot}} \tag{7.33}$$

The torque $\mathbf{N}$ is given by:

$$\mathbf{N} = \mathbf{x} \times \mathbf{T} \tag{7.34}$$

In computing the above torque, which is applied to the filament $\mathbf{u}$, we have approximated the distance between the motor and the center of mass with the distance between the intersection point of the filaments and the center of mass of the considered filament. This is allowed because the physical size of the motor protein is commonly much smaller than the size of the filaments. The component of the rotational velocity around the center of mass, $\mathbf{V_{rot}} = \mathbf{x} \times \boldsymbol{\omega}$, along the string, is:

$$V_{rot} \sin\phi = \frac{T\, x^2}{\gamma_{rot}} \sin^2\phi \tag{7.35}$$

Eq. (7.31) and Eq. (7.35) are given for the motor head $\mathbf{M}$. Similar relations can now be written for the other head, $\mathbf{M}'$, which walks on the other filament. Using all these expressions together with Eq. (7.28), we can derive from Eq. (7.30) the following expression for the absolute value of the tension:

$$T = \frac{v_M(\cos\phi + \cos\phi')}{\frac{2}{\zeta_\perp} + \left(\frac{v_M}{F_M} + \frac{1}{\zeta_{||}} - \frac{1}{\zeta_\perp}\right)(\cos^2\phi + \cos^2\phi') + \frac{1}{\gamma_{rot}}(x^2\, \sin^2\phi + x'^2\, \sin^2\phi')} \tag{7.36}$$

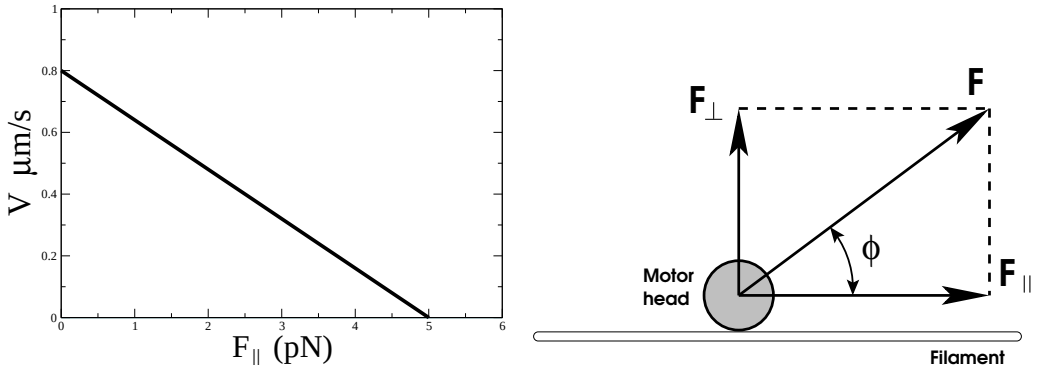

(a) (b)

Figure 7.3: Tangential Load (for example see *Howard* [102]). In our model, it is assumed that the *force-velocity* relation (a) is not affected by the transversal component applied on the motor.

The double head motor complex can be oriented in many ways with respect to the filaments. For a given angle θ there are possible many values of the angles ϕ and ϕ'. In the following we consider the average values of these angles as

$$\phi = \phi' = \frac{\pi}{2} - \frac{\theta}{2} \tag{7.37}$$

For these average angles, we evaluate the string tension as:

$$T = \frac{v_M \sin\frac{\theta}{2}}{\frac{1}{\zeta_\perp} + \left(\frac{v_M}{F_M} + \frac{1}{\zeta_{||}} - \frac{1}{\zeta_\perp}\right)\sin^2\frac{\theta}{2} + \frac{1}{2\gamma_{rot}}(x^2 + x'^2)\sin^2\frac{\theta}{2}} \tag{7.38}$$

For kinesin we have [1]

$$\frac{v_M\,\zeta_{||}}{F_M} \ll 1 \tag{7.39}$$

and therefore we neglect the ratio $\frac{v_M}{F_M}$ in the expression for the tension. In dilute systems we have (see *Dhont* [100] and *Doi & Edwards* [99]):

$$\frac{\gamma_{rot}}{L^2} = \frac{\zeta_{||}}{6} = \frac{\zeta_\perp}{12} \tag{7.40}$$

where L is the length of a filament. It thus follows:

$$T = \frac{\zeta_{||} v_M \,\sin\frac{\theta}{2}}{1 - \frac{1}{2}\cos^2\frac{\theta}{2} + \frac{3}{4}\frac{x^2+x'^2}{(L/2)^2}\cos^2\frac{\theta}{2}} \tag{7.41}$$

It can be shown that the quantity α:

$$\alpha = \frac{1}{2}\cos^2\frac{\theta}{2}\left(1 - \frac{3}{2}\frac{x^2 + x'^2}{(L/2)^2}\right) \tag{7.42}$$

[1] $F_M/\zeta_{||} = F_M \frac{\ln(L/d)}{2\pi\eta L}$. For filaments, $L = 10\,\mu m$, $d = 25\,nm$, the viscosity of cytoplasm $\eta = 0.05\,pN\,s\,\mu m^{-2}$, then $F_M/\zeta_{||} \approx 9\mu m\,s^{-1}$. It follows that $v_M\zeta_{||}/F_M \approx 0.1$ for a motor maximal velocity $v_M = 0.8\mu m\,s^{-1}$.

is subunitary:

$$|\alpha| \leq 1 \tag{7.43}$$

Indeed, since $x \leq L/2$ and $x' \leq L/2$, then:

$$-1 \leq \alpha \leq 1/2 \tag{7.44}$$

Then, the tension can be expressed as:

$$T = \zeta_{||} v_M \sin\frac{\theta}{2}(1 + \alpha + \alpha^2 + \cdots) \tag{7.45}$$

For the rest of the present thesis we consider that the following is a satisfactory approximation

$$T \approx T_M \sin\frac{\theta}{2} \tag{7.46}$$

where $T_M = \zeta_{||}\, v_M \approx 0.5\, pN$ and represents the strength of the motor.

Finally, we mention that a complete expression for $\alpha(\boldsymbol{\xi},\, \mathbf{u},\, \mathbf{u}')$, which can be derived from Eq. (7.42), is given by:

$$\alpha = \frac{1}{4}(1 + \hat{\mathbf{u}} \cdot \hat{\mathbf{u}}')\left(1 - \frac{3}{8}\frac{1}{(L/2)^2}\left(\frac{(\boldsymbol{\xi} \cdot (\hat{\mathbf{u}}' - \hat{\mathbf{u}}))^2}{(1 - \hat{\mathbf{u}} \cdot \hat{\mathbf{u}}')^2} + \frac{(\boldsymbol{\xi} \cdot (\hat{\mathbf{u}}' + \hat{\mathbf{u}}))^2}{(1 + \hat{\mathbf{u}} \cdot \hat{\mathbf{u}}')^2}\right)\right) \tag{7.47}$$

7.2.4 The Linear and Angular Velocities (Summary)

We can conclude our discussion about microscopic modeling by deriving the filament velocities if we take into account the expression Eq. (7.46) for the active force. We obtain the following expressions for the individual translational velocities

$$\begin{cases} \mathbf{v}(\boldsymbol{\xi},\, \hat{\mathbf{u}},\, \hat{\mathbf{u}}') &= -\frac{T_M}{\pi}\left(\frac{1}{\zeta_{||}} - \frac{1}{\zeta_\perp}\right)(1 - \hat{\mathbf{u}} \cdot \hat{\mathbf{u}}')\,\hat{\mathbf{u}} + \frac{T_M}{\pi}\frac{1}{\zeta_\perp}(\hat{\mathbf{u}}' - \hat{\mathbf{u}}) \\ \mathbf{v}'(\boldsymbol{\xi},\, \hat{\mathbf{u}},\, \hat{\mathbf{u}}') &= -\frac{T_M}{\pi}\left(\frac{1}{\zeta_{||}} - \frac{1}{\zeta_\perp}\right)(1 - \hat{\mathbf{u}} \cdot \hat{\mathbf{u}}')\,\hat{\mathbf{u}}' - \frac{T_M}{\pi}\frac{1}{\zeta_\perp}(\hat{\mathbf{u}}' - \hat{\mathbf{u}}) \\ \mathbf{v}_{rel}(\boldsymbol{\xi},\, \hat{\mathbf{u}},\, \hat{\mathbf{u}}') &= \frac{T_M}{\pi}\left(\frac{1}{\zeta_{||}} - \frac{1}{\zeta_\perp}\right)(1 - \hat{\mathbf{u}} \cdot \hat{\mathbf{u}}')\,(\hat{\mathbf{u}}' - \hat{\mathbf{u}}) + \frac{T_M}{\pi}\frac{2}{\zeta_\perp}(\hat{\mathbf{u}}' - \hat{\mathbf{u}}) \end{cases} \tag{7.48}$$

The corresponding expressions for the angular velocities are:

$$\begin{cases} \boldsymbol{\omega}(\boldsymbol{\xi},\, \hat{\mathbf{u}},\, \hat{\mathbf{u}}') &= \frac{T_M}{\pi\gamma_R}\,\boldsymbol{\xi} \times \hat{\mathbf{u}}' \\ \boldsymbol{\omega}'(\boldsymbol{\xi},\, \hat{\mathbf{u}},\, \hat{\mathbf{u}}') &= -\frac{T_M}{\pi\gamma_R}\,\boldsymbol{\xi} \times \hat{\mathbf{u}} \\ \boldsymbol{\omega}_{rel}(\boldsymbol{\xi},\, \hat{\mathbf{u}},\, \hat{\mathbf{u}}') &= \frac{T_M}{\pi\gamma_R}\,\boldsymbol{\xi} \times (\hat{\mathbf{u}}' + \hat{\mathbf{u}}) \end{cases} \tag{7.49}$$

7.3 Smoluchowski Equation and Moment Expansion

If we consider a system of rigid rods, with diameter D and length L, then the density distribution function $\psi(\mathbf{r},\, \hat{\mathbf{u}},\, t)$ for finding a particle at a position $\mathbf{r}$, with an orientation $\hat{\mathbf{u}}$, at a given moment of time t, satisfies the normalization condition

$$\int d\mathbf{r} \int d\hat{\mathbf{u}}\, \psi(\mathbf{r}, \hat{\mathbf{u}}, t) = N \tag{7.50}$$

and obeys the conservation law (see [100, 99]):

$$\partial_t \psi(\mathbf{r}, \hat{\mathbf{u}}, t) + \boldsymbol{\nabla}_{\mathbf{r}} \cdot \mathbf{J} + \mathcal{R} \cdot \mathbf{J}_R = \mathbf{0} \tag{7.51}$$

In the last equation we introduced the operator $\mathcal{R} = \hat{\mathbf{u}} \times \boldsymbol{\partial}_{\hat{\mathbf{u}}}$, which applies only to the orientational degrees of freedom, and we denoted the translation and rotation currents as $\mathbf{J}$ and $\mathbf{J}_R$ respectively. The general expressions for these currents are given by

$$\mathbf{J} = -\mathbf{D} \cdot \boldsymbol{\nabla}_{\mathbf{r}} \psi - \frac{1}{k_B T} \mathbf{D} \cdot (\psi \boldsymbol{\nabla}_{\mathbf{r}} V_{ex}) + \mathbf{J}^{act} \tag{7.52}$$

$$\mathbf{J}_R = -D_R \mathcal{R} \psi - \frac{1}{k_B T} D_R \, \psi \, \mathcal{R} V_{ex} + \mathbf{J}_R^{act} \tag{7.53}$$

We can identify three types of contributions in these equations. One contribution to these currents is coming from pure diffusion, *i.e.* terms $\propto \boldsymbol{\nabla}_{\mathbf{r}} \psi, \, \mathcal{R}\psi$, another comes from *hard core repulsion*, *i.e.* terms $\propto \boldsymbol{\nabla}_{\mathbf{r}} V_{ex}, \; \mathcal{R} V_{ex}$, and finally the *active* currents, $\mathbf{J}^{act}$ and $\mathbf{J}_R^{act}$. Explicit expressions for these terms will be given below.

The diffusion coefficient $\mathbf{D}$ is a tensor of second rank and it is given by:

$$\mathbf{D} = D_{\parallel} \hat{\mathbf{u}}\hat{\mathbf{u}} + D_{\perp} (\mathbf{I} - \hat{\mathbf{u}}\hat{\mathbf{u}}) \tag{7.54}$$

These coefficients, together with the rotational difussion coefficient D_R, satisfy Einstein relations [99]

$$D_{||} = \frac{k_B T}{\zeta_{||}}, \; D_{\perp} = \frac{k_B T}{\zeta_{\perp}}, \; D_R = \frac{k_B T}{\zeta_R} \tag{7.55}$$

In the following we will derive the evolution equation for *irreducible* moments. For this, we have to multiply both sides of Eq. (7.51) by the components of the irreducible tensors $\overline{\mathbf{T}}^{(l)}(\hat{\mathbf{u}})$, which we defined in Eq. (7.185). This result is integrated over all possible orientations $\hat{\mathbf{u}}$, and finally the moment equation is derived with the use of moment definitions from Eq. (7.196). We are interested in an irreducible tensor expansion like Eq. (7.202), up to the second rank, $l \leq 2$. The result is a set of differential equations that couples the density ρ, as the zero rank moment, the polarization $\mathbf{t}$, as the first rank moment, and the nematic order parameter $\overline{\mathbf{Q}}^{(2)}$, as the second rank *irreducible* moment. We will limit the discussion in this thesis to linear contributions only. However, we are interested to derive a phase diagram that shows *large scale* instabilities of the homogeneous and isotropic state, and we expect therefore that expansions up to second order in the derivatives of the relevant quantities are sufficient.

7.3.1 Diffusion of Free Rods

The simplest case is the case of free rods, *i.e.* no active or hard core repulsion. The moment equations are derived following the program that we have described above. The second rank moment is the nematic order parameter $\overline{\mathbf{Q}}^{(2)}$, which is a traceless symmetric tensor, and a consistency check

shows that this property is preserved by the evolution equation of this moment.

$$\partial_t \rho = \frac{D_{||} + (d-1)D_\perp}{d} \boldsymbol{\nabla}_{\mathbf{r}}{}^2 \rho + (D_{||} - D_\perp)\, \boldsymbol{\nabla}_{\mathbf{r}} \boldsymbol{\nabla}_{\mathbf{r}} : \overline{\mathbf{Q}}^{(2)} \tag{7.56}$$

$$\partial_t \mathbf{t} = \frac{D_{||} + (d+1)D_\perp}{d+2} \boldsymbol{\nabla}_{\mathbf{r}}{}^2 \mathbf{t} + 2\frac{D_{||} - D_\perp}{d+2} \boldsymbol{\nabla}_{\mathbf{r}} \boldsymbol{\nabla}_{\mathbf{r}} \cdot \mathbf{t} - (d-1)\, D_R\, \mathbf{t} \tag{7.57}$$

$$\begin{aligned} \partial_t \overline{\mathbf{Q}}^{(2)} &= -2d\, D_R\, \overline{\mathbf{Q}}^{(2)} + 2\frac{D_{||} - D_\perp}{d\,(d+2)} \left(\boldsymbol{\nabla}_{\mathbf{r}} \boldsymbol{\nabla}_{\mathbf{r}} \rho - \boldsymbol{\nabla}_{\mathbf{r}}{}^2 \rho\, \frac{\mathbf{I}^{(2)}}{d} \right) \\ &+ \frac{D_{||} + (d+3)D_\perp}{d+4} \boldsymbol{\nabla}_{\mathbf{r}}{}^2 \overline{\mathbf{Q}}^{(2)} \\ &+ 2\frac{D_{||} - D_\perp}{d+4} \left(\boldsymbol{\nabla}_{\mathbf{r}} \boldsymbol{\nabla}_{\mathbf{r}} \cdot \overline{\mathbf{Q}}^{(2)} + \left(\boldsymbol{\nabla}_{\mathbf{r}} \boldsymbol{\nabla}_{\mathbf{r}} \cdot \overline{\mathbf{Q}}^{(2)} \right)^T - 2\, \boldsymbol{\nabla}_{\mathbf{r}} \boldsymbol{\nabla}_{\mathbf{r}} : \overline{\mathbf{Q}}^{(2)}\, \frac{\mathbf{I}^{(2)}}{d} \right) \end{aligned} \tag{7.58}$$

7.3.2 Excluded Volume Interaction

In order to include the effect of the excluded volume interactions, we follow the *effective potential* approach discussed in Ref. [101].

The contribution to the currents are

$$\mathbf{J} = -\frac{1}{k_B\, T} \mathbf{D} \cdot (\psi \boldsymbol{\nabla}_{\mathbf{r}} V_{ex}) \tag{7.59}$$

$$\mathbf{J}_R = -\frac{1}{k_B\, T} D_R\, \psi\, \mathcal{R} V_{ex} \tag{7.60}$$

where the effective potential V_{ex} is given by

$$V_{ex}(\mathbf{r}, \hat{\mathbf{u}}) = k_B\, T \int_{\hat{\mathbf{u}}'} \int_{\boldsymbol{\xi}}' \psi(\mathbf{r} + \boldsymbol{\xi}, \hat{\mathbf{u}}') \tag{7.61}$$

In the last expression, the prime restricts the integral to the excluded volume.

Our aim is to study *large scale instabilities*, and therefore the relevant length scale of the emerging pattern is expected to be much larger than the linear size of a single filament. Because of this, the running variable $\boldsymbol{\xi}$ in the above excluded volume integral can be regarded as a small variable, and we therefore expand $\psi(\mathbf{r} + \boldsymbol{\xi}, \hat{\mathbf{u}}')$ in Taylor series (see also [101]).

$$\psi(\mathbf{r} + \boldsymbol{\xi}, \hat{\mathbf{u}}') = \psi(\mathbf{r}, \hat{\mathbf{u}}') + \xi_i'\, \mathbf{e}_i' \cdot \boldsymbol{\nabla}_{\mathbf{r}} \psi(\mathbf{r}, \hat{\mathbf{u}}') + \frac{\xi_i' \xi_j'}{2} (\mathbf{e}_i' \cdot \boldsymbol{\nabla}_{\mathbf{r}})(\mathbf{e}_j' \cdot \boldsymbol{\nabla}_{\mathbf{r}}) \psi(\mathbf{r}, \hat{\mathbf{u}}') \tag{7.62}$$

In the above expression we have defined the vectors:

$$\mathbf{e}_1' = \frac{\hat{\mathbf{u}}' + \hat{\mathbf{u}}}{|\hat{\mathbf{u}}' + \hat{\mathbf{u}}|}, \quad \mathbf{e}_2' = \frac{\hat{\mathbf{u}}' - \hat{\mathbf{u}}}{|\hat{\mathbf{u}}' - \hat{\mathbf{u}}|}, \quad \mathbf{e}_3' = \mathbf{e}_1' \times \mathbf{e}_2' \tag{7.63}$$

Eq. (7.61) becomes

$$\frac{V_{ex}(\mathbf{r}, \hat{\mathbf{u}})}{k_B\, T} = \int_{\hat{\mathbf{u}}'} \int_{\boldsymbol{\xi}}' \left(\psi(\mathbf{r}, \hat{\mathbf{u}}') + \xi_i'\, \mathbf{e}_i' \cdot \boldsymbol{\nabla}_{\mathbf{r}} \psi(\mathbf{r}, \hat{\mathbf{u}}') + \frac{\xi_i' \xi_j'}{2} (\mathbf{e}_i' \cdot \boldsymbol{\nabla}_{\mathbf{r}})(\mathbf{e}_j' \cdot \boldsymbol{\nabla}_{\mathbf{r}}) \psi(\mathbf{r}, \hat{\mathbf{u}}') \right) \tag{7.64}$$

The integrals over the excluded volume give the results:

$$\int' d\boldsymbol{\xi}' = \Gamma_0 \tag{7.65}$$
$$\int' d\boldsymbol{\xi}\, \xi_i' = 0 \tag{7.66}$$
$$\int' d\boldsymbol{\xi}\, \xi_i'\xi_j' = \delta_{ij}\Gamma_i, \;\; i = 1,\, 2,\, 3 \tag{7.67}$$

where

$$\Gamma_0 = 2\, D\, L^2\, \sin\theta \equiv \gamma_0 \sin\theta \tag{7.68}$$
$$\Gamma_1 = \frac{D\, L^4}{6}(1+\cos\theta)\, \sin\theta \equiv \gamma_1\, (1+\cos\theta)\, \sin\theta \tag{7.69}$$
$$\Gamma_2 = \frac{D\, L^4}{6}(1-\cos\theta)\, \sin\theta \equiv \gamma_2\, (1-\cos\theta)\, \sin\theta \tag{7.70}$$
$$\Gamma_3 = \frac{2}{3} D^3\, L^2\, \sin\theta = \mathcal{O}(D^4) \tag{7.71}$$

By making use of $\hat{\mathbf{u}}' \cdot \hat{\mathbf{u}} = \cos\theta$ and the definitions of the $\mathbf{e}_i'$ vectors from Eq. (7.63), the *rhs* of Eq. (7.64) becomes:

$$\begin{aligned}\frac{V_{ex}(\mathbf{r},\hat{\mathbf{u}})}{k_B\, T} = \int d\hat{\mathbf{u}}' \;\; & \Big(\gamma_0 \sqrt{1-(\hat{\mathbf{u}}\cdot\hat{\mathbf{u}}')^2}\,\psi(\mathbf{r},\hat{\mathbf{u}}') \\ & + \frac{\gamma_1}{4}\sqrt{1-(\hat{\mathbf{u}}\cdot\hat{\mathbf{u}}')^2}\,((\hat{\mathbf{u}}'+\hat{\mathbf{u}})\cdot\boldsymbol{\nabla}_{\mathbf{r}})((\hat{\mathbf{u}}'+\hat{\mathbf{u}})\cdot\boldsymbol{\nabla}_{\mathbf{r}})\psi(\mathbf{r},\hat{\mathbf{u}}') \\ & + \frac{\gamma_1}{4}\sqrt{1-(\hat{\mathbf{u}}\cdot\hat{\mathbf{u}}')^2}\,((\hat{\mathbf{u}}'-\hat{\mathbf{u}})\cdot\boldsymbol{\nabla}_{\mathbf{r}})((\hat{\mathbf{u}}'-\hat{\mathbf{u}})\cdot\boldsymbol{\nabla}_{\mathbf{r}})\psi(\mathbf{r},\hat{\mathbf{u}})\Big)\end{aligned} \tag{7.72}$$

We have just neglected the term proportional to D^3, since the aspect ratio of our rods is very large.

We can make use of the Taylor expansion:

$$\sqrt{1-(\hat{\mathbf{u}}\cdot\hat{\mathbf{u}}')^2} = 1 - \frac{(\hat{\mathbf{u}}\cdot\hat{\mathbf{u}}')^2}{2} + \mathcal{O}((\hat{\mathbf{u}}\cdot\hat{\mathbf{u}}')^4) \tag{7.73}$$

because there is a small probability of having $(\hat{\mathbf{u}}\cdot\hat{\mathbf{u}}')^2$ close to one, *i.e.* when the convergence of the Taylor series fails. Indeed our argument is consistent with the fact that we study instabilities in a disordered system and therefore there is a small probability of having two parallel filaments.

$$\begin{aligned}\frac{V_{ex}(\mathbf{r},\hat{\mathbf{u}})}{k_B\, T} = \int d\hat{\mathbf{u}}' \;\; \Bigg(& \gamma_0\left(1-\frac{(\hat{\mathbf{u}}\cdot\hat{\mathbf{u}}')^2}{2}\right)\psi(\mathbf{r},\hat{\mathbf{u}}') \\ & + \frac{\gamma_1}{2}\left(1-\frac{(\hat{\mathbf{u}}\cdot\hat{\mathbf{u}}')^2}{2}\right)(\hat{\mathbf{u}}'\hat{\mathbf{u}}'+\hat{\mathbf{u}}\hat{\mathbf{u}}) : \boldsymbol{\nabla}_{\mathbf{r}}\boldsymbol{\nabla}_{\mathbf{r}}\,\psi(\mathbf{r},\hat{\mathbf{u}}')\Bigg)\end{aligned} \tag{7.74}$$

Translational Current

We now focus on translational current only. The Smoluchowski equation is:

$$\partial_t\, \psi(\mathbf{r},\, \hat{\mathbf{u}},\, t) \propto -\boldsymbol{\nabla}_{\mathbf{r}} \cdot \mathbf{J}(\mathbf{r},\, \hat{\mathbf{u}}) \tag{7.75}$$

The equations for the first relevant moments are:

$$\partial_t \begin{pmatrix} \rho(\mathbf{r}) \\ \mathbf{t}(\mathbf{r}) \\ \overline{\mathbf{Q}}^{(2)}(\mathbf{r}) \end{pmatrix} \propto -\int d\hat{\mathbf{u}} \begin{pmatrix} \mathbf{1} \\ \hat{\mathbf{u}} \\ \hat{\mathbf{u}}\,\hat{\mathbf{u}} - \frac{\mathbf{I}}{d}^{(2)} \end{pmatrix} \boldsymbol{\nabla}_{\mathbf{r}} \cdot \mathbf{J}(\mathbf{r},\, \hat{\mathbf{u}}) \tag{7.76}$$

Now we proceed to compute the contribution to translational current moments from the excluded volume interaction:

$$-\boldsymbol{\nabla}_{\mathbf{r}} \cdot \mathbf{J}(\mathbf{r},\, \hat{\mathbf{u}}) = \boldsymbol{\nabla}_{\mathbf{r}} \cdot \mathbf{D} \cdot \left(\psi(\mathbf{r},\, \hat{\mathbf{u}})\, \boldsymbol{\nabla}_{\mathbf{r}} \frac{V_{ex}(\mathbf{r},\, \hat{\mathbf{u}})}{k_B\, T} \right) \tag{7.77}$$

In a more explicit form one has:

$$\begin{aligned} -\int d\hat{\mathbf{u}} \boldsymbol{\nabla}_{\mathbf{r}} \cdot \mathbf{J}(\mathbf{r},\, \hat{\mathbf{u}}) \;\; &= \;\; \int d\hat{\mathbf{u}} \int d\hat{\mathbf{u}}'\, \boldsymbol{\nabla}_{\mathbf{r}} \cdot \Big(D_{\|} \hat{\mathbf{u}}\hat{\mathbf{u}} + D_{\perp} (\mathbf{I} - \hat{\mathbf{u}}\hat{\mathbf{u}}) \Big)\, \psi(\mathbf{r},\, \hat{\mathbf{u}}) \cdot \boldsymbol{\nabla}_{\mathbf{r}} \\ &\quad \left(1 - \frac{(\hat{\mathbf{u}} \cdot \hat{\mathbf{u}}')^2}{2} \right) \left(\gamma_0\, \psi(\mathbf{r},\, \hat{\mathbf{u}}') + \frac{\gamma_1}{2} (\hat{\mathbf{u}}'\hat{\mathbf{u}}' + \hat{\mathbf{u}}\hat{\mathbf{u}}) : \boldsymbol{\nabla}_{\mathbf{r}} \boldsymbol{\nabla}_{\mathbf{r}}\, \psi(\mathbf{r}, \hat{\mathbf{u}}') \right) \end{aligned} \tag{7.78}$$

If the the $\mathbf{Q}$ -moments are expressed in terms of irreducible tensors, we have the result for the *translational current contribution* in the *linear approximation*:

$$\partial_t\, \rho(\mathbf{r}) \;\; = \;\; \gamma_0\, \rho_0\, \frac{2d-1}{2\,d} \left(\frac{D_{||} + (d-1)\, D_{\perp}}{d} \right) \boldsymbol{\nabla}_{\mathbf{r}}{}^2\, \rho - \gamma_0\, \rho_0 \frac{D_{||} - D_{\perp}}{d\,(d+2)} \boldsymbol{\nabla}_{\mathbf{r}} \boldsymbol{\nabla}_{\mathbf{r}} : \overline{\mathbf{Q}}^{(2)} \tag{7.79}$$

$$\partial_t\, \mathbf{t}(\mathbf{r}) \;\; = \;\; 0 \tag{7.80}$$

$$\begin{aligned} \partial_t\, \overline{\mathbf{Q}}^{(2)}(\mathbf{r}) \;\; &= \;\; \gamma_0\, \rho_0\, \frac{2\,d-1}{d\,(d+2)} (D_{||} - D_{\perp}) \left(\boldsymbol{\nabla}_{\mathbf{r}} \boldsymbol{\nabla}_{\mathbf{r}}\, \rho - \boldsymbol{\nabla}_{\mathbf{r}}{}^2\, \rho\, \frac{\mathbf{I}}{d}^{(2)} \right) \\ &- \;\; \gamma_0\, \rho_0\, \frac{D_{||} + (d+3)\, D_{\perp}}{d\,(d+2)\,(d+4)}\, \boldsymbol{\nabla}_{\mathbf{r}}{}^2\, \overline{\mathbf{Q}}^{(2)} \\ &- \;\; 2\gamma_0\, \rho_0\, \frac{D_{||} - D_{\perp}}{d\,(d+2)\,(d+4)} \left(\boldsymbol{\nabla}_{\mathbf{r}} \boldsymbol{\nabla}_{\mathbf{r}} \cdot \overline{\mathbf{Q}}^{(2)} + \left(\boldsymbol{\nabla}_{\mathbf{r}} \boldsymbol{\nabla}_{\mathbf{r}} \cdot \overline{\mathbf{Q}}^{(2)} \right)^{\mathrm{T}} - 2 \boldsymbol{\nabla}_{\mathbf{r}} \boldsymbol{\nabla}_{\mathbf{r}} : \overline{\mathbf{Q}}^{(2)}\, \frac{\mathbf{I}}{d}^{(2)} \right) \end{aligned} \tag{7.81}$$

Rotational Current

We focus this time on the rotational contribution from the excluded volume effect to the Smoluchowski equation:

$$\partial_t\, \psi(\mathbf{r},\, \hat{\mathbf{u}},\, t) \propto -(\hat{\mathbf{u}} \times \partial_{\hat{\mathbf{u}}}) \cdot \mathbf{J}_R(\mathbf{r},\, \hat{\mathbf{u}}) \tag{7.82}$$

$$\partial_t \begin{pmatrix} \rho(\mathbf{r}) \\ \mathbf{t}(\mathbf{r}) \\ \overline{\mathbf{Q}}^{(2)}(\mathbf{r}) \end{pmatrix} \propto -\int d\hat{\mathbf{u}} \begin{pmatrix} \mathbf{1} \\ \hat{\mathbf{u}} \\ \hat{\mathbf{u}}\,\hat{\mathbf{u}} - \frac{\mathbf{I}}{d}^{(2)} \end{pmatrix} (\hat{\mathbf{u}} \times \partial_{\hat{\mathbf{u}}}) \cdot \mathbf{J}_R(\mathbf{r},\, \hat{\mathbf{u}}) \tag{7.83}$$

The excluded volume contribution to the rotational current is:

$$\mathbf{J}_R = -D_R\, \psi(\mathbf{r},\, \hat{\mathbf{u}})\, (\hat{\mathbf{u}} \times \partial_{\hat{\mathbf{u}}})\, \frac{V_{ex}(\mathbf{r},\, \hat{\mathbf{u}})}{k_B\, T} \tag{7.84}$$

Identity 1 *For any scalar function A and B that depends on the unit vector $\hat{\mathbf{u}}$ only, the following is true:*

$$\left(\hat{\mathbf{u}} \times \partial_{\hat{\mathbf{u}}}\right) \cdot \left(A \left(\hat{\mathbf{u}} \times \partial_{\hat{\mathbf{u}}}\right) B\right) = \boldsymbol{\nabla}_{\hat{\mathbf{u}}} \cdot \left(A \, \boldsymbol{\nabla}_{\hat{\mathbf{u}}} \, B\right) \tag{7.85}$$

With the help of the above identity we have:

$$-\left(\hat{\mathbf{u}} \times \partial_{\hat{\mathbf{u}}}\right) \cdot \mathbf{J}_R = D_R \, \boldsymbol{\nabla}_{\hat{\mathbf{u}}} \cdot \left(\psi(\mathbf{r},\, \hat{\mathbf{u}}) \, \boldsymbol{\nabla}_{\hat{\mathbf{u}}} \, \frac{V_{ex}(\mathbf{r},\, \hat{\mathbf{u}})}{k_B \, T}\right) \tag{7.86}$$

Theorem 1 *(Gauss) For any vectorial function $\mathbf{A}$ which depends on the unit vector $\hat{\mathbf{u}}$ only, the following is true:*

$$\int d\hat{\mathbf{u}} \, \boldsymbol{\nabla}_{\hat{\mathbf{u}}} \cdot \mathbf{A} = (d-1) \int d\hat{\mathbf{u}} \, \hat{\mathbf{u}} \cdot \mathbf{A} \tag{7.87}$$

Corollary 1 *(Gauss) For any scalar function $\psi(\hat{\mathbf{u}})$ which depends on the unit vector $\hat{\mathbf{u}}$ only, the following is true:*

$$\int d\hat{\mathbf{u}} \, \boldsymbol{\nabla}_{\hat{\mathbf{u}}} \, \psi(\hat{\mathbf{u}}) = (d-1) \int d\hat{\mathbf{u}} \, \hat{\mathbf{u}} \, \psi(\hat{\mathbf{u}}) \tag{7.88}$$

If we apply this theorem directly to compute the rotational contribution to the zero-th moment:

$$\begin{aligned} \partial_t \, \rho(\mathbf{r}) &= \int d\hat{\mathbf{u}} \, D_R \, \boldsymbol{\nabla}_{\hat{\mathbf{u}}} \cdot \left(\psi(\mathbf{r},\, \hat{\mathbf{u}}) \, \boldsymbol{\nabla}_{\hat{\mathbf{u}}} \, \frac{V_{ex}(\mathbf{r},\, \hat{\mathbf{u}})}{k_B \, T}\right) \\ &= 2 \, D_R \int d\hat{\mathbf{u}} \, \psi(\mathbf{r},\, \hat{\mathbf{u}}) \, \hat{\mathbf{u}} \cdot \boldsymbol{\nabla}_{\hat{\mathbf{u}}} \, \frac{V_{ex}(\mathbf{r},\, \hat{\mathbf{u}})}{k_B \, T} \\ &= 0 \end{aligned} \tag{7.89}$$

because $\hat{\mathbf{u}} \cdot \boldsymbol{\nabla}_{\hat{\mathbf{u}}} = 0$. For the other moments we obtain the following results:

$$\begin{aligned} \partial_t \, \mathbf{t}(\mathbf{r}) &= -D_R \int d\hat{\mathbf{u}} \, \psi(\mathbf{r},\, \hat{\mathbf{u}}) \, \boldsymbol{\nabla}_{\hat{\mathbf{u}}} \frac{V_{ex}(\mathbf{r},\, \hat{\mathbf{u}})}{k_B \, T} \\ \partial_t \, \overline{\mathbf{Q}}^{(2)}(\mathbf{r}) &= -D_R \int d\hat{\mathbf{u}} \, \psi(\mathbf{r},\, \hat{\mathbf{u}}) \left(\boldsymbol{\nabla}_{\hat{\mathbf{u}}} \frac{V_{ex}(\mathbf{r},\, \hat{\mathbf{u}})}{k_B \, T} \, \hat{\mathbf{u}} + \hat{\mathbf{u}} \, \boldsymbol{\nabla}_{\hat{\mathbf{u}}} \frac{V_{ex}(\mathbf{r},\, \hat{\mathbf{u}})}{k_B \, T}\right) \end{aligned} \tag{7.90}$$

Finally we use Eq. (7.74) for the explicit expression of the excluded volume potential V_{ex}, and we obtain the following results for *the rotational contribution in the linear approximation*:

$$\partial_t \, \rho(\mathbf{r}) = 0 \tag{7.91}$$

$$\partial_t \, \mathbf{t}(\mathbf{r}) = 0 \tag{7.92}$$

$$\begin{aligned} \partial_t \, \overline{\mathbf{Q}}^{(2)}(\mathbf{r}) &= \frac{2 D_R \, \gamma_0 \, \rho_0}{d+2} \overline{\mathbf{Q}}^{(2)} + \frac{2 D_R \, \gamma_1 \, \rho_0}{(d+2)(d+4)} \boldsymbol{\nabla}_{\mathbf{r}}{}^2 \, \overline{\mathbf{Q}}^{(2)} \\ &- D_R \, \gamma_1 \, \rho_0 \, \frac{2d^2 + 3d - 4}{d \, (d+2)^2} \left(\boldsymbol{\nabla}_{\mathbf{r}} \boldsymbol{\nabla}_{\mathbf{r}} \, \rho - \boldsymbol{\nabla}_{\mathbf{r}}{}^2 \rho \, \frac{\mathbf{I}^{(2)}}{d}\right) \\ &+ \frac{4 \, D_R \, \gamma_1 \, \rho_0}{(d+2) \, (d+4)} \left(\boldsymbol{\nabla}_{\mathbf{r}} \boldsymbol{\nabla}_{\mathbf{r}} \cdot \overline{\mathbf{Q}}^{(2)} + \left(\boldsymbol{\nabla}_{\mathbf{r}} \boldsymbol{\nabla}_{\mathbf{r}} \cdot \overline{\mathbf{Q}}^{(2)}\right)^{\mathrm{T}} - 2 \, \boldsymbol{\nabla}_{\mathbf{r}} \boldsymbol{\nabla}_{\mathbf{r}} : \overline{\mathbf{Q}}^{(2)} \, \frac{\mathbf{I}^{(2)}}{d}\right) \end{aligned} \tag{7.93}$$

7.3.3 Active Interaction

Consider again the system of two filaments. If the relative translational and angular velocity of the first filament, *i.e.* $(\mathbf{r},\,\hat{\mathbf{u}})$, are $\mathbf{v}_{rel}(\boldsymbol{\xi},\,\hat{\mathbf{u}},\,\hat{\mathbf{u}}')$ and $\boldsymbol{\omega}_{rel}(\boldsymbol{\xi},\,\hat{\mathbf{u}},\,\hat{\mathbf{u}}')$, then the active translational and rotational currents are given by:

$$\mathbf{J}^{act}(\mathbf{r},\,\hat{\mathbf{u}}) = \int d\hat{\mathbf{u}}' \int' d\xi\, \mathbf{v}_{rel}(\boldsymbol{\xi},\,\hat{\mathbf{u}},\,\hat{\mathbf{u}}')\,\psi(\mathbf{r},\,\hat{\mathbf{u}})\psi(\mathbf{r}+\xi,\,\hat{\mathbf{u}}) \tag{7.94}$$

$$\mathbf{J}_R^{act}(\mathbf{r},\,\hat{\mathbf{u}}) = \int d\hat{\mathbf{u}}' \int' d\xi\, \boldsymbol{\omega}_{rel}(\boldsymbol{\xi},\,\hat{\mathbf{u}},\,\hat{\mathbf{u}}')\,\psi(\mathbf{r},\,\hat{\mathbf{u}})\psi(\mathbf{r}+\xi,\,\hat{\mathbf{u}}) \tag{7.95}$$

For the model that we use, the expressions for the velocities were derived as in Eq. (7.48) and Eq. (7.49), and we use those expressions in the form

$$\begin{cases} \mathbf{v}_{rel}(\boldsymbol{\xi},\,\hat{\mathbf{u}},\,\hat{\mathbf{u}}') = A\,(1-\hat{\mathbf{u}}\cdot\hat{\mathbf{u}}')\,(\hat{\mathbf{u}}'-\hat{\mathbf{u}}) + B\,(\hat{\mathbf{u}}'-\hat{\mathbf{u}}) \\ \boldsymbol{\omega}_{rel}(\boldsymbol{\xi},\,\hat{\mathbf{u}},\,\hat{\mathbf{u}}') = C\;\boldsymbol{\xi}\times(\hat{\mathbf{u}}'+\hat{\mathbf{u}}) \end{cases} \tag{7.96}$$

where the coefficients are given by

$$A = \frac{T_M}{\pi}\left(\frac{1}{\zeta_{||}}-\frac{1}{\zeta_\perp}\right),\quad B = \frac{T_M}{\pi}\frac{2}{\zeta_\perp},\quad C = \frac{T_M}{\pi\gamma_R} \tag{7.97}$$

Active Translational Current

The contribution to Smoluchowski equation is $\partial_t\,\psi(\mathbf{r},\,\hat{\mathbf{u}},\,t) \propto -\nabla\cdot\mathbf{J}^{act}(\mathbf{r},\,\hat{\mathbf{u}})$. Using the same expansion like Eq. (7.62) we derive:

$$-\nabla\cdot\mathbf{J}^{act}(\mathbf{r},\,\hat{\mathbf{u}}) = -\nabla\cdot\int d\hat{\mathbf{u}}'\int' d\xi\left(A\,(1-\hat{\mathbf{u}}\cdot\hat{\mathbf{u}}')\,(\hat{\mathbf{u}}'-\hat{\mathbf{u}}) + B\,(\hat{\mathbf{u}}'-\hat{\mathbf{u}})\right)\psi(\mathbf{r},\hat{\mathbf{u}})\,\psi(\mathbf{r},\hat{\mathbf{u}}') \tag{7.98}$$

Here we kept the expansion in $\boldsymbol{\xi}$ only up to the zeroth order. The first reason is that the linear term gives zero when it is integrated over the excluded volume area. The second reason is that the quadratic term involves third order space derivatives for $\psi(\mathbf{r},\,\hat{\mathbf{u}},\,t)$, which we disregard since small length scale details are not relevant. However, the quadratic term also has a contribution to second order space derivatives, but that contribution is not linear. After performing the spatial integral, we obtain

$$\begin{aligned} &-\quad \nabla\cdot\mathbf{J}^{act}(\mathbf{r},\,\hat{\mathbf{u}}) = \\ &-\quad \nabla\cdot\int d\hat{\mathbf{u}}'\left(A\,(1-\hat{\mathbf{u}}\cdot\hat{\mathbf{u}}')\,(\hat{\mathbf{u}}'-\hat{\mathbf{u}}) + B\,(\hat{\mathbf{u}}'-\hat{\mathbf{u}})\right)\psi(\mathbf{r},\hat{\mathbf{u}})\,\psi(\mathbf{r},\hat{\mathbf{u}}')\,\gamma_0\,\sqrt{1-(\hat{\mathbf{u}}\cdot\hat{\mathbf{u}}')^2} \end{aligned} \tag{7.99}$$

We used this expression to derive the evolution equation for moments, and keeping only linear contributions we obtain the following result for *the contribution from the active translational currents*:

$$\left\{\begin{array}{rcl} \partial_t \rho & = & 0 \\ \partial_t \mathbf{t} & = & \gamma_0 \rho_0 \frac{-A-2B+5Ad+3Bd+2Ad^2+2Bd^2}{d^2(d+2)} \boldsymbol{\nabla}_{\mathbf{r}} \rho \\ & + & \gamma_0 \rho_0 \frac{-2A-4B+7Ad+3Bd+2Ad^2+2Bd^2}{2d(d+2)} \boldsymbol{\nabla}_{\mathbf{r}} \cdot \overline{\mathbf{Q}}^{(2)} \\ \partial_t \overline{\mathbf{Q}}^{(2)} & = & \gamma_0 \rho_0 \frac{(A+B)(2d+3)}{2(d+2)^2} \left(\boldsymbol{\nabla}_{\mathbf{r}} \mathbf{t} + \left(\boldsymbol{\nabla}_{\mathbf{r}} \mathbf{t} \right)^T - 2 \boldsymbol{\nabla}_{\mathbf{r}} \cdot \mathbf{t} \, \frac{\mathbf{I}^{(2)}}{d} \right) \end{array}\right.$$

Active Rotational Current

The contribution to Smoluchowski equation is $\partial_t \psi(\mathbf{r},\, \hat{\mathbf{u}},\, t) \propto -\nabla \cdot \mathbf{J}_R^{act}(\mathbf{r},\, \hat{\mathbf{u}})$. Using the same expansion like Eq. (7.62) we derive:

$$-\hat{\mathbf{u}} \times \partial_{\hat{\mathbf{u}}} \cdot \mathbf{J}_R^{act}(\mathbf{r},\, \hat{\mathbf{u}}) = -\hat{\mathbf{u}} \times \partial_{\hat{\mathbf{u}}} \cdot \int d\hat{\mathbf{u}}' \int' d\xi\, C\, \boldsymbol{\xi} \times (\hat{\mathbf{u}}' + \hat{\mathbf{u}})\, \psi(\mathbf{r}, \hat{\mathbf{u}})\, \xi_i' \mathbf{e}_i' \cdot \boldsymbol{\nabla}_{\mathbf{r}} \psi(\mathbf{r}, \hat{\mathbf{u}}') \tag{7.101}$$

This time we have a contribution only from the linear term of the expansion for $\psi(\mathbf{r} + \boldsymbol{\xi},\, \hat{\mathbf{u}})$. The reason is, as we can see, the angular velocity $\boldsymbol{\omega}$ brings in a linear factor in ξ, and the steric integral is non-zero only for even powers of $\boldsymbol{\xi}$ components. When we perform the spatial integral, the result is

$$-\hat{\mathbf{u}} \times \partial_{\hat{\mathbf{u}}} \cdot \mathbf{J}_R^{act}(\mathbf{r},\, \hat{\mathbf{u}}) = C\, \gamma_1\, \hat{\mathbf{u}} \times \partial_{\hat{\mathbf{u}}} \cdot \int d\hat{\mathbf{u}}'\; \psi(\mathbf{r}, \hat{\mathbf{u}})\, (\hat{\mathbf{u}}' + \hat{\mathbf{u}}) \times \boldsymbol{\alpha} \tag{7.102}$$

where we have defined the vector

$$\boldsymbol{\alpha} = \sqrt{1 - (\hat{\mathbf{u}} \cdot \hat{\mathbf{u}}')^2}\, (\hat{\mathbf{u}}\hat{\mathbf{u}} + \hat{\mathbf{u}}'\hat{\mathbf{u}}') \cdot \boldsymbol{\nabla}_{\mathbf{r}} \psi(\mathbf{r},\, \hat{\mathbf{u}}') \tag{7.103}$$

We used this expression to derive the evolution equation for moments, and keeping only linear contributions we obtain the following result for *the contribution from the active rotational currents*:

$$\left\{\begin{array}{rcl} \partial_t \rho & = & 0 \\ \partial_t \mathbf{t} & = & \gamma_1 \rho_0 C \frac{3-d-2d^2}{2d^2(d+2)} \boldsymbol{\nabla}_{\mathbf{r}} \rho + \gamma_1 \rho_0 C \frac{3-d-2d^2}{2d(d+2)} \boldsymbol{\nabla}_{\mathbf{r}} \cdot \overline{\mathbf{Q}}^{(2)} \\ \partial_t \overline{\mathbf{Q}}^{(2)} & = & \gamma_1 \rho_0 C \frac{2d+3}{2(d+2)^2} \left(\boldsymbol{\nabla}_{\mathbf{r}} \mathbf{t} + \left(\boldsymbol{\nabla}_{\mathbf{r}} \mathbf{t} \right)^T - 2 \boldsymbol{\nabla}_{\mathbf{r}} \cdot \mathbf{t} \, \frac{\mathbf{I}^{(2)}}{d} \right) \end{array}\right. \tag{7.104}$$

7.3.4 The Evolution Equations of Moments (Summary)

Here we summarize our results for the evolution equations of moments, with contributions up to the linear order from both excluded volume and active interaction, according to the microscopic model, which we presented in this chapter.

$$
\begin{aligned}
\partial_t \rho &= \frac{D^{||} + (d-1)D^{\perp}}{d}\left(1 + \gamma_0\,\rho_0 \frac{2d-1}{2d}\right) {\boldsymbol{\nabla}_{\mathbf{r}}}^2 \rho + (D^{||} - D^{\perp})\left(1 - \frac{\gamma_0\,\rho_0}{d\,(d+2)}\right) \boldsymbol{\nabla}_{\mathbf{r}} \boldsymbol{\nabla}_{\mathbf{r}} : \overline{\mathbf{Q}}^{(2)} \\
\\
\partial_t \mathbf{t} &= \frac{D^{||} + (d+1)D^{\perp}}{d+2} {\boldsymbol{\nabla}_{\mathbf{r}}}^2 \mathbf{t} + 2\frac{D^{||} - D^{\perp}}{d+2} \boldsymbol{\nabla}_{\mathbf{r}} \boldsymbol{\nabla}_{\mathbf{r}} \cdot \mathbf{t} - (d-1)\mathbf{D}^{rot}\mathbf{t} \\
&+ \left(\gamma_0\,\rho_0 \frac{-A - 2B + 5A\,d + 3B\,d + 2A\,d^2 + 2B\,d^2}{d^2\,(d+2)} + \gamma_1 \rho_0\, C \frac{3 - d - 2d^2}{2d^2\,(d+2)}\right) \boldsymbol{\nabla}_{\mathbf{r}} \rho \\
&+ \left(\gamma_0\,\rho_0 \frac{-2A - 4B + 7A\,d + 3B\,d + 2A\,d^2 + 2B\,d^2}{2d\,(d+2)} + \gamma_1 \rho_0\, C \frac{3 - d - 2d^2}{2d\,(d+2)}\right) \boldsymbol{\nabla}_{\mathbf{r}} \cdot \overline{\mathbf{Q}}^{(2)} \\
\\
\partial_t \overline{\mathbf{Q}}^{(2)} &= \left(\frac{D^{||} + (d+3)D^{\perp}}{d+4}\left(1 - \frac{\gamma_0\,\rho_0}{d\,(d+2)}\right) + 2\frac{D^{rot}\gamma_1\,\rho_0}{(d+2)\,(d+4)}\right) {\boldsymbol{\nabla}_{\mathbf{r}}}^2 \overline{\mathbf{Q}}^{(2)} \\
&+ \left(2\frac{D^{||} - D^{\perp}}{d+4}\left(1 - \frac{\gamma_0\,\rho_0}{d\,(d+2)}\right) + 4\frac{D^{rot}\gamma_1\,\rho_0}{(d+2)\,(d+4)}\right)\left(\boldsymbol{\nabla}_{\mathbf{r}}\,\boldsymbol{\nabla}_{\mathbf{r}} \cdot \overline{\mathbf{Q}}^{(2)} + \left(\boldsymbol{\nabla}_{\mathbf{r}}\,\boldsymbol{\nabla}_{\mathbf{r}} \cdot \overline{\mathbf{Q}}^{(2)}\right)^{\mathrm{T}} - 2\,\boldsymbol{\nabla}_{\mathbf{r}}\,\boldsymbol{\nabla}_{\mathbf{r}} : \overline{\mathbf{Q}}^{(2)}\,\frac{\mathbf{I}^{(2)}}{d}\right) \\
&- 2d\,D^{rot}\left(1 - \frac{\gamma_0\,\rho_0}{d\,(d+2)}\right)\overline{\mathbf{Q}}^{(2)} \\
&+ \left(2\frac{D^{||} - D^{\perp}}{d\,(d+2)}\left(1 + \gamma_0 \rho_0 \frac{2d-1}{2d}\right) - D^{rot}\gamma_1\,\rho_0 \frac{2d^2 + 3d - 4}{d\,(d+2)^2}\right)\left(\boldsymbol{\nabla}_{\mathbf{r}} \boldsymbol{\nabla}_{\mathbf{r}} \rho - \frac{\mathbf{I}^{(2)}}{d} {\boldsymbol{\nabla}_{\mathbf{r}}}^2 \rho\right) \\
&+ \left(\gamma_0\,\rho_0 \frac{(A+B)(3+2d)}{2\,(d+2)^2} + \gamma_1\,\rho_1\,C \frac{3+2d}{2(d+2)^2}\right)\left(\boldsymbol{\nabla}_{\mathbf{r}}\,\mathbf{t} + \left(\boldsymbol{\nabla}_{\mathbf{r}}\,\mathbf{t}\right)^{\mathrm{T}} - 2\,\boldsymbol{\nabla}_{\mathbf{r}} \cdot \mathbf{t}\,\frac{\mathbf{I}^{(2)}}{d}\right)
\end{aligned}
$$

7.4 Linear Stability Analysis

7.4.1 Linear Coupled Moment Equation

In the last section we have derived the coupled evolution equations for the moments up to the linear order. In order to simplify our analysis, we rewrite those equations with new notations for the coefficients.

$$\left\{\begin{array}{rcl} \partial_t \rho & = & D_{00}\,{\boldsymbol\nabla_{\mathbf r}}^2 \rho + D_{02}\,\boldsymbol\nabla_{\mathbf r}\boldsymbol\nabla_{\mathbf r} : \overline{\mathbf Q}^{(2)} \\ \partial_t \mathbf t & = & D_{11}^0\,{\boldsymbol\nabla_{\mathbf r}}^2 \mathbf t + D_{11}^1\,\boldsymbol\nabla_{\mathbf r}\boldsymbol\nabla_{\mathbf r}\cdot\mathbf t + D_{11}\,\mathbf t + A_{10}\,\boldsymbol\nabla_{\mathbf r}\rho + A_{12}\boldsymbol\nabla_{\mathbf r}\cdot\overline{\mathbf Q}^{(2)} \\ \partial_t \overline{\mathbf Q}^{(2)} & = & D_{22}^0\,{\boldsymbol\nabla_{\mathbf r}}^2\,\overline{\mathbf Q}^{(2)} + D_{22}^1\left(\boldsymbol\nabla_{\mathbf r}\,\boldsymbol\nabla_{\mathbf r}\cdot\overline{\mathbf Q}^{(2)} + \left(\boldsymbol\nabla_{\mathbf r}\,\boldsymbol\nabla_{\mathbf r}\cdot\overline{\mathbf Q}^{(2)}\right)^{\mathrm T} - 2\,\boldsymbol\nabla_{\mathbf r}\,\boldsymbol\nabla_{\mathbf r} : \overline{\mathbf Q}^{(2)}\,\tfrac{\mathbf I}{d}^{(2)}\right) \\ & + & D_{22}\,\overline{\mathbf Q}^{(2)} + D_{20}\left(\boldsymbol\nabla_{\mathbf r}\boldsymbol\nabla_{\mathbf r}\rho - \tfrac{\mathbf I}{d}^{(2)}{\boldsymbol\nabla_{\mathbf r}}^2\rho\right) + A_{21}\left(\boldsymbol\nabla_{\mathbf r}\,\mathbf t + \left(\boldsymbol\nabla_{\mathbf r}\,\mathbf t\right)^{\mathrm T} - 2\,\boldsymbol\nabla_{\mathbf r}\cdot\mathbf t\,\tfrac{\mathbf I}{d}^{(2)}\right) \end{array}\right.$$

We consistently use letter D's for all *passive* and *entropic* contributions, and A's for all the corresponding *active* contributions. The exact algebrical expressions for all these coefficients can be read off by making a direct comparison between Eq. (7.105) and Section 7.3.4.

In the following we are going to present the linear stability analysis for the equations Eq. (7.105). For this purpose, it is not necessary to know the exact expressions for these coefficients. It is however sufficient to know their signs, which can be derived if we insert exact expressions for the translational, $D_{||}$ and $D_\perp$, and rotational diffusion coefficients, D_R.

We study the case when the rotational diffusion is dominating the translational diffusion. This is precisely the case of the dilute limit (see *Doi & Edwards* and *Dhont* [100, 99]), and the relationships between the diffusion constants are:

$$\left\{\begin{array}{l} D_{||} = \frac{D^R}{6} \\ D_\perp = \frac{D^R}{12} \end{array}\right. \tag{7.106}$$

In this case then we can settle for sure the sign of the coefficients:

$$D_{00} > 0 \tag{7.107}$$

$$D_{11}^0 > 0,\quad D_{11}^1 > 0,\quad D_{11} < 0 \tag{7.108}$$

$$A_{10} < 0,\quad A_{12} < 0 \tag{7.109}$$

$$D_{22}^0 > 0,\quad D_{22}^1 > 0\quad D_{20} < 0 \tag{7.110}$$

$$A_{21} > 0 \tag{7.111}$$

The exact expressions for the coefficients

$$D_{02} = \left(D_{||} - D_\perp\right)\left(1 - \frac{\gamma_0\,\rho_0}{d\,(d+2)}\right),\qquad D_{22} = -2\,d\,D_R\left(1 - \frac{\gamma_0\,\rho_0}{d\,(d+2)}\right) \tag{7.112}$$

show that their signs are changed at a specific value of the density, $\rho_c = d(d+2)/\gamma_0$, which is the critical density of the *isotropic-nematic* instability (see below). With respect to this value for the density we have the following signs:

$$D_{02} > 0 \text{ and } D_{22} < 0,\quad \text{for } \rho_0 < \rho_c \tag{7.113}$$

$$D_{02} < 0 \text{ and } D_{22} > 0,\quad \text{for } \rho_0 > \rho_c \tag{7.114}$$

7.4.2 Periodic Boundary Conditions

We consider the Fourier components of the moments, $\rho_{\mathbf{k}}$, $\mathbf{t}_{\mathbf{k}}$, $\overline{\mathbf{Q}}^{(2)}_{\mathbf{k}}$. The corresponding equations for these components can be rewritten in a more convenient form if we decompose the Fourier components of the polarization $\mathbf{t}_{\mathbf{k}}$ into the *longitudinal*, $\mathbf{t}^{||}_{\mathbf{k}}$, and *transversal*, $\mathbf{t}^{\perp}_{\mathbf{k}}$, components:

$$k^2\,\mathbf{t}_{\mathbf{k}} \;\; = \;\; \mathbf{t}_{\mathbf{k}}{}^{||} + \mathbf{t}_{\mathbf{k}}{}^{\perp} = \mathbf{k}\,\mathbf{k}\cdot\mathbf{t}_{\mathbf{k}} - \mathbf{k}\times(\mathbf{k}\times\mathbf{t}_{\mathbf{k}}) \tag{7.115}$$

We make a similar decomposition for the second rank tensor $\overline{\mathbf{Q}}^{(2)}$:

$$k^4\,\overline{\mathbf{Q}}^{(2)} = \mathbf{k}\,\mathbf{k}\left(\mathbf{k}\,\mathbf{k} : \overline{\mathbf{Q}}^{(\mathbf{2})}_{\mathbf{k}}\right) - \mathbf{k}\;\;\mathbf{k}\times(\mathbf{k}\times\mathbf{k}\cdot\overline{\mathbf{Q}}^{(\mathbf{2})}_{\mathbf{k}}) - k^2\;\;\mathbf{k}\times(\mathbf{k}\times\overline{\mathbf{Q}}^{(\mathbf{2})}_{\mathbf{k}}) \tag{7.116}$$

Then, the evolution equation for the Fourier components of the moments can be written in the form:

$$\partial_t\,\mathbf{V}_{\mathbf{k}} = M_{\mathbf{k}}\,\mathbf{V}_{\mathbf{k}} \tag{7.117}$$

where the "vector" $\mathbf{V}_{\mathbf{k}}$ is

$$\mathbf{V}_{\mathbf{k}} = \begin{pmatrix} (\mathbf{k}\,\mathbf{k} - \mathbf{I}^{(2)})\,\rho_{\mathbf{k}} \\ (\mathbf{k}\,\mathbf{k} - \mathbf{I}^{(2)})\mathbf{t}_{\mathbf{k}}\cdot\mathbf{k} \\ (\mathbf{k}\,\mathbf{k} - k^2\,\mathbf{I}^{(2)})\,\mathbf{k}\,\mathbf{k} : \overline{\mathbf{Q}}^{(2)}_{\mathbf{k}} \\ \mathbf{k}\;\times\;(\mathbf{k}\times\mathbf{t}_{\mathbf{k}})\,\mathbf{k} \\ \mathbf{k}\times(\mathbf{k}\times\mathbf{k}\cdot\overline{\mathbf{Q}}^{(2)}_{\mathbf{k}})\,\mathbf{k} \\ \mathbf{k}\times(\mathbf{k}\times\overline{\mathbf{Q}}^{(2)}_{\mathbf{k}}) \end{pmatrix} \tag{7.118}$$

and the matrix $M_{\mathbf{k}}$ is given by:

$$
M_{\mathbf{k}} = \begin{pmatrix}
-D_{00}\,k^2 & 0 & -D_{02} & 0 & 0 & 0 \\
i\,A_{10}\,k^2 & D_{11} - (D_{11}^0 + D_{11}^1)\,k^2 & i\,A_{12} & 0 & 0 & 0 \\
-D_{20}\big(1-\frac{1}{d}\big)\,k^4 & 2\,i\,A_{21}\left(1-\frac{1}{d}\right)k^2 & D_{22} - \Big(D_{22}^0 + 2\,D_{22}^1\left(1-\frac{1}{d}\right)\Big)\,k^2 & 0 & 0 & 0 \\
0 & 0 & 0 & D_{11} - D_{11}^0\,k^2 & i\,A_{12} & 0 \\
0 & 0 & 0 & i\,A_{21}\,k^2 & D_{22} - (D_{22}^0 + D_{22}^1)\,k^2 & 0 \\
\frac{D_{20}}{d}k^2 & -2\,i\,\frac{A_{21}}{d} & 2\frac{D_{22}^1}{d} & i\,A_{21} & -D_{22}^1 & D_{22} - D_{22}^0\,k^2
\end{pmatrix}
$$

7.4.3 Variable Separation and Eigenvalue Problem

In order to solve the equation Eq. (7.117) we use the following ansatz

$$\mathbf{V_k} = e^{\lambda\, t}\, \tilde{\mathbf{V}}_\mathbf{k} \tag{7.119}$$

In this case the equation becomes

$$\lambda \tilde{\mathbf{V}}_\mathbf{k} = M_\mathbf{k}\, \tilde{\mathbf{V}}_\mathbf{k} \tag{7.120}$$

As we can see the separation of variables leads to the eigenvalue problem of the matrix M. The eigenvalues λ are solutions of the following equation:

$$\det(M_\mathbf{k} - \lambda\, \mathbf{I}^{(6)}) = 0 \tag{7.121}$$

The matrix $M_\mathbf{k}$, which we have derived in Section 7.4.2, is a *Gauss block diagonal* matrix. We can readily see that one eigenvalue is:

$$\lambda_1 = D_{22} - D^0_{22}\, k^2 \tag{7.122}$$

In order to derive the rest of the eigenvalues, we decompose the secular matrix into two block-diagonal matrixes:

$$M^1_\mathbf{k} = \begin{pmatrix} -D_{00}\, k^2 & 0 & -D_{02} \\ i\, A_{10}\, k^2 & D_{11} - (D^0_{11} + D^1_{11})\, k^2 & i\, A_{12} \\ -D_{20}\big(1 - \frac{1}{d}\big)\, k^4 & 2\, i\, A_{21}\, \big(1 - \frac{1}{d}\big)\, k^2 & D_{22} - \Big(D^0_{22} + 2\, D^1_{22}\, \big(1 - \frac{1}{d}\big)\Big)\, k^2 \end{pmatrix} \tag{7.123}$$

$$M^2_\mathbf{k} = \begin{pmatrix} D_{11} - D^0_{11}\, k^2 & iA_{12} \\ iA_{21}\, k^2 & D_{22} - (D^0_{22} + D^1_{22})\, k^2 \end{pmatrix} \tag{7.124}$$

7.4.4 Isotropic-Nematic Instability

In the previous section we have anticipated that one of the eigenvalues is $\lambda_1 = D_{22} - D^0_{22}\, k^2$. The corresponding *eigenvector* $\tilde{\mathbf{V}}_\mathbf{k}$ has all of the components equal to zero, except $\mathbf{k} \times (\mathbf{k} \times \overline{\mathbf{Q}}^{(2)}_\mathbf{k})$. Since the other components are zero, it means that $\rho_\mathbf{k} = 0$, $\mathbf{t_k} = 0$ and $\mathbf{k} \cdot \overline{\mathbf{Q}}^{(2)}_\mathbf{k} = 0$. If we make the inverse Fourier transform for these components we see that for this state we have a constant density, $\rho = \rho_0$, and no polarization, $\mathbf{t} = 0$.

The explicit expression of the eigenvalue Eq. (7.122) is

$$\lambda_1 = -2\, d\, D_R\, \left(1 - \frac{\gamma_0\, \rho_0}{d\,(d+2)}\right) - k^2\, \left(\frac{D^{||} + (d+3) D^{\perp}}{d+4}\left(1 - \frac{\gamma_0\, \rho_0}{d\,(d+2)}\right) + 2\frac{D^{rot}\gamma_1\, \rho_0}{(d+2)\,(d+4)}\right) \tag{7.125}$$

From the general form Eq. (7.119), we see that there are instabilities for positive values of the eigenvalues. We see that $\lambda_1 < 0$ if the density of the filaments is less than a critical value

$$\rho_0 < \rho_c = \frac{d\,(d+2)}{\gamma_0} \tag{7.126}$$

where $\gamma_0 = 2\,D\,L^2$ is the excluded volume for rods. We summarize this case in Fig. 7.4. We see that, when the density is larger that its critical value ρ_c, the first mode to become unstable corresponds to the zero wavenumber $\mathbf{k} = 0$. An instability with $\mathbf{k} = 0$ means that the order parameter $\overline{\mathbf{Q}}^{(2)}$ remains homogeneous. As a conclusion, we identify this instability as the *isotropic-nematic* instability. We can see that motors play no role, and the instability is driven only by the excluded volume interaction.

We can see from Eq. (7.126) that the critical density ρ_c scales with the inverse of the excluded volume. This is an encouraging qualitative result, since this is well established for the isotropic-nematic transitions for hard rods [73]. We stress that the result Eq. (7.126) is derived for both 2D and 3D case.

7.4.5 Instabilities at Constant Density

We now compute the eigenvalues that correspond to the matrix M_k^2 from Eq. (7.124). The matrix M_k^2 is a block matrix inside the matrix M_k from Section 7.4.2. The eigenvectors, which correspond to the general eigenvalue problem Eq. (7.120), have the form

$$\tilde{\mathbf{V}}_{\mathbf{k}}^{23} = \begin{pmatrix} 0 \\ 0 \\ 0 \\ \mathbf{k} \times (\mathbf{k} \times \mathbf{t}_{\mathbf{k}})\,\mathbf{k} \\ \mathbf{k} \times (\mathbf{k} \times \mathbf{k} \cdot \overline{\mathbf{Q}}_{\mathbf{k}}^{(\mathbf{2})})\,\mathbf{k} \\ \mathbf{k} \times (\mathbf{k} \times \overline{\mathbf{Q}}_{\mathbf{k}}^{(\mathbf{2})})\,\mathbf{k} \end{pmatrix} \tag{7.127}$$

The first three entries of this vector are zero, and this corresponds to the following equations:

$$\rho_{\mathbf{k}} = 0 \tag{7.128}$$

$$\mathbf{t}_{\mathbf{k}} \cdot \mathbf{k} = 0 \tag{7.129}$$

$$\mathbf{k}\,\mathbf{k} \,:\, \overline{\mathbf{Q}}_{\mathbf{k}}^{(\mathbf{2})} = 0 \tag{7.130}$$

If we make the inverse Fourier transform for the vector $\tilde{\mathbf{V}}_{\mathbf{k}}^{23}$, we have for the space representation

$$\rho = \rho_0 = const \tag{7.131}$$

$$\boldsymbol{\nabla}_{\mathbf{r}} \cdot \mathbf{t} = 0 \tag{7.132}$$

$$\boldsymbol{\nabla}_{\mathbf{r}}\,\boldsymbol{\nabla}_{\mathbf{r}} \,:\, \overline{\mathbf{Q}}^{(2)} = 0 \tag{7.133}$$

$$\boldsymbol{\nabla}_{\mathbf{r}} \times \mathbf{t} \neq 0 \tag{7.134}$$

$$\boldsymbol{\nabla}_{\mathbf{r}} \times \boldsymbol{\nabla}_{\mathbf{r}} \cdot \overline{\mathbf{Q}}^{(\mathbf{2})} \neq 0 \tag{7.135}$$

$$\boldsymbol{\nabla}_{\mathbf{r}} \times \overline{\mathbf{Q}}^{(\mathbf{2})} \neq 0 \tag{7.136}$$

$$\tag{7.137}$$

Now, in order to derive the eigenvalues λ_{23} for this case, we denote as $\tilde{\mathbf{v}}_{\mathbf{k}}^{23}$ the nonzero component of the vector $\tilde{\mathbf{V}}_{\mathbf{k}}^{23}$ (from Eq. (7.127)):

$$\tilde{\mathbf{v}}_{\mathbf{k}}^{\mathbf{23}} = \begin{pmatrix} \mathbf{k} \times (\mathbf{k} \times \mathbf{t}_{\mathbf{k}})\,\mathbf{k} \\ \mathbf{k} \times (\mathbf{k} \times \mathbf{k} \cdot \overline{\mathbf{Q}}_{\mathbf{k}}^{(2)})\,\mathbf{k} \\ \mathbf{k} \times (\mathbf{k} \times \overline{\mathbf{Q}}_{\mathbf{k}}^{(\mathbf{2})}) \end{pmatrix} \tag{7.138}$$

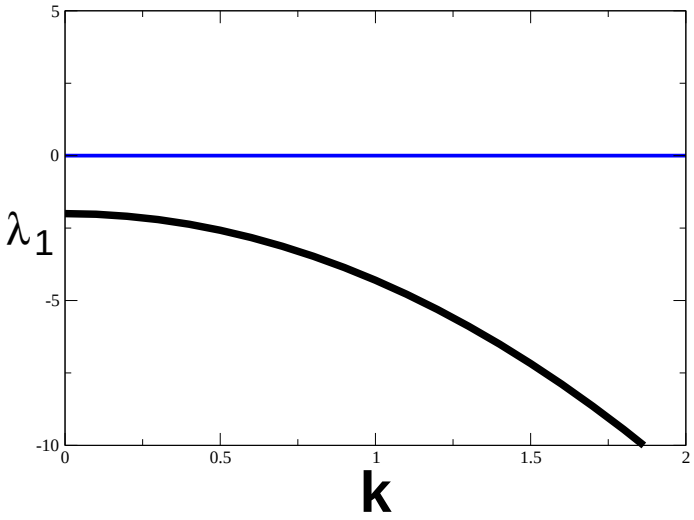

(a) $\rho_0 < \rho_c$

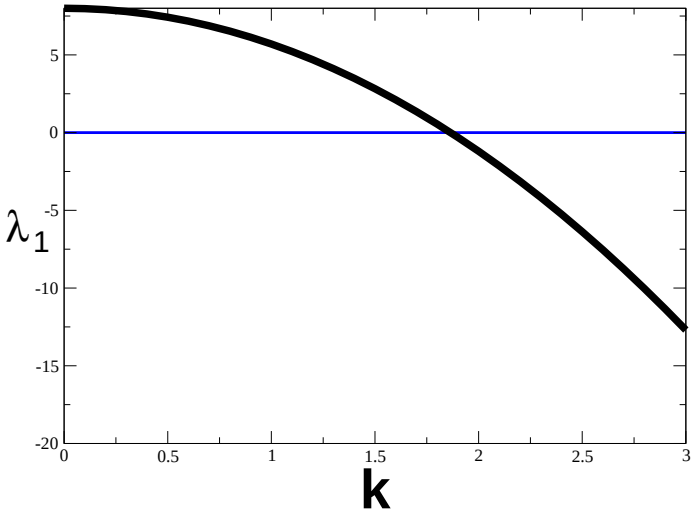

(b) $\rho_0 > \rho_c$

Figure 7.4: *Isotropic-nematic* instabilities. This instability is driven by hard core interaction only, and motors play no role.

Using this notation, we can rewrite the eigenvalue problem as:

$$\lambda\,\tilde{\mathbf{v}}^{\mathbf{23}}_{\mathbf{k}} = \begin{pmatrix} D_{11} - D^0_{11}\,k^2 & iA_{12} & 0 \\ iA_{21}\,k^2 & D_{22} - (D^0_{22} + D^1_{22})\,k^2 & 0 \\ i\,A_{21} & -D^1_{22} & D_{22} - D^0_{22}\,k^2 \end{pmatrix} \tilde{\mathbf{v}}^{\mathbf{23}}_{\mathbf{k}} \tag{7.139}$$

One eigenvalue of this problem is

$$\lambda_1 = D_{22} - D^0_{22}\,k^2,$$

which corresponds to the isotropic-nematic instability, as we have seen in the previous section. The other two eigenvalues are given by the equation:

$$\det \begin{Vmatrix} D_{11} - D^0_{11}\,k^2 - \lambda & iA_{12} \\ iA_{21}\,k^2 & D_{22} - (D^0_{22} + D^1_{22})\,k^2 - \lambda \end{Vmatrix} = 0 \tag{7.140}$$

The solutions of this equation are:

$$\begin{aligned} \lambda_{2,3} &= \frac{1}{2} D_{11} + D_{22} - (D^0_{11} + D^0_{22} + D^1_{22})\,k^2 \\ &\pm \frac{1}{2}\sqrt{-4\,A_{12}\,A_{21}\,k^2 + \left(D_{11} - D_{22} + (-D^0_{11} + D^0_{22} + D^1_{22})\,k^2\right)^2} \end{aligned} \tag{7.141}$$

Density homogeneous instabilities: small k limit.

We consider λ_2 as the largest of the eigenvalues from Eq. (7.141). In the limit of large wavelengths we have:

$$\lambda_2 = \frac{D_{11} + D_{22} + |D_{11} - D_{22}|}{2} + \mathcal{O}(k^2) = \begin{cases} D_{11} + \mathcal{O}(k^2) & \text{for } D_{11} > D_{22} \\ D_{22} + \mathcal{O}(k^2) & \text{for } D_{11} < D_{22} \end{cases} \tag{7.142}$$

Because

$$D_{11} = -(d-1)\,D_R, \quad \text{and} \quad D_{22} = -2dD_R\left(1 - \frac{\gamma_0\,\rho_0}{d\,(d+2)}\right) \tag{7.143}$$

it is easy to see that λ_2 is becoming positive for $\rho > \rho_c$ (see also Fig 7.5).

Density homogeneous instabilities: large k limit.

Since the theory that we present is designed for large scales, it is necessary to make the consistency check that instabilities are not developing in the limit of small wavelengths, *i.e.* when $k \to \infty$. In this limit we have

$$\begin{aligned} \lambda_2 &\approx \frac{-(D^0_{11} + D^0_{22} + D^1_{22})k^2 + |\,-D^0_{11} + D^0_{22} + D^1_{22}|\,k^2}{2} \\ &= \frac{1}{2}\begin{cases} -2\,D^0_{11}\,k^2 & \text{for } D^0_{22} + D^1_{22} > D^0_{11} \\ -(D^0_{22} + D^1_{22})\,k^2 & \text{for } D^0_{22} + D^1_{22} > D^0_{11} \end{cases} \end{aligned} \tag{7.144}$$

The coefficients $D^0_{22},\ D^0_{11}$ and D^1_{22} are known to be positive, and it follows from the last relations that

$$\lambda_2 < 0 \quad \text{for large } k \tag{7.145}$$

Density homogeneous instabilities: finite wave length instability.

Since we know that in both limits of large and small k the eigenvalues are negative $\lambda_{2,3} < 0$, we investigate now if it is possible that at least one of them can become positive at some ***finite*** value of k. In order to check if one of these eigenvalues is changing the sign we have to study if the equation

$$\lambda_2 \, \lambda_3 = 0 \tag{7.146}$$

has *real* roots in k. We write the last equation in the following explicit form:

$$D_{11} \, D_{22} + (A_{12} \, A_{21} - D^0_{11} \, D_{22} - D_{11}(D^0_{22} + D^1_{22}))k^2 + D^0_{11}(D^0_{22} + D^1_{22})k^4 = 0 \tag{7.147}$$

We regard this equation as a quadratic equation in k^2. Its discriminant

$$\Delta = (A_{12} \, A_{21} - D^0_{11} \, D_{22} - D_{11}(D^0_{22} + D^1_{22}))^2 - 4 \, D_{11} \, D_{22} \, D^0_{11}(D^0_{22} + D^1_{22}) \tag{7.148}$$

has to be necessarily positive if the k^2 roots are real. The Viète relations can predict the signs of the roots, in the case that these are real:

$$\begin{aligned} k_1^2 + k_2^2 &= -\frac{A_{12} \, A_{21} - D^0_{11} \, D_{22} - D_{11}(D^0_{22} + D^1_{22})}{D^0_{11}(D^0_{22} + D^1_{22})} \\ k_1^2 \, k_2^2 &= \frac{D_{11} \, D_{22}}{D^0_{11}(D^0_{22} + D^1_{22})} \end{aligned} \tag{7.149}$$

The discriminant Δ and the sum $k_1^2 + k_2^2$ are larger than zero if the absolute value of the product $A_{12} \, A_{21}$ is larger than a certain critical value, which depends on the other coefficients. This implies that there is required a certain strength for the motors in order to trigger instabilities. From Viète relations, we see that the sum and the product of the roots are positive, which means finite wave length instability. For densities larger than the nematic densities, $\rho_0 > \rho_c$, the roots $k^2_{1,2}$ are both real but of opposite signs, which means that *only* one of them, k_1 or k_2 must imaginary. However, the other root is real. This discussion is summarized in Fig. 7.5, where we exemplify our results with numerical values for all the parameters that are involved.

Finally, we stress that, based on the sign analysis of the D's and A's coefficients, the eigenvalues $\lambda_{2,3}$ are both real, and therefore no Hopf bifurcations are expected.

7.4.6 Instabilities towards Inhomogeneous States

We compute now the eigenvalues that correspond to the matrix M^1_k from Eq. (7.123). The matrix M^1_k is a block matrix inside the matrix M_k from Section 7.4.2. The eigenvectors, which correspond to the general eigenvalue problem Eq. (7.120), have the form

$$\tilde{\mathbf{V}}^{456}_{\mathbf{k}} = \begin{pmatrix} (\mathbf{k}\,\mathbf{k} - \mathbf{I}^{(\mathbf{2})}) \, \rho_{\mathbf{k}} \\ (\mathbf{k}\,\mathbf{k} - \mathbf{I}^{(\mathbf{2})}) \, \mathbf{t}_k \cdot \mathbf{k} \\ (\mathbf{k}\,\mathbf{k} - \mathbf{I}^{(\mathbf{2})}) \, \mathbf{k}\,\mathbf{k} : \overline{\mathbf{Q}}^{(2)}_{\mathbf{k}} \\ 0 \\ 0 \\ \mathbf{k} \times (\mathbf{k} \times \overline{\mathbf{Q}}^{(\mathbf{2})}_{\mathbf{k}}) \, \mathbf{k} \end{pmatrix} \tag{7.150}$$

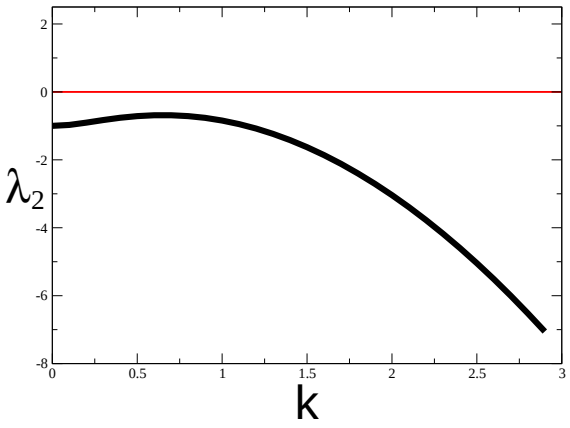

(a) $\rho_0 < \rho_c$, weak motors

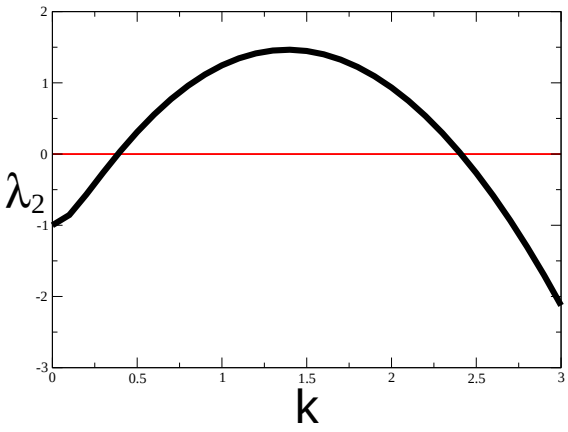

(b) $\rho_0 < \rho_c$, strong motors

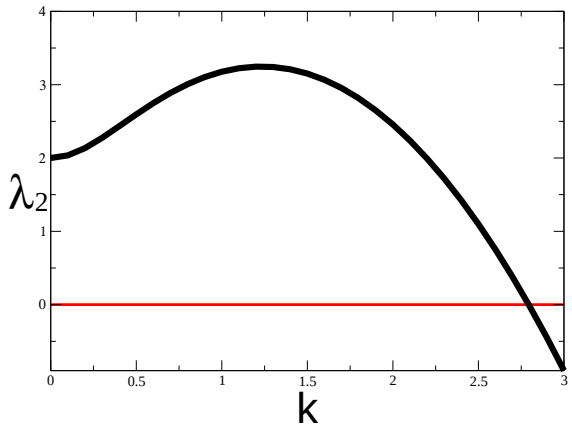

(c) $\rho_0 > \rho_c$

Figure 7.5: Homogeneous instabilities. For low density, (a) and (b), only strong motors can trigger an instability ($\lambda_2 > 0$). For large density, (c), instabilities are driven by hard core interaction and motors are not playing a significant role.

The two zero entries of this vector correspond to the equation:

$$\mathbf{k} \times \mathbf{t}_{\mathbf{k}} = 0 \tag{7.151}$$
$$\mathbf{k} \times \mathbf{k} \cdot \overline{\mathbf{Q}}^{(\mathbf{2})}_{\mathbf{k}} = 0 \tag{7.152}$$

If we make the inverse Fourier transform for the vector $\tilde{\mathbf{V}}^{456}_{\mathbf{k}}$, we have for the space representation

$$\boldsymbol{\nabla}_{\mathbf{r}}\, \rho \neq 0 \tag{7.153}$$
$$\boldsymbol{\nabla}_{\mathbf{r}} \cdot \mathbf{t} \neq 0 \tag{7.154}$$
$$\boldsymbol{\nabla}_{\mathbf{r}}\, \boldsymbol{\nabla}_{\mathbf{r}} : \overline{\mathbf{Q}}^{(2)} \neq 0 \tag{7.155}$$
$$\boldsymbol{\nabla}_{\mathbf{r}} \times \mathbf{t} = 0 \tag{7.156}$$
$$\boldsymbol{\nabla}_{\mathbf{r}} \times \boldsymbol{\nabla}_{\mathbf{r}} \cdot \overline{\mathbf{Q}}^{(\mathbf{2})} = 0 \tag{7.157}$$
$$\boldsymbol{\nabla}_{\mathbf{r}} \times \overline{\mathbf{Q}}^{(\mathbf{2})} \neq 0 \tag{7.158}$$
$$\tag{7.159}$$

Now, in order to derive the eigenvalues λ_{456} for this case, we denote as $\tilde{\mathbf{v}}^{456}_{\mathbf{k}}$ the nonzero component of the vector $\tilde{\mathbf{V}}^{456}_{\mathbf{k}}$ (from Eq. (7.150)):

$$\tilde{\mathbf{v}}^{\mathbf{456}}_{\mathbf{k}} = \begin{pmatrix} (\mathbf{k}\,\mathbf{k} - \mathbf{I}^{(\mathbf{2})})\, \rho_{\mathbf{k}} \\ (\mathbf{k}\,\mathbf{k} - \mathbf{I}^{(\mathbf{2})})\, \mathbf{t}_k \cdot \mathbf{k} \\ (\mathbf{k}\,\mathbf{k} - \mathbf{I}^{(\mathbf{2})})\, \mathbf{k}\,\mathbf{k} : \overline{\mathbf{Q}}^{(2)}_{\mathbf{k}} \\ \mathbf{k} \times (\mathbf{k} \times \overline{\mathbf{Q}}^{(\mathbf{2})}_{\mathbf{k}}) \end{pmatrix} \tag{7.160}$$

Using this notation, we can rewrite the eigenvalue problem as:

$$\lambda\, \tilde{\mathbf{v}}^{\mathbf{456}}_{\mathbf{k}} = m^{456}_k\ \tilde{\mathbf{v}}^{\mathbf{456}}_{\mathbf{k}} \tag{7.161}$$

Where the matrix m^{456}_k is

$$\begin{pmatrix} -D_{00}\, k^2 & 0 & -D_{02} & 0 \\ i\, A_{10}\, k^2 & D_{11} - (D^0_{11} + D^1_{11})\, k^2 & i\, A_{12} & 0 \\ -D_{20}\big(1 - \frac{1}{d}\big)\, k^4 & 2\, i\, A_{21}\, \big(1 - \frac{1}{d}\big)\, k^2 & D_{22} - \Big(D^0_{22} + 2\, D^1_{22}\, \big(1 - \frac{1}{d}\big)\Big)\, k^2 & 0 \\ \frac{D_{20}}{d} k^2 & -2\, i\, \frac{A_{21}}{d} & 2\frac{D^1_{22}}{d} & D_{22} - D^0_{22}\, k^2 \end{pmatrix} \tag{7.162}$$

Again, one of the eigenvalues is $\lambda_1 = D_{22} - D^0_{22}\, k^2$, which corresponds to the isotropic-nematic instabilities, and we have discussed it Section 7.4.4.

The last three eigenvalues to be determined, $\lambda_{4,5,6}$, are the eigenvalues of the matrix M_1 from

Eq. (7.123):

$$\det\left\|\begin{array}{ccc} -D_{00}\,k^2-\lambda & 0 & -D_{02} \\ i\,A_{10}\,k^2 & D_{11}-(D_{11}^0+D_{11}^1)\,k^2-\lambda & i\,A_{12} \\ -D_{20}\big(1-\frac{1}{d}\big)\,k^4 & 2\,i\,A_{21}\,\big(1-\frac{1}{d}\big)\,k^2 & D_{22}-\Big(D_{22}^0+2\,D_{22}^1\,\big(1-\frac{1}{d}\big)\Big)\,k^2-\lambda \end{array}\right\| = 0 \tag{7.163}$$

We can write this equation in a more explicit form:

$$\begin{aligned} &\left(D_{11} \;\; -(D_{11}^0+D_{11}^1)\,k^2-\lambda\right)\left(D_{00}\,k^2+\lambda\right)\left(D_{22}-\Big(D_{22}^0+2\,D_{22}^1\,\Big(1-\frac{1}{d}\Big)\Big)\,k^2-\lambda\right) \\ &\quad + \quad D_{02}\,D_{20}\,\Big(1-\frac{1}{d}\Big)\left(D_{11}-(D_{11}^0+D_{11}^1)\,k^2-\lambda\right)k^4 \\ &\quad + \quad 2\,A_{21}\,\Big(1-\frac{1}{d}\Big)\left(A_{12}(D_{00}\,k^2+\lambda)-D_{02}\,A_{10}\,k^2\right)=0 \end{aligned} \tag{7.164}$$

Density instabilities: the small k limit.

It is not difficult to derive the roots of the cubic equation in the limit of large wavelengths $k \to 0$:

$$\begin{cases} \lambda_4 = D_{11}-(D_{11}^0+D_{11}^1)\,k^2+\mathcal{O}(k^4) \\ \lambda_5 = -D_{00}\,k^2+\mathcal{O}(k^4) \\ \lambda_6 = D_{22}-\left(D_{22}^0+2D_{22}^1\Big(1-\frac{1}{d}\Big)\right)k^2+\mathcal{O}(k^4) \end{cases} \tag{7.165}$$

Since $D_{11} = -(d-1)\,D_R < 0$, $D_{00} > 0$, it follows that $\lambda_{45} < 0$. However, since $D_{22} = -2\,d\,D_R\,(1-\gamma_0\,\rho_0/d\,(d+2))$, it follows that $\lambda_6 < 0$ only for densities that are smaller than the critical density $\rho < \rho_c$ (see Fig. 7.6).

Density instabilities: the large k limit.

In this limit all the eigenvalues scale like k^2:

$$\lambda \approx \gamma\,k^2, \qquad k \to \infty \tag{7.166}$$

We take this form for the eigenvalues λ in order to insert it in Eq. (7.164). In doing this, we derive the following equation for γ:

$$(D_{11}^0+D_{11}^1+\gamma)\left((D_{00}+\gamma)\Big(D_{22}^0+2\,D_{22}^1\,\Big(1-\frac{1}{d}\Big)+\gamma\Big)-D_{02}\,D_{20}\,\Big(1-\frac{1}{d}\Big)\right)=0 \tag{7.167}$$

We can immediately see that one of the roots is $\gamma_4 = -(D_{11}^0+D_{11}^1)$, *i.e.*

$$\lambda_4 = -(D_{11}^0+D_{11}^1)\,k^2 < 0, \quad k \to \infty \tag{7.168}$$

This shows that the consistency condition of having no instability for small wavelengths for this eigenvalue is satisfied.

The other two γ roots satisfy the quadratic equation:

$$\begin{aligned} \gamma^2 &+ \gamma\left(D_{00} + D_{22}^0 + 2\,D_{22}^1\left(1-\frac{1}{d}\right)\right) \\ &+ D_{00}\left(D_{22}^0 + 2\,D_{22}^1\left(1-\frac{1}{d}\right)\right) - D_{02}\,D_{20}\left(1-\frac{1}{d}\right) = 0 \end{aligned} \tag{7.169}$$

The discriminant and Viète relations for the last equations are:

$$\begin{cases} \Delta &= \left(D_{00} - D_{22}^0 - 2\,D_{22}^1\left(1-\frac{1}{d}\right)\right)^2 + 4\,D_{02}\,D_{20}\left(1-\frac{1}{d}\right) \\ \gamma_5+\gamma_6 &= -\left(D_{00} + D_{22}^0 + 2\,D_{22}^1\left(1-\frac{1}{d}\right)\right) \\ \gamma_5\,\gamma_6 &= D_{00}\left(D_{22}^0 + 2\,D_{22}^1\left(1-\frac{1}{d}\right)\right) - D_{02}\,D_{20}\left(1-\frac{1}{d}\right) \end{cases} \tag{7.170}$$

Low Density $\rho_0 < \rho_c$. In this case we have $D_{02}\,D_{20} < 0$ and the roots can be either real or complex. In the case when the roots are real, their sum is negative and the product is positive, which means that $\gamma_{5,6} < 0$. In case that the roots are complex, they must be complex conjugate. More, their sum is negative, as we can see from the Viète relations. Since the real part of these roots is half of their sum, we have:

$$\mathcal{R}e(\lambda_{5,6}) = \mathcal{R}e(\gamma_{5,6})k^2 < 0, \;\; k \to \infty \tag{7.171}$$

High Density $\rho_0 > \rho_c$. Now $D_{02}\,D_{20} < 0$, *i.e.* $\Delta > 0$ and the roots are real. From Viète relations it follows that their sum is negative. If we use the explicit expressions for D coefficients, a little algebra can show that their product is positive.

$$\lambda_{5,6} = \gamma_{5,6}\,k^2 < 0, \;\; k \to \infty \tag{7.172}$$

Density instabilities: finite wave length instabilities and the case of strong motors

Since we know the asymptotic behavior in both large and small wavelength limits, we can extract some information about the intermediate wavelengths. For instance, when $\rho_0 < \rho_c$, all three roots are negative in both limits of long and short wavelengths. Using Viète relations for the product of all three roots of Eq. (7.164) we could identify the wavenumbers k for which this product is zero. At these specific wavenumber values, one of the eigenvalues is changing its sign, and we eventually have finite wavelength instabilities. The Viète relations for the product $\lambda_4\lambda_5\lambda_6$ is a quadratic equation in k^2 and it is relatively easy to determine the wavelengths at which instabilities may occur.

The equation $\lambda_4\lambda_5\lambda_6 = 0$ is equivalent to the following equation in k^2:

$$k^2\,(a\,k^4 + b\,k^2 + c) = 0 \tag{7.173}$$

The coefficients $a,\ b,\ c$ are given by:

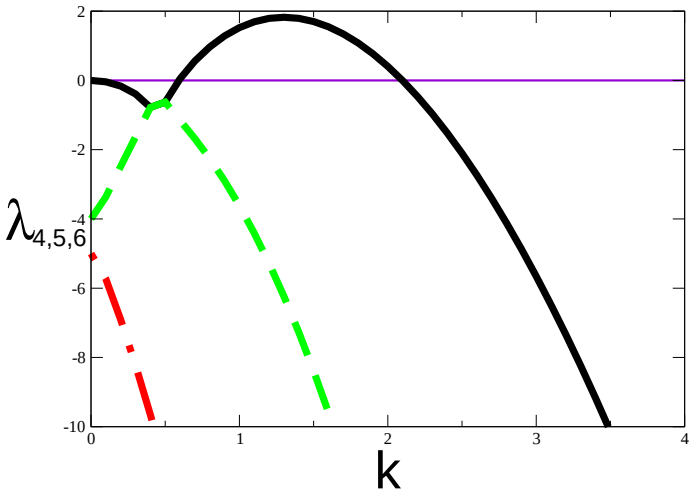

(a) $\rho_0 < \rho_c$, strong motors

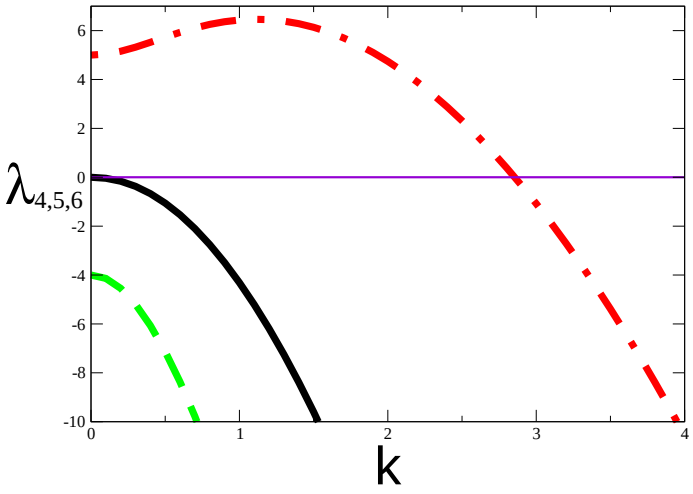

(b) $\rho_0 > \rho_c$

Figure 7.6: Density instabilities. In the limit of strong motors *only one* branch of the dispersion relation become unstable. Parameters: (a) $D_{00} = 5.0$, $D_{02} = 1.0$, $D_{20} = -5.0$, $D_{11} = -6.0$, $D_{22} = -9.0$, $D^0_{11} = 1.0$, $D^0_{22} = 7.0$, $A_{12} = -14.0$, $A_{21} = 14.0$, $D^1_{22} = 4.0$, $D^1_{11} = 0.5$, $A_{10} = -14.0$, $d = 3$; (b) $D_{00} = 4.0$, $D_{02} = -0.3$, $D_{20} = -6.0$, $D_{11} = -4.0$, $D_{22} = 5.0$, $D^0_{11} = 1.0$, $D^0_{22} = 7.0$, $A_{12} = -14.0$, $A_{21} = 6.0$, $D^1_{22} = 1.0$, $D^1_{11} = 0.5$, $A_{10} = -14.0$, $d = 3$. The numerical values for these parameters are consistent with their theoretical expressions that we have presented in Section 7.3.4.

$$\left\{\begin{array}{l} a = -\frac{1}{d}(D^0_{11}+D^1_{11})\Big((d-1)D_{02}\,D_{20} - D_{00}\Big(-2\,D^1_{22}+d(D^0_{22}+2\,D^1_{22})\Big)\Big) \\ b \;=\; 2\,A_{12}\,A_{21}D_{00}\left(1-\frac{1}{d}\right) - 2A_{10}\,A_{21}\,D_{02}\left(1-\frac{1}{d}\right) \\ \qquad +D_{02}\,D_{11}\,D_{20}\left(1-\frac{1}{d}\right) - 2\,D_{00}\,D_{11}\,D^1_{22}\left(1-\frac{1}{d}\right) \\ \qquad -D_{00}\Big(D_{11}\,D^0_{22} + D_{22}\,(D^0_{11}+D^1_{11})\Big) \\ c = D_{00}\,D_{11}\,D_{22} \end{array}\right. \tag{7.174}$$

Again, in the case of strong motors, *i.e.* the *active* products $A_{12}A_{21}$ and $A_{10}A_{21}$ are larger than a specific values, the discriminant $\Delta = \sqrt{b^2 - 4\,a\,c}$ is positive. It means that we have k^2 real roots.

Low Density: $\rho_0 < \rho_c$. In this case $a > 0,\ b < 0,\ c > 0$, which implies that

$$\left\{\begin{array}{lcl} k_1^2\,k_2^2 &=& \frac{c}{a} > 0 \\ k_1^2 + k_2^2 &=& -\frac{b}{a} > 0 \end{array}\right. \tag{7.175}$$

It means that both roots, $k_1^2,\ k_2^2$, are positive, *i.e.*, one branch of the dispersion relation is becoming positive at some $k_1 > 0$ value and then negative at another value $k_2 > k_1 > 0$.

High Density: $\rho_0 > \rho_c$. In this case we have $a > 0,\ b < 0,\ c < 0$, *i.e*:

$$\left\{\begin{array}{lcl} k_1^2\,k_2^2 &=& \frac{c}{a} < 0 \\ k_1^2 + k_2^2 &=& -\frac{b}{a} > 0 \end{array}\right. \tag{7.176}$$

It follows that in this case we have *only one* positive root, say k_1, which means that it must be the mechanical branch which is unstable at zero wavenumber, and is changing its sign at the value k_1 of the wavenumber. We exemplify our discussion in Fig. 7.6, where we use some specific numerical values for the coefficients, which are consistent with the full expressions that we have shown in Section 7.3.4.

7.5 Discussion and Open Questions

We have presented a microscopic model for active gels, which are made of stiff filaments that are cross linked by motor proteins. The first step, which is needed to understand how this system self-organize, and how large scale patterns could emerge, is to investigate how instabilities are driven by motors starting from a completely disordered system, *i.e.* a homogeneous and isotropic system.

We have considered in our analysis three competing types of dynamics. One is the ubiquitous Brownian dynamics, which tends to disorganize the system, the second corresponds to the excluded volume repulsion between the rods, and the last is the active dynamics that is imposed by the activity of the motor proteins.

We implement the microscopic description at hand at the level of mean field approach. We present this theory in the form of coupled differential equations for the moments of the one particle probability distribution function $\psi(\mathbf{r},\,\hat{\mathbf{u}},\,t)$. The corresponding moments of interest are the particle density $\rho(\mathbf{r},\,t)$, the polarization $\mathbf{t}(\mathbf{r},\,t)$, which describes the local average orientation, and the nematic order parameter $\overline{\mathbf{Q}}^{(2)}(\mathbf{r},\,t)$, which describes the local ordering of the filaments.

The linear stability analysis of this system gave both encouraging and consistent results. First of all, when all the motors are switched off, the only possibility is the isotropic-nematic instability as in liquid crystal systems. The critical density ρ_c for this transition scales with the inverse of the excluded volume of hard rods, Eq. (7.126), which is in perfect agreement with the Onsager theory for the entropic driven transitions in hard rod systems [73].

The main interesting result is the possibility of motor driven instabilities for particle densities that are below the isotropic-nematic critical value. This is a self consistent result of the theory that we present, because the instabilities and the phase diagram that we derive are valid in the limit of low densities. For example, we stress that in defining the active currents (see Section 7.3.3), we have approximated the 2-particle probability distribution by the product between two 1-particle probability distributions, which is valid only in dilute systems. The dilute limit of our system turns out to be very important in driving the instabilities. We can understand this by using the simple argument that, for filaments to get aligned by the motors, a low rotational drag could help the motors to do the job more efficiently. In contrast, in the opposite limit of high density, the system may be kinetically arrested and no ordering is possible, no matter how strong the motors are. In our theory, this argument is reflected by the negative signs of the active coefficients A_{12} and A_{10} (see Eq. (7.105) Section 7.3.4), since a different sign of these coefficients wipes out all the motor-driven instabilities that we have presented in this chapter.

Another aspect of the instabilities, which we have described, is that we need motors with a strength above a certain threshold in order to overcome the disorganizing effect of the diffusion. This adds neatly as a self-consistent aspect. However, a close look at the linear stability analysis shows that motors with relatively different strengths may drive different kinds of instabilities. To be more exact, our theory suggest that relatively weak motors can drive only instabilities with constant density, a kind of polarized nematic state, whereas stronger motors can drive density instabilities, which may correspond to aster, bundle, or even preprophase band formation. This is an interesting aspect, since we can suspect that in the case of higher plant cells a different regulation of motor protein activity may lead to completely different forms of microtubule self-organization, *e.g.* the transversal interphase array and the preprophase band at the onset of mitosis.

Appendix A: Technical Background

A.1 Moments of the Distribution Function

Let us consider elongated particles as being at the position $\mathbf{r}$, and having the orientation $\hat{\mathbf{u}}$ at a given moment of time t. We associate to these particles the *density distribution function* $\psi(\mathbf{r},\, \hat{\mathbf{u}},\, t)$, which fulfills the normalization condition:

$$\int d\mathbf{r} \int d\hat{\mathbf{u}}\, \psi(\mathbf{r},\, \hat{\mathbf{u}},\, t) = N \tag{7.177}$$

where N is the total number of particles in the system. For this function, we define its n-rank moment as

$$\mathbf{Q}^{(n)}(\mathbf{r},\, t) = \int d\hat{\mathbf{u}}\, \underbrace{\hat{\mathbf{u}} \ldots \hat{\mathbf{u}}}_{n\,\text{times}} \psi(\mathbf{r},\, \hat{\mathbf{u}},\, t) \tag{7.178}$$

The $zero$ and $first$ rank moments are the density distribution function $\rho(\mathbf{r},\, t)$, and the polarization $\mathbf{t}(\mathbf{r},\, t)$:

$$\left\{ \begin{array}{lcl} \mathbf{Q}^{(0)} & = & \rho(\mathbf{r},\, t) \\ \mathbf{Q}^{(1)} & = & \mathbf{t}(\mathbf{r},\, t) \end{array} \right. \tag{7.179}$$

For a complete description of our system we need more than two moments. For example, a system of antiparallel filaments gives zero polarization $\mathbf{t} = 0$, but the system is still orientationally ordered. Then, as we have seen in the previous chapter, the second rank moment is needed:

$$\mathbf{Q^{(2)}}(\mathbf{r},\, t) = \int d\hat{\mathbf{u}}\, \hat{\mathbf{u}}\hat{\mathbf{u}}\; \psi(\mathbf{r},\, \hat{\mathbf{u}},\, t) \tag{7.180}$$

The second moment $\mathbf{Q^{(2)}}(\mathbf{r},\, t)$ is a second rank tensor and it is used to describe the degree of ordering independent of the polarization. Since $\hat{\mathbf{u}}$ is a unit vector, it follows that the trace of the dyadic product $\hat{\mathbf{u}}\hat{\mathbf{u}}$ is

$$\mathrm{Tr}\, \hat{\mathbf{u}}\hat{\mathbf{u}} = \sum_{i=1,2,3} u_i^2 \equiv 1 \tag{7.181}$$

From this and from the definition of the moments, Eq. (7.180), it follows that:

$$\mathrm{Tr}\, \mathbf{Q^{(2)}}\,(\mathbf{r},\, t) = \rho(\mathbf{r},\, t) \tag{7.182}$$

This property is independent on the specific orientational density distribution $\psi(\mathbf{r}, \hat{\mathbf{u}},\, t)$. Because our aim is to define independent moments one can introduce the *traceless* tensor:

$$\overline{\mathbf{Q}}^{(2)}(\mathbf{r},\, t) = \int d\hat{\mathbf{u}}\, \psi(\mathbf{r}, \hat{\mathbf{u}},\, t)\, \left(\hat{\mathbf{u}}\hat{\mathbf{u}} - \frac{\mathbf{I}}{d}\right) \tag{7.183}$$

This is also known as the nematic order parameter. It is a *symmetric* and *traceless* tensor, and it is due to this property that it belongs to the class of *irreducible* tensors.

A.2 Irreducible Tensors

Definition 1 *An* irreducible Cartesian *tensor of rank n is any n-rank tensor $\overline{\mathbf{a}}^{(n)}$ that gives zero if it is* contracted *to δ_{ij}-Kronecker tensor (which is symmetric) and to Levi-Civita ϵ_{ijk} tensor (which is anti-symmetric):*

$$\begin{aligned} \delta_{\mu_i\mu_j}\, \overline{\mathrm{a}}^{(\mathrm{n})}_{\mu_1,\ldots,\mu_i,\ldots,\mu_j,\ldots\mu_n} &= 0 \\ \epsilon_{\mu\mu_k\mu_l}\, \overline{\mathrm{a}}^{(\mathrm{n})}_{\mu_1,\ldots,\mu_k,\ldots,\mu_l,\ldots\mu_n} &= 0 \end{aligned} \tag{7.184}$$

Notation 1 *In our notation, any irreducible tensor has an* over-bar *as* $\overline{\mathbf{a}}^{(\mathrm{n})}$.

The relations Eq. (7.184) show that it is not possible to get a non-zero lower rank tensor if contractions to Kronecker and Levi-Civita tensors are made.

An irreducible tensor of rank n has $2\,n + 1$ independent components, if it is associated to the $SO(3)$ symmetry group, and *only two* independent components in the case of the symmetry group $SO(2)$.

We stress that an arbitrary rank two tensor $\mathbf{a}$ is not irreducible unless it is symmetric and traceless. Any such tensor can be decomposed into a symmetric and antisymmetric part

$$\mathrm{a}_{\mu\,\nu} = \mathrm{a}^{sym}_{\mu\,\nu} + \mathrm{a}^{asym}_{\mu\,\nu}$$

where

$$\mathrm{a}^{sym}_{\mu\,\nu} = \frac{1}{2}(\mathrm{a}_{\mu\,\nu} + \mathrm{a}_{\nu\,\mu})$$

$$\mathrm{a}^{asym}_{\mu\,\nu} = \frac{1}{2}(\mathrm{a}_{\mu\,\nu} - \mathrm{a}_{\nu\,\mu})$$

The trace of the symmetric part $\mathbf{a}^{symm}$ can be subtracted and the result is an irreducible tensor $\bar{\mathbf{a}}$.

$$\bar{\mathbf{a}} = \mathbf{a}^{sym} - \mathbf{I}\,\frac{\mathrm{Tr}\,\mathbf{a}}{d}$$

One can guess and it can be shown (see [104]) that this operation can be generalized to any Cartesian tensor of any rank: if doing the corresponding symmetry operations one can extract the irreducible part $\bar{\mathbf{a}}_{\mu,\ldots\nu}$ from any given $\mathbf{a}_{\mu,\ldots\nu}$. According to this observation, the irreducible part of the dyadic product between two vectors $\mathbf{a}\,\mathbf{b}$ is:

$$\overline{\mathbf{a}\,\mathbf{b}} = \frac{1}{2}(\mathbf{a}\,\mathbf{b} + \mathbf{b}\,\mathbf{a}) - \frac{\mathbf{I}}{d}\,(\mathbf{a}\cdot\mathbf{b})$$

Notation 2 *Consider an arbitrary unit vector $\hat{\mathbf{u}}$ in either 2D or 3D case. We denote the irreducible part of the n-rank cartesian tensor $\underbrace{\hat{\mathbf{u}}\ldots\hat{\mathbf{u}}}_{n\,times}$ as*

$$\overline{\mathbf{T}}^{(n)}(\hat{\mathbf{u}}) = \overline{\underbrace{\hat{\mathbf{u}}\ldots\hat{\mathbf{u}}}_{n\,times}} \tag{7.185}$$

Theorem 2 . *For the irreducible tensor $\overline{\mathbf{T}}^{(l)}(\hat{\mathbf{u}})$ we have*

$$\begin{cases} \nabla^2_{\hat{\mathbf{u}}}\,\overline{\mathbf{T}}^{(l)}\,(\hat{\mathbf{u}}) = -l(l+1)\,\overline{\mathbf{T}}^{(l)}\,(\hat{\mathbf{u}}) & \text{for SO(3)}; \quad l = 0,\,1,\,2,\,\ldots \\ \nabla^2_{\hat{\mathbf{u}}}\,\overline{\mathbf{T}}^{(m)}\,(\hat{\mathbf{u}}) = -m^2\,\overline{\mathbf{T}}^{(m)}\,(\hat{\mathbf{u}}) & \text{for SO(2)}; \quad m = 0,\,1,\,2,\ldots \end{cases} \tag{7.186}$$

where $\hat{\mathbf{u}}$ denotes an arbitrary vector on the unit sphere.

Corollary 2 . *In the case of SO(3) symmetry group, the irreducible Cartesian tensor of rank l, $\overline{\mathbf{T}}^{(l)}(\hat{\mathbf{u}})$, is orthogonal to any of the spherical harmonics $Y_{l\,m}(\hat{\mathbf{u}})$:*

$$\left\langle \overline{\mathbf{T}}^{(l)}(\hat{\mathbf{u}}) | Y_{l'\,m}(\hat{\mathbf{u}}) \right\rangle = 0 \quad \text{for any } l \neq l' \tag{7.187}$$

where the *inner product* $\langle .|. \rangle$ between two functions $h_1(\hat{\mathbf{u}})$ and $h_2(\hat{\mathbf{u}})$ is defined as

$$\langle h_1(\hat{\mathbf{u}}) | h_2(\hat{\mathbf{u}}) \rangle = \int d\hat{\mathbf{u}}\, h_1^*(\hat{\mathbf{u}})\, h_2(\hat{\mathbf{u}}) \tag{7.188}$$

Proof: Because $\nabla^2_{\hat{\mathbf{u}}}$ is Hermitian:

$$\left\langle \nabla^2_{\hat{\mathbf{u}}} \overline{\mathbf{T}}^{(l)}(\hat{\mathbf{u}}) | Y_{l'm}(\hat{\mathbf{u}}) \right\rangle = \left\langle \overline{\mathbf{T}}^{(l)}(\hat{\mathbf{u}}) | \nabla^2_{\hat{\mathbf{u}}} Y_{l'm}(\hat{\mathbf{u}}) \right\rangle \tag{7.189}$$

It follows from Theorem 2:

$$-l(l+1)\left\langle \overline{\mathbf{T}}^{(l)}(\hat{\mathbf{u}}) | Y_{l'm}(\hat{\mathbf{u}}) \right\rangle = -l'(l'+1)\left\langle \overline{\mathbf{T}}^{(l)}(\hat{\mathbf{u}}) | Y_{l'm}(\hat{\mathbf{u}}) \right\rangle \tag{7.190}$$

or even more:

$$(l(l+1) - l'(l'+1))\left\langle \overline{\mathbf{T}}^{(l)}(\hat{\mathbf{u}}) | Y_{l'm}(\hat{\mathbf{u}}) \right\rangle = 0 \tag{7.191}$$

which proves the corollary.

Corollary 3 *In the case of SO(2) symmetry group, any irreducible Cartesian tensor of rank n,* $\overline{\mathbf{T}}^{(m)}(\hat{\mathbf{u}})$*, is orthogonal to any of the Fourier components* $e^{\pm i\, m'\, \theta}$*:*

$$\left\langle \overline{\mathbf{T}}^{(m)}(\hat{\mathbf{u}}) | e^{\pm i\, m'\, \theta} \right\rangle = 0 \quad \text{for any } m \neq m' \tag{7.192}$$

In the above relation, the unitary vector $\hat{\mathbf{u}}$ *is* $\hat{\mathbf{u}} = (\cos\theta,\, \sin\theta)$*, and* θ *is the 2D polar angle.*

In the case of 3D, a complete proof for Theorem 2 is given in Ref. [104]. The interesting property shown in Eq. (7.186) is that an irreducible Cartesian tensor can be regarded as an eigenvector of the total angular momentum operator $-\nabla^2_{\hat{\mathbf{u}}}$ and it gives the same set of eigenvalues as the spherical harmonics $Y_{l\,m}(\hat{\mathbf{u}})$:

$$\nabla^2_{\hat{\mathbf{u}}}\, Y_{l\,m}(\hat{\mathbf{u}}) = -l(l+1)\, Y_{l\,m}(\hat{\mathbf{u}}) \tag{7.193}$$

A.3 Expansion into Irreducible Tensor Series

Let us consider the 3D case. We can expand the probability distribution function into a series of spherical harmonics:

$$\psi\,(\mathbf{r},\hat{\mathbf{u}},\,t) = \sum_{l=0}^{\infty} \sum_{m=-l}^{l} c_{l\,m}(\mathbf{r},\,t)\, Y_{l\,m}(\hat{\mathbf{u}}) \tag{7.194}$$

The coefficients $c_{l\,m}$ are given by

$$c_{l\,m}(\mathbf{r},\,t) = \int d\hat{\mathbf{u}}\, Y^*_{l\,m}(\hat{\mathbf{u}})\, \psi\,(\mathbf{r},\hat{\mathbf{u}},\,t) \tag{7.195}$$

We define now the *irreducible moments* $\overline{\mathbf{Q}}^{(l)}(\mathbf{r})$ of this distribution

$$\overline{\mathbf{Q}}^{(l)}(\mathbf{r},\,t) = \int d\hat{\mathbf{u}}\, \psi(\mathbf{r},\,\hat{\mathbf{u}},\,t)\, \overline{\mathbf{T}}^{(l)}(\hat{\mathbf{u}}) \tag{7.196}$$

Given the Corollary 2 we have the expansion for the irreducible tensors

$$\overline{\mathbf{T}}^{(l)}(\hat{\mathbf{u}}) = \sum_{m=-l}^{l} \mathbf{t}^{(l)}_m\, Y_{l\,m}(\hat{\mathbf{u}}) \tag{7.197}$$

The tensor $\mathbf{t}^{(l)}_m$ is called the *spherical component of the irreducible tensor* $\overline{\mathbf{T}}^{(l)}(\hat{\mathbf{u}})$. The representation space for the irreducible representation can be changed to the one that is generated by the spherical components $\{\mathbf{t}^{(l)}_m\}_{m=-l,\ldots,l}$. The inner product over this space is defined as the full contractions between tensors. In this case, the spherical harmonics in Eq. (7.197) can be regarded as coefficients, which are given by

$$Y_{l\,m}(\hat{\mathbf{u}}) = \mathbf{t}^{*(l)}_m || \overline{\mathbf{T}}^{(l)}(\hat{\mathbf{u}}) \tag{7.198}$$

In the last equation we mean by $||$ the full tensorial contraction, and we denoted by $\mathbf{t}^{*(l)}_m$ as the complex conjugate of the spherical tensor $\mathbf{t}^{(l)}_m$. We introduce the expression Eq. (7.198) for the spherical harmonics into Eq. (7.195), and we obtain:

$$c_{l\,m}(\mathbf{r},\,t) = \int d\hat{\mathbf{u}}\, \mathbf{t}^{(l)}_m || \overline{\mathbf{T}}^{(l)}(\hat{\mathbf{u}})\, \psi\,(\mathbf{r},\hat{\mathbf{u}},\,t) \tag{7.199}$$

Now, given the definition Eq. (7.196) for the *irreducible* moments $\overline{\mathbf{Q}}^{(l)}(\mathbf{r})$, then we have from the last equation

$$c_{l\,m} = \mathbf{t}_m^{(l)} || \overline{\mathbf{Q}}^{(l)}(\mathbf{r}) \tag{7.200}$$

If we reintroduce this expression into Eq. (7.194), we obtain

$$\psi\left(\mathbf{r}, \hat{\mathbf{u}},\, t\right) = \sum_{l=0}^{\infty} \sum_{m=-l}^{l} \mathbf{t}_m^{(l)} || \overline{\mathbf{Q}}^{(l)}(\mathbf{r},\, t)\, Y_{l\,m}(\hat{\mathbf{u}}) \tag{7.201}$$

Finally, from Eq. (7.197), the last equation can be rewritten in the form

$$\psi(\mathbf{r},\, \hat{\mathbf{u}},\, t) = \sum_{l \geq 0} \overline{\mathbf{T}}^{(l)}(\hat{\mathbf{u}}) || \overline{\mathbf{Q}}^{(l)}(\mathbf{r},\, t) \tag{7.202}$$

This expression represents the expansion of the probability distribution function $\psi(\mathbf{r},\, \hat{\mathbf{u}})$ into a series of irreducible tensors $\overline{\mathbf{T}}^{(l)}(\hat{\mathbf{u}}) = \underbrace{\overline{\hat{\mathbf{u}} \ldots \hat{\mathbf{u}}}}_{l\,\text{times}}$. The coefficients of this series are the irreducible moments $\overline{\mathbf{Q}}^{(l)}(\mathbf{r},\, t)$, which are given by Eq. (7.196).

Bibliography

[1] Alberts B., A. Johnson, J. Lewis, M. Raff, K. Roberts, and P. Walter. *Molecular biology of the cell*. Garland Science, New York, 4th edition, 2002.

[2] Mitchison T. and Kirschner M. *Dynamic instability of microtubule growth.* Nature, **373**:161-164, 1984.

[3] Weisenberg R.C., W.J. Deery, and P.J. Dickinson. *Tubulin-nucleotide interactions during polymerization and depolymerization of microtubules*. Biochemistry, **15**:4248-54, 1976.

[4] Desai A. and T. J. Mitchison. *Microtubule polymerization dynamics*. Annual Review Of Cell And Developmental Biology, **13**:83-117, 1997.

[5] Arnal I., E. Karsenti, and A. A. Hyman. *Structural transitions at microtubule ends correlate with their dynamic properties in Xenopus egg extracts*. Journal Of Cell Biology, **149**:767-774, 2000.

[6] Tran P. T. and F. Chang. *Microtubule force production and nuclear positioning in the fission yeast cell*. Cell Motility And The Cytoskeleton **54**:189-189, 2003.

[7] Tran P. T., L. Marsh, V. Doye, S. Inoue, and F. Chang. *A mechanism for nuclear positioning in fission yeast based on microtubule pushing (vol 153, pg 397, 2001)*. Journal Of Cell Biology **153**:891-891, 2001.

[8] Holy T. E., M. Dogterom, B. Yurke, and S. Leibler. *Assembly and positioning of microtubule asters in microfabricated chambers*. Proceedings Of The National Academy Of Sciences Of The United States Of America **94**:6228-6231, 1997.

[9] Peskin C. S., G. M. Odell, and G. F. Oster. *Cellular motions and thermal fluctuations - the brownian ratchet*. Biophysical Journal, **65**:316-324, 1993.

[10] Chretien D., S. D. Fuller, and E. Karsenti. *Structure of growing microtubule ends: Two dimensional sheets close into tubes at variable rates*. Journal Of Cell Biology, **129**:1311-1328, 1995.

[11] Lauffenburger D. A. and A. F. Horwitz. *Cell migration: A physically integrated molecular process*. Cell, **84**:359-369, 1996.

[12] Cramer L. P., T. J. Mitchison, and J. A. Theriot. *Actin-dependent motile forces and cell motility*. Current Opinion In Cell Biology, **6**:82-86, 1994.

[13] Janmey P., Cunningham C., Oster G., and Stossel T. *Cytoskeletal networks and osmotic pressure in relation to cell structure and motility. Swelling Mechanics: From Clays to Living Cells and Tissues.* T. Karalis, editor. Springer-Verlag, Heidelberg, 1992.

[14] Miyamoto H. and Hotani H. *Polymerization of microtubules within liposomes produces morphological change in their shape.* Taniguchi International Symposium on Dynamics of Microtubules. H. Hotani, editor. The Taniguchi Foundation, Taniguchi, Japan. 220-242., 1998.

[15] Fygenson D. K., M. Elbaum, B. Shraiman, and A. Libchaber. *Microtubules and vesicles under controlled tension*. Physical Review E, **55**:850-859, 1997.

[16] Hill T. L. *Linear aggregation theory in cell biology.* Springer-Verlag, New York Berlin Heidelberg, 1987.

[17] Hill T. and Kirschner M. *Bioenergetics and kinetics of microtubule and actin filament assembly and dissasembly.* International Review of Cytology, **78**:1-125, 1982.

[18] Kramers H.A. *Brownian motion in a field of force and the diffusion model of chemical reactions*. Physica, **7**:284-304, 1940.

[19] Dogterom M. and B. Yurke. *Measurement of the force-velocity relation for growing microtubules*. Science, **278**:856-860, 1997.

[20] Janson M. E. and Dogterom M. *Scaling of microtubule force-velocity curves obtained at different tubulin concentration*. in press.

[21] Mogilner A. and Oster G. *Cell motility driven by actin polymerization.* Biophysical Journal, **71**:3030-3045, 1996.

[22] Mogilner A. and G. Oster. *The physics of lamellipodial protrusion*. European Biophysics Journal With Biophysics Letters, **25**:47-53, 1996.

[23] Mogilner A. and G. Oster. *The polymerization ratchet model explains the force-velocity relation for growing microtubules*. European Biophysics Journal With Biophysics Letters, **28**:235-242, 1999.

[24] Arfken B. George and Weber J. Hans. *Mathematical Methods for Physicists*. Academic Press, fourth edition, 1995.

[25] Murray R. Spiegel. *Laplace Transforms, Shaum's Outline Series.* McGraw-Hill Book Company, New York, 1965.

[26] Landau L.D. and Lifschitz E.M. *Theory of Elasticity*. Pergamon, New York, 1986.

[27] Inoue S. and E. D. Salmon. *Force generation by microtubule assembly disassembly in mitosis and related movements*. Molecular Biology Of The Cell, **6**:1619-1640, 1995.

[28] Tran P. T., L. Marsh, V. Doye, S. Inoue, and F. Chang. *A mechanism for nuclear positioning in fission yeast based on microtubule pushing*. Journal Of Cell Biology, **153**:397-411, 2001.

[29] Janson M.E. *Force Generation by Growing Microtubules*. Ph.D. Thesis, Amolf, Amsterdam, The Netherlands, 2002.

[30] Kolomeisky A. B. and M. E. Fisher. *Force-velocity relation for growing microtubules*. Biophysical Journal, **80**:149-154, 2001.

[31] Muller-Reichert T., D. Chretien, F. Severin, and A. A. Hyman. *Structural changes at microtubule ends accompanying GTP hydrolysis: Information from a slowly hydrolyzable analogue of GTP, guanylyl (alpha,beta)methylenediphosphonate*. Proceedings Of The National Academy Of Sciences Of The United States Of America, **95**:3661-3666, 1998.

[32] van Doorn G. S., C. Tanase, B. M. Mulder, and M. Dogterom. *On the stall force for growing microtubules*. European Biophysics Journal With Biophysics Letters, **29**:2-6, 2000.

[33] Janson M. E., M. E. de Dood, and M. Dogterom. *Dynamic instability of microtubules is regulated by force*. Journal Of Cell Biology, **161**:1029-1034, 2003.

[34] Walker R. A., E. T. Obrien, N. K. Pryer, M. F. Soboeiro, W. A. Voter, H. P. Erickson, and E. D. Salmon. *Dynamic instability of individual microtubules analyzed by video light-microscopy - rate constants and transition frequencies*. Journal Of Cell Biology, **107**:1437-1448, 1988.

[35] Drechsel D. N., A. A. Hyman, M. H. Cobb, and M. W. Kirschner. *Modulation of the dynamic instability of tubulin assembly by the microtubule-associated protein tau*. Molecular Biology Of The Cell, **3**:1141-1154, 1992.

[36] VanBuren V., D. J. Odde, and L. Cassimeris. *Estimates of lateral and longitudinal bond energies within the microtubule lattice*. Proceedings Of The National Academy Of Sciences Of The United States Of America, **99**:6035-6040, 2002.

[37] Walker R. A., N. K. Pryer, and E. D. Salmon. *Dilution of individual microtubules observed in real-time invitro - evidence that cap size is small and independent of elongation rate*. Journal Of Cell Biology, **114**:73-81, 1991.

[38] Walker R. A., S. Inoue, and E. D. Salmon. *Asymmetric behavior of severed microtubule ends after ultraviolet microbeam irradiation of individual microtubules invitro*. Journal Of Cell Biology, **108**:931-937, 1989.

[39] Cyr R. J. and B. A. Palevitz. *Organization of cortical microtubules in plant-cells*. Current Opinion In Cell Biology, **7**:65-71, 1995.

[40] Wasteneys G. O. *Microtubule organization in the green kingdom: chaos or self-order?* Journal Of Cell Science, **115**:1345-1354, 2002.

[41] Sonobe S. *Cell model systems in plant cytoskeleton studies*. International Review Of Cytology - A Survey Of Cell Biology, Vol 175, **175**:1-27, 1997.

[42] Mineyuki Y. *The preprophase band of microtubules: Its function as a cytokinetic apparatus in higher plants*. International Review Of Cytology - A Survey Of Cell Biology, Vol 187, **187**:1-49, 1999.

[43] Vos J. W., M. Dogterom, and A. M. C. Emons. *Microtubules become more dynamic but not shorter during preprophase band formation: a possible "search-and-capture" mechanism for microtubule translocation*. Cell Motility and the Cytoskeleton, **57:246-258**, 2004.

[44] Marc J., C. L. Granger, J. Brincat, D. D. Fisher, T. H. Kao, A. G. McCubbin, and R. J. Cyr. *A GFP-MAP4 reporter gene for visualizing cortical microtubule rearrangements in living epidermal cells*. Plant Cell, **10**:1927-1939, 1998.

[45] McCurdy D. W. and B. E. S. Gunning. *Reorganization of cortical actin microfilaments and microtubules at preprophase and mitosis in wheat root-tip cells - a double label immunofluorescence study*. Cell Motility And The Cytoskeleton, **15**:76-87, 1990.

[46] Granger C. L. and R. J. Cyr. *Microtubule reorganization in tobacco BY-2 cells stably expressing GFP-MBD*. Planta, **210**:502-509, 2000.

[47] Granger C. L. and R. J. Cyr. *Use of abnormal preprophase bands to decipher division plane determination*. Journal Of Cell Science, **114**:599-607, 2001.

[48] Mineyuki Y., J. Marc, and B. A. Palevitz. *Relationship between the preprophase band, nucleus and spindle in dividing allium cotyledon cells*. Journal Of Plant Physiology, **138**:640-649, 1991.

[49] Gimenez-Abian M. I., L. Utrilla, J. L. Canovas, G. Gimenez-Martin, M. H. Navarrete, and C. De la Torre. *The positional control of mitosis and cytokinesis in higher-plant cells*. Planta, **204**:37-43, 1998.

[50] Molchan T. M., A. H. Valster, and P. K. Hepler. *Actomyosin promotes cell plate alignment and late lateral expansion in Tradescantia stamen hair cells*. Planta, **214**:683-693, 2002.

[51] Sugimoto K., R. E. Williamson, and G. O. Wasteneys. *Wall architecture in the cellulose-deficient rsw1 mutant of Arabidopsis thaliana: microfibrils but not microtubules lose their transverse alignment before microfibrils become unrecognizable in the mitotic and elongation zones of roots*. Protoplasma, **215**:172-183, 2001.

[52] Sugimoto K., R. E. Williamson, and G. O. Wasteneys. *New techniques enable comparative analysis of microtubule orientation, wall texture, and growth rate in intact roots of Arabidopsis*. Plant Physiology, **124**:1493-1506, 2000.

[53] Emons A. M. C. and B. M. Mulder. *How the deposition of cellulose microfibrils builds cell wall architecture*. Trends In Plant Science, **5**:35-40, 2000.

[54] Mulder B. M. and A. M. C. Emons. *A dynamical model for plant cell wall architecture formation*. Journal Of Mathematical Biology, **42**:261-289, 2001.

[55] Emons A. M. C. and B. M. Mulder. *The making of the architecture of the plant cell wall: How cells exploit geometry*. Proceedings Of The National Academy Of Sciences Of The United States Of America, **95**:7215-7219, 1998.

[56] Emons A. M. C., J. H. N. Schel, and B. M. Mulder. *The geometrical model for microfibril deposition and the influence of the cell wall matrix*. Plant Biology, **4**:22-26, 2002.

[57] Fischer K. and P. Schopfer. *Physical strain-mediated microtubule reorientation in the epidermis of gravitropically or phototropically stimulated maize coleoptiles*. Plant Journal, **15**:119-123, 1998.

[58] Fischer K. and P. Schopfer. *Interaction of auxin, light, and mechanical stress in orienting microtubules in relation to tropic curvature in the epidermis of maize coleoptiles*. Protoplasma, **196**:108-116, 1997.

[59] Hush J. M. and L. Overall. *Cortical microtubule reorientation in higher plants: Dynamics and regulation*. Journal Of Microscopy-Oxford, **181**:129-139, 1996.

[60] Zandomeni K. and P. Schopfer. *Mechanosensory microtubule reorientation in the epidermis of maize coleoptiles subjected to bending stress*. Protoplasma, **182**:96-101, 1994.

[61] Zandomeni K. and P. Schopfer. *Reorientation of microtubules at the outer epidermal wall of maize coleoptiles by phytochrome, blue-light photoreceptor, and auxin*. Protoplasma, **173**:103-112, 1993.

[62] Yuan M., P. J. Shaw, R. M. Warn, and C. W. Lloyd. *Dynamic reorientation of cortical microtubules, from transverse to longitudinal, in living plant-cells*. Proceedings Of The National Academy Of Sciences Of The United States Of America, **91**:6050-6053, 1994.

[63] Panteris E., P. Apostolakos, and B. Galatis. *The effect of taxol on triticum preprophase root-cells - preprophase microtubule band organization seems to depend on new microtubule assembly*. Protoplasma, **186**:72-78, 1995.

[64] Dhonukshe P. and T. W. J. Gadella. *Alteration of microtubule dynamic instability during preprophase band formation revealed by yellow fluorescent protein-CLIP170 microtubule plus-end labeling*. Plant Cell, **15**:597-611, 2003.

[65] Whittington A. T., O. Vugrek, K. J. Wei, N. G. Hasenbein, K. Sugimoto, M. C. Rashbrooke, and G. O. Wasteneys. *MOR1 is essential for organizing cortical microtubules in plants*. Nature, **411**:610-613, 2001.

[66] Stoppin V., A. M. Lambert, and M. Vantard. *Plant microtubule-associated proteins (MAPs) affect microtubule nucleation and growth at plant nuclei and mammalian centrosomes*. European Journal Of Cell Biology, **69**:11-23, 1996.

[67] Jiang C. J. and S. Sonobe. *Identification and preliminary characterization of a 65-kda higher-plant microtubule-associated protein*. Journal Of Cell Science, **105**:891-901, 1993.

[68] Chan J., C. G. Jensen, L. C. W. Jensen, M. Bush, and C. W. Lloyd. *The 65-kDa carrot microtubule-associated protein forms regularly arranged filamentous cross-bridges between microtubules*. Proceedings Of The National Academy Of Sciences Of The United States Of America, **96**:14931-14936, 1999.

[69] Rutten T., J. Chan, and C. W. Lloyd. *A 60-kDa plant microtubule-associated protein promotes the growth and stabilization of neurotubules in vitro*. Proceedings Of The National Academy Of Sciences Of The United States Of America, **94**:4469-4474, 1997.

[70] Chan J., G. M. Calder, J. H. Doonan, and C. W. Lloyd. *EB1 reveals mobile microtubule nucleation sites in Arabidopsis*. Nature Cell Biology, **5**:967-971, 2003.

[71] Eleftheriou E. P. and B. A. Palevitz. *The effect of cytochalasin-d on preprophase band organization in root-tip cells of allium*. Journal Of Cell Science, **103**:989-998, 1992.

[72] Hitt A. L., A. R. Cross, and R. C. Williams. *Microtubule solutions display nematic liquid-crystalline structure*. Journal Of Biological Chemistry, **265**:1639-1647, 1990.

[73] Onsager L. *The effects of shape on the interaction of colloidal particles*. Ann. N.Y. Acad. Sci., **51**:627, 1949.

[74] Lagomarsino M. C., M. Dogterom, and M. Dijkstra. *Isotropic-nematic transition of long, thin, hard spherocylinders confined in a quasi-two-dimensional planar geometry*. Journal Of Chemical Physics, **119**:3535-3540, 2003.

[75] Chaikin P. M. and T. C. Lubensky. *Principles of condensed matter physics*. Cambridge, 1995.

[76] Shaw S. L., R. Kamyar, and D. W. Ehrhardt. *Sustained microtubule treadmilling in Arabidopsis cortical arrays*. Science, **300**:1715-1718, 2003.

[77] Marco Cosentino Lagomarsino. *Biologically inspired problems concerning semiflexible filaments*. PhD thesis, AMOLF, Amsterdam, 2004.

[78] Lloyd C. W. and R. W. Seagull. *A new spring for plant cell biology: microtubules as dynamic helices*. Trend in Biochemical Sciences, **10**:476-478, 1985.

[79] Lloyd C. W. *Helical microtubular arrays in onion root hairs*. Nature, **305**:311-313, 1983.

[80] Lloyd C. W. *Toward a dynamic helical model for the influence of microtubules on wall patterns in plants*. International Review of Cytology, **86**, 1984.

[81] Lloyd C. and J. Chan. *Helical microtubules arrays and spiral growth*. The Plant Cell, **14**:2319-2324, 2002.

[82] Lloyd C. and P. Hussey. *Microtubule-associated proteins in plants - Why we need a map*. Nature Reviews Molecular Cell Biology, **2**:40-47, 2001.

[83] Nedelec F., T. Surrey, and E. Karsenti. *Self-organisation and forces in the microtubule cytoskeleton*. Current Opinion In Cell Biology, **15**:118-124, 2003.

[84] Nedelec F. J., T. Surrey, A. C. Maggs, and S. Leibler. *Self-organization of microtubules and motors*. Nature, **389**:305-308, 1997.

[85] Takiguchi K. *Heavy-meromyosin induces sliding movements between antiparallel actin-filaments*. Journal Of Biochemistry, **109**:520-527, 1991.

[86] Urrutia R., M. A. McNiven, J. P. Albanesi, D. B. Murphy, and B. Kachar. *Purified kinesin promotes vesicle motility and induces active sliding between microtubules invitro*. Proceedings Of The National Academy Of Sciences Of The United States Of America, **88**:6701-6705, 1991.

[87] Surrey T., F. Nedelec, S. Leibler, and E. Karsenti. *Physical properties determining self-organization of motors and microtubules*. Science, **292**:1167-1171, 2001.

[88] Surrey T., M. B. Elowitz, P. E. Wolf, F. Yang, F. Nedelec, K. Shokat, and S. Leibler. *Chromophore-assisted light inactivation and self-organization of microtubules and motors*. Proceedings Of The National Academy Of Sciences Of The United States Of America, **95**:4293-4298, 1998.

[89] Nedelec F. *Computer simulations reveal motor properties generating stable antiparallel microtubule interactions*. Journal Of Cell Biology, **158**:1005-1015, 2002.

[90] Nakazawa H. and K. Sekimoto. *Polarity sorting in a bundle of actin filaments by two-headed myosins*. Journal Of The Physical Society Of Japan, **65**:2404-2407, 1996.

[91] Kruse K., A. Zumdieck, and F. Julicher. *Continuum theory of contractile fibres*. Europhysics Letters, **64**:716-722, 2003.

[92] Kruse K., S. Camalet, and F. Julicher. *Self-propagating patterns in active filament bundles*. Physical Review Letters, **87**:138101, 2001.

[93] Kruse K. and F. Julicher. *Actively contracting bundles of polar filaments*. Physical Review Letters, **85**:1778-1781, 2000.

[94] Lee H. Y. and M. Kardar. *Macroscopic equations for pattern formation in mixtures of microtubules and molecular motors*. Physical Review E, **64**:056113, 2001.

[95] Bassetti B., M. C. Lagomarsino, and P. Jona. *A model for the self-organization of microtubules driven by molecular motors*. European Physical Journal B, **15**:483-492, 2000.

[96] Kim J., Y. Park, B. Kahng, and H. Y. Lee. *Self-organized patterns in mixtures of microtubules and motor proteins*. Journal Of The Korean Physical Society, **42**:162-166, 2003.

[97] Kruse K., J. F. Joanny, F. Julicher, J. Prost, and K. Sekimoto. *Asters, vortices, and rotating spirals in active gels of polar filaments*. Physical Review Letters, **92**:, 2004.

[98] Cross M. C. and P. C. Hohenberg. *Pattern-formation outside of equilibrium*. Reviews Of Modern Physics, **65**:851-1112, 1993.

[99] Doi M. and S.F. Edwards. *The Theory of Polymer Dynamics*. Oxford, 1986.

[100] Dhont J.K.G. *An Introduction to Dynamics of Colloids*. Elsevier, 1996.

[101] Liverpool T. B. and M. C. Marchetti. *Instabilities of isotropic solutions of active polar filaments*. Physical Review Letters, **90**:, 2003.

[102] Howard J. *Mechanics of Motor Proteins and the Cytoskeleton*. Sinauer, 2000.

[103] Kruse K. and F. Julicher. *Self-organization and mechanical properties of active filament bundles*. Physical Review E, **67**:051913, 2003.

[104] Hess S. and W. Köler. *Formeln Zur Tensor-Rechnung*. Palm & Enke Erlangen, 1980.

[105] Gradshteyn I.S. and I.M. Ryzhik. *Tables of Integrals Series, and Products*. Academic Press, Inc., fifth edition, 1994.

[106] Kruse K. and K. Sekimoto. *Growth of fingerlike protrusions driven by molecular motors*. Physical Review E, **66**:, 2002.

[107] Kruse K. *A dynamic model for determining the middle of Escherichia coli*. Biophysical Journal, **82**:618-627, 2002.

[108] Nedelec F., T. Surrey, and A. C. Maggs. *Dynamic concentration of motors in microtubule arrays*. Physical Review Letters, **86**:3192-3195, 2001.

[109] Lloyd C. and J. Chan. *Helical microtubule arrays and spiral growth*. Plant Cell, **14**:2319-2324, 2002.

[110] Azimzadeh J., J. Traas, and M. Pastuglia. *Molecular aspects of microtubule dynamics in plants*. Current Opinion In Plant Biology, **4**:513-519, 2001.

[111] Wasteneys G. O. *The cytoskeleton and growth polarity*. Current Opinion In Plant Biology, **3**:503-511, 2000.

[112] Papaseit C., N. Pochon, and J. Tabony. *Microtubule self-organization is gravity-dependent*. Proceedings Of The National Academy Of Sciences Of The United States Of America, **97**:8364-8368, 2000.

[113] Lloyd C. *How I learned to love carrots: the role of the cytoskeleton in shaping plant cells*. Bioessays, **21**:1061-1068, 1999.

[114] Genre A. and P. Bonfante. *Cytoskeleton-related proteins in tobacco mycorrhizal cells: gamma-tubulin and clathrin localisation*. European Journal Of Histochemistry, **43**:105-111, 1999.

[115] Genre A. and P. Bonfante. *A mycorrhizal fungus changes microtubule orientation in tobacco root cells*. Protoplasma, **199**:30-38, 1997.

[116] Tabony J. *Morphological bifurcations involving reaction-diffusion processes during microtubule formation*. Science, **264**:245-248, 1994.

[117] Tabony J. and D. Job. *Gravitational symmetry-breaking in microtubular dissipative structures*. Proceedings Of The National Academy Of Sciences Of The United States Of America, **89**:6948-6952, 1992.

[118] Asada T., S. Sonobe, and H. Shibaoka. *Microtubule translocation in the cytokinetic apparatus of cultured tobacco cells*. Nature, **350**:238-241, 1991.

[119] Hasezawa S., J. Marc, and B. A. Palevitz. *Microtubule reorganization during the cell-cycle in synchronized by-2 tobacco suspensions*. Cell Motility And The Cytoskeleton, **18**:94-106, 1991.

[120] Mineyuki Y. and B. A. Palevitz. *Relationship between preprophase band organization, f-actin and the division site in allium - fluorescence and morphometric studies on cytochalasin-treated cells*. Journal Of Cell Science, **97**:283-295, 1990.

[121] Dhonukshe P., A. M. Laxalt, J. Goedhart, T. W. J. Gadella, and T. Munnik. *Phospholipase D activation correlates with microtubule reorganization in living plant cells*. Plant Cell, **15**:2666-2679, 2003.

[122] Liu B., J. Marc, H. C. Joshi, and B. A. Palevitz. *A gamma-tubulin-related protein associated with the microtubule arrays of higher-plants in a cell cycle-dependent manner*. Journal Of Cell Science, **104**:1217-1228, 1993.

Summary

Biological systems are complex heterogeneous and far from equilibrium systems. The fundamental questions posed by the *physics* of such systems are what the force generation mechanisms are, and how energy is processed and distributed among the components inside them. In answering these questions we can understand how motion is generated and how the system is organized, which means a significant step toward grasping these systems in their full complexity. A systematic program means first the identification of the components, and studying its properties and interplay with other components. How these components integrates into a higher level of organization, comes as a secondary step.

The cytoskeleton is a key ingredient of the living cell. The cytoskeleton is a complex of biopolymers which self-assembles and organize inside the living cells. There are many important functions that cytoskeleton fulfills. One is to give shape and rigidity to the cell, another is that cytoskeletal biopolymers serves as tracks for material transport across the cell. The examples could continue with the locomotion of cell, which is possible only due to the rearrangement of the cytoskeleton.

This thesis is concerned with the physical aspects of microtubules, which represent a part of the cytoskeleton. Microtubules are tubular protein aggregates, which are particularly stiff. These biopolymers were originally discovered as the scaffold of the mitotic spindle, which is the cell division apparatus that separates the genetic material among the daughter cells. An important property of microtubules is the alternation between growing and shrinking states, a behavior which is termed as *dynamic instability* and make microtubules unique in the realm of polymers. It is precisely this property that makes possible for microtubules to be involved in multi scale dynamics, *i.e.* assembly-disassembly and organization.

In making the time scale separation, some particular aspects of microtubule assembly and organization are presented and analyzed in two different parts of this thesis. The attention is focused on growing microtubules only, *i.e.* the dynamic instability does not play any role in the processes that are considered.

In the first part of this thesis, it is investigated in detail the microtubule force production mechanism during self-assembly. In general, any polymer can generate force during polymerization. If the seed of the polymer is fixed, then polymer can push against an arbitrary object, if the insertion of subunits are allowed due to gap opening between the tip of the polymer and the corresponding object. The required gap openings are possible due to the thermal fluctuations, and it is due to this reason that the object that generates force by exploiting the thermal fluctuations is called *Brownian ratchet*. This particular type of motor does not contradicts the second law of thermodynamics, which forbids work production in isothermal systems. The problem is avoided as the system is out of equilibrium. In our example of the polymerization ratchet, the dynamics is driven by the chemical polymerization energy, which is simply converted into work by the Brownian ratchet mechanism itself. Microtubules that work as Brownian ratchets can be regarded as a particular type of a *molecular (nano-)motor*.

In Chapter 3, the concept of Brownian ratchet is applied to microtubules. The main feature

which is incorporated to this concept is the collective character of the microtubule growth, since these polymers are composed of many filaments. One important question is to investigate what is the maximum force that this particular type of molecular motor can generate. A second question is to see how the velocity of growth depends on the opposing force that an external object can exert. Does the velocity of growth depend on the relative arrangements of microtubule protofilaments inside the assembly? In other words, given its internal structure is there a optimal way that the microtubule can grow under load condition? The way that the investigation is carried out is that the model details are extracted with the help of computer simulations, and compared directly with experimental data.

In Chapter 4, different regimes of microtubule growth are considered. Quantitative comparisons with available experimental data are successful in all cases, but a large number of free parameters justifies the need for different experiments. However, some qualitative aspects, such as the microtubule end structure can limit the number of possibilities, since end details were already observed in experiments. More exactly, cryo-electron microscope images show that microtubuls develop open sheets like structures at their end during growth. The disappearance of these structures is correlated in experiments with a hypothetical switch mechanism that triggers dynamic instabilities. Therefore, it appears natural to expect that a realistic growth model should reproduce such end structures. The model suggests that there is a sensitive relationship between the size of these structures and both the kinetic rates and the strength of the lateral bonds between protofilaments. Although the comparison with experiments is not fully quantitative, the analysis suggests that it is likely that the lateral bonding between the protofilaments is relatively week, *i.e.* a couple of thermal energies $k_B T$ per subunit.

In the second part of the thesis, I discuss some physical aspects regarding the organization of microtubules. In general, not referring only to microtubules, the importance of understanding the cytoskeleton organization is manifold. From physical point of view, the questions that are addressed in this thesis belong to the much broader context of pattern formation in far from equilibrium systems. Here, the fundamental problem is to find the relationship between the macroscopic properties of organized dissipative systems and their microscopic details that drive the system out of thermodynamic equilibrium. From the biological point of view, the investigation of the cytoskeleton organization is tightly related to understanding the biological functional role that different biopolymer arrangements assume in living cells.

In Chapter 5, the attention is focused on the microtubule organization in higher plant cells. Particularly, the microtubule arrangements that appear in interphase cells or prior to their division have received a lot of attention from biologists in the past, but still little is known about the driving organization mechanism. In interphase plant cells, the microtubules organize on the cortex of the cell in a parallel array, which is oriented transversely to the main axis of the cell. Just before the onset of the division, this array narrows to a preprophase band which marks on the cortex the location of the separation wall between the daughter cells. From physical point of view, in this chapter is addressed the question if it is possible that passive factors could be responsible for such organized arrays. One possibility in this respect is the nematic transition driven by excluded volume interaction, which is a well known phenomenology from the physics of liquid crystals. This implies a direct relationship between the degree of ordering and the density of microtubules. A second possibility is that bending elasticity of microtubules is the driving factor for organizing microtubules on the cortex. Since the bending elasticity is an intrinsic property of microtubules, the organization in this case can be termed more exactly as *self*-organization.

Active factors are the best candidates in driving large scale patterns in filamentous systems. In the past, the ability of motor proteins to organize filaments is demonstrated in both experiments

and computer simulations. However, understanding the phase diagram remains an open theoretical problem. Based on phase diagram analysis, a minimal set of conditions can be derived in order to reproduce a particular phenomenology. In the last two chapters, two different approaches are adopted. In Chapter 6, a mean field Landau type theory is developed. In this case, the phenomenology of filamentous systems is described with no reference to microscopic details and the basic constrains, which are imposed, are the symmetries that the physical system is supposed to fulfill. This generic method reproduce the possibility of a transverse stripe that closely resembles the preprophase band in plant cells. This encouraging result suggests that cytoskeletal array like those observed in plant cells can be described by a mean field theory.

In Chapter 7, a microscopic model is introduced, and based on this I derive the macroscopic evolution equations. The procedure is meant to meet the results that are derived in the generic approach, which is presented in Chapter 6. Besides the active components, I introduced also the passive interaction due to steric exclusion between filaments. The passive components alone are responsible for isotropic-nematic instabilities at high density, which drive the system to a liquid crystalline ordered phase. However, the active components can drive pattern formation in this system at densities that are below the critical value that corresponds to passive driven instabilities. The study in this chapter is limited at the level of linear stability analysis. However, the obtained results suggest that the stable arrays might be homogeneous nematic polar patterns, vortices, and asters. These features are consistent with the results obtained from other methods, like computer simulations or *in vitro* experiments, which are present in the literature. A full understanding of the emergent patterns requires the consideration of non-linear terms in evolution equations, which is the objective of future projects.

Samenvatting

Biologische systemen zijn complexe, heterogene systemen ver uit evenwicht. De fundamentele vragen die de fysica van deze systemen oproept zijn: wat is de aard van de mechanismen die krachten genereren en hoe wordt energie verwerkt en verdeelt binnen deze systemen. Door deze vragen te beantwoorden kunnen we begrijpen hoe beweging opgewekt wordt en hoe deze systemen zichzelf organiseren, en dus een grote stap maken in het doorgronden ervan in al hun complexiteit. Een systematisch programma van onderzoek begint met het identificeren van de componenten, hun eigenschappen en hun onderlinge interacties. Hoe deze componenten vervolgens integreren tot een hoger organisatienivo is een tweede stap.

Het cytoskelet is een van de belangrijkste onderdelen van de levende cel. Het is een complex van biopolymeren die zichzelf opbouwen en organiseren binnen de cel. Het cytoskelet vervult vele belangrijke taken. Een ervan is om vorm en stevigheid aan de cel te verlenen. Een ander is om als transportbanen te dienen voor het verplaatsen van stoffen binnen de cel. Ook cel-voortbeweging kan genoemd worden, iets dat mogelijk wordt gemaakt door de dynamische reorganisatie van de cytoskelet polymeren.

Dit proefschrift richt zich op de fysische eigenschappen van microtubuli, die een van de componenten van het cytoskelet vormen. Microtubuli zijn stijve buisvormige eiwit-aggregaten. Ze zijn oorspronkelijk ontdekt als het raamwerk van de zogenaamde kernspoel, het mechaniek dat het genetisch materiaal van de cell over de dochtercellen verdeelt bij de celdeling. Een belangrijke eigenschap van microtubuli is hun voortdurend “schakelen” tussen een groeiende en een krimpende toestand, een gedrag dat *dynamische instabiliteit* wordt genoemd en hun uniek maakt binnen het rijk der polymeren. Het is precies deze eigenschap die het mogelijk maakt dat microtubuli een rol spelen bij dynamica op verschillende tijd- en lengte schalen met name opbouw, afbraak en ruimtelijk organisatie.

Door een scheiding te maken tussen verschillende tijdschalen, kunnen de verschillende aspecten van de groei aan de ene kant en de ruimtelijke organisatie aan de andere kant in aparte delen van het proefschrift behandeld worden. We richten ons daarbij speciaal op groeiende microtubuli, m.a.w. we laten de dynamische instabiliteit buiten beschouwing in de processen die wij beschouwen.

In het eerste deel van het proefschrift onderzoeken wij in detail het mechanisme van krachtenproductie tijdens de groei van microtubuli. In principe kan ieder polymeer krachten opwekken tijdens polymerisatie. Als een uiteinde van het polymeer vast zit dan kan het andere uiteinde voortdurend tegen een ander microscopisch object aanduwen mits er zo nu en dan genoeg ruimte tussen polymeer-tip en object is dat nieuwe eenheden aan het polymeer gehecht kunnen worden. Deze openingen kunnen onstaan doordat zowel het polymeer als het object onderhevig zijn aan thermische fluctuaties. Een mechanisme dat op deze wijze krachten produceert met behulp van thermische fluctuaties wordt wel een “Browns palrad” genoemd (Engels: Brownian ratchet). Een dergelijke “motor” lijkt de tweede hoofdwet van de thermodynamica te schenden die verbied dat uit aan systeem bij een vaste temperatuur werk wordt onttrokken. Dit is hier echter geen beperking daar deze systemen buiten evenwicht zijn. In het voorbeeld van de polymerisatie “ratchet” wordt de

dynamica gevoed door de chemische energie die vrijkomt bij de polymerisatie en omgezet wordt in arbeid. Microtubuli die langs deze weg arbeid leveren kunnen gezien worden als *moleculaire (nano-)motoren.*

In Hoofdstuk 3 wordt het idee van het Brownse palrad toegepast op microtubuli. Het belangrijkste nieuwe ingredient dat toegevoegd wordt aan dit concept, is het collectieve karakter van de groei van microtubuli, aangezien deze polymeren bestaan uit meerder filamenten. Een belangrijke vraag is wat de maximale kracht is die deze motor kan leveren. Een tweede algemenere vraag is hoe de groeisnelheid afhangt van de tegenkracht uitgeoefend door een ander object. Hangt de groeisnelheid af van de ondetlinge configuratie van de protofilamenten van de microtubule? Met andere woorden, gegeven zijn structuur, is er een optimale manier voor een microtubule om tegen een kracht in te groeien. Wij onderzoeken dit voornamelijk door met behulp van computersimulaties modellen voor microtubule groei door te rekenen en te vergelijken met experimentele gegevens.

In Hoofdstuk 4 worden verschillende parameter-regimes voor microtubule groei beschouwd. De kwantitatieve vergelijking met de experimentele gegevens blijkt in haast alle gevallen succesvol, al is door het grote aantal van vrije parameters de noodzaak voor meer experimenten evident. Toch kunnen ook nu al kwalitatieve aspecten, zoals de structuur van het microtubule uiteinde, het aantal mogelijke modellen inperken. Zo laten cryo-elektronen microscopie beelden zien dat groeiende microtubuli een open plaatvormig uiteinde ontwikkelen. Het verdwijnen van deze eindstructuur wordt experimenteel in verband gebracht met het hypothetische schakel mechanisme dat de dynamische instabiliteit veroorzaakt. Het is dus redelijk aan te nemen dat een realistisch model voor groei dergelijke structuren reproduceert. Ons model laat zien dat er een gevoelige afhankelijkheid bestaat tussen de kinetische constanten en de laterale bindingenergie tussen de protofilamenten en de omvang van de eind-structuren. Alhoewel de vergelijking met de experimentele waarden niet volledig kwantitatief is, suggereert onze analyse wel dat de laterale binding tussen de protofilamenten relatief zwak is en slechts in de orde van enige kT per subeenheid.

In het tweede deel van het proefschrift behandel ik enige fysische aspecten van de ruimtelijke organisatie van microtubuli. Het belang van het begrip van de organisatie van het cytoskelet in het algemeen, en dus niet alleen van de microtubuli, is groot. Vanuit natuurkundig oogpunt, horen de vragen die in dit proefschrift aan de orde komen tot het veel bredere veld van patroonvorming in niet-evenwichts systemen. Het fundamentele vraagstuk hier is de relatie tussen de macroscopische eigenschappen van dissipatieve systemen en hun microscopische bouwstenen. Vanuit biologisch perspectief is het onderzoek naar de structuur van het cytoskelet nauw verweven met de functionele rol die biopolymere structuren spelen in de levende cel.

In hoofdstuk 5 richten wij onze aandacht op de organisatie van microtubuli in hogere planten cellen. Speciaal de microtubule structuren die gevonden worden in de interfase en vlak voor de celdeling hebben veel aandacht van de biologen gekregen, maar er is nog maar weinig bekend van de optredende organiserende mechanismes. In interfase cellen vormen de microtubuli de zogenaamde corticale microtubuli die dwars georienteerd is op de lange as van de cel. Net voor de deling vernauwd deze corticale microtubuli zich tot de preprofaseband die aangeeft waar de scheidingswand tussen de dochtercellen komt te liggen. Wij beschouwen vanuit natuurkundig perspectief welke *passieve* factoren een rol zouden kunnen spelen voor de waargenomen georganiseerde structuren. Een mogelijkheid dat uitgesloten volume interacties tussen de microtubuli aanleiding geven tot de vorming van een nematisch geordende structuur, welbekend uit de fysica van vloeibare kristallen. Dit mechanisme impliceert dat er een directe relatie moet bestaan tussen de dichtheid van de microtubuli en de graad van hun ordening. Een tweede mogelijkheid is dat de buigingsenergie van de microtubuli een drijvende factor is in de organisatie van de microtubuli op de cel cortex. Aangezien buigingselasticiteit een intrinsieke eigenschap is van microtubuli kunnen

we hier van *zelf-organisatie* spreken.

Actieve factoren zijn echter de beste kandidaten om grootschalige patroonvorming in filamenteuze systemen te bewerkstelligen. In het verleden werd reeds vastgesteld, zowel in experimenten als door middel van computer simulaties, dat motor eiwitten in staat zijn systemen van staafvormige deeltjes ruimtelijk te organiseren. Het volledige fasediagram van dergelijke systemen blijft echter nog steeds een open theoretische vraag. Op basis van een analyse van het fasediagram, is het mogelijk een minimale set van condities af te leiden die tot een bepaalde fenomenologie leiden. In de laatste twee hoofdstukken van het proefschrift worden twee verschillende aanpakken in deze richting ontwikkeld.

In Hoofdstuk 6 wordt een Landau-achtige gemiddelde veld theorie opgezet. In deze benadering wordt het gedrag van filamenteuze systemen beschreven zonder te referen aan de microscopische details. De enige echte voorwaarden die aan het systeem gesteld worden zijn het voldoen aan de gebruikelijke symmetrie eiegenschappen. Een van de resultaten van deze generieke benadering is de beschrijving van een transversale streep-fase, die veel lijkt op de waargenomen preprofase-band. Dit bemoedigende resultaat suggereert dat het inderdaad mogelijk is bestaande cytoskelet structuren vi deze aanpak te beschrijven.

In Hoofdstuk 7 wordt een microscopische theorie geintroduceerd op basis waarvan vervolgens de macroscopische evolutievergelijkingen worden afgeleid. Deze procedure is bedoeld om de generieke resultaten van Hoofdstuk 6 van onder-af her af te leiden. Afgezien van de actieve componenten, introduceer ik ook op dit niveau de sterische wisselwerkingen tussen de filamenten. Deze passieve interacties zijn verantwoordelijke voor de de isotroop-nematische instabiliteit die optreedt bij hogere dichtheden en het systeem drijven naar een vloeibaar kristallijn georedende fase. De actieve componenten echter zijn in staat het systeem al reeds bij veel lagere dichtheden tot patroonvorming te dwingen. De studie in dit hoofdstuk beperkt zich tot een lineaire stabiliteits analyse. De behaalde resultaten geven aan dat mogelijke stabiele patronen optreden in de vorm van nematische oplijning, vortices en asters. Deze observaties zijn consistent met de resultaten van eerdere benaderingen, zoals in vitro experimenten en computer simulaties. Een volledig inzicht in de optredende patronen vergt een analyse van de niet-lineaire termen in de evolutie vergelijkingen, hergeen het doel is van toekomstig onderzoek.

List of Publications

G.S. v Doorn, C. Tanase, B.M. Mulder, M. Dogterom
On the stall force for growing microtubules
Eur Biophys J (2000), p 29.

Tanase C., M. Dogterom, B.M. Mulder
Modeling the force production mechanism in growing microtubules (I)
In preparation

Tanase C., M. Dogterom, B.M. Mulder
Modeling the force production mechanism in growing microtubules (II): the lateral affinity between microtubule protofilaments
In preparation

Dogterom M, Janson ME, Faivre-Moskalenko C, Van der Horst A, Kerssemakers JWJ, Tanase C, Mulder BM
Force generation by polymerizing microtubules
Appl Phys A, 75 (2): 331-336 AUG 2002.

Cosentino Lagomarsino M., C. Tanase, B.M. Mulder, M. Dogterom
Modeling the dynamic spring with microtubules in micro-fabricated chambers
In preparation

Tanase C., M. Cosentino Lagomarsino, M. Dogterom, B.M. Mulder
Large scale instabilities driven by active components in filamentous systems
In preparation

Zumdieck A., M. Cosentino Lagomarsino, C. Tanase, B.M. Mulder, M. Dogterom, K. Karsten, F. Julicher
Mean field approach to preprophase band formation as motor-filament self-organization process
In preparation

Acknowledgments

This work would not have been possible without the help and support of many people. Part of this thesis is a result of a direct collaboration with a number of people to whom I wish to express my thanks.

First of all I am greatful to Bela Mulder, who offered me staunch support in innumerable circumstances. Bela gave me the opportunity and resources in pursuing different subjects. He motivated, and encouraged me many times during all these years. Potential flaws in some of the models that I used to consider would not have been corrected without his critical eye.

Marileen Dogterom was among the first persons who introduced me to biological physics, a very new and challenging field for me. With Marcel Janson I had many discussions about microtubule experiments, which helped me in modeling. Together with Marco Cosentino Lagomarsino I worked on the plant cell project, and I had the opportunity to exchange experience with a great colleague.

I thank Jan Vos and Anne Mie Emons for helpful discussions, and for patiently answering to my countless naive questions about the plant project.

Many thanks to Frank Julicher and Karsten Kruse for the opportunity of being introduced, together with Marco, to a new theoretical procedure, which is used in understanding a particular class of complex systems. Alexander Zumdieck worked together with us. I also want to thank Alexander, Karsten, and Frank for the very good time during our stay in Dresden.

Bela, thanks a lot again for your help and effort in reading the manuscript carefully. My trust in your proofreading gave me some comfort during writing. Marileen, Karsten, Frank, Jan, Anne Mie, and Simon gave many useful suggestions after reading the manuscript, and helped me in identifying and correcting some serious mistakes.

I am very pleased to remember my high school years, under the supervision of Viorel Malinovschi. He was the teacher who introduced me to the “untamed” world of theoretical physics.

Special thanks to my paranimfen, George and Adrian. To my parents, and to all people back home, for the warmth they allways offer to me and Mirela during holidays. To Camelia, Nelu, Lili, Radu, Violeta, and Cristian.

Dear Mirela, your support, trust, and patience are only examples to show how much I owe to you. Thanks for being. Your smile always gives me strength and motivation.

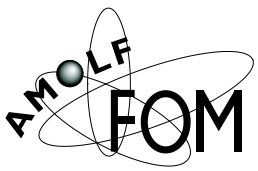

The work described in this thesis was performed at the FOM-Institute for Atomic and Molecular Physics, Kruislaan 407, 1098 SJ, Amsterdam, The Netherlands. The work is part of the research program of the Stichting voor Fundamenteel Onderzoek der Materie (FOM) and was made possible by financial support from the Nederlandse Organisatie voor Wetenschappelijk Onderzoek (NWO).